Prepared for:

Hydraulic roughness in sediment-laden flow

May, 2007

Prepared for:

Hydraulic roughness in sediment-laden flow

Supervisors:

prof.dr.ir. M.J.F. Stive
dr.ir. J.H. Winterwerp
dr.ir. Z.B. Wang
dr. D.S. van Maren

May, 2007

voor mijn vader

Preface

This report describes a research into the interaction between suspended sediment and hydrodynamics. More specifically it deals with hydraulic roughness in sediment-laden flow. The research study forms the completion of my Master's program Hydraulic Engineering at Delft University of Technology. For the greater part it was performed at WL | Delft Hydraulics. I was privileged to stay 3 months at the State Key Laboratory of Estuarine and Coastal Research, East China Normal University in Shanghai, China. I am grateful that I was given the opportunity to graduate in such a stimulating environment.

I would like to thank the people that were involved in this graduation project. First of all I want to express great gratitude to prof.dr.ir. M.J.F. Stive, who has been motivating and understanding throughout my whole Master's program. I would like to thank my supervisors at WL | Delft Hydraulics: dr.ir. J.H. Winterwerp, dr. D.S. van Maren and dr. ir. Z.B. Wang, and my supervisors at SKLEC in Shanghai for their hospitality: prof. P. Ding, prof. Q. He and dr. K. Hu

Furthermore I would like to thank Daan for his support and patience and for the effort he made and the time he spend on marking my writings. Gijs and Ties for helping me out. My colleague students at the 'Afstudeereiland': Pieter, Marjella, Inge, Paula, Ali and Robbert-Jan. I also thank Marcia and Erik. And finally I want to thank my housemates and the rest of my friends for making the period during graduation more fun.

Marieke Lely

Delft, 25 May 2007

Contents

List of Symbols

A	cross-sectional area
A_0	integration constant, *Coleman* [1986]
A_1	Monin-Obukhov coefficient *Taylor and Dyer* [1977]
A_2	Monin-Obukhov coefficient *Itakura and Kishi* [1980]: $A_2 = 7$
A_3	Monin-Obukhov coefficient *Adams and Weatherly* [1981]: $A_3 = 5.5$
a	reference level
a_{eb}	break-up efficiency parameter
a_*	empirical constant equation (3-21): $a_* = 0.76$
a_1	empirical constant, *Toorman* [2000]: $a_1 = 7.7$
b	flow width
b_*	empirical constant equation (3-21): $b_* = 1.45$
b_1	empirical constant, *Toorman* [2000]: $b_1 = 1/0.6$
C	Chézy coefficient
$C_{2\mathrm{Dh}}$	Chézy coefficient for 2Dh model without sediment effect
$C_{2\mathrm{Dh},\,b}$	Chézy coefficient for 2Dh model with sediment effect, determined through roughness parameterisation
$C_{2\mathrm{Dh},eff}$	Chézy coefficient for 2Dh model with sediment effect, determined through calibration
$C_{3\mathrm{D}}$	Chézy coefficient for 3D model without sediment effect
$C_{3\mathrm{D},eff}$	Chézy coefficient for 3D model with sediment effect, determined through calibration
C_b	surplus value Chézy coefficient due to sediment effect, determined through roughness parameterisation
C_z	turbulent vertical transport of suspended sediment
c	suspended sediment concentration by mass
c_D	drag coefficient, *Byun and Wang* [2005]
c_a	reference mass concentration

c_{gel}	gelling concentration
$\bar{c}$	depth-averaged suspended sediment concentration by mass
c_V	suspended sediment concentration by volume
c_f	dimensionless friction coefficient
$c_{1\varepsilon}$	coefficients in $k-\varepsilon$ turbulence model, *Winterwerp* [2001]
$c_{2\varepsilon}$	coefficients in $k-\varepsilon$ turbulence model, *Winterwerp* [2001]
$c_{3\varepsilon}$	coefficients in $k-\varepsilon$ turbulence model, *Winterwerp* [2001]
c_μ	coefficients in $k-\varepsilon$ turbulence model, *Winterwerp* [2001]
c_{1k}	coefficient in the $k-\omega$ turbulence model, *Yoon and Kang* [2005]
c_{2k}	coefficient in the $k-\omega$ turbulence model, *Yoon and Kang* [2005]
$c_{1\omega}$	coefficient in the $k-\omega$ turbulence model, *Yoon and Kang* [2005]
$c_{2\omega}$	coefficient in the $k-\omega$ turbulence model, *Yoon and Kang* [2005]
$c_{3\omega}$	coefficient in the $k-\omega$ turbulence model, *Yoon and Kang* [2005]
c_4	coefficient in the $k-\omega$ turbulence model, *Yoon and Kang* [2005]
c_γ	coefficient in the $k-\omega$ turbulence model, *Yoon and Kang* [2005]
D	particle size
D_e	equilibrium floc diameter
D_m	diameter of mud flocs
D_p	diameter of primary particles
D_s	molecular diffusion coefficient
E_b	rate of sediment exchange between bed and water column
e_c	efficiency coefficient for coagulation in flocculation model
e_d	efficiency coefficient for diffusion in flocculation model
F_t	damping function for momentum, *Toorman* [2000]
F_s	damping function for mixing (diffusity), *Toorman* [2000]
F_y	yield strength of flocs
f	Darcy-Weisbach friction factor

f_s	Darcy-Weisbach friction factor for sediment-laden flow, *Itakura and Kishi* [1980]
Δf	difference between two tidal frequencies
f_s	shape factor
f_{sed}	shape factor for sediment
G	dissipation parameter: $G = \sqrt{(\varepsilon/\nu)}$
g	acceleration of gravity
h	water depth
i_b	slope of the bottom
i_w	slope of the free surface
K_k	empirical parameter in consolidation module of 1DV model
K_p	empirical parameter in consolidation module of 1DV model
K_y	empirical parameter in consolidation module of 1DV model
K_μ	empirical parameter in consolidation module of 1DV model
K_1	coefficient in equation (3-10): $K_1 = 0.76h^{1.45}$
K_2	coefficient in equation (3-18)
k_b	Boltzman constant: $k_b = 1.38 \cdot 10^{-23}$ J/K
k	turbulent kinetic energy
k_A	$k_A = 0.75 e_c \pi\, e_d / f_s \rho_s D_p$, Appendix B
k_B	$k_B = k'_B / n_f$, Appendix B
k_s	dimension of wall roughness elements
k'_A	flocculation parameter: $k'_A = 1.5 e_c \pi\, e_d$
k'_B	floc break-up parameter: $k'_B = a_{eb} D_p^{-p} \left(\mu_s / F_y\right)^q$
k_N	$\left(D_p^{n_f - 3} / f_s \rho_s\right)^{\frac{1}{n_f}}$, Appendix B
L_t	turbulent length scale (mixing length)
l	characteristic length scale
L_{MO}	Monin-Obukhov length scale
M	empirical erosion parameter

m	coefficient in equation (3-1)
N	number concentration of mud flocs
n	Manning coefficient
n_c	empirical parameter in consolidation model
n_f	fractal dimension
n_1	empirical constant, *Toorman* [2000]: $n_1 = 0.85$
P	perimeter
P_t	tidal prism
p_f	exponent in flocculation model: $p_f = 3 - n_f$, Appendix B
p_s	effective stress
Q	river flow rate
q_f	exponent in flocculation model: $q_f = 0.5$, Appendix B
R	hydraulic radius
Re	Reynolds number
Re_p	particle Reynolds number: $\mathrm{Re}_p = w_{s,r} D/\nu$
Ri	gradient Richardson number
Ri_f	flux Richardson number
Ri_*	bulk Richardson number
$S(x)$	ramp function: $S = x$ for $x > 0$ and $S = 0$ for $x \le 0$, Appendix B
T	duration tidal cycle
T_{obs}	duration of observation
T_{rel}	relaxation time
T_w	absolute water temperature
U	characteristic velocity
U	horizontal flow velocity: $U = u + u'$
u	horizontal flow velocity averaged over the turbulent time-scale
u'	fluctuating component of the horizontal velocity
$\bar{u}$	depth-averaged horizontal flow velocity
u_*	shear velocity
u_{*c}	critical shear velocity

u_b	horizontal flow velocity near the bottom
u_t	characteristic velocity in a turbulent flow
u_m	horizontal velocity at the top of the logarithmic boundary layer
$u_{\max}$	maximum value of the horizontal velocity
$\bar{u}_0$	desired depth-averaged flow velocity, Appendix B
W	vertical velocity
w	vertical flow velocity averaged over the turbulent time-scale
w_s	settling velocity of sediment
$w_{s,r}$	settling velocity of individual particle
w'	fluctuating component of the vertical velocity
w'_{RMS}	RMS value of the vertical turbulent velocity fluctuations
x	horizontal coordinate
z	vertical coordinate
z_b	bed level
z_*	relative depth, $z_* = z/h$
z_{bc}	apparent roughness height, Appendix B
z_s	level of the water surface
z_{wc}	roughness length for current and waves
z_0	roughness height
α_0	coefficient in equation (3-1)
α_1	modification factor, *Toorman* [2000]
α_*	multiplication factor, $z_{0,1} = \alpha_* z_{0,2}$
α_τ	proportionality constant: $\tau_b = \alpha_\tau \bar{u}$
α_L	coefficient related to the mixing length, *Umeyama and Gerritsen* [1992]
α_s	stratification parameter, *Simmons* [1955]
β	Rouse number: $\beta = w_s/\kappa u_*$
δ_l	thickness of laminar sub layer

δ_t	thickness of turbulent boundary layer
γ_1	empirical constants, *Soulsby and Wainwright* [1987]
γ_2	empirical constants, *Soulsby and Wainwright* [1987]
γ_L	adjustable constant, *Umeyama and Gerritsen* [1992]
Γ	gamma function, equation (A-3)
Γ_t	eddy diffusivity
Γ_c	diffusion coefficient in consolidation formula
Γ_t^c	eddy diffusity for sediment, *Winterwerp* [2001]
$\Gamma_{t(s)}$	eddy diffusity for sediment-laden flow, *Toorman* [2000]
ε	turbulent energy dissipation
ζ	Monin-Obukhov stability parameter
ζ_{cr}	critical value of Monin-Obukhov stability parameter: $\zeta_{cr} = 0.03$
η	molecular viscosity
η_t	turbulent viscosity
θ_d	non-dimensional threshold shear stress for deposition: $\theta_d = \tau_b / \tau_d$
θ_e	non-dimensional threshold shear stress for deposition: $\theta_e = \tau_b / \tau_e$
κ	Von Kármàn coefficient
κ_s	Von Kármàn coefficient for sediment-laden flow
μ_s	dynamic viscosity of sediment suspension
ν	kinematic viscosity
ν_s	kinematic viscosity for sediment-laden flow
ν_{δ_t}	kinematic viscosity in the logarithmic boundary layer, *Coleman* [1986]
$\nu_{t(s)}$	eddy viscosity for sediment-laden flow
ν_t	eddy viscosity
Ξ_s	settling function
Π	wake strength coefficient, *Coleman* [1986]
ρ	density of the fluid
ρ_f	floc density

$\rho_{f,e}$	equilibrium floc density
ρ_s	density of sand
ρ_w	density of water
ρ'	fluctuating component of the density
ρ_0	density of the fluid near the bottom
σ_t	turbulent Prandtl–Schmidt number
σ_t^k	turbulent Prandtl–Schmidt number for k, *Winterwerp* [2001]
σ_t^ε	turbulent Prandtl–Schmidt number for ε, *Winterwerp* [2001]
σ_t^c	turbulent Prandtl–Schmidt number for sediment, *Winterwerp* [2001]
τ	shear stress
τ_b	bottom shear stress
τ_d	threshold shear stress for deposition
τ_e	threshold shear stress for erosion
τ_{xz}^s	inter-particle stresses
τ_s	surface shear stress
τ_{sf}	side wall friction
τ_y	yield stress
Φ	non-dimensional shear
ϕ	volumetric concentration of mud flocs
ϕ_*	min {1, ϕ}, Appendix B
ϕ_p	volumetric concentration of primary particles
φ	$\varphi = A_1 \nu_s / u_* L_{MO}$, *Itakura and Kishi* [1980]
φ_1	$\varphi_1 = A_1 k_s / L_{MO}$, *Itakura and Kishi* [1980]
φ_2	$\varphi_2 = A_1 h / L_{MO}$, *Itakura and Kishi* [1980]
ω	characteristic time scale of the turbulence, *Yoon and Kang* [2005]
ω_{WR}	functional symbol for the wake region function, *Coleman* [1986]

Summary

Most estuarine, and some coastal, areas are characterised by large amounts of fine-grained cohesive and non-cohesive sediments. At sufficiently high concentrations, sediment transport in suspension may significantly influence the hydrodynamics. In sediment-laden flow with concentrations of approximately $c \geq 0.5\,\mathrm{g/l}$, stratification may occur due to a vertical gradient of sediment concentration. In a stratified flow, turbulence is damped due to buoyancy destruction. According to many reports in literature buoyancy destruction results in a decrease of effective hydraulic roughness. Furthermore, the sediment induced stratification causes an appreciable modification of the vertical profiles of velocity, vertical eddy viscosity and shear stresses (e.g. *Winterwerp* [2001]). Considering the propagation of a tidal wave in estuaries, the decrease of roughness results in an increase of the depth-averaged velocity and an increase of tidal amplitudes of the water level.

When modelling flow behaviour in estuarine and coastal environments, vertical gradients of horizontal velocity and sediment and salt concentration in stratified systems can only be simulated with three dimensional numerical modelling. However a full three dimensional model is not always practical. The wide shallow domains that occur in civil engineering practice make depth-averaged simulation often necessary in view of the computational demands. However no theoretically accepted, justifiable parameterisation for effective hydraulic roughness in turbulent sediment-laden flow exists to date. Therefore the effect of suspended sediment on tidal propagation in estuaries is not accounted for in 2Dh modelling. This makes 2Dh modelling intrinsically less accurate than 3D. In case the flow contains an appreciable amount of suspended sediment it is difficult to reliably predict flow behaviour in estuaries through 2Dh modelling. In depth-averaged equations solved in 2Dh models, the bottom shear stress is explicitly prescribed using a friction coefficient. The reduction of hydraulic roughness due to stratification can in this case effectively be accounted for by alteration of the friction coefficient.

By applying theories commonly used for stratified flow in the earth's atmosphere and taking into account the free surface effects, the following depth-averaged friction law was derived:

$$\frac{\bar{u}}{u_*} = \frac{1}{\kappa}\left[\ln\left\{\frac{h}{z_0}\right\} - 1\right] + \left(K_1(h)\right)\left(Ri_*\beta\right)^m$$

$$\frac{\bar{u}}{u_*} = \frac{1}{\kappa}\left[\ln\left\{\frac{h}{z_0}\right\} - 1\right] + \left(0.76h^{1.45}\right)\left(Ri_*\beta\right) \qquad \text{for} \qquad h \le 10 \text{ m}$$

$$\frac{\bar{u}}{u_*} = \frac{1}{\kappa}\left[\ln\left\{\frac{h}{z_0}\right\} - 1\right] + \left(0.76h^{1.45}\right)\left(Ri_*\beta\right)^{1.3} \qquad \text{for} \qquad h \ge 10 \text{ m}$$

With:

$$\frac{\bar{u}}{u_*} = \frac{C_0}{\sqrt{g}} + \frac{C_b}{\sqrt{g}}$$

$$\frac{C_{eff}}{\sqrt{g}} = \frac{C_0}{\sqrt{g}} + \frac{C_b}{\sqrt{g}}$$

This friction law is validated by numerical experiments with the 1DV POINT MODEL. These numerical experiments show that the buoyancy effect is small compared to the integral effect of sediment in nature that is reported in literature.

To further evaluate the depth-averaged roughness parameterisation it is applied to a numerical model of the Yangtze Estuary (China). Calibration shows that the bottom of the Yangtze Estuary is very smooth even without the buoyancy effect, and that the buoyancy effect decreases the effective roughness further. For the Yangtze Estuary the buoyancy effect is properly simulated by the depth-averaged roughness parameterisation. Through the parameterisation the effective Chézy coefficient is increased from $C_{2\mathrm{Dh}} = 110 \text{ m}^{1/2}/\text{s}$ for clear water to $C_{2\mathrm{Dh},b} \approx 125 \text{ m}^{1/2}/\text{s}$ for flow conditions commonly found in the Yangtze Estuary. Thereby the sediment-induced error in 2Dh modelling is reduced by approximately 75%. From this it is concluded that 2Dh modelling becomes more accurate through application of the roughness parameterisation.

Several other issues can be done that might increase the reliability of 2Dh models even more. For example it is recommended to implement the roughness parameterisation in the numerical code of DELFT3D-FLOW, so that the effective hydraulic roughness is continuously updated with feedback to hydrodynamics and sediment transport.

1 Introduction

1.1 Background

Most estuarine, and some coastal, areas are characterised by large amounts of fine-grained cohesive and non-cohesive sediments. The presence of these sediments is of great importance. It may be valuable, e.g. to ecosystems, to the economy (beaches attract tourism) or to safety. However the presence of sediment is not always desirable, e.g. it may be a nuisance to coastal management and port authorities. Sedimentation in harbour basins and fairways may obstruct shipping. In that case sediment must be removed, for instance by dredging. The prediction of sediment transport based on an understanding of its processes can be of great importance.

Sediment transport depends on fluid dynamics. However fluid dynamics is also strongly influenced by the presence of suspended sediment. In shallow water flows, laden with large amounts of sediment (approximately concentrations $c \geq 0.5\,\mathrm{g/l}$), stratification may occur due to a vertical gradient of sediment concentration. In a stratified flow, buoyancy destruction damps turbulence (section 2.3.2). According to literature buoyancy destruction may be the explanation for apparent drag reduction in sediment laden flow. This apparent drag reduction may result in an increase of the depth-averaged velocity and an increase of tidal amplitudes of the water level in estuaries. This has been verified by field studies. For example in the Amazon it has been shown that the presence of suspended sediment allows larger tidal amplitudes of the water level (*Vinzon and Metha* [2001], *Gabioux et al.* [2004]). Furthermore, the sediment-induced stratification may cause an appreciable modification of the vertical profiles of velocity, vertical eddy viscosity and shear stresses (e.g. *Winterwerp* [2001]). Prediction of water levels and current velocities to the right order of magnitude is of great importance to coast and river engineers.

Nowadays numerical models are widely used for engineering and scientific purposes. The interaction between sediment and the turbulent water movement is an important aspect in such models. The present study is dedicated to the interaction between sediment and hydraulic roughness, with the intention to improve predictability of depth-averaged

numerical models. More accurate predictions can lead to a better understanding, which can finally lead to social and economical benefits in coastal regions.

1.2 Problem description

A literature study conducted within this research revealed that one effect of suspended sediment on the flow behaviour can be interpreted as a stratification effect. The sediment-induced stratification damps turbulence due to buoyancy destruction. Many researchers claim that this buoyancy effect is quite significant. Studies reported on an effective reduction of the Von Kármàn coefficient by 50% (*Vanoni* [1977]), a decrease of bottom shear stress by 45% (*Adams and Weatherly* [1981]) and a decrease of turbulent kinetic energy level of 40% (*Adams and Weatherly* [1981]). *Winterwerp* [2001] showed that three dimensional numerical models are able to account for the stratification effects induced by the interaction between suspended sediment and the turbulent water movement.

Vertical gradients of horizontal velocity and sediment and salt concentration in a stratified system can only be modelled with three dimensional numerical modelling. However, a full three dimensional model is not always practical. The wide shallow domains that occur in civil engineering practice make depth-averaged simulation often necessary in view of the computational demands. When integrated over depth, the model cannot compute the stratification effects and therefore sediment transport and flow behaviour will not be simulated properly.

For flows over rough boundaries, turbulent shear dominates the resistance of the flow. Suspended sediment suppresses the development of turbulence, so that the resistance is reduced. The suspended sediment effect has often been reported as an apparent smoothing of the bed. Literature on numerical studies of a flow area with high concentrations of suspended sediment often report on extreme values for the roughness coefficients, e.g. effective Chézy coefficients of around 120 $m^{1/2}/s$ (*PDC* [1999], *Van Ormondt* [2004]). In depth-averaged equations solved in so called 2Dh models, the bottom shear stress is explicitly prescribed using a friction coefficient. In these 2Dh models the apparent smoothing effect due to stratification can be simulated by adjusting the friction coefficient. However, currently no reliable parameterisation for hydraulic roughness in sediment-laden flow can be found in literature, of which the author is aware, so that the suspended sediment effect is not properly included in present 2Dh models.

Problem definition

Currently no theoretically accepted, justifiable parameterisation for effective hydraulic roughness of turbulent sediment-laden flow exists. Therefore the effect of suspended sediment on tidal propagation in estuaries cannot be accounted for in 2Dh modelling. This makes it difficult to reliably predict flow behaviour in estuaries through 2Dh modelling, in case the flow contains an appreciable amount of suspended sediment.

1.3 Objectives

The aim of the project is to define a parameterisation for the effect of suspended sediment on the effective hydraulic roughness in turbulent sediment-laden flow. This parameterisation can be used to efficiently model the flow behaviour in estuaries, using depth-averaged models. Together with the problem definition this leads to the following research question:

How can the effect of suspended sediment on effective hydraulic roughness in sediment-laden flow be parameterised so that it can be properly simulated with a depth-averaged numerical model?

This research question is analyzed through assessment of the following hypotheses:

- The damping of turbulence due to sediment induced stratification will result in a significant decrease of the effective hydraulic roughness.
- An effective way to account for the suspended sediment effect in 2Dh models is to correct the effective hydraulic roughness: 2Dh model results will become more accurate.

The set-up of this research study is as follows:

1. Literature Study (Chapter 2)
   This literature study gives insights into the existing theories on sediment-laden flow.
2. Theory on hydraulic roughness in sediment-laden flow (Chapter 3)
   From the literature study a theory on hydraulic roughness in sediment-laden flow is derived. A depth-averaged roughness parameterisation is set up.
3. 1DV POINT MODEL (Chapter 3)
   By use of the 1DV point model the parameterisation is validated.
4. Yangtze Estuary Model (Chapter 4 and 5)

In order to see whether a depth-averaged model indeed becomes model accurate, the parameterisation will be applied to a practical case, i.e. the Yangtze Estuary. Chapter 4 presents the calibration of both the three dimensional model and the depth-averaged model. After calibration, the parameterisation is applied. The results are presented in Chapter 5. These results are compared with the results of the calibration runs.

Furthermore chapter 6 presents a discussion in which the hypotheses will be analysed. In the seventh and last chapter, the conclusions of this research are formulated as well as recommendations for further research on this topic.

2 The suspended sediment effect: A literature review

2.1 Introduction

There are numerous publications on the effect of suspended sediment on flow behaviour and numerous theories for sediment-laden flow have been developed. However, many questions have not yet been resolved, e.g. whether the effect of sediment on flow behaviour is limited to a certain region in the water column. This chapter presents a short overview of different approaches for modelling the suspended sediment effect.

In section 2.2 and 2.3 first the relevant traditional theory is discussed. Before we treat the modified theories for sediment-laden flow, the scope within which this research is assumed applicable is stated, in section 2.4. Considering these assumptions, several modifications on the clear-water theory have been proposed. Different approaches for modifications that are referred to more often will be discussed in section 2.5 to 2.8. Section 2.9 deals with literature focussing on hydraulic roughness. Finally in section 2.10 there is a brief discussion on the findings concerning the suspended sediment effect and on how to model the effect on hydraulic roughness. Here it is determined what approach will be used for the rest of the research project.

2.2 Hydrodynamics and hydraulic roughness in clear water

The purpose of this section is to cover the aspects of the basic theory on clear water flow that are effected by suspended sediment, e.g. bed roughness, friction coefficient, shear stresses, turbulence and velocity distribution. The traditional theory which is discussed in this section is valid for clear water flow. The equations that are presented are often referred to in literature on sediment-laden flows.

2.2.1 Laminar and turbulent flow

A flow can be characterized as either laminar or turbulent. Whether one deals with a laminar or turbulent flow depends on the Reynolds number:

$$\mathrm{Re} = \frac{Ul}{\nu} \tag{2-1}$$

where U is a characteristic velocity of the flow, l a characteristic length scale and ν is the kinematic viscosity. For small Reynolds numbers ($\mathrm{Re} < 1000$) viscosity dominates and the flow will be laminar. In civil engineering applications large dimensions give rise to turbulence ($\mathrm{Re} > 4000$). Open channel flows are almost always turbulent. In this research the flow is assumed to be turbulent.

Turbulent motion is an irregular or random motion. Therefore one needs a statistical approach to describe turbulent flow. In turbulent flow, exchange of momentum is caused by irregularly moving (fluid) parcels. The parcels move both horizontally and vertically. The instantaneous velocity components in the horizontal and vertical direction can be defined as:

$$\begin{aligned} U &= u + u' \\ W &= w + w' \end{aligned} \tag{2-2}$$

where U and W are the instantaneous velocities in horizontal and vertical direction, u and w are the horizontal and vertical velocity averaged over the turbulent time scale and u' and w' are the fluctuating components of the velocity.

Turbulent open channel flows consist of several regions, which are classified as follows. Near the bottom there is the thin viscous sub-layer where there is almost no turbulence. Measurements have shown that the viscous shear stress in this layer is constant and equal to the bottom shear stress. The flow in this layer is laminar. Above this layer, there is a transition layer. In the transition layer viscosity and turbulence are equally important. Above the transition layer, the flow becomes predominantly turbulent. In the turbulent layer viscous shear stress is negligible. The Prandtl's mixing length theory was developed for this layer and leads to the logarithmic velocity profile, which will be discussed later on. Higher

up in the water column, outside the logarithmic layer one finds the turbulent outer layer or wake region.

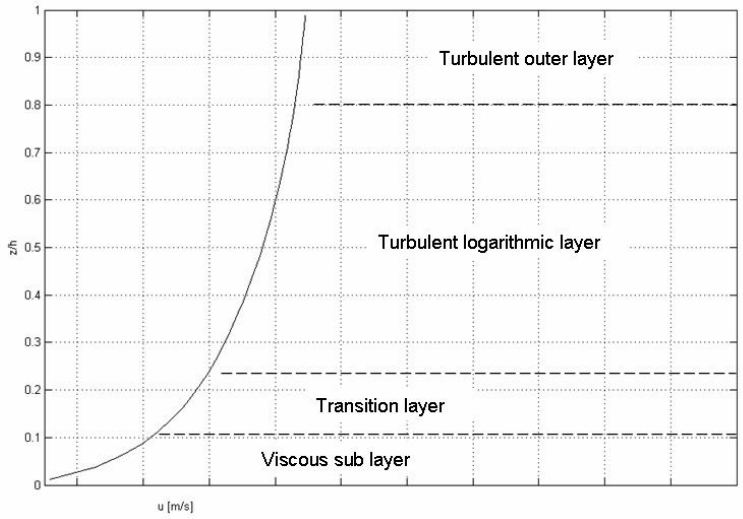

Figure 2.1: Structure of the water column

2.2.2 Constitutive relations in a turbulent flow

The average shear stress in the flow is assumed to be proportional to the velocity gradient. This proportionality is dependent on the viscosity. In laminar flow this results in the following expression:

$$\tau = \rho \nu \frac{\mathrm{d}u}{\mathrm{d}z} \tag{2-3}$$

$$\text{with } \nu = \frac{\eta}{\rho} \tag{2-4}$$

where τ is the shear stress, η is the molecular viscosity, ρ is the density of the fluid and $\mathrm{d}u/\mathrm{d}z$ is the velocity gradient in vertical (z) direction. For turbulent flow this relation changes to:

$$\tau = \rho \nu_t \frac{\mathrm{d}u}{\mathrm{d}z} \tag{2-5}$$

with $\nu_t = \frac{\eta_t}{\rho}$ (2-6)

where η_t is the turbulent viscosity and ν_t is the eddy viscosity. The kinematic viscosity ν is a characteristic of the fluid, while the turbulent eddy viscosity ν_t is a characteristic of the turbulent flow.

The eddy viscosity can be modelled as the product of a velocity (u_t) and a length scale (L_t), which can be interpreted as the magnitude of the turbulent eddies.

$$\nu_t = u_t L_t \tag{2-7}$$

Following Prandtl's mixing length hypothesis, the velocity that characterizes the turbulence fluctuations is proportional to the velocity difference in the mean flow over a distance L_t and can be expressed as follows:

$$u_t = L_t \frac{\mathrm{d}u}{\mathrm{d}z} \tag{2-8}$$

Substituting (2-7) and (2-8) into (2-5), gives an expression for the shear stress, i.e.:

$$\tau = -\rho \underbrace{L_t^{\,2} \left|\frac{\mathrm{d}u}{\mathrm{d}z}\right|}_{\nu_t} \frac{\mathrm{d}u}{\mathrm{d}z} \tag{2-9}$$

u_t depends on the shear in the flow and is, based on dimensional arguments, proportional to the shear velocity, i.e.:

$$u_* = L_t \frac{\mathrm{d}u}{\mathrm{d}z} = \sqrt{\tau_b / \rho} \tag{2-10}$$

The characteristic length scale is assumed to be proportional to the distance from the wall according to $L_t = \kappa z$, in which κ is the Von Kármàn coefficient, which for clear water has

a value of 0.41. Thus the following equations for the turbulent boundary layer can be derived:

$$\nu_t = \kappa u_* z \tag{2-11}$$

$$\tau = \rho \kappa u_* z \frac{\mathrm{d}u}{\mathrm{d}z} \tag{2-12}$$

where z is the height above the bed.

2.2.3 Velocity profile in a turbulent flow

Close to the wall the local shear stress can be assumed to be equal to the bottom shear stress $\tau \approx \tau_b$. Equation (2-12) can be rewritten into:

$$\frac{\mathrm{d}u}{\mathrm{d}z} = \frac{u_*}{\kappa}\frac{1}{z} \tag{2-13}$$

Integration of equation (2-13) gives the well known logarithmic velocity profile:

$$\frac{u}{u_*} = \frac{1}{\kappa}\ln\frac{z}{z_0} \tag{2-14}$$

where z_0 is the integration constant, also referred to as the roughness height.

Integrating (2-14) over depth (h) gives the depth-averaged velocity for clear water flow:

$$\frac{\bar{u}}{u_*} = \left[\frac{1}{\kappa}\ln\left(\frac{h}{z_0}\right) - 1\right] \tag{2-15}$$

In the case of hydraulically smooth flow there is a viscous sub-layer. The viscous shear stress is constant in the viscous sublayer and equal to the bottom shear stress:

After integrating $\tau_b = \rho\nu \left.\frac{\mathrm{d}u}{\mathrm{d}z}\right|_{z=0}$, the viscous velocity profile becomes:

$$u(z) = \frac{\tau_b/\rho}{\nu} z = \frac{u_*^2}{\nu} z \qquad (2\text{-}16)$$

2.2.4 Smooth and rough wall conditions

Turbulent flows can be divided into flows with hydraulically smooth and hydraulically rough wall conditions. Whether one deals with a relatively smooth or rough condition depends on the relative roughness δ_l/k_s, where k_s is the dimension of the wall roughness elements and δ_l is the thickness of the laminar sub-layer. In case $k_s << \delta$ the wall is hydraulically smooth and the roughness elements are within the laminar sub-layer close to the wall and do not penetrate into the turbulent flow region. In case these roughness elements are large enough to penetrate into the turbulent mean flow region, the wall is hydraulically rough.

Hydraulically smooth wall conditions

For hydraulically smooth wall conditions z_0 is proportional to the thickness of the viscous, laminar, sub-layer (δ_l). The thickness of the laminar sub-layer δ_l is proportional to ν/u_*. This yields z/z_0 proportional to z/δ_l or $u_* z/\nu$. Nikuradse's measurements under hydraulically smooth wall conditions showed that:

$$z_0 = \frac{\nu}{9u_*} \qquad (2\text{-}17)$$

Hydraulically rough wall conditions

Based on dimensional arguments, z_0 for hydraulically rough conditions is proportional to Nikuradse's roughness parameter k_s. From this it follows that z/z_0 is proportional to z/k_s. Nikuradse showed through measurements that:

$$z_0 = \frac{k_s}{30} \qquad (2\text{-}18)$$

2.2.5 Friction coefficient from logarithmic velocity profile

Because the bed shear stress can be written as the product of the flows momentum and a friction coefficient it is common to write:

$$\tau_b = \rho u_*^2 = c_f \rho \bar{u}^2 \tag{2-19}$$

where c_f is the dimensionless friction coefficient.

From this it can be derived that:

$$\frac{\bar{u}}{u_*} = \frac{1}{\sqrt{c_f}} \tag{2-20}$$

Substituting equation (2-20) into equation (2-15) one finds the following expression for the friction coefficient c_f:

$$\frac{1}{\sqrt{c_f}} = \left[\frac{1}{\kappa} \ln\left(\frac{h}{z_0} \right) - 1 \right] \tag{2-21}$$

For open channel flows the wall conditions are in most cases hydraulically rough. If the expression for hydraulically rough conditions (2-18) is substituted into equation (2-21) the following relation results:

$$\frac{1}{\sqrt{c_f}} = \left[\frac{1}{\kappa} \ln\left(\frac{30h}{k_s} \right) - 1 \right] \tag{2-22}$$

In equation (2-22) the friction coefficient c_f only depends on the relative roughness h/k_s.

2.2.6 Empirical roughness formulas

In the next section two famous empirical roughness formulas will be discussed: the Chézy and Manning formulas. It will be shown how they are related to each other. In this research project, titled 'Hydraulic roughness in sediment-laden flow', one of the aspects that is to be investigated is how the roughness coefficient changes due to the presence of a sediment load in the flow. Several researchers have already reported significant changes of the Manning and Chézy coefficients (*PDC* [1999], *Wang et. al.* [1998], *Winterwerp* [1999]). Furthermore, both parameters are often used as input parameters in numerical models, e.g. in the numerical model DELFT3D. It has been shown that these models can be very sensitive to changes of the Chézy of Manning coefficient (*Wang* [1994]). In the next section the formulas for clear water flow will be derived.

Chézy

In a turbulent rough flow τ_b is proportional to $\bar{u}^2$, which can be expressed as:

$$\tau_b = \alpha_\tau \bar{u}^2 \tag{2-23}$$

where α_τ is a proportionality constant. For a uniform flow the following relation can be defined (*Battjes*, lecture notes [2002]) :

$$\tau_b = \rho g R i_b \tag{2-24}$$

where g is the acceleration due to gravity and R is the hydraulic radius, which is the wet cross section of a channel divided by the wet surface or perimeter (A/P) and i_b is the slope of the channel, which for uniform steady flows is equal to the slope of the free surface, i_w.

Substituting (2-23) into equation (2.24) gives:

$$\bar{u} = \sqrt{\frac{\rho g}{\alpha_\tau} R i_b} \tag{2-25}$$

Grouping the constants results in the Chézy equation:

$$\bar{u} = C\sqrt{Ri_b} \tag{2-26}$$

where C is the Chézy coefficient.

Substituting equation (2-16) into equation (2-24) gives the following relation for the depth-averaged velocity:

$$\bar{u} = \frac{1}{\sqrt{c_f}}\sqrt{gRi_b} \tag{2-27}$$

So that:

$$C = \sqrt{\frac{g}{c_f}} \quad \text{or} \quad c_f = \frac{g}{C^2} \tag{2-28}$$

From equation (2-28) one can easily recognise the dimension of the Chézy coefficient. The dimension of C is $L^{1/2}/T$, which is the dimension of $\sqrt{g}$.

With the above relations, equation (2.20) can be rewritten to:

$$\frac{\bar{u}}{u_*} = \frac{C}{\sqrt{g}} \tag{2-29}$$

From equation (2-22) another expression for the Chézy coefficient can be derived, i.e.:

$$C = 5.57\sqrt{g}\ \log\left(12\frac{R}{k_s}\right) = 18\log\left(\frac{12R}{k_s}\right) \tag{2-30}$$

Manning

The second formulation, which is often used to express the hydraulic roughness is the formulation of Manning. Manning's semi-empirical relation is the following:

$$\bar{u} = \frac{1}{n} R^{2/3} \sqrt{i_w} \qquad (2\text{-}31)$$

in which n is often referred to as Manning's n. The dimension of n is $L^{-1/3}/T$. The formula only holds for hydraulically rough conditions. Manning's n depends on gravitational acceleration as well as on the roughness of the bottom. However n is independent of the viscosity.

The relation between Manning and Chézy coefficient is the following:

$$C = \frac{R^{1/6}}{n} \qquad (2\text{-}32)$$

2.3 Turbulent mixing in stratified flows

2.3.1 General

In a turbulent flow, turbulence affects the vertical velocity distribution and shear stresses, as well as vertical profiles of density, salinity, suspended sediment, temperature, etc. In a stratified flow, the vertical density distribution not only affects the flow behaviour, but also the intensity and structure of the turbulent movements. This results in a mutual effect on velocity and density profiles caused by both the density differences as well as by turbulence.

As was shown in section 2.2.2., according to Prandtl's mixing length hypothesis the (turbulent) shear stress can be expressed by:

$$\tau = -\rho \underbrace{L_t^{\,2} \left| \frac{\mathrm{d}u}{\mathrm{d}z} \right|}_{\nu_t} \frac{\mathrm{d}u}{\mathrm{d}z}$$

This equation represents the vertical transport of horizontal momentum, with ν_t the turbulent viscosity. A parabolic viscosity profile, which leads to the logarithmic velocity profile, is written as:

$$\nu_t = \kappa u_* h z_* (1 - z_*) \tag{2-33}$$

Where $z_* = z/h$. Assuming that the presence of suspended matter does not influence the turbulence in the flow, then the turbulent transport of matter (e.g. suspended sediment) can be analysed in the same way as transport of momentum, i.e.:

$$C_z = \underbrace{-L_s^2 \left|\frac{\mathrm{d}u}{\mathrm{d}z}\right|}_{\Gamma_t^c} \frac{\mathrm{d}c}{\mathrm{d}z} \tag{2-34}$$

where C_z is the turbulent transport and Γ_t^c is the turbulent (eddy) diffusity of suspended matter (e.g. suspended sediment).

However, inreality, vertical density differences do affect turbulence. A vertical density gradient, with density decreasing from bottom to surface, has a stabilising effect on turbulent movements. The stability can be expressed by the gradient Richardson number:

$$Ri = \frac{-g \dfrac{\partial \rho}{\partial z}}{\rho \left(\dfrac{\partial u}{\partial z}\right)^2} \tag{2-35}$$

In stratified flow, for the vertical transport of fluid or suspended matter work must be done. As a result the vertical velocity components and the mixing length, depend on the level of stratification, thus on the gradient Richardson number. To account for the stratification effect it is hypothesised (*Kranenburg* [1998]) that the turbulent transport and shear stress depend on the gradient Richardson number, according to:

$$C_z = -L_s^2 \left|\frac{\mathrm{d}u}{\mathrm{d}z}\right| \frac{\mathrm{d}c}{\mathrm{d}z} F(Ri) \tag{2-36}$$

$$\tau = -L_t^2 \left|\frac{\mathrm{d}u}{\mathrm{d}z}\right| \frac{\mathrm{d}u}{\mathrm{d}z} G(Ri) \tag{2-37}$$

where $F(Ri)$ and $G(Ri)$ are damping functions depending on the gradient Richardson number. Some alternatives of this hypothesis can be found in the discussion on the suspended sediment effect (section 2.5 to 2.8).

2.3.2 The buoyancy effect

The buoyancy effect follows directly from the theory on turbulent mixing in stratified flows. The flow in an open channel, which is subject to our research, is almost always a turbulent flow. Where there is a velocity gradient in an open channel flow, turbulence is produced. A turbulent fluctuation will induce a turbulent shear stress. Near the bottom of a channel there is a strong gradient, which results in a large production of turbulence. Sediment in the flow is held in suspension by turbulent fluctuations. Suspended sediment may induce a density gradient. A density gradient over the water column has a stabilizing effect on the turbulent fluctuations. Damping of the turbulent movements reduces the turbulent mixing of sediment, which in turn results in a stronger density gradient. This positive feedback between the suspended sediment and the turbulence field may cause a catastrophic collapse of the vertical turbulence structure. The stabilization of turbulent movements due to suspended sediment is known as the buoyancy effect. In a two-dimensional channel flow with sediment in suspension, the downward flux of sediment due to settling must be balanced by an upward flux due to turbulence lifting. So to keep the sediment in suspension, or buoyant, work must be done. A change in turbulence intensity due to a fluid density gradient in the water column caused by suspended sediment causes the velocity profile to be different from the clear water case.

2.4 Suspended sediment theory: Introduction

In the previous sections the basic theory for clear water was discussed. To account for the effect of the presence of suspended sediment in the flow, many researchers thought of a modification of the clear water theory. This resulted in many suspended sediment theories. To validate these theories numerical model were set up. Analytical model results were compared with numerical model results or experimental data. Furthermore to analyse numerical models, results were compared with observation data. In the section 2.5 to 2.8 suspended sediment theories and different approaches for analysing these theories will be discussed. First, in section 2.4.1 the research field is marked out by initial assumptions.

2.4.1 Scope of the theory: Assumptions

Non-cohesive versus cohesive suspended sediment

One of the characteristics of sediment-laden flow is the type of the suspended sediment. One can make a distinction between cohesive and non-cohesive suspended sediment. *Winterwerp* [2001] discusses the difference between cohesive and non-cohesive sediments in their interactions with turbulent flow. Consider a steady state flow at its carrying capacity with non-cohesive sediment in suspension. When the flow velocity decreases, or the amount of suspended sediment increases, the carrying capacity will be exceeded, which results in deposition of part of the sediment load. Upon deposition the non-cohesive sediments form a rigid bed at which turbulent production is possible. This is different for a sediment-laden flow close to its sediment-carrying capacity with a cohesive sediment load. When the flow velocity decreases cohesive sediments form a fluid mud layer. Over this mud-layer there is little turbulence production and hence turbulent mixing is strongly damped. This can result in a total collapse of the vertical turbulence field. For non-cohesive sediment the buoyancy effect yields appreciable stratification effects at already moderate sediment concentrations, while for cohesive sediment the same amount of sediment can result in a complete collapse of the turbulence flow field. This research focuses on the concentration regime below capacity concentration. In this regime, the sub-saturated high-concentration regime, the suspended sediment effect becomes important, affecting the vertical concentration and velocity profiles. Here it is assumed that in this sub-saturated regime the suspended sediment effect is similar for both cohesive and non-cohesive sediment, so the type of suspended sediment is irrelevant for the parameterisation of the suspended sediment effect. The different concentration regimes as they are defined by *Winterwerp* [2001, 2006] will be further discussed in the next section.

Low, medium and very high concentrations

As was already anticipated in the previous section sediment-laden flow can be characterised by its concentration level of the suspended sediment. According to *Winterwerp* [2006] three concentration regimes can be distinguished. He introduced a stability diagram which distinguishes between (low and high) sub-saturated flow, super-saturated flow, and hyper-concentrated sub-saturated flow. At low concentrations the flow is sub-saturated, the water column is able to carry more sediment and bed erosion can occur. Due to the presence of sediment in the flow, turbulent fluctuations are damped. When concentration increases, the

concentration level may reach a certain point at which the turbulent fluctuations are damped completely, which results in a collapse of turbulence and of the concentration profile; sub-saturated becomes super-saturated. When the concentration increases even further, hindered settling becomes important, which reduces the energy required to keep the sediment in suspension. Due to hindered settling effects the fluid can carry more sediment: super-saturated flow becomes hyper-concentrated sub-saturated flow. This research focuses on the high-concentrated, sub-saturated regime, up to ca. 15 g/l.

The transition between the different regimes can be quantified by the flux Richardson number (Ri_f) related to the sediment concentration.

$$Ri_f = -\frac{g\overline{w'\rho'}}{\rho\overline{u'w'}\partial u/\partial z} \qquad (2\text{-}38)$$

where u' and w' denote the fluctuating parts of the horizontal and vertical velocity components respectively, ρ is the density of the water-sediment mixture and ρ' is the fluctuating component of the density and g is the gravitational acceleration. In general a prime denotes a fluctuating part and an over bar denotes averaged over the turbulent timescale. Ri_f is defined as the ratio of the buoyancy destruction and production term. Figure 2.2 shows Ri_f as a function of volumetric concentration (in figure 2.2 expressed as c_v). First Ri_f increases with increasing c_V, however when the sediment concentration increases further, Ri_f decreases again. In figure 2.2 one can recognise the different flow conditions (e.g. sub- and super-saturated).

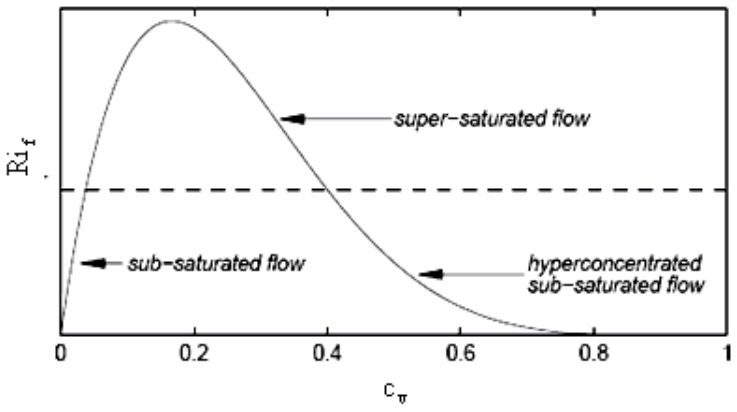

Figure 2.2: Relation between the flux Richardson number and the volumetric sediment concentration (Winterwerp [2001])

Two-phase versus single-phase approach

One of the contradicting view points that was found in literature is that the sediment-water mixture can either be treated as a single phase fluid or a two phase fluid. In this research it is assumed that the sediment-laden fluid can be treated as single phase. This means that the sediment particles follow the (turbulent) water movement exactly. It is argued that this assumption is justified if $w_s << w'_{RMS}$, where w_s is the settling velocity of sediment and w'_{RMS} is a measure for the (RMS value of the) turbulent velocity fluctuations (*Uittenbogaard* [1994], *Winterwerp* [2001]). Because w_s is in the order of 0.1-1 mm/s and $w'_{RMS} \approx u_*$, with u_* in the order of 1 cm/s, according to Uittenbogaard the assumption generally holds for fine-grained sediment with a particle diameter up to ca. 200 μm. *Winterwerp* [2001] simulated laboratory experiments by *Coleman* [1981] with the 1DV Point Model. The 1DV model also assumed a singe phase fluid. The 1DV results were in good agreement with the results of Coleman's laboratory experiments. The results of the numerical experiments support the assumption of a single phase fluid for sediment-laden flow with fine-grained sediment suspensions. In Appendix B the 1DV point model is explained in more detail. In contrast *Kovacs* [1998] and *Muste et al.* [2005] for example support a two-phase flow perspective. However, in the experiments of *Muste et al.* [2005] sediment particles with diameters of 0.21 mm to 0.25 mm were used. This is outside the range for which the single phase assumption is valid. This study focuses on suspensions of fine sediment for which the single-phase description is valid.

2.5 Modification of the velocity profile: Von Kármàn

Different researchers have different ideas about how to account for the effect of sediment on the flow profile. Many proposed to change the Von Kármàn coefficient. Furthermore different ideas exist on the region of the water column that is affected by suspended sediment. Some researchers focussed on changing the profile of the lower, logarithmic, region of the water column, while others focussed on the wake profile or the entire profile. In this chapter different views on the modification of the velocity profile will be discussed and specific attention will be paid to the consequences of this modification for the hydraulic roughness.

One frequently reported observation is that in flows with sediment particles in suspension, the Von Kármàn coefficient κ in equation (2.14) decreases with increasing sediment concentration. A reduction of κ changes the shape of the log-part of the velocity profile. This concept originates from experimental studies, i.e. *Vanoni* [1946, 1977], *Einstein and Chien* [1955] and *Elata and Ippen* [1961]. The concept of a reduced κ has been widely supported in following investigations.

Vanoni [1946, 1977] carried out a number of flume experiments. He established the effective Von Kármàn coefficient κ_s from the slope of the flow velocity profile plotted on semi-logarithmic axes, derived from experimental data points. According to *Vanoni* his experimental results show that the κ decreases from about 0.4 for clear water to about 0.2 for high concentrations. The results are shown in figure 2.3.

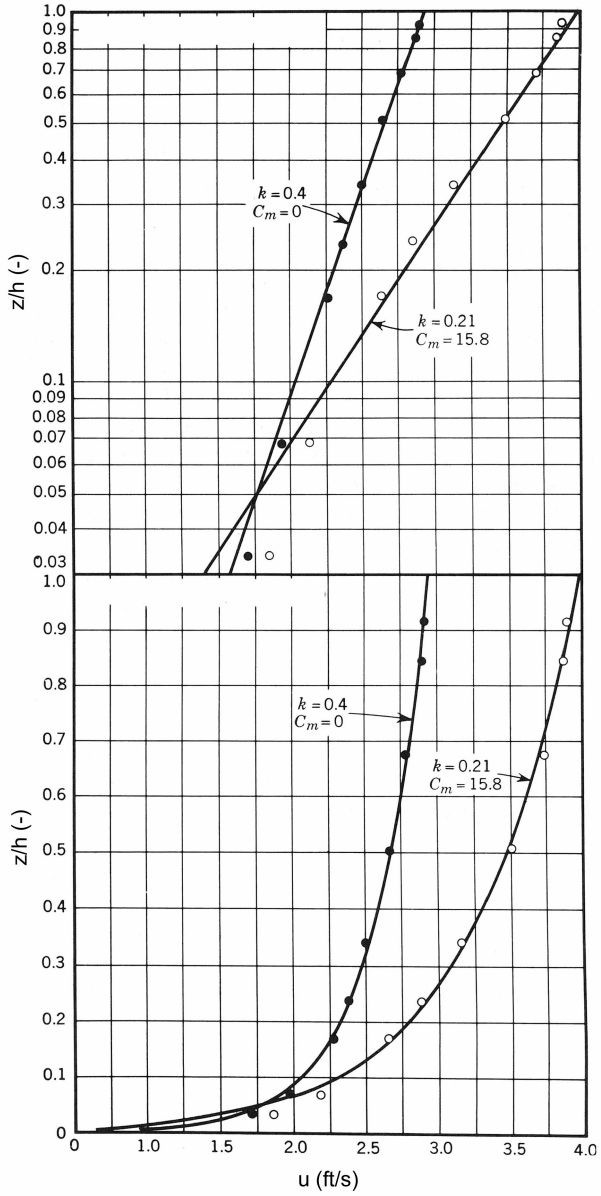

Figure 2.3: Semi-logarithmic and linear graphs of velocity profiles from Vanoni [1977]

Also *Einstein and Chien* [1955] hypothesized that κ must be reduced in the lower part of the water column in a sediment-laden flow. The authors argue that due to the presence of sediment the energy balance near the bed - where mean flow energy is converted to turbulent energy – is changed. Because of that they assumed that the turbulence pattern and thus the velocity profile changes which can be accounted for by a change of κ. Einstein and Chien further assumed that in turbulent sediment-laden flows momentum is not only transported by the exchange of water particles, but also by the exchange of sediment particles. The velocity fluctuations of sediment particles would increase the shear stress in the flow. In accordance with the Prandtl mixing length theory Einstein and Chien give the

following expression for a modified shear stress τ at an elevation z in a sediment-laden flow:

$$\tau = \left(1 + \frac{\rho_s - \rho_w}{\rho_w} \bar{c}\right) \rho_w L_t^{\,2} \frac{\mathrm{d}u}{\mathrm{d}z} \left|\frac{\mathrm{d}u}{\mathrm{d}z}\right| \tag{2-39}$$

where ρ_s and ρ_w are the density of sand and water respectively and L_t is the (Prandtl) turbulent mixing length.

Also *Elata and Ippen* [1961] agree on a modification of the Von Kármàn coefficient. However, strikingly, they explicitly state that the change the velocity profile in a sediment-laden flow relative to clear-water flow cannot be attributed to a damping of turbulence.

Vanoni [1977] states that: "Because all of the evidence is in agreement, it can be concluded that the effect of suspended sediment in a flow is to reduce the value of the Von Kármàn κ below its value for clear fluid." This statement is contradicted by *Coleman* [1981, 1986]. Coleman opposes the idea of reducing κ. He argues that in the period during which these studies were done the knowledge on boundary layer flow was limited. He states that in these early days researchers assumed that the logarithmic law of the wall could be applied in ranges much further away from the wall. This assumption originates from misinterpretation of experimental velocity profile data, which showed no wake region because of turbulence entering the measurement section from upstream. So during their studies, *Vanoni* [1946], *Einstein and Chien* [1955] and *Elata and Ippen* [1961] would be unaware of the existence of the wake region. After re-analyses of the experimental data of *Vanoni* [1946] and *Einstein and Chien* [1955], Coleman concluded that in each case the data from which κ was obtained, were high up in the flow, beyond the region of validity of logarithmic law of the wall, i.e. in the wake region. Coleman concluded that there is no significant difference of κ.

Coleman gives the following equation for the entire velocity profile above the viscous sub layer (logarithmic part and wake region) of a sediment-laden flow:

$$\frac{u}{u_*} = \frac{1}{\kappa} \ln \frac{u_* z}{\nu} + A_0 - \left(\frac{\Delta u}{u_*}\right)_R - \left(\frac{\Delta u}{u_*}\right)_S + \frac{\Pi}{\kappa} \omega_{WR} \left(\frac{u_* z}{\nu} \frac{\nu_{\delta_t}}{u_* \delta_t}\right) \tag{2-40}$$

where A_0 is a smooth-boundary velocity profile integration constant, Δu is a velocity profile shift, $\left(\Delta u/u_*\right)_R$ is a function for velocity reduction due to boundary roughness and the term $\left(\Delta u/u_*\right)_S$ is a velocity reduction function due to suspended sediment, Π is the wake strength coefficient, ω_{WR} is a functional symbol for the wake region function, δ_t is the thickness of the logarithmic boundary layer, ν_{δ_t} is the kinematic viscosity in the logarithmic boundary layer.

The last term on the right side of equation (2-40) is the wake region augmentation function, while the logarithmic part op the velocity profile can be expressed by:

$$\frac{u}{u_*} = \frac{1}{\kappa}\ln\frac{u_* z}{\nu} + A_0 - \left(\frac{\Delta u}{u_*}\right)_R - \left(\frac{\Delta u}{u_*}\right)_S \qquad (2\text{-}41)$$

After comparing measured data points and data obtained from calculations, Coleman concluded that the wake strength coefficient Π is affected by the presence of suspended sediment. According to Coleman, figure 2.4 indicates the existence of a universal $\Pi(Ri)$ function independent of particle size, ranging from a clear water asymptote of about 0.2 to a suspension capacity asymptote of about 0.9. Here Ri_* is the bulk flow Richardson number, which can be expressed as:

$$Ri_* = \frac{g\delta_t\left(\rho_s - \rho_0\right)}{\left\langle\rho\right\rangle u_m^2} \qquad (2\text{-}42)$$

where ρ_0 is the sediment-water mixture density near the bottom, $\left\langle\rho\right\rangle$ is the average sediment-water mixture density and u_m is the local velocity at the top of the logarithmic boundary layer.

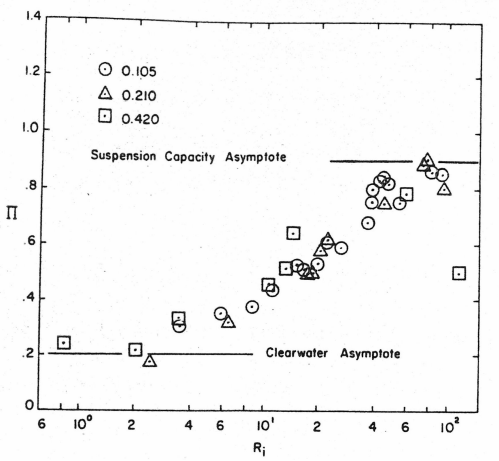

Figure 2.4: Wake strength (Π) coefficient plotted against Richardson number (Ri)

Furthermore Coleman observed that the thickness of the log-region is reduced and that the suspended sediment causes a downward shift of $(\Delta u/u_*)$ in the logarithmic part of the velocity profile and that this shift does depend on the particle size (figure 2.5).

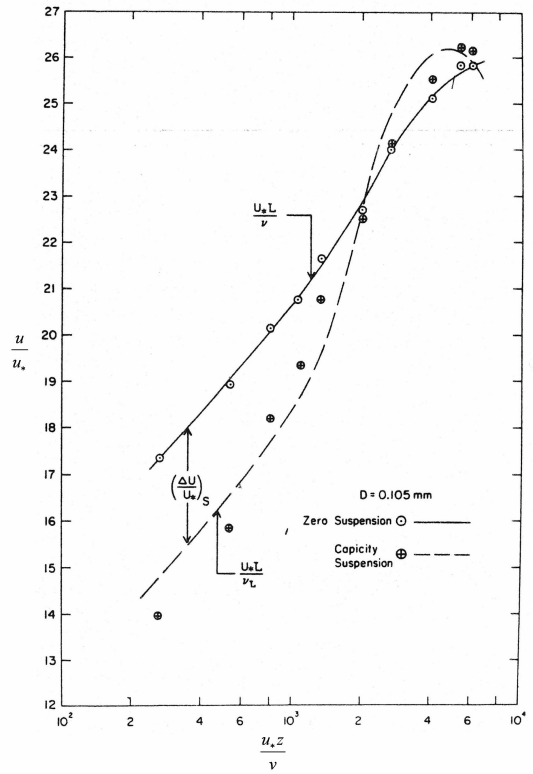

Figure 2.5: Velocity profile for clear-water and capacity suspension flows in experiments with 0.105 mm sand

Concerning a change of the velocity profile, *Winterwerp* [2001] noticed that a steepening of the near-bed velocity gradients must imply a decrease of the velocity gradient higher in the water column, when the flow rate is kept constant. His numerical simulation of Coleman's

laboratory experiments predicted both the decrease of the Von Kármàn coefficient and the change of the velocity defect law. Winterwerp's numerical simulations will be discussed in more detail in section 2.6.1.

2.6 Viscosity approach

As was described in the previous chapter some researchers attempted to account for the effect by formulating a sediment dependent expression for the velocity profile. Another way to account for the effect is through modification of the expression for the viscosity, which lies at the basis of the shape of the velocity profile.

In order to be able to model the eddy viscosity one often makes use of turbulence closure models. As was explained in section 2.2.2, the eddy viscosity can be described as the product of a characteristic turbulence length scale and characteristic turbulent velocity. The length scale can be defined directly or, like the characteristic velocity, can be derived from a $k-\varepsilon$ (or $k-\omega$) turbulence closure model. In a depth-averaged model this kind of turbulence closure model cannot be used. Then the turbulent viscosity is chosen as an empirical expression over the vertical.

This section presents sediment induced modifications of different turbulence models and modifications of an expression for mixing length. Numerical models that make use of a modified turbulence closure model were set up and their results were compared with observation data. Furthermore the analyses of field measurements in the Amazon estuary will be discussed.

2.6.1 Modification of the $k-\varepsilon$ turbulence model

Winterwerp [2001] argues that changes in flow behaviour due to the presence of suspended sediment can be explained from stratification effects (see section 2.3). To simulate the stratification processes in the vertical Winterwerp used the 1DV POINT MODEL. He studied the particle-fluid interaction by use of this 1DV POINT MODEL. The model is based on Delft Hydraulics' model DELFT3D, from which all horizontal gradients have been stripped except for the longitudinal pressure gradient. The model consists of the continuity equation for the water phase, the momentum equation, the mass balance equation for the

suspended sediment, a turbulence closure model and an equation of state, which relates fluid density to suspended sediment concentration, salinity and temperature. To account for the buoyancy effect the $k-\varepsilon$ turbulence closure model includes a buoyancy destruction term:

$$\frac{\partial k}{\partial t}=\frac{\partial}{\partial z}\left(\left(\nu_t+\frac{\nu_t}{\sigma_t^k}\right)\frac{\partial k}{\partial z}\right)-\overline{u'w'}\frac{\partial u}{\partial z}-\frac{g}{\rho}\overline{\rho'w'}-\varepsilon \tag{2-43}$$

$$\frac{\partial \varepsilon}{\partial t}=\frac{\partial}{\partial z}\left(\left(\nu_t+\frac{\nu_t}{\sigma_t^\varepsilon}\right)\frac{\partial \varepsilon}{\partial z}\right)-c_{1\varepsilon}\frac{\varepsilon}{k}\overline{u'w'}\frac{\partial u}{\partial z}-\left(1-c_{3\varepsilon}\right)\frac{g}{\rho}\overline{\rho'w'}-c_{2\varepsilon}\frac{\varepsilon^2}{k} \tag{2-44}$$

where σ_t^k and σ_t^ε are the turbulent Prandtl–Schmidt numbers for k and ε, respectively, $c_{1\varepsilon}$, $c_{2\varepsilon}$ and $c_{3\varepsilon}$ are coefficients. The second and third terms on the right-hand side in equation (2-43) are referred to as shear production and buoyancy destruction of turbulent kinetic energy, respectively. Their inversed ratio is the flux Richardson number Ri_f (equation 2-35).

Equation (2-43) and (2-44) are transport equations for the turbulent kinetic energy k and a transport equation of the dissipation of turbulent kinetic energy per unit of mass ε respectively. Again a prime denotes the fluctuating part and an overbar means averaged over the turbulent time scale.

The turbulent sediment transport terms are modelled as gradient type of transport. The eddy viscosity and the eddy diffusivity are given by:

$$\nu_t=c_\mu\frac{k^2}{\varepsilon} \tag{2-45}$$

$$\Gamma_t^c=\frac{\nu_t}{\sigma_t^c} \tag{2-46}$$

where ν_t and Γ_t^c are the eddy viscosity and the eddy diffusity, respectively. Furthermore σ_t^c is the turbulent Prandtl–Schmidt number for sediment and c_μ is a coefficient.

The values of the coefficients in the turbulence model $c_{1\varepsilon}$, $c_{2\varepsilon}$, $c_{3\varepsilon}$ and c_{μ} are derived from experiments in stable stratified flows.

Winterwerp simulated the experiments by Coleman with the 1DV model to analyse the effect of sediment induced buoyancy. The measured velocity profiles and concentration profiles were properly predicted by the simulations that included the sediment induced buoyancy term in the turbulence closure model.

Furthermore Winterwerp argues that in case of a constant energy slope in the 1DV model, the effective bed friction will decrease as a result of turbulence damping and the flow will accelerate. During acceleration more turbulence is produced which may result in more mixing and thereby may distort the stratification effect.

2.6.2 Modification of the $k-\omega$ turbulence model

To account for the buoyancy effect *Yoon and Kang* [2005] modified the $k-\omega$ turbulence closure model. Yoon and Kang used a flow and sediment transport model that includes a continuity equation for the water phase and a Reynolds averaged Navier-Stokes (momentum) equation, a balance equation for suspended sediment and the $k-\omega$ turbulence closure model. In this turbulence model k is the turbulent kinetic energy and ω is the ratio of turbulence dissipation rate ε to the turbulent kinetic energy and may be regarded as a characteristic time scale of the turbulence. The $k-\omega$ model equations are:

$$\frac{\partial k}{\partial t}+w\frac{\partial k}{\partial z}=\tau\frac{\partial U}{\partial z}-c_{1k}k\omega+\frac{\partial}{\partial z}\left[\left(\nu+c_{2k}\nu_t\right)\frac{\partial k}{\partial z}\right] \tag{2-47}$$

$$\frac{\partial \omega}{\partial t}+W\frac{\partial \omega}{\partial z}=c_{1\omega}\frac{\omega}{k}\tau\frac{\partial U}{\partial z}-c_{2\omega}\omega^2+\frac{\partial}{\partial z}\left[\left(\nu+c_{3\omega}\nu_t\right)\frac{\partial \omega}{\partial z}\right] \tag{2-48}$$

For clear-water the eddy viscosity ν_t in this turbulence closure model is given by:

$$\nu_t=c_4\frac{k}{\omega} \tag{2-49}$$

In the above equations c_{1k}, c_{2k}, $c_{1\omega}$, $c_{2\omega}$, $c_{3\omega}$ and c_4 are coefficients in the $k-\omega$ turbulence closure model.

To account for the effect of suspended sediment on the flow Yoon and Kang modified the $k-\omega$ turbulence model. They proposed a new eddy viscosity that considers the effect of suspended sediment following the mixing length theory of *Einstein and Chien* [1955], equation (2-36). This resulted in the following expression for the eddy viscosity in sediment-laden flow:

$$\nu_t = c_\gamma \frac{k}{\omega}\left[1+\left(1-\frac{\rho_w}{\rho_s}\right)c\right] \qquad (2\text{-}50)$$

where c_γ is a coefficient of the $k-\omega$ turbulence closure model. Upon comparison of the numerical results with Coleman's experimental results, reasonable agreement was obtained.

2.6.3 Viscosity: a field study

Based on their analyses of data obtained from measurements on the Brazilian shelf in the estuary mouth of the Amazon collected under AMASSEDS during 1989-1991, *Vinzon and Metha* [2001] concluded that an increase in viscosity in the boundary layer inhibits turbulence development. They assumed that these viscous effects can be attributed to the presence of high suspended sediment concentration (10 – 100 g/l). Vinzon and Metha showed that modification of the viscosity based on measurement data, results in a non-logarithmic velocity profile and a change of the bottom shear stress over the tidal cycle. Their calculations agreed well with the observation in the Amazon estuary.

With numerical simulations of the flow in the Amazon shelf, *Gabioux et al.* [2004] showed that the presence of fluid mud in the Amazon estuary has significant effect on the tidal wave propagation. Gabioux et al. assumed that the presence of the fluid mud layers leads to an increase in the fluid viscosity and density and reduces the bottom shear stress thus affecting the tidal wave propagation. To study this effect they carried out four numerical simulations. Two simulations considered sand or sand and consolidated mud and used the traditional

turbulence parameterization. The other two simulations considered a fluid mud layer with a viscous parameterization as was proposed by *Vinzon and Metha* [2001].

The results of the Amazon shelf model simulations correlate with observations (AMASSEDS), only if the effect of the fluid mud layers is taken into account. The results showed that the simulation with sand beds or sand and consolidated mud deposits underestimate the tidal amplification by 40% - 50%.

2.7 Mixing Length

Another way to modify the eddy viscosity is through a modification of the mixing length. In literature various expressions for a modified mixing length in sediment-laden flow exist.

Umeyama and Gerritsen [1992] proposed a new mixing length theory, which accounts for the effect of the sediment load. Umeyama and Gerritsen modified the mixing length theory of *Henderson* [1966]. Henderson's original equation was:

$$L_t = \kappa z \left(1 - \frac{z}{\delta_t}\right)^{0.5} \tag{2-51}$$

It was modified to:

$$L_t = \kappa z \left(1 - \frac{z}{\delta_t}\right)^{\alpha_L} \tag{2-52}$$

to allow for a better fit. α_L is a coefficient related to the mixing length. Umeyama and Gerritsen let the mixing length vary with the sediment concentration, through the exponent α_L, i.e.:

$$\alpha_L = \frac{1}{2}\left(1 + \gamma_L \frac{c}{c_a}\right) \tag{2-53}$$

where c is the mass concentration of suspended sediment, c_a is the reference mass concentration at $z = a$ in which a is a reference level and γ_L is an adjustable constant which depends on several characteristics of the sediment-laden flow. For verification of their model they used experimental data from different researchers, i.e. *Vanoni* [1946], *Einstein and Chien* [1955] and *Coleman* [1981]. Umeyama and Gerritsen used their modified mixing length hypothesis to calculate vertical velocity distributions for clear-water flow and sediment-laden flow. The analytical velocity distributions agreed well with velocity distributions obtained from the experimental data, provided that the appropriate value of γ_L was chosen.

Mazumder and Goshal [2005] elaborated on the theory of *Umeyama and Gerritsen* [1992]. To account for the effect of suspended sediment on the vertical velocity and sediment concentration profiles they modified the mixing length in the same way. But besides the mixing length they modified the turbulent shear stress and the settling velocity by letting it decrease with increasing sediment concentration. They verified their model with experimental data (*Vanoni* [1946], *Einstein and Chien* [1955] and *Coleman* [1981]). The model results and experimental data showed quite a good agreement.

2.8 Stratification; Monin-Obukhov

In section 2.3 it was already explained that a density gradient can change the velocity and concentration profile. If one assumes that suspended sediment can cause such a density gradient then the theory on stratification may contribute to the derivation of a suspended sediment theory. Using the theory of stratified boundary flows enabled many researchers to explain the observed effects in a physically satisfying manner. Furthermore many researchers assumed an analogy between the stratification that arises within a channel flow due to gradients in sediment concentrations and stratification that appears in the atmosphere due to temperature gradients. This analogy was used to parameterise sediment-laden flow. Numerical model results or observation data were used to verify the parameterisations.

Within climatology and meteorology the Monin-Obukhov length is defined as the height above the earth surface, where mechanically produced (by vertical shear) turbulence is in balance with the dissipative effect of negative buoyancy. At this height the flux Richardson number equals 1. The Monin-Obukhov length (L_{MO}) is given by:

$$L_{MO} = \frac{\overline{\rho} u_*^3}{\kappa g \overline{\rho' w'}} \tag{2-54}$$

Besides this length scale a Monin-Obukhov stability parameter can be defined:

$$\zeta = z / L_{MO} = \frac{g \kappa z \overline{\rho' w'}}{\overline{\rho} u_*^3} \tag{2-55}$$

This is the ratio of the potential energy required at a particular level in the flow to equalise the density difference and to level the concentration, to the turbulent kinetic energy supplied by the shear at that level. This parameter is a measure for the magnitude of the reduction of the frictional effect of turbulence due to the extra work required to mix the sediment. When comparing the stratified atmosphere with the stratified channel flow, the effect of suspended sediment can be assessed by investigating ζ .

Several researchers have proposed that this theory can be adapted for open channel flow. *Barenblatt* [1953] was probably the first to elaborate on this analogy. *Taylor and Dyer* [1977] followed the approach of *Barenblatt* [1953] and used the following expression to account for the suspended sediment effect on the velocity profile:

$$u = \frac{u_*}{\kappa} \left(\ln \frac{z}{z_0} + A_1 \frac{z}{L_{MO}} \right) \tag{2-56}$$

where $A_1 = 5.2$ and L_{MO} is the Monin-Obukhov parameter in a sediment laden flow.

Also *Itakura and Kishi* [1980] used the similarity theory for their theory on sediment-laden flow. They reanalysed the data of *Vanoni* [1946], *Einstein and Chien* [1955] and some others. For their description of the velocity distribution they used the Monin-Obukhov theory to account for the buoyancy effect. Itakura and Kishi derived the following expressions for the velocity distribution for hydraulically rough and smooth conditions respectively:

$$\frac{u}{u_*} = 8.5 + \frac{1}{\kappa}\left(\ln\frac{z}{k_s} + \varphi_1 \frac{z}{k_s} \right) \qquad \text{for} \qquad \frac{u_* k_s}{\nu_s} > 70 \tag{2-57}$$

$$\text{with } \varphi_1 = A_2 \frac{k_s}{L_{MO}} \tag{2-58}$$

$$\frac{u}{u_*} = 5.5 + \frac{1}{\kappa}\left(\ln\frac{u_* z}{\nu_s} + \varphi \frac{u_* z}{\nu_s} \right) \text{ for } \qquad \frac{u_* k_s}{\nu_s} < 5 \tag{2-59}$$

$$\text{with } \varphi = A_2 \frac{\nu_s}{u_* L_{MO}} \tag{2-60}$$

In the equations above ν_s is the kinematic viscosity for sediment-laden flow, i.e.: $\nu_s = \nu\left(1 + 2.5 c_V\right)$ (*Elata and Ippen* [1961], *Itakura and Kishi* [1980]), c_V is the volumetric sediment concentration at height *z* above the bottom, A_2 is a Monin-Obukhov coefficient and L_{MO} is the Monin-Obukhov length scale. According to Itakura and Kishi the coefficient A_2 has a value of around 7 for many velocity distributions in flows with suspended sediment. Furthermore they derived the following expression for the Monin-Obukhov length in sediment-laden flow based on the energy distribution in sediment-laden flow:

$$\frac{1}{L_{MO}} = \frac{\kappa g\left[\left(\rho/\rho_s\right) - 1\right] w_s \bar{c}}{u_*^3} \tag{2-61}$$

According to Itakura and Kishi the velocity distribution for sediment-laden flow in defect form can be expressed as follows:

$$\frac{u - u_{\max}}{u_*} = \frac{1}{\kappa}\left[\ln\frac{z}{h} + \phi_2\left(\frac{z}{h} - 1\right) \right] \tag{2-62}$$

$$\text{with } \phi_2 = A_2 \frac{h}{L_{MO}} \tag{2-63}$$

where $u_{\max}$ is the maximum value of the horizontal velocity at a certain point in the vertical and h is the depth of the channel

From the modified velocity distribution Itakura and Kishi derived an expression for the hydraulic roughness in sediment-laden flow. This will be discussed in section 2.9.
Further work was presented by *Adams and Weatherly* [1981]. They formulated a numerical model of the ocean bottom boundary layer of Florida Street in order to get a better understanding of the buoyancy effect of suspended sediment particles on the structure and dynamics of the bottom boundary layer. The vertical eddy viscosity was modelled with a turbulence closure model (Mellor Yamada level II). To account for the buoyancy effect, they included a buoyancy destruction term in the turbulence closure model. The model results showed reasonable agreement with field observation in Florida Street. The results indicated that the boundary layer response to a suspended sediment concentration gradient is to reduce the level of turbulence significantly.

Furthermore they developed a new formulation for the velocity profile over the 'logarithmic' layer, derived from atmospheric theories. They used the numerical model data to analyse the newly developed theory. In analogy with equation (2-54) they defined the Monin-Obukhov length scale for the suspended sediment case as follows:

$$L_{MO} = \frac{u_*^2}{\kappa^2 gz\left[(\rho_s - \rho)/\rho\right]\partial c/\partial z} \tag{2-64}$$

In the stratified boundary layer of the suspended flow, L_{MO} varies with height.

Adams and Weatherly assume that the non-dimensional shear (Φ) in the lower part of the bottom boundary layer is a universal function of ζ, i.e.:

$$\frac{\kappa z}{u_*}\frac{\partial U}{\partial z} = \Phi(\zeta) \tag{2-65}$$

They plotted the non-dimensional velocity shear against ζ. The data points were derived from the output of their numerical model. A least squares fit of the data yielded:

$$\Phi = 1 + A_3\zeta \tag{2-66}$$

where $A_3 = 5.5$. Integrating equation (2-65) for the logarithmic boundary layer and substituting $L_{MO} = z/Ri_f$ yields:

$$u = \frac{u_*}{\kappa}\left(\ln\frac{z}{z_0} + 5.5\int_{z_0}^{z} \frac{Ri_f}{z} dz \right) \qquad (2\text{-}67)$$

If Ri_f is assumed to be constant then this equation reduces to:

$$u = \frac{u_*}{\kappa_s} \ln\frac{z}{z_0} \qquad (2\text{-}68)$$

where $\kappa_s = \kappa/(1 + A_3 Ri_f)$ and κ_s may be interpreted as a modification of the Von Kármàn constant. According to the model results of Adams and Weatherly the current speed (made non-dimensional with u_*) increases with height above the bottom, to a maximum of about 125% relative to clear water flow. The increase of the slope of the velocity profile has frequently been accounted for by decreasing the Von Kármàn constant. By applying the similarity theory derived from atmospheric boundary layer studies, Adams and Weatherly are able to give a physical explanation for the reduction of the Von Kármàn coefficient. Furthermore they observe a significant reduction of u_*.

Soulsby and Wainwright [1987] also used the analogy between the stratification in the atmosphere and stratification in a sediment-laden flow to investigate the effect of suspended sediment. From this analogy they derived a criterion under which it is permissible to neglect the sediment effect. They state that in the atmosphere the stratification effect can be neglected if the Monin-Obukhov stability parameter is sufficiently small, i.e.:

$$\zeta < 0.03$$

They assume that this same criterion holds for the suspended sediment effect.

Soulsby and Wainwright derived an expression for the Monin-Obukhov stability parameter for sediment-laden flow. Their expression includes a pick-up function of *Smith and McLean* [1977]. Their expression for ζ is the following:

$$\zeta = \frac{g\kappa\gamma_1 w_s(\rho_s - \rho_w)(u_*^2 - u_{*c}^2)}{\rho_w u_*^3 u_{*c}^2}\left\{\frac{\gamma_2\rho_w(u_*^2 - u_{*c}^2)}{g(\rho_s - \rho_w)}\right\}^{\beta} z^{(1-\beta)} \qquad (2\text{-}69)$$

where $\beta = w_s/\kappa u_*$ is the Rouse number, γ_1 and γ_2 are empirical coefficients and u_{*c} is the critical shear velocity above which bed-load movement of sediment takes place. The stability parameter for sediment-laden flow is a function of u_*, the particle diameter D and z and of physical properties of the sediment-material and the water.

Soulsby and Wainwright assume that sediment can not remain in suspension in case the following criterion holds:

$$\beta = \frac{w_s}{\kappa u_*} > 3$$

To investigate the dependence of the stability parameter ζ on D, u_* and z Soulsby and Wainwright plotted several contours of ζ in a $D - u_*$ plane, which resulted in a stability diagram (figure 2.6). The contour lines separate different regimes. Each regime has distinctive characteristics in terms of sediment stratification effects and the resulting shape of the velocity profile.

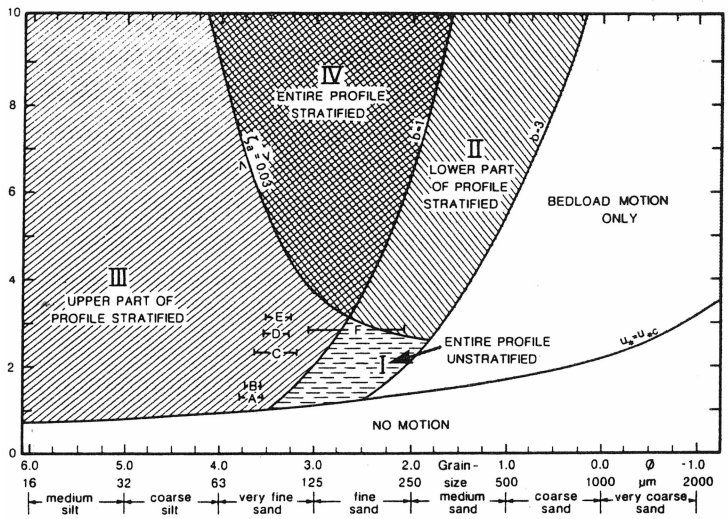

Figure 2.6: Summary of the effect of stratification induced by suspended sediment on velocity profiles, and its dependence on flow velocity and grain-size for quartz in sea-water.

The different regimes can be described as follows:

Regime I: $1 < \beta < 3,\ \zeta_a < 0.03$: Stratification is not significant at the bed and becomes even less so with increasing height.

Regime II: $1 < \beta < 3,\ \zeta_a > 0.03$: The flow is significantly stratified at the bed, but becomes less so with increasing height, until a height is reached at which $\zeta_a = 0.03$.

Regime III: $0 < \beta < 1,\ \zeta_a < 0.03$: Near the bed the density is constant, but ζ increases with height.

Regime IV: $0 < \beta < 1,\ \zeta_a > 0.03$: The flow is significantly stratified at the bed and becomes even more so with increasing height.

Furthermore if $u_* < u_{*c}$ there will be no motion and if $u_* > u_{*c}, \beta > 3$ there will be bed motion only.

Soulsby and Wainwright state that if the suspended sediment effect is neglected while $\zeta_a > 0.03$ the value of u_* will be overestimated.

2.9 Literature on hydraulic roughness

The practical purpose of this research project is to make it possible to simulate the tidal propagation of sediment-laden flow with a depth-averaged numerical model. One way to do

this is to parameterise the effect of the suspended sediment as a 'bottom effect', e.g. effect on bottom friction. Many researchers argued that the suspended sediment results in an increase of flow velocity and a decrease of hydraulic roughness. In 2Dh this could be simulated by lowering the bottom friction. In literature there are theories that propose a modification of the hydraulic roughness. In the next section literature on hydraulic roughness will be discussed.

Elata and Ippen [1961] concluded from their experimental data that the apparent Chézy coefficient decreases with increasing sediment concentration for volumetric concentration up to 20%. For concentration higher than 20% they observed a slight increase of the Chézy coefficient. Both for decreasing as for increasing the Chézy coefficient their experiments showed that the difference was no more than 5% compared to the Chézy coefficient for clear water flow. Elata and Ippen concluded that the Chézy coefficient for flows with suspended sediment differs only slightly from the Chézy coefficient for clear water flows.

Contrary to *Elata and Ippen* [1961] most of the literature on the roughness effect of suspended sediment find a significant decrease of roughness. *Itakura and Kishi* [1980] derived a hydraulic resistance law for sediment-laden flow from their modified velocity distribution (equation 2-57 and 2-59). Integrating (2-57) and (2-59) gives the depth-averaged velocity $\bar{u}$:

$$\frac{\bar{u}}{u_*} = 6.0 + \frac{1}{\kappa}\left(\ln\frac{h}{k_s} + \frac{\phi_2}{2\kappa} \right) \quad \text{for} \quad \frac{u_* k_s}{\nu_s} > 70 \tag{2-70}$$

$$\frac{\bar{u}}{u_*} = 3.0 + \frac{1}{\kappa}\left(\ln\frac{u_* h}{\nu_s} + \frac{\phi_2}{2\kappa} \right) \quad \text{for} \quad \frac{u_* k_s}{\nu_s} < 5 \tag{2-71}$$

Assuming $\nu = \nu_s$, Itakura and Kishi find the following relationship between the Darcy-Weisbach friction factors for clear water and sediment-laden flows:

$$\sqrt{\frac{8}{f_s}} = \sqrt{\frac{8}{f}} + \frac{\phi_2}{2\kappa} \tag{2-72}$$

where f and f_s are the Darcy-Weisbach friction factors for clear water and sediment-laden flows, respectively. Equation (2-72) shows that the friction factor for sediment-laden flow is less than the friction factor for clear water flow.

Further work on reduced roughness in sediment-laden flow was presented by *Toorman* [2000]. Toorman also assumed the sediment effect to be a stratification effect. He proposed that the difference between homogeneous and stratified fluids can be expressed by semi-empirical correction factors, damping functions. Toorman gives the following definition for the damping functions:

$$\nu_{t(s)} = \nu_t F_t \tag{2-73}$$

$$\Gamma_{t(s)} = \Gamma_t F_s = \nu_t \frac{F_s}{\sigma_t} \tag{2-74}$$

Where $\nu_{t(s)}$ and $\Gamma_{t(s)}$ are the eddy viscosity and eddy diffusity in a stratified, sediment-laden flow respectively. F_t is the damping function for momentum and F_s is the damping function for mixing (diffusity), so that:

$$\sigma_{t(s)} = \sigma_t \frac{F_t}{F_s} \tag{2-75}$$

$$\kappa_s = F_t \kappa \tag{2-76}$$

$$L_{t(s)} = F_t L_t \tag{2-77}$$

where σ_t the turbulent Prandtl Schmidt number, $\sigma_{t(s)}$ and $L_{t(s)}$ are the Prandtl Schmidt number and the mixing length in sediment-laden flow respectively.

The new theory was implemented in a numerical model, both into the Prandtl's mixing theory and in the $k-\varepsilon$ turbulence model. In the $k-\varepsilon$ turbulence model damping by buoyancy effects was included through a buoyancy destruction term.

Through application of the damping functions Toorman found an expression for the near-wall velocity profile in sediment-laden flow. Furthermore Toorman estimated the value for u_* in sediment laden flow. Toorman states that the u_* is a crucial parameter in modelling wall turbulence. The shear velocity is required for the calculation of the near-wall boundary conditions for velocity, turbulent kinetic energy and turbulent dissipation rate.

Through application of the modified parameters Toorman proposed the following modification of the velocity profile:

$$u = \frac{u_*}{\kappa}\left(\ln\left\{ \frac{z}{z_0} \right\} + \int_{z_0}^{z} \mathrm{d}z \left\{ \frac{1-F_t}{zF_t} \right\} \right) \tag{2-78}$$

This corresponds to the following expression with a modification factor for the roughness height z_0:

$$u = \frac{u_*}{\kappa} \ln \frac{z}{\alpha_1(z) z_0} \tag{2-79}$$

where α_1 is a friction correction factor. The corresponding velocity gradient is:

$$\frac{\partial u}{\partial z} = \frac{u_*}{\kappa_0 z}\left(1 + \frac{z}{\alpha_1}\frac{\partial \alpha_1}{\partial z} \right) \tag{2-80}$$

From this it follows that:

$$F_t^{-1} = 1 + \frac{z}{\alpha_1}\frac{\partial \alpha_1}{\partial z} \tag{2-81}$$

Through application of the numerical model Toorman found that the modification factor α_1 is a function of w_s/u_* and of the Richardson number. From numerical experiments, he derived the following empirical formula:

$$\alpha_1 = \exp\left[-\left(1+a_1\, w_s/u_*\right)1-\exp\left(-b_1 Ri^{n_1}\right)\right] \tag{2-82}$$

where $a_1 = 7.7$, $b_1 = 1/0.6$ and $n_1 = 0.85$. With this formula the shift of the velocity profile Δu can be calculated, i.e. the shift is equal to:

$$\Delta u = -\left(u_*/\kappa\right)\ln\left(\alpha_1\right) \tag{2-83}$$

Byun and Wang [2005] examined the effect of sediment induced stratification on sediment transport and tidal dynamics in a region on the southwest coast of Korea. They used a sediment transport model coupled with a three-dimensional tidal hydrodynamic model.
They state that feedback between sediment-transport dynamics and hydrodynamics is an important factor in modelling sediment transport dynamics in tidally dominated, turbid, coastal environments. According to Byun and Wang a suitable approach to simulate the effects of this feedback is to use a modified bottom-drag coefficient as a stability function, together with the inclusion of the stratification effect on the hydrodynamics. Byun and Wang modified the drag coefficient c_f by introducing a stability function $\left(1+A_3 Ri_f\right)$. They derived the following expression for the modified drag coefficient that they used in their numerical model:

$$c_f = \left[\frac{\kappa}{\left(1+A_3 Ri_f\right)\ln\left(\left(h+z_b\right)/z_0\right)}\right]^2 \tag{2-84}$$

While the bottom stress is given by:

$$\tau_b = \rho c_f \left|u_b\right| u_b$$

Numerical experiments with and without the effects of sediment stratification showed different results. Byun and Wang argued that these differences are due to the reduction in turbulent mixing and bottom stress caused by the presence of a suspended sediment-induced stratification. The sediment effect resulted in a reduction of the erosion rates, an increase of the spatial extend of deposition areas, a significant decrease of rates and spatial extend of net suspended-sediment transport and an increase of the vertical gradient in sediment concentration in the water column.

Thompson et al. [2006] examined the change in bed shear stress from flume measurements, by investigating the drag coefficient c_D. They found drag reduction for concentrations up to 20 g/L. They observed a reduction of the value of the drag coefficient up to 50% compared to clear water. For higher concentrations, up to 200 g/L the drag coefficient returned to its clear water value again. They showed that for concentrations below 200 g/L, the acceleration due to the suspended sediment effect outweighs the deceleration due to an increase in fluid viscosity and an increase in fluid mass.

2.10 Discussion

Studies reported in literature all show a significant effect of the suspended sediment on the flow structure in open channel flow. This means that the traditional theory for clear water flow does not hold for sediment-laden flow. To model the suspended sediment effect, early investigations concluded that the Von Kármàn coefficient must be reduced for sediment-laden flow. This conclusion was mainly based on a best fit through experimental data. Later studies looked for a physically more satisfying explanation for changes of the flow structure. Many researchers concluded that the effect of suspended sediment is a stratification effect. Literature on field observations also report on stratification effects due to suspended sediment, for example in the Ems Estuary (*Winterwerp* [1999]), in the Yangtze Estuary (*Yang et al.* [2002]), in the Amazon (*Vinzon and Metha* [2001]) and in the deep ocean of Florida Street (*Adams and Weatherly* [1980]. It was concluded that in sediment-laden flow, damping of turbulence by buoyancy is the underlying principle of changes in concentration and velocity profiles, compared to clear-water flow. This does not mean that the idea of a reduction of the Von Kármàn coefficient is wrong. *Adams and Weatherly* [1981] showed that changes due to the buoyancy effect can be interpreted as a change of the Von Kármàn coefficient. Furthermore it is concluded that it depends on the specific flow and sediment

characteristics, whether the major effect is found near the bed or higher in the water column, as was conceptually shown by the stability diagram of *Soulsby and Wainwright* [1981].

The buoyancy effect was modelled in various ways. Literature reports on numerical models that include the effect in a turbulence closure model. Several researchers included a buoyancy destruction term in the turbulence closure model to account for the damping of turbulence (*Toorman* [2000], *Winterwerp* [2001], *Yoon and Kang* [2005]). Comparison with experimental data showed favourable results.

For an expression of the modified velocity profile one often comes across a relation with the dimensionless Richardson number or Monin-Obukhov stability parameter, which is derived from atmospheric theories. The Richardson number and the Monin-Obukhov stability parameter are both a measure for damping of turbulence in a stratified flow. Correlations between the modified expressions and numerical or experimental data validate the use of these dimensionless parameters to express the buoyancy effect, e.g. *Adams and Weatherly* [1981]. Because it was observed that the damping of turbulence results in apparent smoothing, the above mentioned relations were used to derive an expression for the effective hydraulic roughness in sediment-laden flow. One way is to integrate the modified velocity profile (see e.g. *Itakura and Kishi* [1980]) resulting in an expression for the depth integrated velocity including a term that represents a roughness reduction. The approach of using the Monin-Obukhov stability parameter to derive an expression for hydraulic roughness, has proven to be an efficient theory: Correlations with numerical model results have been very convincing. The theory will be followed in this research project.

3 Roughness parameterization

3.1 Introduction

Many studies reported in literature show an appreciable effect of suspended sediment on the turbulence properties of open-channel flow. The effect is present even at moderate sediment concentrations. Based on a thorough literature study (chapter 2) it was concluded that suspended sediment induces stratification. In a stratified boundary flow turbulent mixing is hindered due to the buoyancy effect. Previous investigations (e.g. *Taylor and Dyer* [1977], *Itakura and Kishi* [1980], *Soulsby and Wainwright* [1987]) showed that a convincing method to model the stratification effect is by using existing theories developed for the earth's atmosphere. For many researchers the analogy between the stratification that arises within a channel flow due to gradients in sediment concentrations and stratification that appears in the atmosphere due to temperature gradients, provided a physical background to model the behaviour of sediment-laden flow. This study elaborates on the similarity theory and applies theories on heat- and/or salinity-induced stratification effects to derive a parameterization for sediment-induced reduction of effective hydraulic roughness.

Barenblatt [1953] introduced the Monin-Obukhov length scale $L_{MO} \equiv \rho u_*^3 / \kappa g \overline{\rho' w'}$ to establish a damping function for the eddy viscosity. The Monin-Obukhov length scale can be regarded as a measure for the turbulent mixing length in stratified flow. Following Barenblatt, it is assumed that the log-linear velocity profile for sediment-laden flow can be expressed as (*Winterwerp* [2007], personal communication):

$$\frac{u}{u_*} = \frac{1}{\kappa}\left[\ln\left(\frac{z}{z_0}\right) + \alpha_0\left(\frac{z}{L_{MO}}\right)^m\right] \tag{3-1}$$

where α_0 and m are coefficients. Herein one can recognize the Monin-Obukhov stability parameter (equation 2-55):

$$\zeta = z/L_{MO} = \frac{g\kappa z\overline{\rho' w'}}{\rho u_*^3}$$

Stratification effects are negligible if $\zeta < \zeta_{cr} = 0.03$ (*Soulsby and Wainwright* [1987]).

Note that equation (3-1) was developed for boundary layer flow in the atmosphere. However there are differences between the dynamics of the stratified boundary flow in shallow water and the dynamics of the stratified boundary flow over the earth's surface are briefly discussed. Next the differences, that are relevant for this research, are briefly discussed.

In fluid mechanics, the boundary layer is the layer of fluid in the immediate vicinity of the bottom boundary, in which the free flow velocity decreases due to viscous and shear effects. In the atmosphere the boundary layer is the air layer near the ground affected by heat, moisture or momentum transfer to or from the surface. These physical quantities such as flow velocity, temperature and moisture display turbulent fluctuations and vertical mixing is strong. The boundary layer extends from 1 to 5 km in height. While temperature and pressure decrease in the lower atmosphere, viscosity increases. The eddy viscosity reaches a maximum at the height where whirlwinds develop best. Contrary to shallow water flow the atmospheric boundary flow is not bounded by a large density jump at the upper boundary. In open channel flow, the surface boundary is formed by the interface between water and air. Because of this interface turbulent fluctuations can hardly penetrate the free surface. Therefore, just below the water surface viscosity is small and turbulent mixing is limited. In figure 3.1 the viscosity profile for the atmospheric boundary layer and the parabolic viscosity profile for shallow water flow have been sketched. The free surface is absent in the atmosphere. Free surface effects are accounted for in equation (3-1), through the coefficients α_0 and m, contrary to the original equation of Barenblatt.

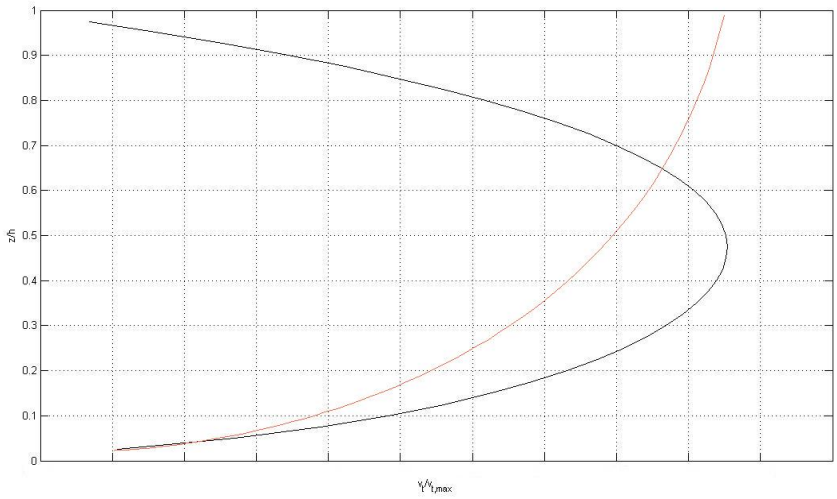

Figure 3.1: A viscosity profile for open channel flow (black line) and a viscosity profile for air flow in the atmosphere (red line)

3.2 Derivation roughness parameterisation

3.2.1 Atmospheric approach

The objective of this research is to parameterise hydraulic roughness in sediment-laden flow in order to be able to include the sediment effect in a 2Dh model. A friction law for depth-averaged hydrodynamic models can be obtained by integrating equation (3-1) over the water depth *h*. For clarity, this is done term by term:

$$\int_0^h \mathrm{d}z \left\{ \frac{u}{u_*} \right\} \equiv \frac{h\bar{u}}{u_*} \tag{3-2}$$

$$\begin{aligned} \int_0^h \mathrm{d}z \left\{ \frac{1}{\kappa} \ln\left\{ \frac{z}{z_0} \right\} \right\} \approx \int_{z_o}^h \mathrm{d}z \left\{ \frac{1}{\kappa} \ln\left\{ \frac{z}{z_0} \right\} \right\} = \frac{1}{\kappa} \Big[z\ln\{z\} - z - z\ln\{z_0\} \Big]_{z_0}^h = \\ = \frac{1}{\kappa} \left[h\ln\left\{ \frac{h}{z_0} \right\} - (h - z_0) \right] \approx \frac{h}{\kappa} \left[\ln\left\{ \frac{h}{z_0} \right\} - 1 \right] \end{aligned} \tag{3-3}$$

Assuming local equilibrium, i.e. $\left(\overline{\rho' w'} = \Delta w_s c;\ \ \Delta = \left(\rho_s - \rho_w\right)/\rho_s\right)$ and substituting equation (2-54), the third term in equation (3-1) is rewritten as:

$$\int_0^h \mathrm{d}z \left\{ \alpha_1 \frac{\kappa g \Delta}{\rho_b u_*^3} \overline{w'c'} z \right\}^m = \int_0^h \mathrm{d}z \left\{ \alpha_1 \frac{\kappa g \Delta}{\rho_b u_*^3} W_s c z \right\}^m \tag{3-4}$$

For β << 1 and assuming a logarithmic velocity profile, the relation between concentration $c(z)$ and its depth-averaged value $\overline{c}$ reads:

$$c\left(z\right) = \overline{c}\, \frac{\sin\left\{\pi\beta\right\}}{\pi\beta} \left(\frac{1 - z/h}{z/h} \right)^{\beta} \quad \text{for } \beta << 1 \tag{3-5}$$

with $\beta = \sigma_T W_s / \kappa u_*$ (3-6)

which is the Rouse number. Hence, the solution to equation (3-4), the details of which are given in the Appendix A, reads:

$$\begin{aligned} \int_0^h \mathrm{d}z \left\{ \alpha_1 \frac{\kappa g \Delta}{\rho_b u_*^3} W_s c z \right\}^m &\approx \frac{h}{\left(m+1\right)} \left\{ \alpha_1 \frac{\kappa g \Delta}{\rho_b u_*^3} W_s h \overline{c} \right\}^m = \\ = K_1 h \left(\frac{g h \left(\rho_b - \rho_w\right)}{\rho_b u_*^2} \frac{\sigma_T W_s}{\kappa u_*} \right)^m &= K_1 h \left(Ri_* \beta \right)^m \end{aligned} \tag{3-7}$$

where K_1 and m are empirical coefficients to be determined and Ri_* is the bulk Richardson number, defined as:

$$Ri_* = \frac{\left(\rho_b - \rho_w\right) g h}{\rho_b u_*^2} \tag{3-8}$$

where ρ_b = bulk density of sediment-laden flow. The bulk density depends on the sediment concentration in accordance with:

$$\rho_b = c + \left(1 - \frac{c}{\rho_s}\right)\rho_w \tag{3-9}$$

Combination of the equations (3-3), (3-4), (3-6) and (3-8) gives the friction law for depth-averaged models, accounting for the effect of suspended sediment on the effective hydraulic resistance:

$$\frac{\bar{u}}{u_*} = \frac{1}{\kappa}\left[\ln\left\{\frac{h}{z_0}\right\} - 1\right] + K_1\left(Ri_*\beta\right)^m \tag{3-10}$$

$$\frac{\bar{u}}{u_*} = \frac{C_0}{\sqrt{g}} + \frac{C_b}{\sqrt{g}} \tag{3-11}$$

$$\frac{C_{eff}}{\sqrt{g}} = \frac{C_0}{\sqrt{g}} + \frac{C_b}{\sqrt{g}} \tag{3-12}$$

where C_0 is the Chézy coefficient in clear water, C_b is the additional Chézy value due to the buoyancy effect and C_{eff} is the effective Chézy coefficient, which is the sum of C_0 and C_b. For very small suspended sediment concentrations ($Ri_* \approx 0$) and/or very fine sediment ($\beta \approx 0$), the outcome is the familiar semi-log law of the wall. For the relation (3-10) that holds for a larger concentration regime, the coefficients K_1 and m have to be assessed experimentally.

Finally it must be noted that the solution expressed by equation (3-10) is not trivial. Next it will be shown that a different approach for the derivation of the depth-averaged friction law results in a similar relation between the effective resistance in depth-averaged flow and the dimensionless parameters Ri_* and β.

3.2.2 Energy approach

Another assessment of the buoyancy effect can be obtained from energy considerations. In sediment-laden flow, due to a vertical density gradient as a result of the vertical distribution of the suspended sediment, buoyancy destruction of turbulent energy occurs. This can be

explained as follows. At the bottom boundary of a channel flow the majority of turbulent energy is produced. Part of the energy is necessary to keep the sediment particles in suspension (=buoyancy destruction), while the rest of the energy is dissipated and diffused by turbulent motion of the sediment water mixture. This means that in a sediment-laden flow less energy is available for the turbulent energy cascade than in clear water flow. The vertical distribution of horizontal velocity for a flow with suspended sediments, therefore will differ from the distribution in a clear water flow. Next it will be shown a derivation of a parameterisation for the effective hydraulic roughness in sediment-laden flow, which is based on the above energy argumentation, results in an expression that is similar to equation (3-10).

production = dissipation + buoyancy destruction:

$$\bar{u}\tau_{eff} = \bar{u}\tau_0 + \int_{z_0}^{h} \Delta g w_s c \, dz \qquad (3\text{-}13)$$

By substituting $\tau_b = c_f \rho \bar{u}^2$ and $c_f = \frac{g}{C^2}$, equation (3-13) can be written as:

$$\rho g \bar{u}^3 \frac{1}{C_{eff}^2} = \rho g \bar{u}^3 \frac{1}{C_0^2} + h \Delta g w_s \bar{c} \qquad (3\text{-}14)$$

Dividing equation (3-14) by ρu_*^3 gives:

$$\frac{\bar{u}^3}{u_*^3} g \frac{1}{C_{eff}^2} = \frac{\bar{u}^3}{u_*^3} g \frac{1}{C_0^2} + \frac{g h \Delta w_s \bar{c}}{\rho u_*^3} \qquad (3\text{-}15)$$

Because the following relations hold:

$$\frac{\bar{u}^3}{u_*^3} = \left(\frac{C}{\sqrt{g}} \right)^3, \text{ so that } \frac{\bar{u}^3}{u_*^3} g \frac{1}{C^2} = \frac{C}{\sqrt{g}}$$

equation (3-14) can be rewritten according to:

$$\frac{C_{eff}}{\sqrt{g}} = \frac{C_0}{\sqrt{g}} - \frac{gh\Delta w_s \bar{c}}{\rho u_*^3} \tag{3-16}$$

This expression is similar to equation (3-10). However the derivation of section 3.2.1 allows to account for the vertical distribution of u and c, which is not the case in 3.2.2.

Another way to rewrite equation (3-13) is as follows:

$$\left(\bar{u}\rho u_*^2\right)_{eff} = \left(\bar{u}\rho u_*^2\right)_0 + h\Delta g w_s \bar{c} \tag{3-17}$$

If equation (3-17) is divided by ρu_*^3 this also leads to:

$$\left(\frac{\bar{u}}{u_*}\right)_{eff} = \left(\frac{\bar{u}}{u_*}\right)_0 + \frac{gh\Delta w_s \bar{c}}{\rho u_*^3}$$

which similar to equation (3-10). The last term on the right hand side can be rewritten in terms of the bulk Richardson number Ri_* and the Rouse number β:

$$\left(\frac{\bar{u}}{u_*}\right)_{eff} = \left(\frac{\bar{u}}{u_*}\right)_0 + \frac{\kappa}{\sigma_t}\frac{gh\left(\rho_b - \rho_w\right)}{\rho_w u_*^2}\frac{\sigma_t w_s}{\kappa u_*}$$

$$\left(\frac{\bar{u}}{u_*}\right)_{eff} = \left(\frac{\bar{u}}{u_*}\right)_0 + K_2 Ri_* \beta$$

$$\left(\frac{C_{eff}}{\sqrt{g}}\right) - \left(\frac{C_0}{\sqrt{g}}\right) = K_2 Ri_* \beta \tag{3-18}$$

where K_2 is an empirical coefficient.

The above derivation shows that, based on an energy argumentation, one gets a similar roughness parameterisation as in equation (3-10). This strengthens the conclusion that the

effect of buoyancy destruction on the effective hydraulic roughness in sediment-laden flow is proportional to $Ri_*\beta$ and can be described by a relation of the form of equation (3-10).

3.3 Theoretical validation

3.3.1 Approach

In the next section the roughness law for depth-averaged models will be validated. Also the coefficients K_1 and m (equation 3-10) will be assessed. To this end the 1DV POINT MODEL will be used. The 1DV POINT MODEL was developed based on DELFT3D-FLOW, the software system of WL | Delft Hydraulics. DELFT3D-FLOW is a three dimensional numerical flow model. The three dimensional model has been converted to the 1DV model by stripping all horizontal gradients, except for the horizontal pressure gradient. DELFT3D-FLOW is used to simulate the water movement and transport of matter in three dimensions. Both the three dimensional model and the 1DV model account for the effects of sediment-induced stratification by including a buoyancy destruction term in the $k-\varepsilon$ turbulence closure model. More details on the three dimensional model DELFT3D-FLOW and the 1DV POINT MODEL can be found in the Appendices B and C respectively.

Assuming that the behaviour of flows laden with fine sediment can be analyzed properly with the hydrodynamic approach implemented in the 1DV POINT MODEL , the output data of this 1DV model will be used as input for the 2Dh friction law, expressed by equation (3-10). There are five variable parameters in equation (3-10), i.e. $\bar{u}$, z_0, h, w_s and $\bar{c}$. These parameters are input parameters for the 1DV POINT MODEL. By varying the values of these input parameters, the sensitivity of the effective hydraulic roughness can be assessed. This assessment will be done through analyses of the relation between $C_{eff}/\sqrt{g}$ (or $\bar{u}/u_*$) and $Ri_*\beta$ for different values of the input parameters. After the friction law for depth-averaged models (equation 3-10) has been analyzed, a least square fit will be used to determine the coefficients K_1 and m.

Section 3.4.1 gives a first impression of the sediment effect. Figures 3.2 to 3.5 show the effect of the sediment induced stratification on the vertical distribution of horizontal

velocity. In the sections 3.4.1 to 3.4.3 the relation between $\left(C_{eff}/\sqrt{g}\right)$ and $\left(Ri_*\beta\right)$ is assessed. The 1DV POINT MODEL was used to generate different values of shear velocity, for increasing depth-averaged suspended sediment concentrations. The resulting data will be discussed. Additionally the influence of the roughness height z_0, the settling velocity w_s and the water depth h are analyzed.

3.3.2 Profiles

Figures 3.2 to 3.5 shows the vertical profiles of the horizontal velocity, the eddy viscosity and the equilibrium sediment concentration for different values of the depth-averaged sediment concentration. For clear water ($\bar{c} = 0$ g/l), a common logarithmic velocity profile and a parabolic eddy viscosity profile are computed. Due to the vertical sediment concentration gradient, the vertical velocity profile for sediment-laden flow will change its shape relative to the logarithmic velocity profile for clear water flow. This illustrates the effect of sediment-induced buoyancy. A stronger gradient results in larger difference between the value of the (local) horizontal velocity in clear water flow and the value of the (local) horizontal velocity in sediment-laden flow. The 1DV POINT MODEL predicts a small, but systematic decrease in eddy viscosity with increasing sediment concentration. It is noted that the major effect of the suspended sediment is seen near the water surface. This is because near the water surface mixing is limited, which results in a large vertical gradient of the suspended sediment concentration there. Due to this large gradient turbulence is damped extensively. Therefore the velocity profile is affected more near the water surface than elsewhere in the water column.

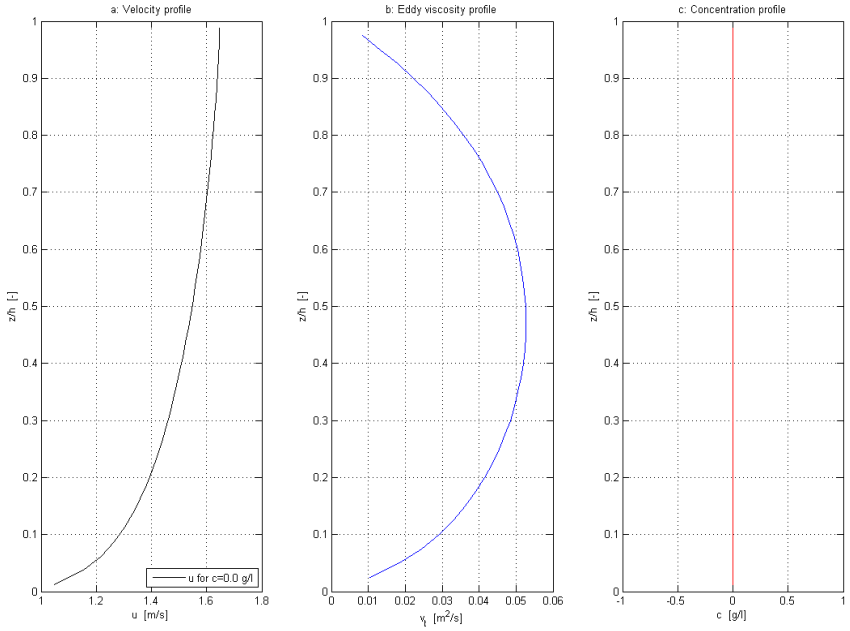

$h = 10$ m; $\bar{u} =$ 1.5 m/s; $\bar{c} =$ 0.0 g/l

Figure 3.2a: Vertical profile of horizontal velocity; Figure 3.2b: Vertical profile of eddy viscosity; Figure 3.2c: Vertical profile of suspended sediment concentration

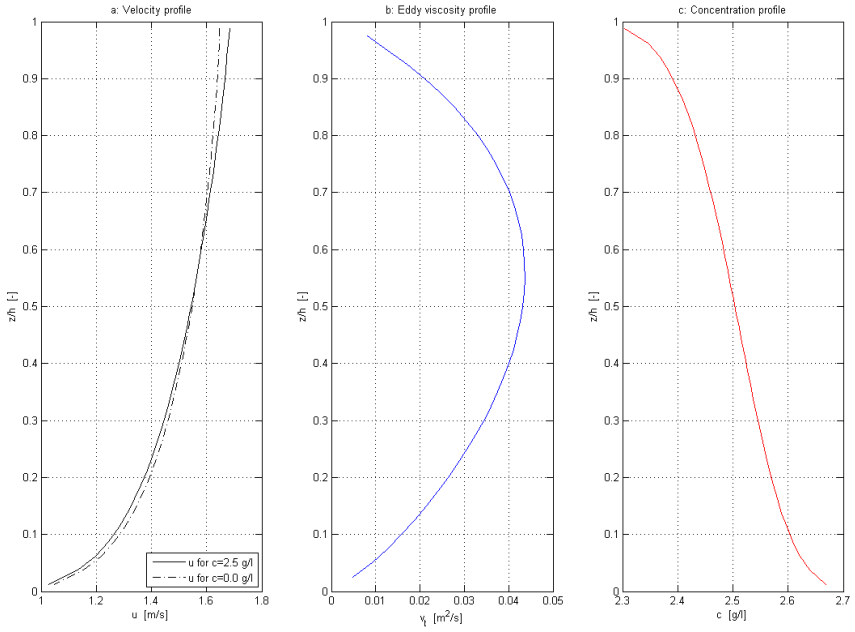

$h = 10$ m; $\bar{u} =$ 1.5 m/s; $\bar{c} =$ 2.5 g/l

Figure 3.3a: Vertical profile of horizontal velocity; Figure 3.3b: Vertical profile of eddy viscosity; Figure 3.3c: Vertical profile of suspended sediment concentration

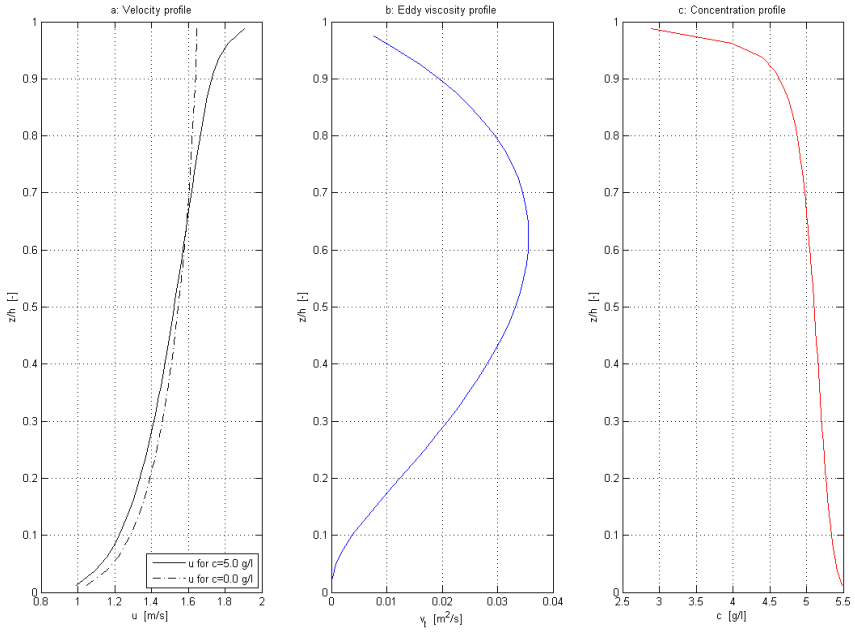

$h = 10$ m; $\bar{u} = 1.5$ m/s; $\bar{c} = 5.0$ g/l

Figure 3.4a: Vertical profile of horizontal velocity; Figure 3.4b: Vertical profile of eddy viscosity; Figure 3.4c: Vertical profile of suspended sediment concentration

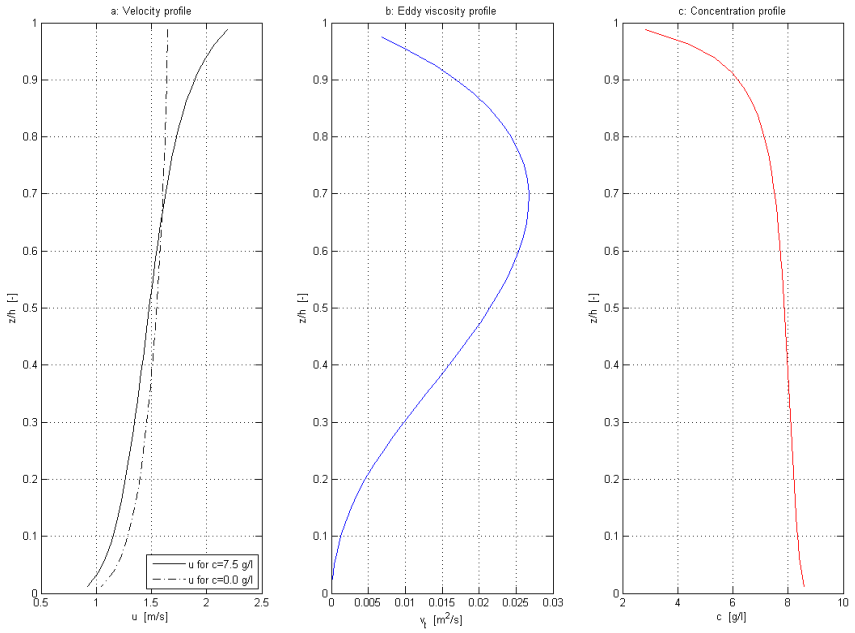

$h = 5$ m; $\bar{u} = 1.5$ m/s; $\bar{c} = 7.5$ g/l

Figure 3.5a: Vertical profile of horizontal velocity; Figure 3.5b: Vertical profile of eddy viscosity; Figure 3.5c: Vertical profile of suspended sediment concentration

3.3.3 Variation of roughness height, z_0

In figure 3.6 $\left(C_{eff}/\sqrt{g}\right)$ has been plotted against $\left(Ri_*\beta\right)$. The graphs show the results of the 1DV POINT MODEL for three different values of $\bar{u}$ and four different values of z_0, for increasing sediment concentration ($\bar{c}$). All other parameters have the same value for each run of the 1DV POINT MODEL. The data points in figure 3.6 are within the low concentration regime. Higher depth-averaged sediment concentrations result, after some time, in a collapse of the vertical turbulence field. In this study, the suspended sediment concentration for cohesive sediment just prior to this collapse is denoted by the term 'saturation concentration'. Here only data for concentrations below saturation are presented. The exact values for the saturation concentration depend on the variables.

Simulations for different values of the depth-averaged velocity and increasing sediment concentration, while keeping other parameters constant, result in coinciding $\left(C_{eff}/\sqrt{g}\right)$ curves. This is in agreement with the depth-averaged friction law, equation (3-10): Formula (3-10) matches the 1DV data accurately. The different curves shift over a vertical distance in the graph relative to each other, but keep the same relation relative to $\left(Ri_*\beta\right)$. This strictly linear translation of the graphs, without deformation, validates the hypothesis that the term for sediment induced drag reduction, i.e. $K_1\left(Ri_*\beta\right)^m$, is independent of the roughness height z_0. The roughness height z_0 is only present in the first term on the right hand side of equation (3-10). This term indicates the crossing point with the y-axis, here represented by the $\left(C_{eff}/\sqrt{g}\right)$ axis. An increase of z_0 results in a decrease of $\left(C_0/\sqrt{g}\right)$, which is defined as $\left(C/\sqrt{g}\right)$ for a zero value of the depth-averaged suspended sediment concentration $\bar{c}$ and thus of $\left(Ri_*\beta\right)$. Only the clear water component of equation (3-10), i.e. the first term on the right hand side, is affected by a change of the roughness height z_0. According to equation (3-10) the distance between two different $\left(C_{eff}/\sqrt{g}\right)$ curves is equal to:

$$\frac{\Delta C_{eff}}{\sqrt{g}} = \frac{1}{\kappa}\ln\alpha_* \qquad (3\text{-}19)$$

Assuming $z_{0,1} = \alpha_* z_{0,2}$, where α_* is a multiplication factor. This can be derived as follows:

$$\left(\frac{\overline{u}}{u_*}\right)_2 - \left(\frac{\overline{u}}{u_*}\right)_1 = \left[\frac{1}{\kappa}\left[\ln\left\{\frac{h}{z_0}\right\} - 1\right] + K_1\left(Ri_*\beta\right)^m\right]_2 - \left[\frac{1}{\kappa}\left[\ln\left\{\frac{h}{z_0}\right\} - 1\right] + K_1\left(Ri_*\beta\right)^m\right]_1 \quad (3\text{-}20)$$

Because $K_1\left(Ri_*\beta\right)^m$ is independent of the roughness height z_0:

$$\left[K_1\left(Ri_*\beta\right)^m\right]_1 = \left[K_1\left(Ri_*\beta\right)^m\right]_2 \quad (3\text{-}21)$$

From this it follows that:

$$\left(\frac{\overline{u}}{u_*}\right)_2 - \left(\frac{\overline{u}}{u_*}\right)_1 = \frac{1}{\kappa}\left[\ln\left\{\frac{h}{z_{0,2}}\right\} - \ln\left\{\frac{h}{z_{0,1}}\right\}\right] \quad (3\text{-}22)$$

$$\left(\frac{\overline{u}}{u_*}\right)_2 - \left(\frac{\overline{u}}{u_*}\right)_1 = \frac{1}{\kappa}\ln\left\{\frac{\frac{h}{z_{0,2}}}{\frac{h}{z_{0,1}}}\right\} \quad (3\text{-}23)$$

$$\left(\frac{\overline{u}}{u_*}\right)_2 - \left(\frac{\overline{u}}{u_*}\right)_1 = \frac{1}{\kappa}\ln\left\{\frac{z_{0,1}}{z_{0,2}}\right\} = \frac{1}{\kappa}\ln\left\{\frac{\alpha_* z_{0,2}}{z_{0,2}}\right\} \quad (3\text{-}24)$$

$$\left(\frac{\overline{u}}{u_*}\right)_2 - \left(\frac{\overline{u}}{u_*}\right)_1 = \frac{\Delta C_{eff}}{\sqrt{g}} = \frac{1}{\kappa}\ln\alpha_* \quad (3\text{-}25)$$

Furthermore, in figure 3.6 the critical value of depth-averaged value of the Monin-Obukhov stability parameter is indicated. The Monin-Obukhov stability parameter can be expressed by (equation 2-55):

$$\zeta = z/L_{MO} = \frac{g\kappa z\overline{\rho' w'}}{\rho u_*^3}$$

This parameter indicates the ratio of the potential energy required at a particular level to suspend the sediment, to the turbulent kinetic energy supplied by shear at that level. In this case the depth average value of this ratio is considered. This average value can be

determined by integrating equation (2-55) over depth h and subsequently dividing it by h, i.e.

$$\int_0^h \zeta = \int_0^h z/L_{MO} = \int_0^h \frac{g\kappa z\overline{\rho' w'}}{\rho u_*^3}$$

$$\int_0^h \zeta = \int_0^h z/L_{MO} = K_1 h\left(Ri_*\beta\right)^m$$

$$\frac{\left(\int_0^h \zeta\right)}{h} = \frac{\left(\int_0^h z/L_{MO}\right)}{h} = K_1\left(Ri_*\beta\right)^m$$

The critical value for the Monin Obukhov stability parameter is $\zeta_{cr} = 0.03$, above which the buoyancy effect is assumed to be significant. From this it follows that:

$$K_1\left(Ri_*\beta\right)^m = 0.03$$

In order to be able to point out the critical value ζ_{cr}, it is assumed that:

$$Ri_*\beta = 0.03$$

Finally, in figure 3.7 the graphs of figure 3.6 are normalised relative to clear water. After normalisation all plots coincide, which is in agreement with equation (3-10).

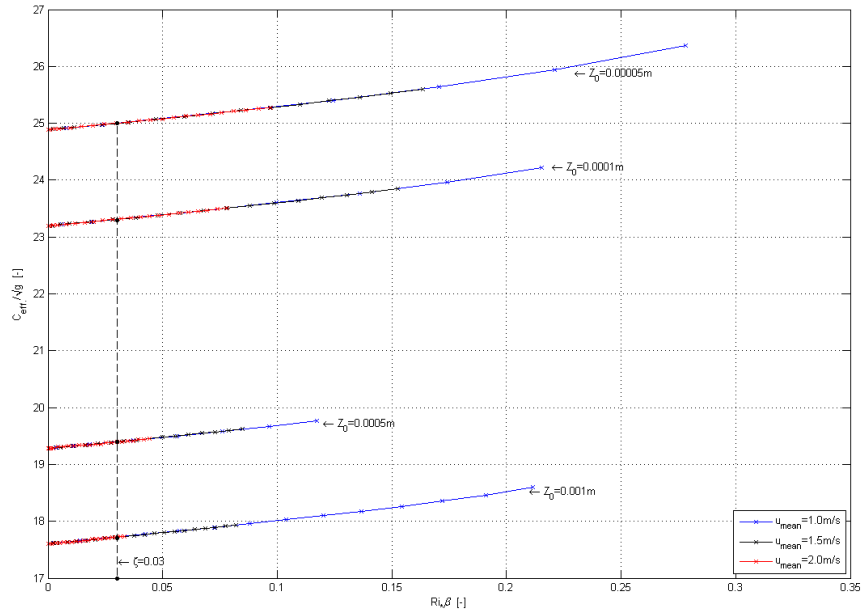

Figure 3.6: Plot $\left(C_{eff}/\sqrt{g}\right)$ *versus* $\left(Ri_*\beta\right)$ *for different values of* $\bar{u}$ *and* z_0*, for increasing values of* $\bar{c}$

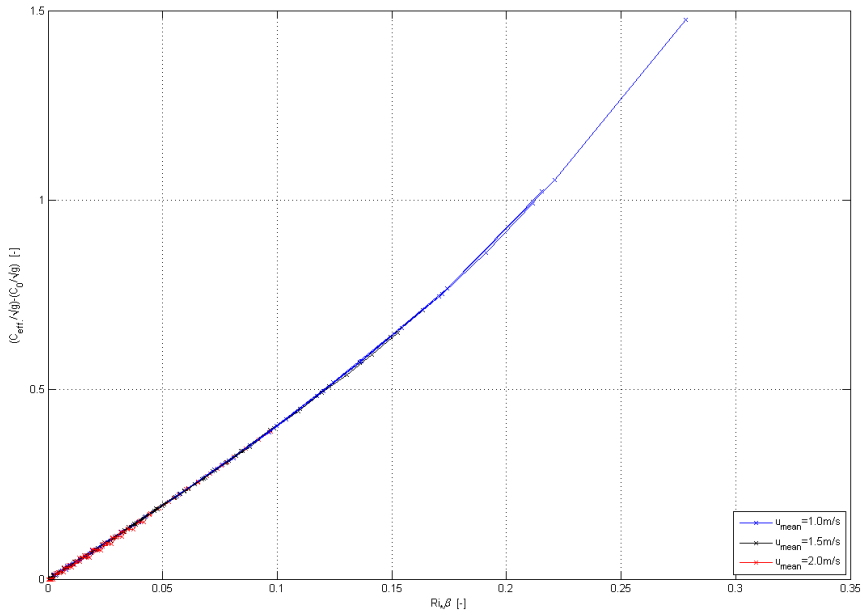

Figure 3.7: Plot $\left(C_{eff}/\sqrt{g}\right)_{\text{norm.}}$ *versus* $\left(Ri_*\beta\right)$*, normalised relative to clear water conditions, for different values of* $\bar{u}$ *and* z_0*, for increasing values of* $\bar{c}$

3.3.4 Variation of settling velocity, w_s

Again the relation between $\left(C_{eff}/\sqrt{g}\right)$ and $\left(Ri_*\beta\right)$ is assessed. Figure 3.8 shows the results of the 1DV POINT MODEL for different values of $\bar{u}$ and w_s for increasing sediment concentration ($\bar{c}$), ceteris paribus. Again the data that is presented is valid for sediment concentrations below saturation. According to this figure the coefficients K_1 and m are independent of $\bar{u}$ and w_s, which is in agreement with the depth-averaged formulation for hydraulic roughness in sediment-laden flow (equation 3-10). Again the point $Ri_*\beta = 0.03$, below which stratification effects can be neglected, is indicated.

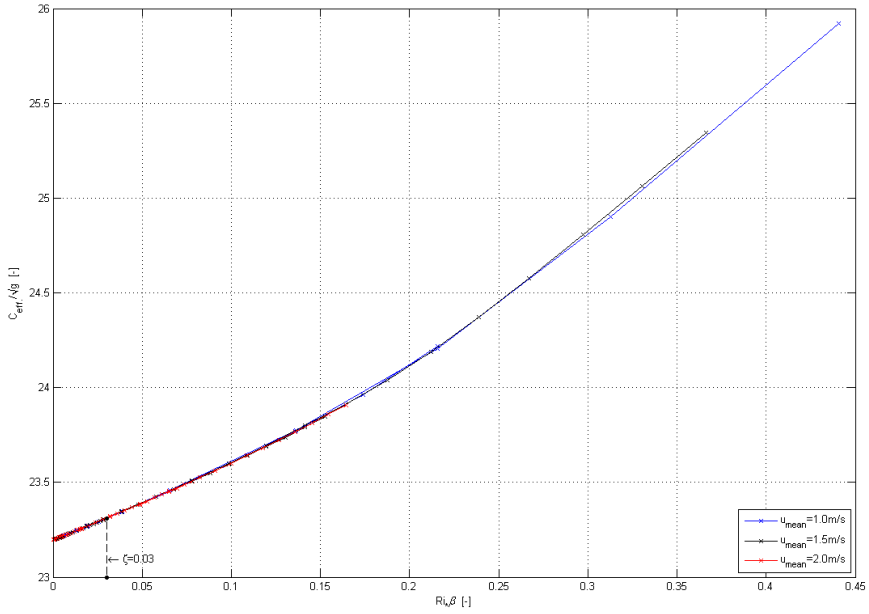

Figure 3.8: Plot $\left(C_{eff}/\sqrt{g}\right)$ *versus* $\left(Ri_*\beta\right)$ *for different values of* $\bar{u}$ *and* w_s, *for increasing values of* $\bar{c}$

3.3.5 Variation of water depth, h

Figure 3.9 shows the relation between $\left(C_{eff}/\sqrt{g}\right)$ and $\left(Ri_*\beta\right)$, for which the data are derived from the results of the 1DV POINT MODEL. This relation has been plotted for different values of $\bar{u}$ and h for increasing suspended sediment concentrations below

saturation, keeping other parameters constant. According to equation (3-10) these plots should result in parallel graphs if the coefficients K_1 and m were independent of h. However the results of the 1DV POINT MODEL in figure 3.9 show a different relation. Plotting $\left(C_{eff}/\sqrt{g}\right)$ versus $\left(Ri_*\beta\right)$, using the output of the 1DV model, results in graphs with increasing slope for increasing water depth. Figure 3.9 indicates that for larger depths, the effective hydraulic roughness decreases more with increasing sediment concentration, than for smaller depths. The 1DV model results suggest that the coefficient K_1 increases with increasing water depth. Furthermore it is observed that below a certain depth, the graphs show a linear increase of $\left(C_{eff}/\sqrt{g}\right)$ for increasing sediment concentration, while above this depth the graphs are non-linear and show a slight flexion. This indicates that above a certain depth, $\left(C_{eff}/\sqrt{g}\right)$ increases more than linearly with increasing sediment concentration, so that the coefficient m becomes larger than one.

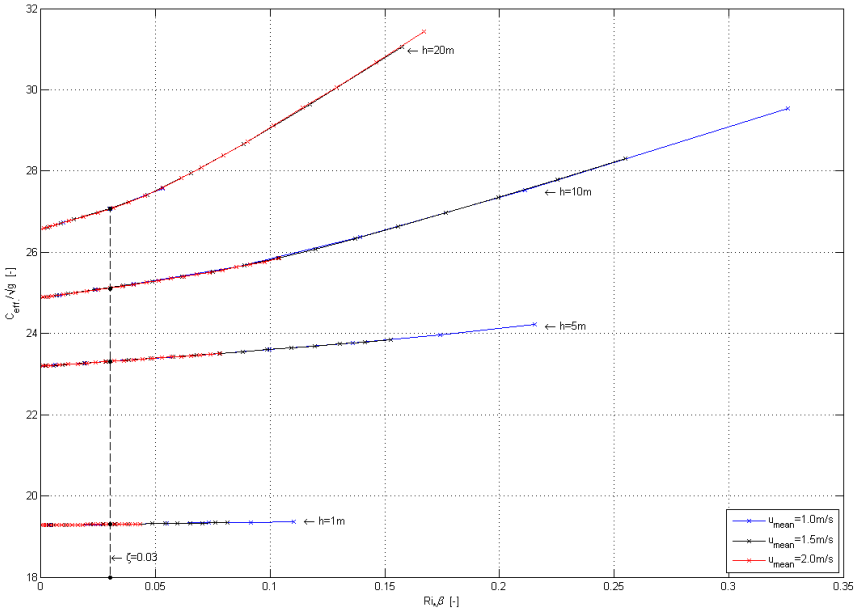

Figure 3.9: Plot $\left(C_{eff}/\sqrt{g}\right)$ *versus* $\left(Ri_*\beta\right)$ *for different values of* $\bar{u}$ *and* h*, for increasing values of* $\bar{c}$

The apparent discrepancy of the numerical results (1DV model) and the analytical results of the depth-averaged friction law (equation 3-10), is most likely due to the free surface effects. These free surface effects are defined as the effects that occur due to the presence of the free surface in open channel flow. The free surface effects scale with depth. Near the

water surface mixing is limited and the kinematic viscosity is small, as can be seen from the parabolic viscosity profile (figure 3.1). For the derivation of the depth-averaged friction law (equation 3-10) theories are used, that were developed for the boundary layer flow in the atmosphere. However in the atmosphere a free surface and thus free surface effects are absent. Therefore the free surface effects are not accounted for in the 'atmospheric theories'. This implies that the friction law, which is based on these atmospheric theories, is not fully applicable to open channel flow.

In order to further analyse this discrepancy, velocity and concentration profiles for different channel depths must be investigated. Figures 3.10, 3.11 and 3.12 show the vertical profiles for velocity and concentration in a channel with a depth of 1 m, 5 m, and 10 m respectively. The velocity profile and concentration profile in figure 3.12 strongly differ from the profiles in figures 3.10 and 3.11. It can be seen that for depth $h = 10$ m there is a strong concentration gradient near the surface. This strong gradient in the top-layer indicates the collapse of the vertical turbulence field there.

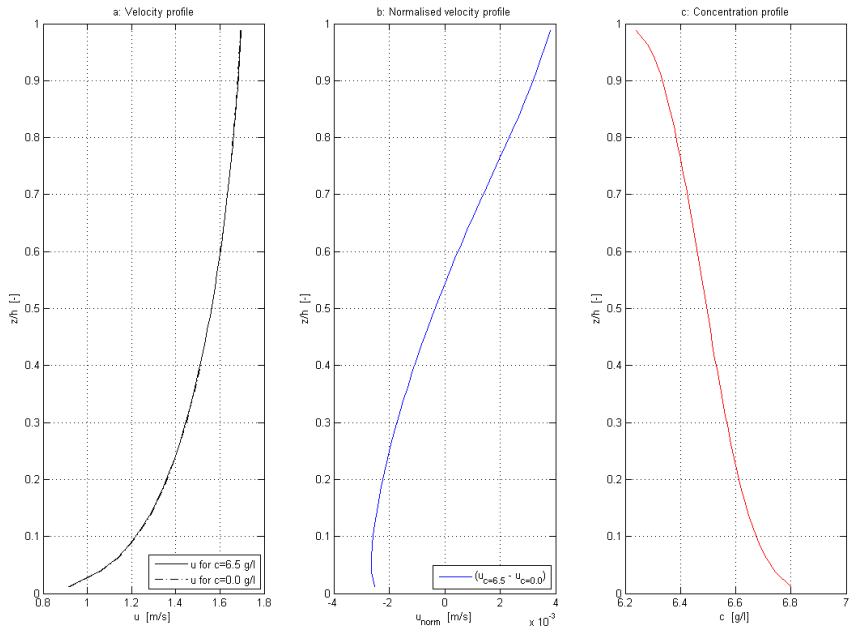

$h = 1$ m; $\bar{u} =$ 1.5 m/s; $\bar{c} =$ 6.5 g/l

Figure 3.10a: Vertical profile of horizontal velocity; Figure 3.10b: Normalised vertical profile for horizontal velocity; Figure 3.10c: Vertical profile of suspended sediment concentration

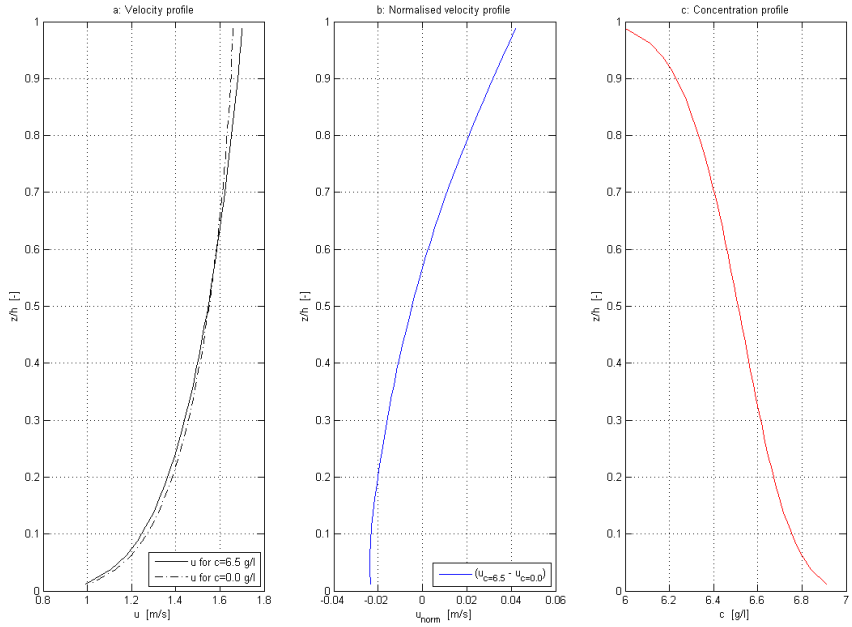

$h = 5$ m; $\bar{u} =$ 1.5 m/s; $\bar{c} =$ 6.5 g/l

Figure 3.11a: Vertical profile of horizontal velocity; Figure 3.11b: Normalised vertical profile for horizontal velocity; Figure 3.11c: Vertical profile of suspended sediment concentration

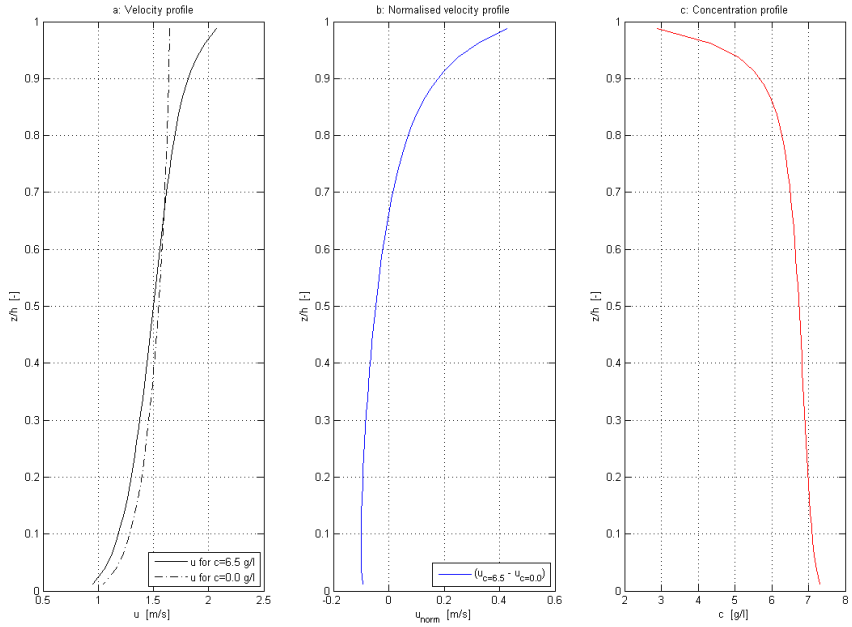

$h = 10$ m; $\bar{u} =$ 1.5 m/s; $\bar{c} =$ 6.5 g/l

Figure 3.12a: Vertical profile of horizontal velocity; Figure 3.12b: Normalised vertical profile for horizontal velocity; Figure 3.12c: Vertical profile of suspended sediment concentration

For the derivation of the depth-averaged friction law it was assumed that the concentration profile can be described by equation (3-5). In figure 3.13 equation (3-5) is plotted for the same conditions as those that hold for figures 3.10 to 3.12 successively. Comparing these analytically derived concentration profiles (figure 3.13) with the numerically derived concentration profiles (figures 3.10, 3.11 and 3.12) it can be concluded that equation (3-5) is valid for a depth of 1m and 5 m, however that for a depth of 10 m the profile cannot be described by equation (3-5).

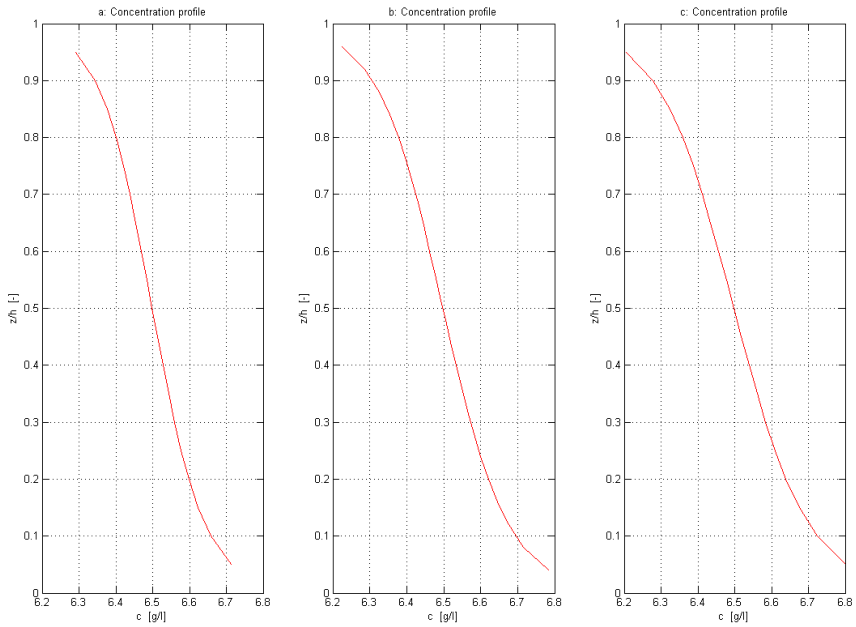

Figure 3.13a: Vertical profile of suspended sediment concentration, $h = 1$ m; $\bar{u} =$ 1.5 m/s; $\bar{c} =$ 6.5 g/l

Figure 3.13b: Vertical profile of suspended sediment concentration, $h = 5$ m; $\bar{u} =$ 1.5 m/s; $\bar{c} =$ 6.5 g/l

Figure 3.13c: Vertical profile of suspended sediment concentration, $h = 10$ m; $\bar{u} =$ 1.5 m/s; $\bar{c} =$ 6.5 g/l

As was anticipated before, this can most likely be explained by the free surface effects, e.g. near the water surface viscosity is small. These free surface effects scale with depth, which can be seen from the expression for the parabolic viscosity profile, i.e.:

$$\nu_t = \frac{\kappa u_*}{h}\left(zh - z^2\right)$$

As the 1DV model results suggest, a possible way to account for the free surface effects is to make the coefficients K_1 and *m* dependent on the water depth. The relations of K_1 and m to h have to be investigated further.

Figure 3.14 shows $\left(C_{eff}/\sqrt{g}\right)$ curves that are normalised relative to the clear water condition, which is represented by $\left(C_0/\sqrt{g}\right)$. According to equation (3-10) these curves can be described by a power function of the form:

$$\left(\frac{\bar{u}}{u_*}\right)-\left(\frac{\bar{u}}{u_*}\right)_0 = K_1\left(Ri_*\beta\right)^m \tag{3-26}$$

$$\left(\frac{\bar{u}}{u_*}\right)-\left(\frac{\bar{u}}{u_*}\right)_0 = \frac{C_{eff}}{\sqrt{g}}-\frac{C_0}{\sqrt{g}} \tag{3-27}$$

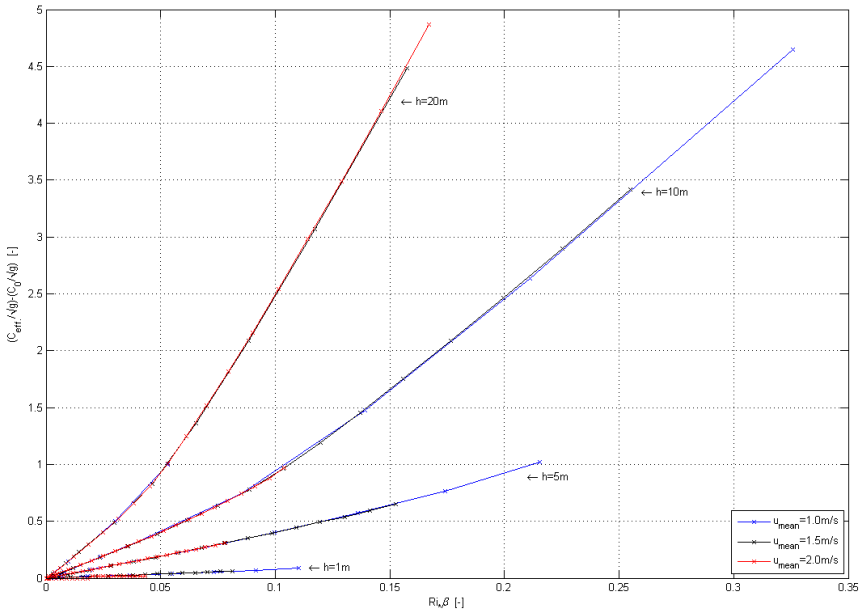

Figure 3.14: Plot $\left(C_{eff}/\sqrt{g}\right)_{\text{norm.}}$ *versus* $\left(Ri_*\beta\right)$*, normalised relative to clear water conditions, for different values of* $\bar{u}$ *and* h*, for increasing values of* $\bar{c}$

In order to find an expression for $K_1 = f(h)$ and $m = f(h)$, power functions are fitted on the 1DV data points using the least square method. The results are shown in figure 3.15. The least square method assumes that the best-fit curve of a given type is the curve that has the minimal sum of the deviations squared (least square error) from a given set of data. In this case, the data set is provided by the 1DV POINT MODEL. For clarity it is noticed that, different than in figure 3.16 where the curves represent the least square fits through the data points, the curves in figure 3.15 are drawn by connecting the subsequent data points. For the least square fits in figure 3.16, it is assumed that the relation between $\left(C_{eff}/\sqrt{g}\right)_{\text{norm.}}$ and $\left(Ri_*\beta\right)$ can be described by a power function of the form of equation (3-26).

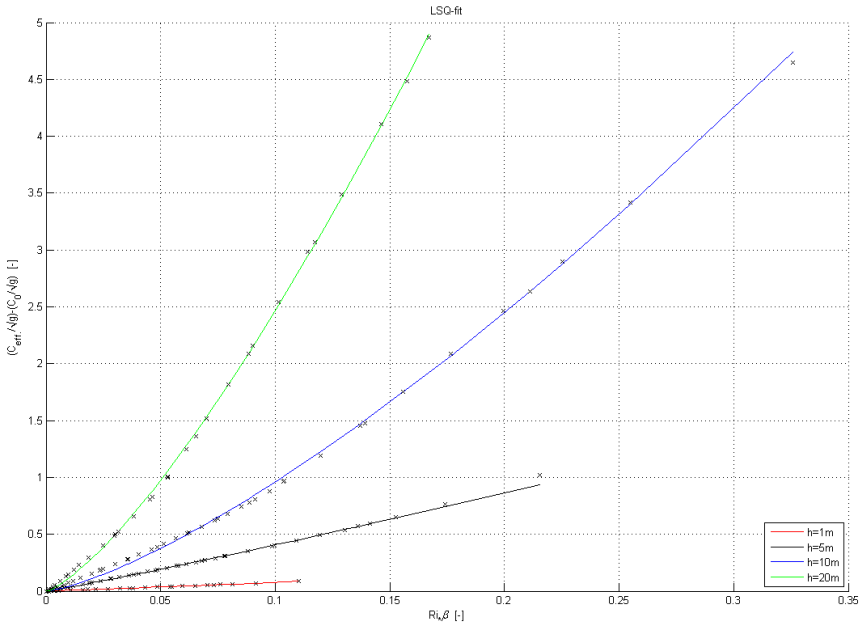

Figure 3.15: Fit through data points describing the relation $\left(C_{eff}/\sqrt{g}\right)_{\text{norm.}}$ *versus* $\left(Ri_*\beta\right)$, *for different values of* $\bar{u}$ *and* h, *for increasing values of* $\bar{c}$

The coefficients K_1 and m can be approximated through application of the least square method to the output data of the 1DV point model. From the least square fit through the 1DV data (figure 3.15) it can be seen that, apparently K_1 increases more than linearly with h. Furthermore it can be seen that only for $h \geq 10$ m the normalised $\left(C_{eff}/\sqrt{g}\right)$ curves deviate from a linear form, which implies a value for m larger than one.

The coefficients K_1 and m have been approximated for different depths. Besides for the water depths presented in figure 3.15 ($h = 1,\ 5,\ 10$ and 20 m) this has been done for $h = 0.2$ m, $h = 0.5$ m, $h = 7$ m, $h = 8$ m and $h = 22$ m. The results are shown in table 3.1 and table 3.2 respectively.

h	***K₁***
0.2	0.13
0.5	0.37
1.0	0.87
5.0	4.90
7.0	8.39
8.0	15.39
10.0	21.56
20.0	56.67
22.0	66.56

Table 3.1: Values of coefficient K_1, for different values of h

h	***m***
0.2	1.00
0.5	1.00
1.0	1.05
5.0	1.08
7.0	1.14
8.0	1.33
10.0	1.35
20.0	1.36
22.0	1.37

Table 3.2: Values of coefficient m, for different values of h

In figure 3.16 and figure 3.17 the values for K_1 and m are scattered against h.

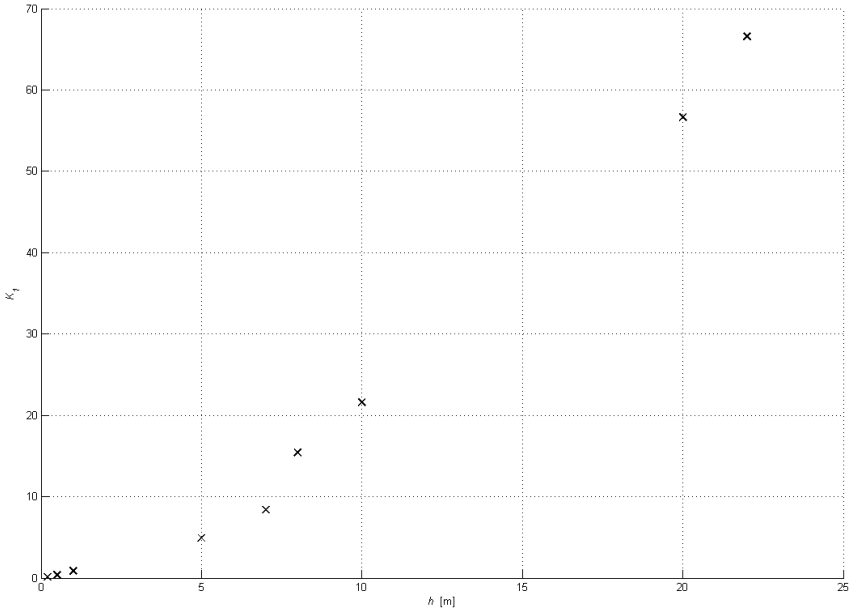

Figure 3.16: Scatter of depth h versus coefficient K_1 (see table 3-1)

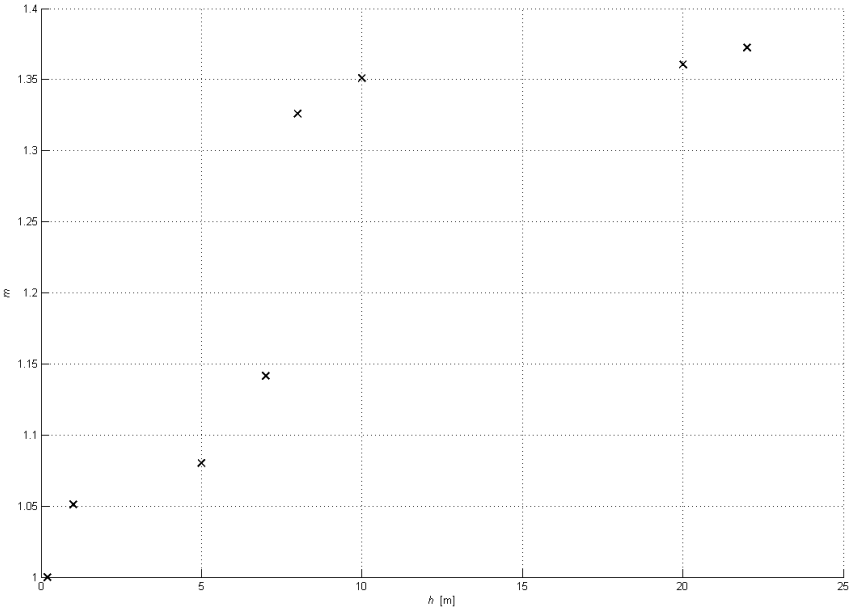

Figure 3.17: Scatter of depth h versus coefficient m (see table 3-2)

First figure 3.16 is considered. The path of the data points in figure 3.16 suggests that the relation between K_1 and h may be described by a power function of the form:

$$K_1 = a_* h^{b_*} \tag{3-28}$$

where a_* and b_* are empirical coefficients. In order to determine the coefficients a_* and b_* again a least square fit is drawn. The type of curve can be described by a power function, while the data set consists of the data presented in table (3-1). The best fit to this power function is shown in figure 3.18. From this least square fit it can be derived that the semi-empirical function $K_1 = f(h)$ can be expressed by:

$$K_1 = 0.76 h^{1.45} \tag{3-29}$$

Which implies that $a_* = 0.76$ and $b_* = 1.45$.

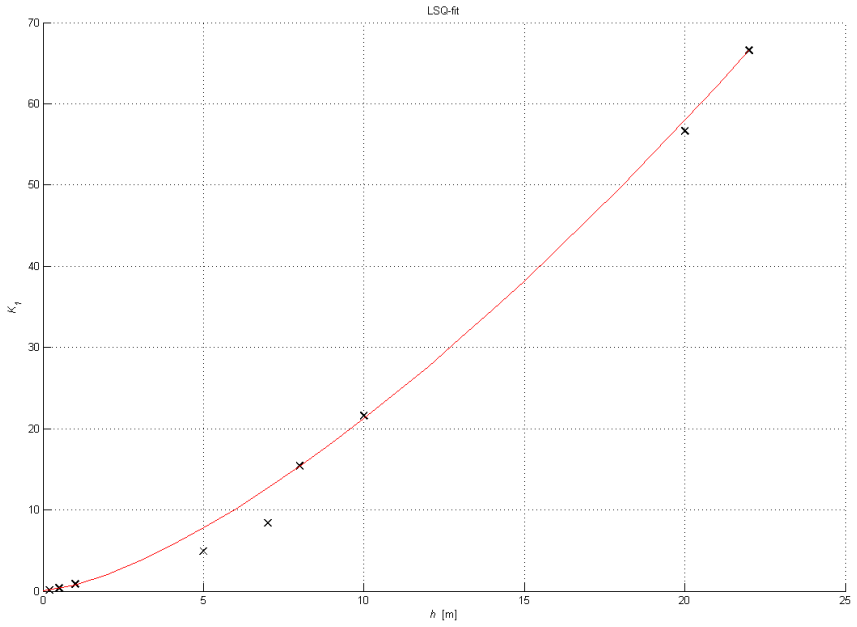

Figure 3.18: Least square fit for depth h versus coefficient K_1 (see table 3-2)

Considering figure 3.17, it may be concluded that no specific functional form for the relation of coefficient m to h exist. However it is speculated that for low values of the water depth the coefficient m has a constant value of 1.0, while for depths $h \geq 10$ m the coefficient m can be approximated by 1.3.

3.4 Depth-averaged friction law

From section 3.1 to 3.3 it can be concluded that the depth-averaged friction law can be described by:

$$\frac{\overline{u}}{u_*} = \frac{1}{\kappa}\left[\ln\left\{\frac{h}{z_0}\right\} - 1\right] + \left(K_1(h)\right)\left(Ri_*\beta\right)^m \qquad (3\text{-}30)$$

$$\frac{\overline{u}}{u_*} = \frac{1}{\kappa}\left[\ln\left\{\frac{h}{z_0}\right\} - 1\right] + \left(0.76h^{1.45}\right)\left(Ri_*\beta\right) \qquad \text{for} \quad h \le 10 \text{ m} \qquad (3\text{-}30a)$$

$$\frac{\overline{u}}{u_*} = \frac{1}{\kappa}\left[\ln\left\{\frac{h}{z_0}\right\} - 1\right] + \left(0.76h^{1.45}\right)\left(Ri_*\beta\right)^{1.3} \qquad \text{for} \quad h \ge 10 \text{ m} \qquad (3\text{-}30b)$$

In Chapter 5, this parameterisation for the effective hydraulic roughness will be tested on a numerical simulation of the tidal propagation in the Yangtze Estuary.

3.5 Sensitivity analysis

This section reflects on the results of the 1DV model and indicates the sensitivity of the buoyancy effect to changes of the variables. Furthermore the Chézy coefficient for two representative conditions for coastal areas is assessed and the results are compared findings of previous studies, as they are reported in literature.

First the situation is considered that the velocity increases (e.g. from 1.0 m/s to 1.5 m/s), while the sediment concentration, the water level, the roughness height and the settling velocity remain constant. From figure 3.19 it can be seen that the effective roughness is reduced more for a lower flow velocity. This can also be derived from equation (3-10). Because the depth average velocity is proportional to the shear velocity, the shear velocity increases with increasing velocity. Furthermore $\left(Ri_*\beta\right)$ is proportional to $\left(u_*^{-3}\right)$, while $\left(C_{eff}/\sqrt{g}\right)$ is proportional to $\left(u_*\right)$. Hence the buoyancy effect decreases with increasing velocity. Furthermore an increase of the sediment concentration results for a lower value of the velocity in a stronger buoyancy effect.

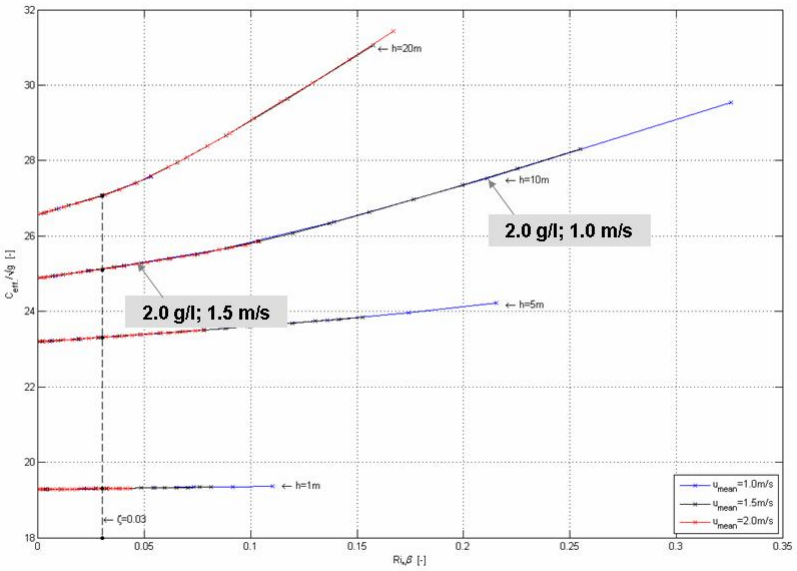

Figure 3.19: Sensitivity to changes of the velocity. Results of the 1DV model.

In case the water depth increases the clear water value of the hydraulic roughness increases. However figure 3.19 indicates that the buoyancy effect does not change significantly, except when the water depth becomes $h \geq 10\,\mathrm{m}$. In that case the free surface effects become significant and the effective roughness decreases more, with increasing sediment concentrations, due to intensification of the stratification effect.

Water that flows faster can carry more sediment, before collapse of the turbulence field. Furthermore in shallower water saturation concentrations are higher. For concentrations above saturation the 1DV model indicates that after some time the vertical turbulence field collapses. For these concentrations the depth-averaged friction law is not valid and does not coincide with the predictions of the 1DV model.

In reality the different parameters ($\bar{u}$, z_0, h, w_s and $\bar{c}$) are related and change simultaneously, both in time and space. For example, when the velocity increases, more sediment will be picked-up from the bottom so that concentrations increase as well. The sensitivity will be further analysed on the basis of a case study for the Yangtze Estuary. Next the order of magnitude of the effective hydraulic roughness in sediment-laden flow is considered for two representative conditions for estuarine areas.

3.5.1 Case I

Clear water:	$z_0 = 0.0005$ m; $w_s = 0.0005$ m/s; $h = 5$ m; $\bar{u} =$ 1,0 m/s; $\bar{c} =$ 0.0 g/l
Sediment-laden flow:	$z_0 = 0.0005$ m; $w_s = 0.0005$ m/s; $h = 5$ m; $\bar{u} =$ 1,0 m/s; $\bar{c} =$ 2.5 g/l

Table 3.3: parameter values for case I

As can be derived from the 1DV model data the different values for the effective Chézy coefficients for clear water and sediment-laden flow (table 3.3) respectively are:

Clear water:

$$C_{eff} = 19.3 \cdot \sqrt{9.81} = 60.4 \ \ \mathrm{m^{1/2}/s}$$

Sediment-laden flow:

$$C_{eff} = 19.7 \cdot \sqrt{9.81} = 61.7 \ \ \mathrm{m^{1/2}/s}$$

Under these conditions the effective hydraulic roughness decreases about 2% relative to clear water.

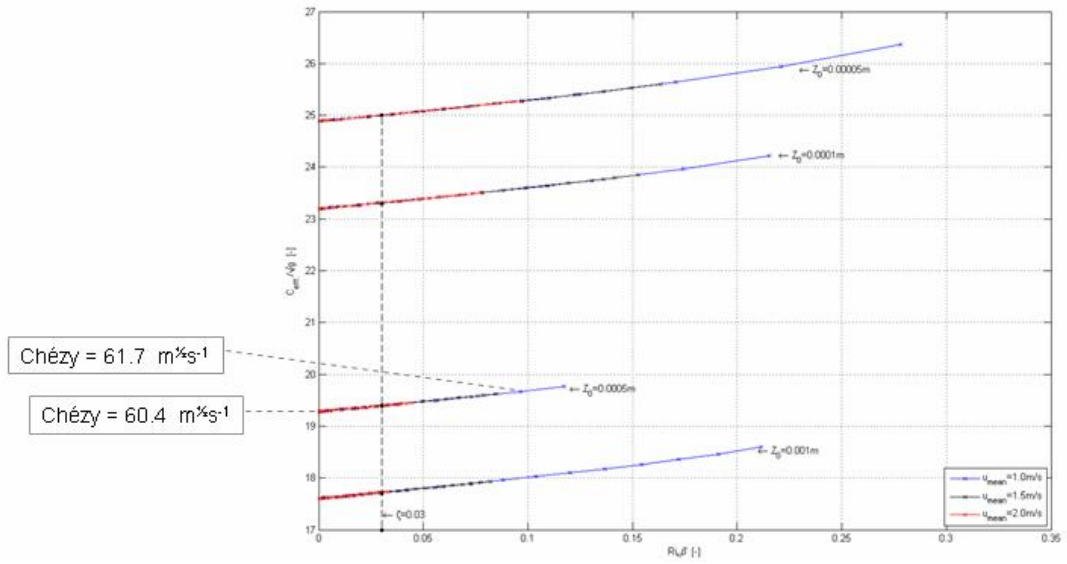

Figure 3.19: Values for Chézy coefficient for case I

3.5.2 Case II

Clear water:	$z_0 = 0.0001$ m; $w_s = 0.0005$ m/s; $h = 20$ m; $\bar{u} =$ 2.0 m/s; $\bar{c} =$ 0.0 g/l
Sediment-laden flow:	$z_0 = 0.0001$ m; $w_s = 0.0005$ m/s; $h = 20$ m; $\bar{u} =$ 2.0 m/s; $\bar{c} =$ 7.5 g/l

Table 3.4: parameter values for case II

Clear water:

$$C_{eff} = 26.6 \cdot \sqrt{9.81} = 83.3 \ \mathrm{m^{1/2}/s}$$

Sediment-laden flow:

$$C_{eff} = 30.1 \cdot \sqrt{9.81} = 94.2 \ \mathrm{m^{1/2}/s}$$

For case II the effective hydraulic roughness decreases approximately 13% relative to clear water. The values of the effective hydraulic roughness in sediment-laden flow that are predicted by the 1DV POINT MODEL are small compared to the reported integral effects in nature (e.g. *Wang* [1994], *Wang et al.* [1998], *Vinzon and Metha* [2001]).

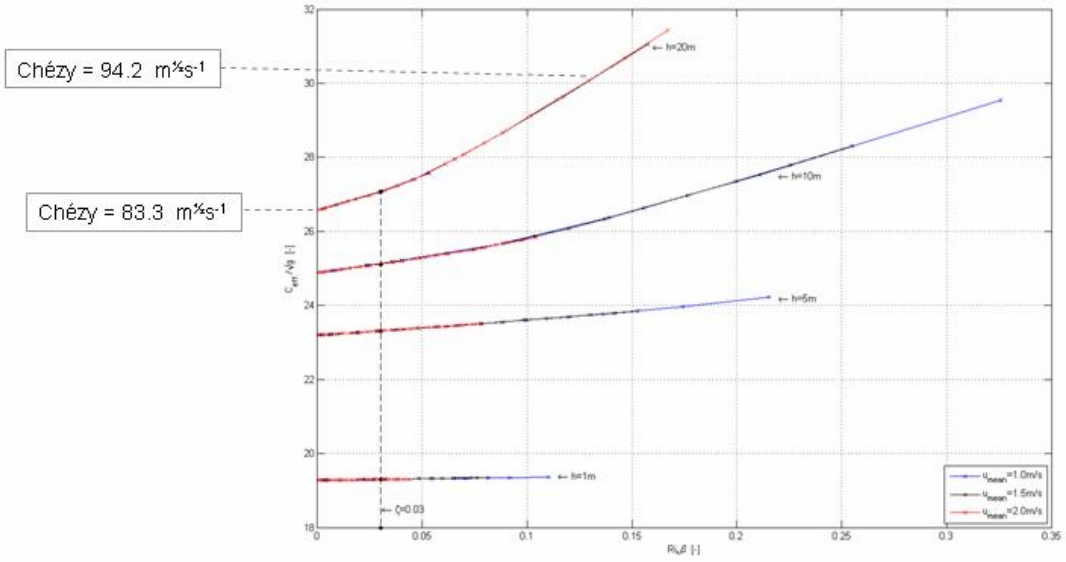

Figure 3.20: Values for Chézy coefficient for case II

Also *Toorman* [2000] derived an empirical roughness parameterisation (equation 2-82, section 2.9). The results for the depth-averaged friction law of the present study (equation 3-

30) are compared with the results of Toorman. The results are plotted in figure 3.21 and 3.22. It can be seen that the buoyancy effect that is predicted by the friction law of Toorman is significantly smaller than the effect that is predicted by the friction law of the present study.

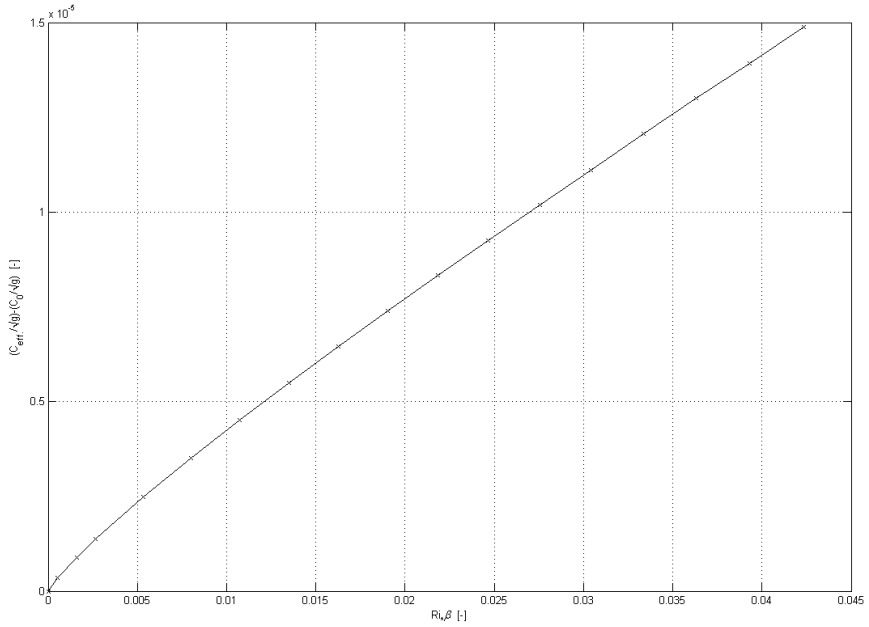

Figure 3.21: Results for the friction law of Toorman [2000]

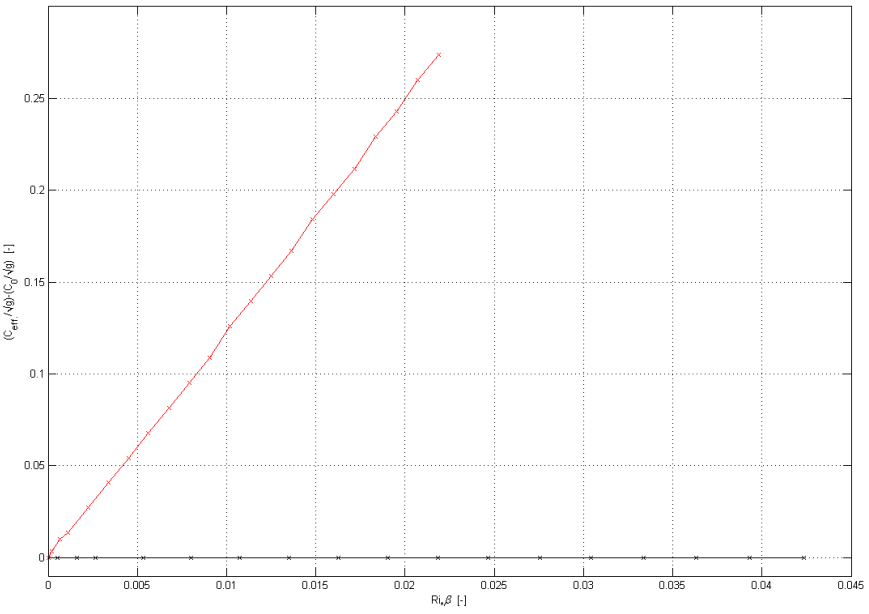

Figure 3.22: Results for equation (3-24) and friction law of Toorman [2000] (black line)

3.6 Discussion

In this chapter a depth-averaged friction law for the effective hydraulic roughness in sediment-laden flow was derived. Hereby the similarity theory, which is proposed in literature by many researchers, was followed. This implies that theories used for stratified boundary flow in the atmosphere, can be adopted for sediment-laden flow in open waters. Using this approach, a preliminary functional form of a depth-averaged friction law was derived (equation 3-10). This friction law suggests that the reduction of the hydraulic roughness due to the sediment-induced buoyancy effect is independent of the roughness height z_0 and is proportional to the bulk Richardson number (Ri_*) and the Rouse number (β). This roughness law was validated through analysis of the results of the 1DV POINT MODEL (figures 3.6, 3.8 and 3.9). From these figures it can be concluded that the reduction of effective hydraulic roughness, in section 3.3 expressed by $(C_{eff}/\sqrt{g})-(C_0/\sqrt{g})$, is independent of z_0. It also shows that below a certain depth there is a linear relation between $(C_{eff}/\sqrt{g})-(C_0/\sqrt{g})$ and $Ri_*\beta$. However the data analysis also showed that the depth-averaged friction law of equation (3-10) is only valid up to a certain depth, i.e. $h \leq 10$ m. The apparent discrepancy of the numerical results and the analytical results of the depth-averaged friction law (equation 3-10) are a result of free surface effects. These effects arise due to the free surface in open channel flow, which is absent in the atmosphere. The free surface effects scale with depth so that for depths larger than $h \approx 10$ m they become significant. Therefore it can be concluded that, although the similarity theory is accepted by many researchers, the atmospheric theories are not fully applicable to the stratified boundary flow in open channels. Through application of the least square method a relation for the effective hydraulic roughness, which is applicable to all depths was derived (equation 3-30).

In section 3.5 the size of the sediment-induced reduction of effective hydraulic roughness is investigated. The 1DV model predicts that the effective hydraulic roughness in sediment-laden flow decreases up to 15%, relative to clear water. If one reflects on literature it can be concluded that this reduction predicted by the 1DV model is relatively small. Mainly reports on field studies and laboratory experiments indicate more significant drag reduction. For example *Wang et al.* [1998] indicate a reduction of approximately 50 % and report on values for Manning's coefficient in parts of the Yellow River of 0.01. Furthermore *Vinzon and Metha* [2001] report an increase of the tidal amplitude of around 50%. However, as was already suggested in literature (*Green and McCave* [1995], *Toorman* [2000]), the observed

drag reduction may not be explained by sediment-induced buoyancy effects alone. It is speculated that part of the drag reduction in nature is caused by remoulding of the bed by very fine sediments. The reduced erosion rates in such a channel bed result in the formation of plane bed or small ripples rather than large dunes, and therefore significantly reduce the bed roughness. In the next chapter these findings will be validated with a (3D and 2Dh) numerical model of the Yangtze Estuary in China.

4 Yangtze Estuary Model

4.1 Introduction

To verify the theory on hydraulic roughness in sediment-laden flow, it is applied to a practical case where sediment concentrations are sufficiently high to influence the effective hydraulic roughness. For this case study the Yangtze Estuary is selected, because here sediment concentrations are high. Data for a model set-up and calibration is available, however limitedly. Reasonable assumptions have to be made for the absent data. For the numerical simulations DELFT3D-FLOW is used, a software package developed by WL | Delft Hydraulics (Appendix C).

This chapter presents the results of calibration runs for both the three dimensional model and the depth-averaged model. As a calibration parameter for flow the Chézy coefficient is used. 3D simulations with sediment taken into account give different results for tidal dynamics than 3D simulations without sediment (as explained in chapter 1). However 2Dh simulations give the same results, either with or without sediment. In traditional 2Dh modelling stratification effects cannot be accounted for. The reduction of effective roughness is accounted for through an afterward correction of the Chézy coefficient, to fit the model results to the existing field data. In 3D modelling this is not necessary, because it is already accounted for in the turbulence model, so that in 3D the Chézy coefficient simply expresses the roughness of the bottom. The Chézy coefficients for the 3D model (with sediment) and 2Dh model that are determined through calibration are expressed by $C_{3D,eff}$ and $C_{2Dh,\,eff}$ respectively. For each simulation the effective roughness can be expressed by an apparent Chézy coefficient. The apparent Chézy coefficient is the sum of different elements, i.e.:

Calibration run 3D model: $C_{3D,eff} = C_{3D} +$ stratification effects

Calibration run 3D model: $C_{2Dh,eff}$

2Dh model with roughness parameterisation: $C_{2Dh,b} = C_{2Dh} + C_b$

C_{2Dh} is the Chézy coefficient without stratification effects and C_b is the surplus value of the Chézy coefficient determined through equation (3-30). The Chézy coefficient $C_{2Dh,\,b}$ will be further discussed in chapter 5. For clarity the definitions of the different Chézy coefficients are summarised in table 4.1.

Apparent Chézy coefficient	*Definition*
C_{2Dh}	Chézy coefficient for 2Dh model without sediment effect.
$C_{2Dh,\,b}$	Chézy coefficient for 2Dh model with sediment effect, which is determined through the roughness parameterisation.
$C_{2Dh,eff}$	Chézy coefficient for 2Dh model with sediment effect, which is determined through calibration. The results of the 2Dh model have been fitted to field data (e.g. tidal components, velocity measurements) by alteration of the Chézy coefficient.
C_{3D}	Chézy coefficient for 3D model without sediment effect
$C_{3D,eff}$	Chézy coefficient for 3D model with sediment effect, which is determined through calibration. The results of the 3D model have been fitted to field data (e.g. tidal components, velocity measurements) by alteration of the Chézy coefficient.
C_b	Surplus value Chézy coefficient due to sediment effect, which is determined through the roughness parameterisation.

Table 4.1: Overview of definitions of apparent Chézy coefficients

Section 4.2 describes the Yangtze Estuary in general, while section 4.3 describes the model set-up for representative conditions in the Yangtze Estuary. Section 4.4 and 4.5 discuss the calibration 3D model and the 2Dh model respectively.

4.2 The Yangtze Estuary

4.2.1 Introduction

The Yangtze River (Changjiang in Chinese), with a length of 6380 km and a catchment-area of 1.8 million km^2, is the largest river in China. It originates from the Tibet Plateau, which is the western part of China. After passing through nine Chinese provinces, it finally flows into the East China Sea, north of Shanghai. The Yangtze River is the fourth sediment carrier in the world. Its river mouth forms an immense delta. This delta receives large amounts of riverine sediment from upstream, which has stimulated continuous land reclamations in the past.

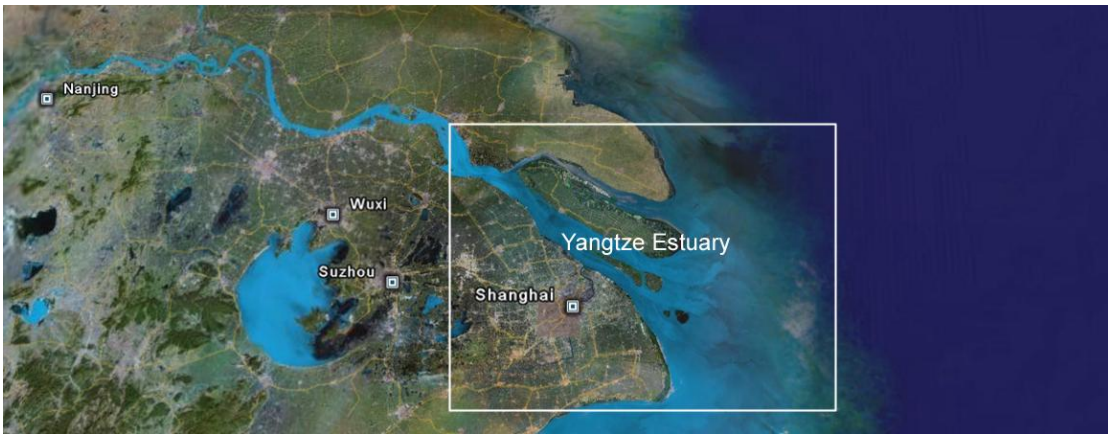

Figure 4.1: Satellite image of the Yangtze Estuary (Source: Google Earth)

The Yangtze Estuary is of great economic value to China; it is the entrance to the Shanghai harbour and the main waterway for seagoing ships. Therefore channels must be kept navigable. The prediction of sediment transport based on an understanding of its processes is of great importance.

The presence of large amounts of sediment and the availability of field data, make the Yangtze Estuary suitable for a case study. Figure 4.2 shows an overview of the Yangtze Estuary with its branches and channel. Furthermore in Appendix D, figures D.2 and D.3 show the water depths within the estuary.

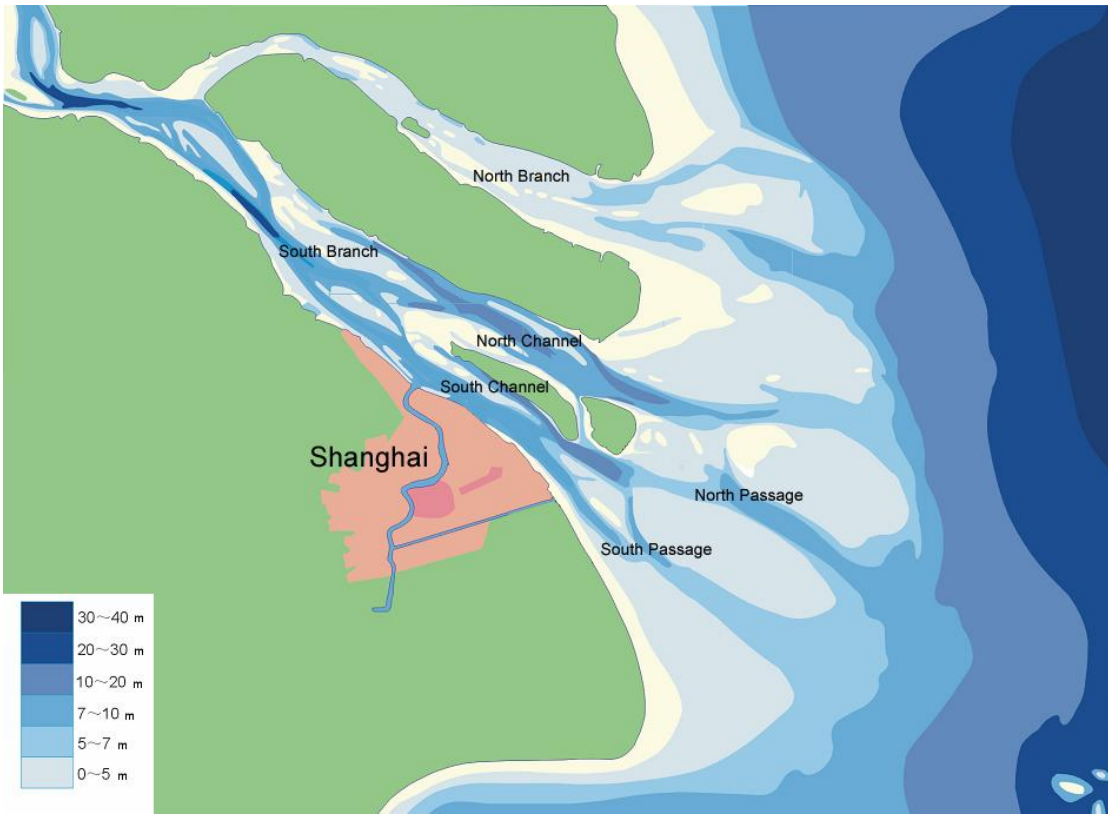

Figure 4.2: Overview Yangtze Estuary (source: PSA meeting presentation, Hu [2006])

4.2.2 General features of the estuary

In this section important characteristics of the Yangtze Estuary concerning tidal flow and suspended sediment transport are discussed. The Yangtze Estuary is mesotidal and the tide is semi-diurnal, with a period of 12 h 25 min. At the mouth the maximum tidal range is 4.62 m, the average tidal range is 2.66 m and the minimum tidal range is 0.17 m (*Wang* [1989]). In different seasons, depending on the tidal range, the tidal prisms of the estuary are:

Flood season, spring tide	$5.3 * 10^9$ m^3
Dry season, spring tide	$3.9 * 10^9$ m^3
Flood season, neap tide	$1.6 * 10^9$ m^3
Dry season, neap tide	$1.3 * 10^9$ m^3

Concerning the river discharge, the following values are measured at Datong hydrologic station (*Wang* [1989], *Wang* [1994]):

Long term annual runoff	912 * 10^9 m^3
Long term average discharge	28 500 m^3/s
Maximum discharge	92 600 m^3/s
Minimum discharge	4620 m^3/s

An important feature of estuaries is the type of mixing, which can be characterised by the stratification parameter α_s (*Simmons* [1955]). This parameter is defined as the ratio of volume of river water coming down the estuary per tidal cycle and the flood volume, i.e.:

$$\alpha_s = \frac{QT}{P_t}$$

where Q is the river flow rate, T is the duration of the tidal cycle and P_t is the tidal prism. The classification of estuaries based on the stratification parameter α_s, is derived from *Simmons* (1955):

Highly stratified	$\alpha_s > 1.0$
Partly mixed	$\alpha_s \approx 0.25$
Well mixed	$\alpha_s < 0.1$

According to *Wang* [1989], for long term fresh water inflow and average tide the stratification parameter α_s has a value of 0.29, which means that generally the Yangtze estuary is partly mixed. However in the flood season during neap tide ($\alpha_s = 2.6$), highly stratified flow occurs, while in the dry season during spring tide ($\alpha_s = 0.05$) the estuary becomes well mixed.

Furthermore, concerning the sediment transport in the Yangtze estuary the following data has been collected at Datong (*Wang* [1989]):

Flood season, average sediment concentration	1.0 kg/m^3
Dry season, average sediment concentration	0.1 kg/m^3
Annual average sediment concentration	0.54 kg/m^3
average annual sediment load	486*10^9 m^3

According to *Chen et al.* [2006] the yearly-averaged near-surface suspended sediment concentration increases from Xuliujing to the south-east of the estuary mouth, increasing further in the northern part of the Hangzhou Bay which is adjacent to the Yangtze estuary. Chen et al. reported that the yearly-averaged near surface suspended sediment concentration is 0.13 kg m^{-3} at Xuliujing, 0.25 kg m^{-3} at Hengsha and 0.36 kg m^{-3} at Sheshan and becomes more than 1 kg m^{-3} towards the north of the Hangzhou Bay. More than 90% of the suspended sediment in the Yangtze estuary consists of fine sediment (<32 μm).

4.3 Model description

For this research a numerical model of the Yangtze Estuary is set up. The next section describes the model set-up. The basic aspects of the model, e.g. the model grid, the bathymetry and the boundary conditions, are derived from previous studies, i.e. *Wang* [1994] and *Van Ormondt* [2004].

4.3.1 Geometry and topography

For the present model the grid of *Van Ormondt* [2004] is used, which in turn originates from *Wang* [1994]. Also the initial bed level is taken from Van Ormondt. For the data that was used to set up the initial bathymetry reference is made to *Wang* [1994]. As a reference level Chart Datum is used, which is the local lowest astronomical level. For the present model it is assumed that this is approximately 4.55 m below Mean Sea Level.

The upper limit of the Yangtze Estuary Model area is the town of Datong (640 km upstream), which is regarded as the location where the tidal wave is completely dissipated. The computational grid of the present model is shown in figure 4.3. Note that the upper part of the river is modelled as a straight, prismatic channel.

Furthermore it is a curvilinear boundary fitted grid of 90(M) x 171(N) grid cells. The averaged grid size is about 3.5 km, the maximum grid size 10 km and the minimum grid size 1 km. The 3D model has 10 layers in the vertical. The relative layer thickness of each layer is presented in table 4.2

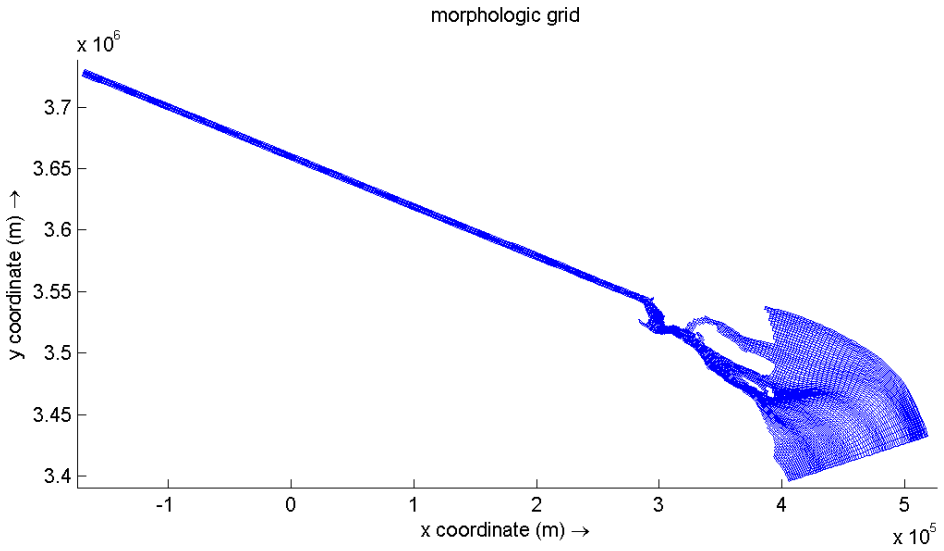

Figure 4.3: Morphologic grid of the Yangtze Estuary model

Layer number	Layer thickness (%)
1	19.5
2	16.3
3	13.7
4	11.5
5	9.6
6	8.1
7	6.8
8	5.7
9	4.8
10	4.0

Table 4.2: Relative layer thickness

layer1=surface layer

layer 10=bottom layer

4.3.2 Boundary conditions for flow

At the upstream boundary the annual mean discharge of the Yangtze River is imposed, which amounts 28500 m³/s. At the open sea boundary tidal constituents are imposed. The

seaward boundary is divided in different sections. For each section a set of tidal components is prescribed. For the data that was used to determine the tidal constituents along the boundary reference is made to *Wang* [1994].

4.3.3 Salinity

At the seaward boundary, a constant salinity level of 31 ppt is imposed. At the upstream boundary the salinity is negligible, therefore zero salinity is defined here. Gravitational circulation, caused by salinity induced stratification, is the driving force of the salt intrusion into the estuary. This stratification effect can only be simulated in three dimensional modelling. Furthermore gravitational circulation and stratification-induced dispersive transport causes extra sediment transport. In a depth-averaged model this stratification induced dispersive transport cannot be simulated and must be compensated by increasing the eddy diffusity coefficient relative to the eddy diffusity in 3D. Salinity-induced dispersive transport locally affects the numerically modelled sediment distribution.

4.3.4 Sediment properties

Field data reported in literature shows that the grain size of bed material ranges from 15 μm to 125 μm, while the grain size of the suspended material ranges from 4 μm to 64 μm (*Wang* [1989], *Shi et al.* [2003]; *Chen et al.* [2006]; *He* [2006] personal correspondence). The settling velocity varies between 0.1 mm/s and 4.0 mm/s (*Wang* [1989], *Shi et al.* [2003]). For the present study a settling velocity of $w_s = 0.4$ mm/s is chosen.

At the upstream boundary a suspended sediment concentration of 2.0 g/l is imposed and at the downstream boundary a concentration of 0.1 g/l. A constant sediment thickness of 0.05m and a uniform sediment concentration is used as initial condition. The present model does not compute bed level changes. Furthermore the following parameters have been applied both for the 3D and for the 2Dh model:

Critical bed shear stress for erosion	0.1 N/m^2
Critical bed shear stress for sedimentation	0.1 N/m^2
Erosion parameter	0.0001 kg/m^2/s

4.3.5 Physical parameters

The bed roughness is modelled with the Chézy coefficient. Due to the sediment-induced buoyancy effect, the Chézy coefficient is expected to be higher for the 2Dh model than for 3D. Through calibration the exact values for the 2Dh and 3D Chézy coefficient are determined (section 4.4 and 4.5).

In 3D the eddy diffusity has a constant value of 1.0 m²/s. To compensate for the stratification induced dispersive transport in 3D modelling, the eddy diffusity in the 2Dh model is 10 m²/s. The numerical time step is 2 minutes, which is small enough to ensure sufficient accuracy.

4.4 Calibration 3D model

In the next section the results of the calibration computations are discussed. Model results for different monitoring stations within the model area are shown in Appendix D. The locations of the monitoring stations are shown in figure D.1. Model results are compared with measurement data, taken from literature. However the available field data is only limited. Furthermore the assumptions (e.g. hydrostatic pressure, no bottom update, no wind, no waves, and annual mean discharge) may cause some discrepancy with nature. A reasonable agreement is satisfactory. The present model simulates a period of two months (February and March) in 2004.

4.4.1 Tidal constituents

For the calibration of the tidal constituents, model results are compared with measurement data from *Wang* [1994]. For the tidal analysis the DELFT3D module TRIANA is used (WL|Delft Hydraulics, 2005). The tidal amplitudes and phases of 10 components are analysed, i.e., O1, K1, P1, M2, S2, K2, N2, M4, MS4 and M6. The components O1, K1, P1, M2, S2, K2 and N2 are astronomical components, while the higher order components are generated locally.

The frequency of the P1 tide is very close to the K1 tide. These two components cannot be accurately separated within two months, because the Reyleigh criterion is violated. The same holds for S2 and K2. The Reyleigh criterion states that tidal frequencies must differ by at least:

$$\Delta f = \frac{360^\circ}{T_{obs}}$$

where Δf is the difference between two tidal frequencies and T_{obs} is the duration of the observation. To still be able to analyse the tidal constituents P1 and K2, P1 is coupled to K1 and K2 is coupled to S2, using the statistical relation between the constituents. The coupling relations are shown in table 4.3.

	P1 coupled to K1	K2 coupled to S2
Amplitude ratio	P1/K1 = 0.199	K2/S2 = 0.573
Phase difference	P1-K1 = -26.83	K2-S2 = -20

Table 4.3: Tidal coupling relations (Wang [1994]).

Table D.1 in Appendix D.1.1 shows both the measured and the computed data for the tidal amplitudes and phases for four different locations within the Yangtze Estuary. Furthermore, table D.1 shows the ratios of the computed to the measured amplitudes and the differences between computed and the measured tidal phases. The closest agreement between the observation data and model results is achieved by applying a Chézy coefficient of $110\ m^{1/2}/s$. This implies that the bottom of the Yangtze is very smooth.

The semi-diurnal tides of M2 and S2 have the largest amplitudes. Also K2 and N2 contribute significantly to the tidal amplitude, about 1/5 of M2 and 1/2 of S2. Due to energy dissipation the astronomical components generally decrease from the sea boundary towards locations more upstream i.e. from Sheshan towards Wusong and Boazhen. This is different for the locally generated components M4, MS4 and M6. The constituent M4 increases when the water depth decreases. This can be explained as follows. If the tidal range is large relative to the water depth, asymmetry of the tidal wave can occur because the effects of friction increase with decreasing water depth. Consequently the higher water travels faster than the lower water, which results in the tidal wave becoming saw toothed in shape with a quick rise at the beginning of the flood tide and a slow fall towards low water. This tidal

distortion is represented by a combination of the main semi-diurnal M2 component and the M4 with a quarter-diurnal period. Because this distortion increases with decreasing water depth, the M4 increases significantly more upstream in the Yangtze Estuary. The overall agreement between the observation data and the computed data is good, both for the amplitudes and for the tidal phases.

Table D.2 shows the results of the tidal analysis of the three dimensional model with a Chézy coefficient of $110\ m^{1/2}/s$ without sediment taken into account. It can be seen that the tidal amplitudes of the different components are generally smaller than those in table D.1. The sediment effect causes larger amplitudes to occur.

4.4.2 Water level

Appendix D.1.2 shows two examples of modelled and observed water levels (figures D.4 to D.7). The vertical axes of the different figures have different values for the water level, because they use different reference levels. However the agreement between the computed and measured elevations (*Wang* [1989], *Wang* [1994] and *Hu et al.* [2000]) is good. The model results show a daily inequality. This inequality can also be observed in figure D.6.

4.4.3 Flow velocity

For the calibration of the flow velocity again data is used that is reported by *Wang* [1989], *Wang* [1994] and *Hu et al.* [2000]. Calibration results are presented for three different locations (figures D.8 to D.14). Comparison between computed and measured depth-averaged flow velocities shows that the tidal current is simulated to the right order of magnitude. Flow velocities around spring tide are of the order of 1.5 m/s, while around neap tide velocities of typically 0.2-0.8 m/s occur.

Figure D.12 shows the results for the depth-averaged velocity for monitoring station SC of both the three dimensional simulation with sediment taken into account and without sediment. When sediment is taken into account velocities are slightly higher, approximately 15%. This can be explained by the sediment effect. Spring-neap tidal variations of this sediment effect can be observed. During spring tide the sediment effect is more pronounced than during neap tide. This may be explained by the fact that during spring tide the

suspended sediment concentrations are higher and vertical gradients are larger (see appendix D.1.5 and D.2.5).

4.4.4 Salinity

Wang [1994] presents survey data of the salinity distribution (figure D.15). Figures D.16 to D.19 show the model results for the horizontal distribution of salinity for different phases of the spring-neap tidal cycle. In general the model results agree well with the data.

Salinity affects the vertical distribution of velocity. The density difference between fresh water and salt water leads to gravitational circulation. The near-bed flow velocity is directed landward and the near-surface flow seaward. The effect of salinity on residual velocity profiles is illustrated in figure 4.3. Figures D.20 to D.23 in Appendix D.1.4 show vertical profiles of velocity, viscosity, sediment concentration and salinity that are computed by the numerical model. Profiles are plotted for monitoring station NB2, which lies within the area of salt intrusion. It can be seen that where there is a strong vertical gradient of salinity, the vertical gradients of horizontal velocity are larger. As was stated in section 4.2.2, during spring tide the Yangtze Estuary is well or partly mixed, while during neap tide stratified flow can occur. This is reflected by the salinity profiles in figures D.20 to D.23. Figures D.22 and D.23 show that, due to gravitational circulation, water in the lower region flows in opposite direction than water in the surface region.

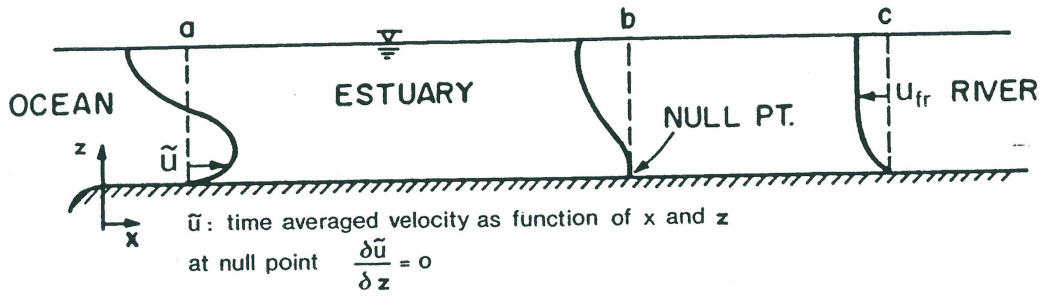

Figure 4.3.a: Salinity effect on velocity
a=flow profile due to gravitational circulation near the sea border
b=residual flow profile more upstream
c=flow profile upstream due to fresh water outflow

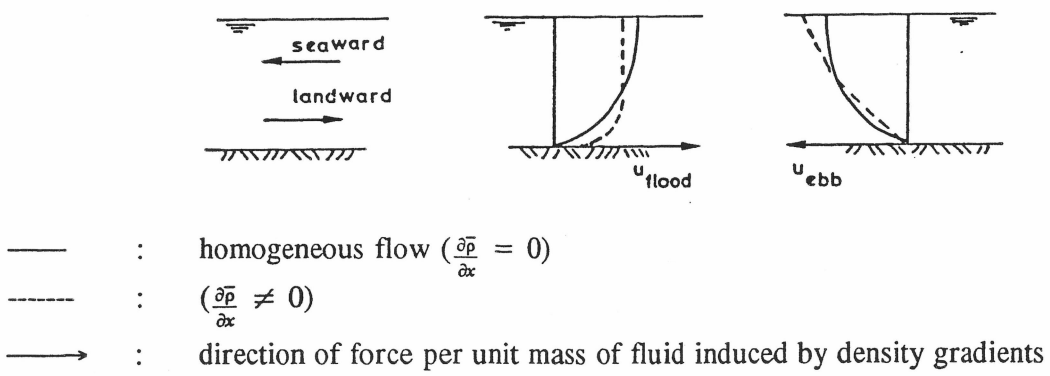

Figure 4.3.b: Salinity effect on velocity. Residual flow profiles due to landward flow (gravitational circulation) and seaward flow (ebb current and/or fresh water outflow)

4.4.5 Sediment

There is only a small amount of experimental data on suspended sediment concentrations in the Yangtze Estuary. *He* [2006] gives a rough indication of the spatial distribution. *Wang* [1989] presents time series of the depth-averaged concentrations for several locations within the estuary. In figures D.24 to D.43 observation data are compared with model results for four different stations.

According to observations in the South Channel (figure D.24) concentrations range from 0.5 g/l to 2 g/l, while the model computes sediment concentrations of 0.5 g/l to 5 g/l. For the North Channel and South Passage these values are of the same order. Very close to the

bottom high concentrations of suspended sediment can be observed. This is reflected by the concentration peaks (up to 30 g/l) in figures D.28, D.33, D.38 and D.43. Generally the model computes slightly higher sediment concentrations than measured. The overall agreement is reasonable.

Furthermore the model results show significant vertical gradients of suspended sediment. It is assumed that where there are large vertical concentration gradients, the effects on the effective hydraulic roughness are also large. It should be noted that both the concentrations of suspended sediment and the vertical gradients are overestimated by the model and therefore also any sediment-induced buoyancy effect.

Chen et al. [2006] report an increase of the sediment concentrations from locations upstream to locations downstream, i.e. from Xuliujing, via Sheshan, towards the Hangzhou Bay. This qualitative description is also valid for the distribution of suspended sediment that is computed by the Yangtze Estuary Model. Figure D.44 shows observation data from *He* [2006] (personal correspondence). It is not clear for which tidal phase, discharge or layer the data holds. Therefore it must be used for a qualitative comparison only.

From comparison between observation data (*Wang* [1989], *Chen et al.* [2006], *He* [2006]) and numerical results it is concluded that the horizontal distribution of the suspended sediment is simulated adequately.

4.5 Calibration 2Dh model

In this section the calibration of the depth-averaged model of the Yangtze Estuary is discussed. As calibration parameter for flow again the Chézy coefficient is used. The depth-averaged model has one computational layer. In definition, the 2Dh model does not account for stratification effects. Through calibration the Chézy coefficient for the depth-averaged model ($C_{2\mathrm{Dh},eff}$) is determined.

4.5.1 Tidal constituents

Tables D.4, D.5 and D.6 show the results of tidal analyses with Chézy coefficients of $110\ \mathrm{m}^{1/2}/\mathrm{s}$, $120\ \mathrm{m}^{1/2}/\mathrm{s}$ and $130\ \mathrm{m}^{1/2}/\mathrm{s}$ respectively. From these analyses it can be

concluded that the closest agreement between computed and measured data is reached for $C_{2\mathrm{Dh},eff} = 130\ \mathrm{m}^{1/2}/\mathrm{s}$.

4.5.2 Water level

From analysis of the computed (figures D.53 and D.54) and observed water levels it can be concluded that model results agree well with measurement data if a Chézy coefficient of $130\ \mathrm{m}^{1/2}/\mathrm{s}$ is assumed.

4.5.3 Flow velocity

Appendix D.2.3 shows the model results for the depth-averaged velocities for different locations. The agreement with the observation data is good. Furthermore figures D.56 to figure D.63 show the results of the 3D simulation with $C_{3\mathrm{D}} = 110\ \mathrm{m}^{1/2}/\mathrm{s}$ (black line), the 2Dh simulation with $C_{2\mathrm{Dh,\ eff}} = 110\ \mathrm{m}^{1/2}/\mathrm{s}$ (red line) and with $C_{2\mathrm{Dh,\ eff}} = 130\ \mathrm{m}^{1/2}/\mathrm{s}$ (blue line). It can be seen that the 2Dh model results for $C_{2\mathrm{Dh,\ eff}} = 130\ \mathrm{m}^{1/2}/\mathrm{s}$ are closer to the 3D model results than the 2Dh model results for $C_{2\mathrm{Dh,\ eff}} = 110\ \mathrm{m}^{1/2}/\mathrm{s}$. The 3D model can compute the sediment-induced buoyancy effect, while in 2Dh this effect is accounted for through alteration of the Chézy coefficient. The 2Dh model with $C_{2\mathrm{Dh,\ eff}} = 130\ \mathrm{m}^{1/2}/\mathrm{s}$ and the 3D model with $C_{3\mathrm{D}} = 110\ \mathrm{m}^{1/2}/\mathrm{s}$ give similar results for the depth-averaged velocities.

4.5.4 Salinity

Figures D.64 to D.67 show the 2Dh model results for the horizontal distribution of salinity for different phases of the spring neap tidal cycle. The effects of gravitational circulation and stratification-induced dispersion cannot be computed by the 2Dh model. To compensate for these effects a higher value for eddy diffusity is applied for the 2Dh model than for 3D model, i.e. 10 m^2/s and 1 m^2/s respectively. However still there is a clear difference between the 2Dh model results and the results of the 3D model (Appendix D.1.4). In the 3D simulation the sea water further intrudes into the estuary and the salt concentrations decrease more gradually from the sea boundary towards the river mouth. In the 3D

simulation the salt intrusion reaches up to the entrance of the North Branch, while in 2Dh salt sea water is not coming close to this area. In 3D modelling the stratification induced dispersive transport and the density driven flow influence the distribution of the salt and sediment concentrations. The agreement between the 2Dh model results and the survey data (*Wang* [1994]) is reasonable, however the 3D model results lead to a better agreement.

4.5.5 Sediment

Appendix D.2.5 shows time series of the depth-averaged suspended sediment concentrations for different stations. 2Dh modelling gives similar results as 3D. Again the concentrations are generally higher than measured. Concerning the horizontal distribution of suspended sediment, the qualitative agreement with the measurement data of *He* [2006] is reasonable. Furthermore differences can be observed between the horizontal distributions simulated in 3D and those simulated in 2Dh. In 3D the sediment is more spread out over the area than in 2Dh. Various processes can cause these differences, amongst which are gravitational circulation, salt-induced dispersive transport and sediment-induced buoyancy.

4.6 Discussion

In this chapter a three dimensional numerical model and a depth-averaged model of the Yangtze Estuary were calibrated. For the numerical simulations DELFT3D-FLOW was used. The tidal propagation and the properties concerning salinity and sediment were well simulated by both models.

Through calibration it was shown that the tidal propagation in 3D modelling agrees well with measurement data for a Chézy coefficient of $C_{3D} = 110\ \mathrm{m}^{1/2}/\mathrm{s}$. This implies that the bottom of the Yangtze Estuary is very smooth. Calibration of the 2Dh model resulted in a value for the Chézy coefficient of $C_{3D} = 130\ \mathrm{m}^{1/2}/\mathrm{s}$. So the Chézy coefficient for 2Dh is higher than for 3D. The surplus value compensates for the apparent smoothing due to sediment-induced stratification.

The results of the calibrations indicate that the reduction of effective hydraulic roughness in sediment-laden flow cannot be explained by the sediment-induced buoyancy effect alone.

The initial low value of the bottom roughness may be explained by the fact that the presence of suspended sediment smoothens the bed, so that bed forms are small.

Furthermore it is noticed that the salinity induced stratification in the 3D simulation, leads to gravitational circulation and stratification induced dispersive transport. Locally this influences the distribution of suspended sediment.

5 Application roughness parameterisation to Yangtze Estuary Model

5.1 Introduction

In this chapter the depth-averaged effective roughness parameterisation for sediment-laden flow is validated by applying it to the Yangtze Estuary. The suspended sediment effect varies in time and space, because the amount of suspended sediment, the water depth and the velocity vary in time and space. The sediment effect not only varies over a tidal cycle, but it also varies over a larger time scale, i.e. over a spring-neap tidal cycle. However for this case study sediment induced reduction of hydraulic roughness is assumed, which is constant in time and the same for the whole estuary. The reduction of effective hydraulic roughness in the Yangtze Estuary is determined through equation (3-30).

In the next sections $C_{2\mathrm{Dh},b}$, which is the sum of $C_{2\mathrm{Dh}}$ and C_b, is computed for two cases. In case I $C_{2\mathrm{Dh},b}$ is determined for a relative smooth bottom ($C_{2\mathrm{Dh}} = 110\ \mathrm{m}^{1/2}/\mathrm{s}$), as was suggested for the Yangtze Estuary in chapter 4, and in case II for a more rough bottom ($C_{2\mathrm{Dh}} = 90\ \mathrm{m}^{1/2}/\mathrm{s}$). The sensitivity of the buoyancy effect to a change in bottom roughness is investigated.

5.2 Case I

In chapter 3 it was concluded that the bottom of the Yangtze Estuary is relatively smooth. In Case I the buoyancy effect in sediment-laden flow over this relative smooth bottom is computed. The values of the input parameters for equation (3-30), that are used here are typical for the Yangtze Estuary. First a mean water depth of $h = 15\ \mathrm{m}$ is assumed. Furthermore the mean suspended concentration $\bar{c} = 2.0\ \mathrm{g/l}$ and the settling velocity $w_s = 0.4\ \mathrm{mm/s}$. The tidal mean value of the absolute depth-averaged velocity can be derived as follows:

$$\overline{\overline{|u|}} = 2\left(\int_0^{\frac{1}{2}T} \mathrm{d}t \left\{ \frac{u}{T} \right\} \right) = 2\left\{ \int_0^{T} \mathrm{d}t \left\{ \frac{\hat{u} \sin \frac{2\pi}{T}}{T} \right\} \right\} = \frac{2\hat{u}}{\pi}$$

where $\overline{\overline{|u|}}$ is the absolute velocity averaged over depth and over the tidal cycle. From Appendix D.1.3 and D.2.3 it can be seen that $\hat{u} \approx 1.4$ m/s averaged over a spring-neap tidal cycle, so that:

$$\overline{\overline{|u|}} = \frac{2}{\pi} \times 1.4 = 0.90 \text{ m/s}$$

It is assumed that the difference between the Chézy coefficient of the 3D model and the Chézy coefficient of the 2Dh model can be attributed mostly to the sediment-induced buoyancy effect, so that $C_{3D,eff} \approx C_{2Dh}$. This leads to the following derivation of the roughness height:

$C_{2Dh} = 18 \log \frac{12h}{k_s}$ (equation 2-30), so that

$k_s = 1.39 \cdot 10^{-4}$ m , and

$$z_0 = \frac{k_s}{30} = 4.65 \cdot 10^{-6} \approx 5 \cdot 10^{-6} \text{m}$$

Figure 5.1 shows the results of the 1DV POINT MODEL for the above settings. The effective roughness $\left(C_{eff} / \sqrt{g} \right)$ is plotted against $\left(Ri_* \beta \right)$.

The 1DV model shows that under these conditions the vertical turbulence field collapses after time of relaxation. Saturation concentration is $\bar{c}_{sat} = 0.8$ g/l. The parameter values are averaged in time and space. In an estuary hydraulic conditions change significantly in time and space, so that actually the collapse of turbulence will not occur instantaneously under these conditions. However, still these conditions are outside the scope of application of equation (3-30), because the under these conditions the velocity profile is no longer

logarithmic and thus the concentration profile cannot be described by a Rouse profile. The reduction of hydraulic roughness can be determined up to saturation. According to friction law the Chézy coefficient at saturation is:

$$C_{2\mathrm{Dh,\,b}} = 39.2 \cdot \sqrt{9.81} = 122.9 \ \mathrm{m^{1/2}/s}$$

The effective hydraulic roughness decreases about 15% relative to clear water. The different curves in figure 5.1 indicate the sensitivity of the effective hydraulic roughness to changes of the parameter values. If a mean depth of $h = 10\,\mathrm{m}$ is assumed, the concentration at saturation is $\bar{c}_{\mathrm{sat}} = 1.4\,\mathrm{g/l}$ and the Chézy coefficient is:

$$C_{2\mathrm{Dh},\,b} = 40.0 \cdot \sqrt{9.81} = 125.3\,\mathrm{m^{1/2}/s}$$

Because it is assumed that the difference between $C_{3\mathrm{D},eff}$ and $C_{2\mathrm{Dh},\,eff}$ is mostly due to the sediment-induced buoyancy effect, $C_{2\mathrm{Dh},\,b} \approx C_{2\mathrm{Dh},\,eff}$ would supports the applicability of the depth-averaged friction law to the Yangtze Estuary. Calibration of the 2Dh model showed that $C_{2\mathrm{Dh},eff} = 130\,\mathrm{m^{1/2}/s}$, while $C_{2\mathrm{Dh},b} \approx 123\,\mathrm{m^{1/2}/s}$ and $C_{2\mathrm{Dh},b} \approx 125\,\mathrm{m^{1/2}/s}$ for $h = 15\,\mathrm{m}$ and $h = 10\,\mathrm{m}$ respectively. The 1DV model indicates that for concentrations above saturation the effective hydraulic roughness decreases further, however not in accordance with equation (3-30). The results of this case study support the validity of the depth-averaged friction law within its scope of application.

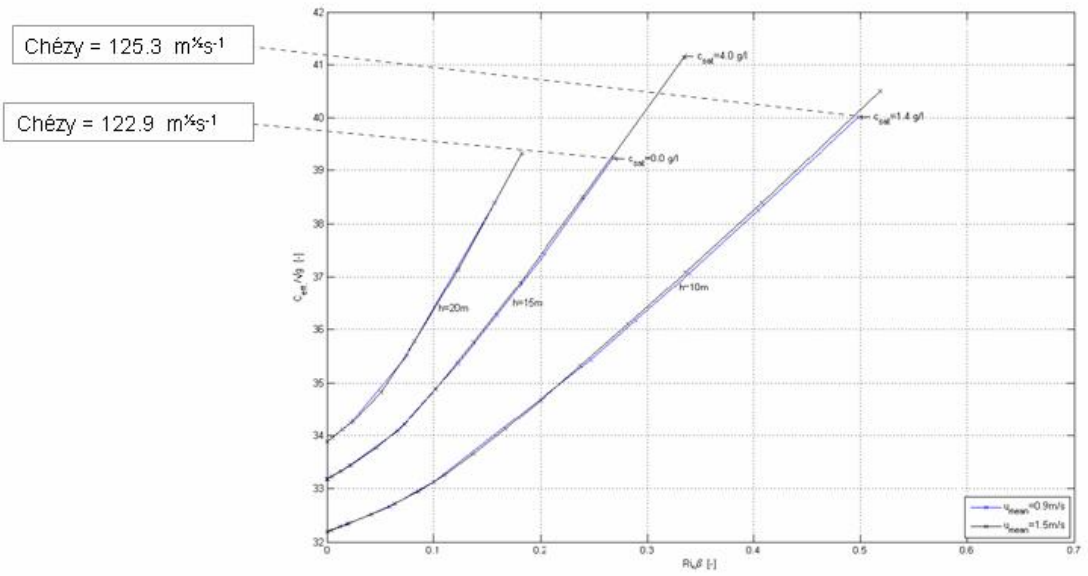

Figure 5.1: Chézy coefficients for case I

5.3 Case II

While the calibration runs showed an optimal agreement with measurement data for $C_{3D,eff} = 110\ \mathrm{m}^{1/2}/\mathrm{s}$, reasonable results were obtained for $C_{3D,eff} = 90\ \mathrm{m}^{1/2}/\mathrm{s}$. This can be seen from table D.3. Case II considers the fictitious situation of a bottom roughness of $C_{2Dh} = 90\ \mathrm{m}^{1/2}/\mathrm{s}$ for the Yangtze Estuary. This results in the following value for a roughness height:

$C_{2Dh} = 18\ \log\frac{12h}{k_s}$ (equation 2-30), so that

$k_s = 1.8 \cdot 10^{-3}\mathrm{m}$, and

$z_0 = \frac{k_s}{30} = 6 \cdot 10^{-6}\mathrm{m}$

Furthermore $h = 15\ \mathrm{m}$, $\bar{c} = 2.0\ \mathrm{g/l}$, $w_s = 0.4\ \mathrm{mm/s}$ and $\overline{\overline{|u|}} = 0.90\ \mathrm{m/s}$.

Again 2.0 g/l is above saturation. However a flow over this rougher bottom can carry more sediment than the previous case. The saturation concentration is $\bar{c}_{\text{sat}} = 1.3\,\text{g/l}$, so that the maximal Chézy coefficient up to saturation is:

$$C_{\text{2Dh},\,b} = 32.9 \cdot \sqrt{9.81} = 103.0\ \text{m}^{1/2}/\text{s}$$

The effective roughness decreases approximately 15 % relative to clear water. However the Chézy coefficient of case II, computed by the parameterisation, does not come close to $C_{\text{2Dh},eff} = 130\ \text{m}^{1/2}/\text{s}$, as was calibrated for the 2Dh model.

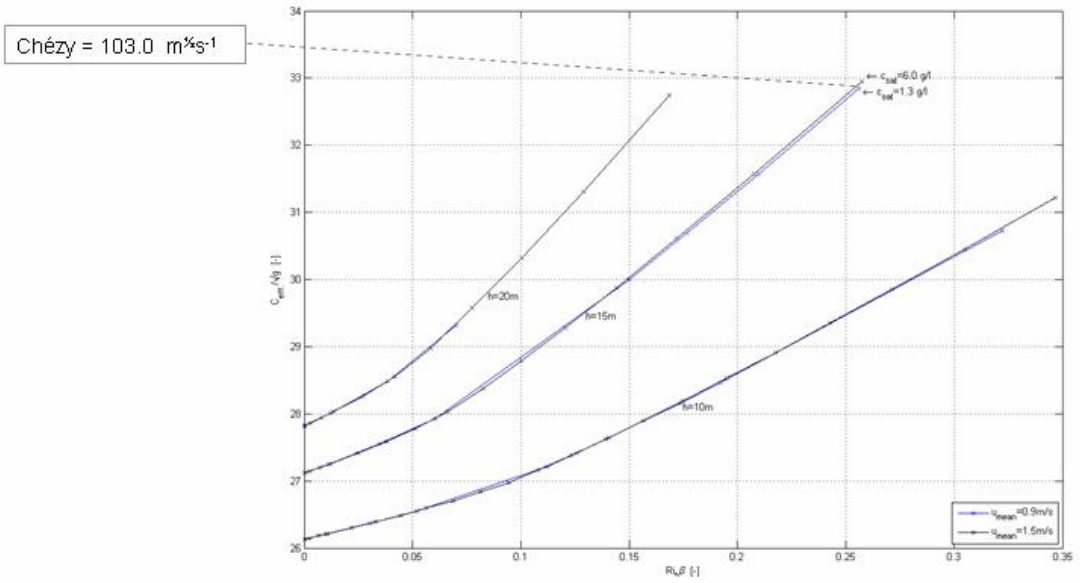

Figure 5.2: Chézy coefficients for case II

5.4 Discussion

In this chapter the parameterisation was applied to the Yangtze Estuary Model. The values of the relevant parameters ($\bar{u}$, z_0, h, w_s and $\bar{c}$) that were used for the friction law are typical for the Yangtze Estuary. Two cases were considered. Case I assumed a smooth bottom for the Yangtze, as was suggested by the results of the 3D calibration. Case II considered a rougher bottom. The 1DV model showed that in both cases the vertical turbulence field collapsed after relaxation time. However, the depth-averaged friction law is only valid for conditions before collapse. Therefore, the reduction of effective roughness

was computed for concentrations up to saturation. It was found that when the roughness parameterisation is applied the results of case I compared better to the results of the calibration than the results of case II.

As has been explained before, a depth-averaged model cannot account for the buoyancy effect while a three dimensional model can. This makes 2Dh modelling intrinsically less accurate than 3D. For the calibration of the 2Dh model this buoyancy effect was compensated by a higher value for the Chézy coefficient. Therefore the difference between the value of $C_{3D,eff}$ ($\approx C_{2Dh}$) and $C_{2Dh,eff}$ can be interpreted as an indication for the size of the error in 2Dh modelling due to the buoyancy effect. The size of the error for the Yangtze model is approximately $C_{2Dh,eff} - C_{2Dh} = 130 - 110 = 20\ \mathrm{m^{1/2}/s}$. In case I the application of the roughness parameterisation resulted in an effective roughness coefficient of $C_{2Dh,b} \approx 125\,\mathrm{m^{1/2}/s}$. This results shows that if the parameterisation is applied the error is reduced to $C_{2Dh,eff} - C_{2Dh,b} = 130 - 125 = 5\ \mathrm{m^{1/2}/s}$. This means that the roughness parameterisation reduced the buoyancy-induced error by 75%.

The results that were presented in this chapter showed that the 2Dh model becomes considerably more accurate by accounting for the sediment effect through the application of depth-averaged roughness parameterisation.

6 Discussion

In this chapter the results of the research as a whole are discussed. For specific discussions on the different elements of the research, the reader is referred to the relevant sections of chapters 2 to 5.

6.1 Roughness parameterisation

In this study a depth-averaged friction law for sediment-laden flow was derived. This friction law was based on theories that are commonly used for the earth's atmosphere, as this was demonstrated by previous studies to be promising. Herein it was assumed that sediment-laden flow is a stratified flow, which provides a physical background for the parameterisation of the effective hydraulic roughness because the sediment-induced stratification suppresses turbulence mixing. As a result, the concentration and velocity profiles change relative to clear water flow and the effective hydraulic roughness is reduced.

The following parameterisation for the effective hydraulic roughness in sediment-laden flow was analytically derived in chapter 3 (equation 3-10):

$$\frac{\bar{u}}{u_*} = \frac{1}{\kappa}\left[\ln\left\{\frac{h}{z_0}\right\} - 1\right] + K_1\left(Ri_*\beta\right)^m$$

This parameterisation shows that the buoyancy effect is proportional to the bulk Richardson number (Ri_*) and the Rouse number (β). Next the 1DV model was used to analyse this roughness parameterisation. The experimental results confirmed the validity of the above equation, however only up to a certain depth. For larger depths it shows a discrepancy with the results of the 1DV model. This can be explained by free surface effects in open channel flow. A free surface is absent in the atmosphere and therefore these effects are not taken into account in the atmospheric theories that were used to derive of the friction law. Because the surface effects scale with depth, they are only noticeable for larger depths. In the surface layer viscosity is low and turbulent mixing is limited. This can result in a collapse of the vertical turbulence field there, which causes a large gradient of the sediment concentration. The Rouse profile that was used to derive equation (3-10) is not valid for large depths. Due

to a strong concentration gradient near the surface, the stratification effect is intensified, so that the effective roughness is reduced more for larger depths. The discrepancy of the friction law with the 1DV model indicated that the atmospheric theories are not fully applicable to stratified shallow water flow. Previous studies that used the similarity theory, of which the author is aware, do not report on these free surface effects in sediment-laden flow. To account for the free surface effects, the coefficient K_1 and m were made dependent on the water depth. The 1DV model predictions were well simulated by the depth-averaged friction law, with the free surface effects included through the coefficients K_1 and m. However $K_1 = f(h)$ and $m = f(h)$ were determined experimentally, so that the challenge remains to find a parameterisation for these coefficients that is based on the physical background, i.e. the actual concentration profiles.

6.2 Significance of the sediment effect

In chapter 1 it was hypothesised that damping of turbulence due to sediment-induced stratification is significant and this will result in a significant decrease of the effective hydraulic roughness. Analysis of the 1DV data showed that the buoyancy effect is limited, but enough to significantly reduce the effective hydraulic roughness. The results suggested that the reported extremely low values for the hydraulic roughness in nature (e.g. *Wang et al.* [1998], *Vinzon and Metha* [2001]), can only partly be attributed to damping of turbulence due to sediment-induced stratification. It is speculated that due to the presence of very fine sediment the channel bed is smoothened and bed forms are small. This implies that the buoyancy effect only contributes a limited proportion to the reduction of the hydraulic roughness in sediment-laden flow. According to the results of the 1DV model, the effective hydraulic roughness decreases approximately 15% relative to clear water.

6.3 Yangtze Estuary Model

The parameterisation was validated by applying it to a numerical model of the Yangtze Estuary. The 3D and the 2Dh model were calibrated for $C_{3D,eff} = 110\ \mathrm{m}^{1/2}/\mathrm{s}$ and $C_{2Dh,eff} = 130\ \mathrm{m}^{1/2}/\mathrm{s}$ respectively. This indicates that the bottom of the Yangtze Estuary is very smooth even without the buoyancy effect, and that the buoyancy effect decreases the effective roughness further. Sediment concentration levels were even exaggerated slightly,

to exemplify the buoyancy effect on flow behaviour. These findings support the supposition that the observed drag reduction cannot be explained by sediment-induced buoyancy effects alone.

The results of the case study were encouraging. Within the scope of applicability the reduction of the effective hydraulic roughness due to buoyancy destruction was of the same order as was indicated by the calibration runs. The roughness parameterisation reduced the buoyancy-induced error in 2Dh modelling by 75%. From this case study it can be concluded that in a 2Dh model the sediment-induced buoyancy effect was effectively accounted for by a correction of the hydraulic roughness. The 2Dh model results become more accurate by accounting for the sediment effect through the application of depth-averaged roughness parameterisation.

The Yangtze Estuary is known as a morphologically very active area. However in the Yangtze Estuary model morphological changes were not taken into account. *Byun and Wang* [2005] report on significant effects of the sediment-induced stratification on the spatial extent of deposition areas and erosion rates in a region on the southwest coast of Korea. This indicates that the presence of suspended sediment also affects morphodynamics. If morphological changes would be included in a numerical model, the application of the roughness parameterisation may establish also more accuracy in 2Dh modelling within the field of morphology. For further research it is recommended to take morphology into account and to investigate the effect of buoyancy on morphological changes.

In this case study the sediment effect was assumed to be constant in time and space. However the relevant parameters, (e.g. sediment concentration, water depth and velocity) are highly variable. Therefore it is expected that in nature the effective roughness varies in time and space. The variability of the roughness coefficient due to sediment-induced buoyancy is confirmed by the report of *Green and McCave* [1995]. This variability of the effective roughness can be accounted for by implementing the roughness parameterisation in the numerical code of DELFT3D. In this way, a continuous update of the effective roughness with feedback to hydrodynamics and sediment transport is realised. Because this may reduce the difference between 3D and 2Dh modelling even further, this implementation is recommended for future research.

Important to notice is that the depth-averaged friction law is valid for conditions up to saturation. In the present study saturation was defined as the critical condition and sediment

concentration above which the vertical turbulence field collapses. The 1DV model showed that for conditions, commonly found in the Yangtze Estuary, after some time of relaxation the turbulence field collapsed. However estuarine areas like the Yangtze are highly hydrodynamically variable. Thus, in reality sediments will not have the time to settle and the collapse of turbulence will probably not occur, because the relaxation time has not passed. However for these conditions the roughness parameterisation is not valid, which limits its scope of applicability.

6.4 3D versus 2Dh

Depth-averaged models are more practical with respect to the necessary computational resources than full three dimensional models. However, a depth-averaged model is less accurate than a three dimensional model, because stratification effects cannot be taken into account. This concerns not only sediment effects but also salinity-induced stratification effects. These salinity-induced stratification effects (i.e. gravitational circulation and stratification-induced dispersive transport) cause significant differences between 2Dh and 3D simulations locally within the model area, as was shown in sections 4.4.4 and 4.5.4. Because of this, the buoyancy effect will be different in 3D and 2Dh, so that if the parameterisation is implemented in 2Dh this will not exactly simulate the buoyancy effect in 3D. An interesting topic for further research is to investigate the effect of salinity-induced stratification on the sediment effect and on tidal dynamics in general. Including the effects of salt in 2Dh modelling may increase the accuracy of the model predictions even further.

6.5 Possible consequences

The calibration of the 3D model showed that in nature the bottom of the Yangtze Estuary is initially very smooth and that the buoyancy effect contributes to the apparent smoothness. This can be an interesting fact for river engineers. In literature researchers express their concerns on a drastic decline in supply of suspended sediment from the Yangtze River to the estuary during the past decades due to human activities, e.g. dam construction (*Yang et al.* [2004, 2005, 2006]). This decline has far reaching consequences on the morphological development of the Yangtze Estuary. Decrease of the accretion rate of the outer delta has already been observed. With the completion of the Three Gorges Dam and more construction projects at hand (e.g. the South-to North Water Diversion Project) erosion of the outer delta is likely to occur in the future (*Yang et al.* [2002]). An increase of the

hydraulic roughness due to a decrease of sediment concentrations will probably worsen the problem. In this research it was speculated that the low roughness values are only partly due to buoyancy destruction, while the greater part may be attributed the absence of bed forms in sediment-laden flow. If this is the case, then the increase of hydraulic roughness in the Yangtze Estuary due to trapping of sediment by the Three Gorges Dam upstream may arise with a certain delay. This will probably result in a slower downstream propagation of floods, and also in increasing water levels at equal discharge. The decrease of the buoyancy effect may be noticeable immediately after construction of the dam, while the increase of the bottom roughness may take some time. It is therefore recommended that the morphology in the part of the Yangtze that is downstream of the dam is closely analysed in the period before and after building of the dam. This event is a unique opportunity to verify whether a rather abrupt change in suspended sediment supply yields a change in bed morphology on a longer timescale. These findings will be valuable for a closer understanding of the effect of fine sediment on actual bed roughness.

7 Conclusions and recommendations

Many studies reported in literature study show an appreciable effect of suspended sediment on turbulent properties at already moderate sediment concentrations. In the present study the suspended sediment effect was defined as the effect on flow behaviour due to sediment-induced buoyancy destruction. Buoyancy destruction reduces the effective hydraulic roughness. However no theoretically accepted, justifiable parameterisation for effective hydraulic roughness in turbulent sediment-laden flow exists to date. Therefore the effect of suspended sediment on tidal propagation in estuaries could not be accounted for in 2Dh modelling, which has a negative effect on the reliability of the 2Dh model predictions. The objective of this research was to parameterise this effect in order to improve the performance of a 2Dh numerical model.

By applying the similarity theory and taking into account the free surface effects, the following roughness parameterisation was derived:

$$\frac{\bar{u}}{u_*} = \frac{1}{\kappa}\left[\ln\left\{\frac{h}{z_0}\right\} - 1\right] + \left(0.76h^{1.45}\right)\left(Ri_*\beta\right) \qquad \text{for} \qquad h \le 10 \text{ m}$$

$$\frac{\bar{u}}{u_*} = \frac{1}{\kappa}\left[\ln\left\{\frac{h}{z_0}\right\} - 1\right] + \left(0.76h^{1.45}\right)\left(Ri_*\beta\right)^{1.3} \qquad \text{for} \qquad h \ge 10 \text{ m}$$

Numerical experiments with the 1DV POINT MODEL validated this depth-averaged friction law. From these experiments it can be concluded that the sediment-induced stratification results in a significant reduction of the effective hydraulic roughness. However the size of the buoyancy effect as indicated by the numerical experiments is small compared to the integral effect in nature that is reported in literature.

The parameterisation was applied to the Yangtze Estuary. Calibration showed that the bottom of the Yangtze Estuary is very smooth even without the buoyancy effect, and that the buoyancy effect decreases the effective roughness further. The 1DV and the DELFT3D model showed that the sediment-induced buoyancy effect can effectively be accounted for by a correction of the roughness coefficient. For the Yangtze Estuary the buoyancy effect was properly simulated by the depth-averaged roughness parameterisation. The inaccuracy

in 2Dh modelling due to the sediment effect was reduced by approximately 75%. From the present study it can be concluded that a depth-averaged model becomes more accurate through application of the roughness parameterisation.

The conclusions of this research show that the application of a parameterisation for buoyancy effects in a depth-averaged model produces promising results. Several other issues can be investigated in order to increase the reliability even more. These issues were addressed in chapter 6 and are summarised below.

The recommendations for further research include:

- Implement the parameterisation into the numerical code of DELFT3D, so that the effective hydraulic roughness is continuously updated with feedback to hydrodynamics and sediment transport.
- Apply the depth-averaged friction law to other estuarine areas than the Yangtze Estuary to investigate its general applicability. It is recommended to apply it to a model area for which there is abundant calibration data, so that the improvement of the model performance as a result of the implementation of the roughness parameterisation can accurately be determined.
- Investigate all effects of depth averaging, amongst which the salinity induced stratification effects. Subsequently determine the impact of integration over depth on the accuracy and applicability of the depth-averaged friction law.
- Study the free surface effects and parameterise them on the basis of their physical background, for example by using the appropriate concentration profiles.
- Further investigate the effects of very fine sediment on the actual bottom roughness.
- Investigate the effect of sediment-induced buoyancy on morphological changes simulated in 2Dh.
- It is recommended to monitor the morphological development of the Yangtze Estuary after closure of the Three Gorges Dam in order to create a better understanding of the sediment processes.

If these recommendations are pursued, the results will lead to significant improvements in the reliability of depth-averaged modelling. These improvements will make the 2Dh model a powerful tool for fast and reliable analysis of large estuarine areas.

References

Adams, C.E. and Weatherly, G.L., (1981), "Suspended-sediment transport and benthic boundary-layer dynamics", Marine Geology, Volt 42, pp 1-18.

Adams, C.E. and Weatherly, G.L., (1986), "Some effects of suspended sediment stratification on an ocean bottom boundary layer", Journal of Geophysical Research, Vol 86, No. C5, pp 4161-4171.

Barenblatt, G.F., (1953), "On the motion of suspended particles in a turbulent stream", Prikladnaja Matematika i Mekhanika, Vol 17, pp 261-274 (English translation).

Battjes, J.A., (2002), "Fluid Mechanics", lecture notes CT2100, Delft University of Technology.

Battjes, J.A., (2002), "Open channel flow", lecture notes CT3310, Delft University of Technology.

Byun, D-S., Wang, X.H., (2005). "The effect of sediment stratification on tidal dynamics and sediment transport patterns", Journal of Geophysical Research, Vol 110

Chen, S-L, Zhang, G-A, Yang, S-L, S, J.Z., (2006), "Temporal variations of fine suspended sediment concentration in the Changjiang River estuary and adjacent coastal waters, China", Journal of hydrology, Vol 331, pp 137-145

Coleman, N.L., (1981), "Velocity profiles with suspended sediment", Journal of Hydraulic Research, Vol 19, No. 3, pp 211-229.

Coleman, N.L., (1986), "Effects of suspended sediment on the open-channel velocity distribution", Water Resources Research, Vol 22, No. 10, pp 1377-1384.

Dyer, K.R., (1994), " Sediment and depositional processes". In: Pye, K., (1994), "Sediment transport and depositional processes", Backwell Scientific Publications, Oxford.

Einstein, H.A. and Chien, N., (1955), "Effects of heavy sediment concentration near the bed on velocity and sediment distribution", MRD Sediment Series No. 8, University of California, Berkeley.

Elata, C., and Ippen, A. T., (1961), "The dynamics of open channel flow with suspensions of neutrally buoyant particles", M.I.T., hydrodynamics laboratory, Technical Report 45, Cambridge.

Gabioux, M., Vinzon, S.B., Piava, M., (2005), "Tidal propagation over fluid mud layers on the Amazon shelf", Continental Shelf Research, Vol 25, pp 113-125

Green, M.O., McCave, I.N., (1995), "Seabed drag coefficient under tidal current in the eastern Irish Sea", Journal of Geophysical Research, Vol 100, pp 16057-16069

Hu, K., Ding, P., Zhu, S.., Cao, Z., (2000), " 2-D current field numerical simulation integrating Yangtze Estuary with Hangzhou Bay", China Ocean Engineering, Vol 14, No 1, pp 89-102

Itakura, T. and Kishi, T., (1980), "Open channel flow with suspended sediments", ASCE, Journal of the Hydraulics Division, Vol 106, No. HY8, pp 1325-1343.

Kranenburg, C, (1998), "Density Currents", lecture notes CTwa5302, Delft University of Technology.

Kovacs, A.E., (1998), "Prandtl's mixing length concept modified for equilibrium sediment-laden flows", Journal of hydraulic engineering, Vol 124, No. 8.

Lau, Y.L and Chu, V.H., (1987), "Suspended sediment effect on turbulent diffusion", 22nd IAHR Congress, Lausanne, pp 221-226

Lyn, D.A., (1988), "A similarity approach to turbulent sediment-laden flows in open channels", Journal fluid Mechanics, Vol 193, pp 1-26

Maren, van, D.S., Winterwerp, J.C., Vriend, de, H.J., Wang, Z.B., Wang, Z-Y, Zhou, J.J., Wu, B.S., "Sediment-induced density effects on channel patters of silt-laden rivers", Proceedings of 2nd international Yellow River Forum, Zhengzou, China.

Mazumder, B.S., Ghoshal, K., (2006), "Velocity and concentration profiles in uniform sediment-laden flow", Applied Mathematical Modelling, Vol 30, pp164-176.

Muste, M., Yu, K., Fujita, I., Ettema, R., (2005), "Two-phase versus mixed-flow perspective on suspended sediment transport in turbulent channel flow"

Ormondt, M., van, (2004), "Yangtze Estuary Model 2004", WL Delft Hydraulics

Os, A.G., van, (1993), "Density currents and salt intrusion", IHE Delft, WL Delft Hydraulics

Port and Delta Consortium, Yangtze Pilot Project, (1999)

Shi, Z., Z, H.J., Eittreim, S.L., Winterwerp, J.C., (2003), "Settling velocity of fine suspended particles in the Changjiang Estuary", China Journal of Asian Earth Sciences, Vol 22, pp 245-251

Simmons, H.B. (1955), "Some effects of upland discharge on estuarine hydraulics", Proc. ASCE, 81, paper no. 792.

Soulsby, R.L. and Wainwright, B.L.S.A., (1987), "A criterion for the effect of suspended sediment on near-bottom velocity profiles", Journal of Hydraulic Research, Vol 25, N0 3, pp 341-356.

Toorman, E.A., (2000) "Modelling of turbulence damping in sediment-laden flow", Part 3: Drag Reduction in sediment-laden turbulent flow, Hydraulics Laboratory, KULeuven, Civil Engineering Department

Uittenbogaard, R.E. (1994), Physics of turbulence: technical report on sub-task 5.2, WL Delft hydraulics

Uijttewaal, W., "Turbulence in Hydraulics", lecture notes CT5312, Delft University of Technology.

Umeyama, M. and Gerritsen, F., (1992), "Velocity distribution in uniform sediment-laden flow", ASCE, Journal of Hydraulic Engineering, Vol 118, No. 2, pp 229–245.

Vanoni, V.A., (1946), "Transportation of suspended sediment by water", ASCE Transactions, Vol 111, pp 67– 133.

Vanoni, V.A., (1977), "Sedimentation Engineering", ASCE, Manuals and Reports on Engineering Practice, No. 54.

Vinzon, S.B., Mehta A.J., (2001), "Boundary layer effects due to suspended sediment in the Amazon River estuary", Proceedings in Marine Science, Coastal and Estuarine Fine Sediment Processes, pp 359-372.

Wang, Z.B. (1989), "Mathematical modelling of morphological processes in estuaries", Ph.D. thesis, Delft University of Technology, The Netherlands .

Wang, Z.B. (1994), Hangzhou Bay Environmental Study, WL Delft Hydraulics.

Wang, Y.W., Larsen, P., Nestmann, F., Dittrich, A., (1998), "Resistance and drag reduction of flows of clay suspension", Journal of Hydraulic Engineering, Vol 124 No.1

Winterwerp, J.C., (1999), "On the dynamics of high-concentrated mud suspensions", Ph.D. thesis, Delft University of Technology, The Netherlands

Winterwerp, J. C., (2001), "Stratification effects by cohesive and non-cohesive sediment", Journal of Geo-physical Research, Vol 106, No. C10, pp 22.559-22.574

Winterwerp, J. C., (2001), "On the flocculation and settling velocity of estuarine mud", Continental Shelf Research, Vol 22, pp 1339-1360

Winterwerp, J.C., (2006), "Stratification effects by fine sediment at low, medium and very high concentrations", Journal of Geo-physical Research, Vol 111

Winterwerp, J. C., de Vriend, H. J., Wang, Z. B., (2003), "Fluid-sediment interactions in silt-laden flow", Proc. of the 1st Int. Yellow River Forum on River Basin Management, Zhengzou, China Vol. II, pp 351-362.

Yang, S.L., Belkin, I.M., Belkina, A.I., Zhoa, Q.Y., Zhu, J., Ding, P.X., (2002), " Delta response to decline in sediment supply from the Yangtze River: evidence of the recent four decades and expectations for the next half-century", Estuarine, Coastal and Shelf Science, Vol 57, pp 689-699

Yang, S.L., Li, M., Dai, S.B., Liu, Z., Zhang, J., Ding, P.X., (2006) "Drastic decrease in sediment supply from Yangtze River and its challenge to coastal wetland management", Geophysical Research Letters, Vol 33, No. L06408.

Yang, S.L., Shi, Z., Zhao, H.Y., Li, P., Dai, S.B., Gao, A., (2004), " Effects of human activities on the Yangtze River suspended sediment flux into the estuary in the last century", Hydrology and Earth System Sciences, Vol 8(6), pp 1210-1216

Yoon, J-Y. and Kang, S-K, (2005), "A numerical model of sediment-laden turbulent flow in an open channel", Journal of Civil Engineering, Vol 32, pp 233-240.

A Solution to equation (3-4)

This appendix describes the details of the solution to equation (3-4) in section 3.1.2.

Equation (3-4) reads:

$$\int_0^h \mathrm{d}z \left\{ \alpha_1 \frac{\kappa g \Delta}{\rho u_*^3} \overline{w'c'} z \right\}^m = \int_0^h \mathrm{d}z \left\{ \alpha_1 \frac{\kappa g \Delta}{\rho u_*^3} W_s c z \right\}^m = \left(\alpha_1 \frac{\kappa g \Delta}{\rho u_*^3} W_s \right)^m \int_0^h \mathrm{d}z \left\{ cz \right\}^m \qquad \text{(A-1)}$$

Equation (3-5) can be rewritten as follows:

$$c(z) = \overline{c} \frac{\sin\{\pi\beta\}}{\pi\beta} \left(\frac{1 - z/h}{z/h} \right)^\beta = c_0 \left(\frac{z}{h} \right)^{-\beta} \left(1 - \frac{z}{h} \right)^\beta \qquad \text{(A-2)}$$

Substituting equation (A-2) into the integral term of (A-1) yields:

$$\begin{aligned}
\int_{z_o}^h \mathrm{d}z \{cz\}^m &= c_0^m \int_0^h \mathrm{d}z \left\{ \left(\frac{z}{h} \right)^{-m\beta} \left(1 - \frac{z}{h} \right)^{m\beta} z^m \right\} = \\
&= c_0^m h^m \int_0^h \mathrm{d}z \left\{ \left(\frac{z}{h} \right)^{m(\beta-1)} \left(1 - \frac{z}{h} \right)^{m\beta} \right\} = \\
&= c_0^m h^{m+1} \int_0^1 \mathrm{d}\zeta \left\{ (\zeta)^{m(\beta-1)} (1-\zeta)^{m\beta} \right\} = \\
&= c_0^m h^{m+1} \frac{\Gamma\{m - m\beta + 1\}\Gamma\{m\beta + 1\}}{\Gamma\{m+2\}} = \\
&= \overline{c}^m \left(\frac{\sin\{\pi\beta\}}{\pi\beta} \right)^m h^{m+1} \frac{\Gamma\{1 + m(1-\beta)\}\Gamma\{1 + m\beta\}}{(m+1)\Gamma\{m+1\}}
\end{aligned} \qquad \text{(A-3)}$$

where Γ = gamma function (N.B. $\Gamma(1) = 1$).

For $\beta << 1$ and $m\,\beta << 1$, (A.3) reduces to:

$$\int_0^h \mathrm{d}z \{cz\}^m \approx \frac{1}{(m+1)} \overline{c}^m h^{m+1} \qquad \text{(A-4)}$$

Substituting equation (A-4) into equation (3-4) leads to equation (3-7), which gives an expression for the term for the reduction of the effective hydraulic roughness, i.e.: $K_1 (Ri_* \beta)^m$.

B The 1DV POINT MODEL

The 1DV POINT MODEL was developed on the basis of DELFT3D-FLOW, the software system of WL | Delft hydraulics to simulate the water movement and transport of matter in three-dimensions, by stripping all horizontal gradients, except the horizontal pressure gradient. This model was originally developed to study the implementation of the $k-\varepsilon$ turbulence model in DELFT3D-FLOW by *Uittenbogaard et al.* [1992] and *Van Kester* [1994]. Later, the model was extended (*Uittenbogaard* [1995]) by incorporating the effects of temperature-induced stratification. The version that is used as a basis to implement the various physical-mathematical formulations derived in the present study, was developed by *Uittenbogaard et al.* [1996].

In Section B.1 the various mathematical-physical formulations of the relevant processes are presented. Section B.2 contains information on the numerical implementation of the equations, and in Section B.3 numerical accuracy aspects are presented.

B.1 The 1DV equations for sediment-laden flow

B.1.1 Water movement

$$\frac{\partial u}{\partial t}+\frac{1}{\rho}\frac{\partial p}{\partial x}=\frac{\partial}{\partial z}\left[\left(\nu+\nu_T\right)\frac{\partial u}{\partial z}+\frac{\tau_{xz}^{s}}{\rho}\right]-\frac{1}{\rho}\frac{2\tau_{sf}}{b} \qquad \text{(B-5)}$$

where:

b = flow width

τ_{xz}^{s} = inter-particle stresses

τ_{sf} = side wall friction

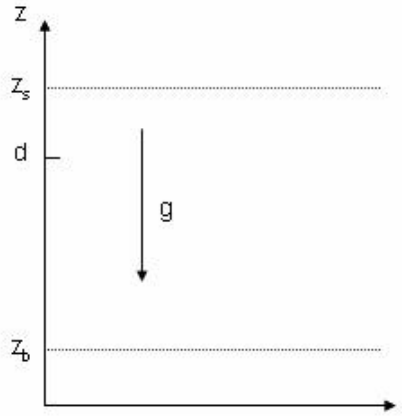

The last term in (B-1) is added to account for side wall friction effects in case of simulating the flow in a confined channel (laboratory flume) of width b. The bed or lower boundary condition is defined at $z = z_b$, and the water surface at $z = z_s(t)$. Hence, the water depth $h = z_s - z_b$. Note that in DELFT3D the following convention is used: $z_s = d + z(t)$; d and z_b are given with respect to a horizontal reference plane. It is noted that by omitting the horizontal advection terms, it is implicitly assumed that the Froude number of the flow is small, which is generally the case in tidal flow. Also the vertical velocity component w is neglected, which is small with respect to the horizontal component u. However, w may be of the same order of magnitude as the settling velocity in converging or diverging flow, for instance over a spatially varying bed. Hence, it should be assumed that the bed is flat and horizontal in the applications with the 1DV POINT MODEL. Vertical velocities induced by variations in water level with time, induced by tidal movements, for instance, are accounted for through the application of the σ-transformation (equation B-36). The pressure term in equation (B-1) is adjusted to maintain a given, time-dependent depth-averaged velocity:

$$\frac{1}{\rho}\frac{\partial p}{\partial x} = \frac{\tau_s - \tau_b}{\rho h} + \frac{\bar{u}(t) - \bar{u}_0(t)}{T_{rel}} \qquad \text{(B-6)}$$

$$u(t) = \frac{1}{h}\int_{z_{bc}}^{z_s} u(z', t)\,\mathrm{d}z' \qquad \text{(B-7)}$$

where:

T_{rel} = relaxation time (see also Appendix B.3)

$\bar{u}_0$ = desired depth-averaged flow velocity

z_{bc} = apparent roughness height

τ_s = surface shear stress

A quadratic friction law, satisfying the log-law, is used:

$$\tau_b = \rho |u_{*b}| u_{*b} \;;\; u_{*b} = \frac{\kappa\, u\left(z_{bc} + \tfrac{1}{2}\Delta z_b\right)}{\ln\left(1 + \tfrac{1}{2}\Delta z_b / z_{bc}\right)} \tag{B-8}$$

where:

The boundary conditions to equation (B-1) read:

$$\tau_b = \left\{ \rho\left(\nu + \nu_t\right)\frac{\partial u}{\partial z} + \tau^s_{xz} \right\}\Bigg|_{z=z_{bc}} \tag{B-9}$$

$$\tau_s = \left\{ \rho\left(\nu + \nu_t\right)\frac{\partial u}{\partial z} + \tau^s_{xz} \right\}\Bigg|_{z=z_s} \tag{B-10}$$

B.1.2 The mass balance for suspended sediment

The transport of sediment is modelled with the advection-diffusion equation for various fractions numbered by the superscript *(i)*:

$$\frac{\partial c^{(i)}}{\partial t} - \frac{\partial}{\partial z}\left\{ w_s^{(i)} c^{(i)} \right\} - \frac{\partial}{\partial z}\left\{ \left(D_s^{(i)} + \partial_t^{(i)} \right)\frac{\partial c^{(i)}}{\partial z} \right\} = 0 \tag{B-11}$$

with

$$w_s^{(i)} = w_{s,r}^{(i)} \frac{\left(1\text{-}\phi_*\right)\left(1\text{-}\phi_p\right)}{\left(1\text{+}2.5\phi\right)} \tag{B-12}$$

to account for hindered settling

where:

$c^{(i)}$ = sediment concentration by mass for fraction (i)

D_s = molecular diffusion coefficient for sediment (equation B-14)

$w_{s,r}$ = settling velocity of individual particle (see equation B-21)

Γ_t = eddy diffusivity (see also equation B-17)

The volumetric concentration of mud flocs ϕ, and the volumetric concentration of their primary particles ϕ_p are related to the mass concentration c and sediment density ρ_s through:

$$\phi = \frac{\sum_{(i)} c^{(i)}}{c_{gel}} \tag{B-13}$$

and

$$\phi_p = \frac{\sum_{(i)} c^{(i)}}{\rho_s} \tag{B-14}$$

where

c_{gel} = gelling concentration (see also equation B-20)

ϕ_* = min {1, ϕ }

At the water surface and the bed the boundary conditions read:

$$\left\{ w_s^{(i)} c^{(i)} \right\}\Big|_{z=z_s} = 0 \quad ; \quad \left\{ \left(D_s + \Gamma_t \right) \frac{\partial c^{(i)}}{\partial z} \right\}\Bigg|_{z=z_s} = 0 \tag{B-15}$$

and

$$\left\{ w_s^{(i)} c^{(i)} \right\}\Big|_{z=z_b} = E_{b,c} \quad ; \quad \left\{ \left(D_s + \Gamma_t \right) \frac{\partial c^{(i)}}{\partial z} \right\}\Bigg|_{z=z_b} = 0 \tag{B-16}$$

At the rigid bed $z = z_b$ the classical formulae of Partheniades and Krone is applied:

$$E_{b,c} = -w_s^{(i)}\ c^{(i)}\mathrm{S}\left(1-\theta_d^{(i)}\right) + M^{(i)}\mathrm{S}\left(\theta_e^{(i)}-1\right) \tag{B-17}$$

in which:

M = empirical erosion parameter

θ_d = non-dimensional threshold shear stress for deposition: $\theta_d = \tau_b/\tau_d$

θ_e = non-dimensional threshold shear stress for deposition: $\theta_e = \tau_b/\tau_e$

τ_d = threshold shear stress for deposition

τ_e = threshold shear stress for erosion

$S(x)$ = ramp function: $S = x$ for $x > 0$ and $S = 0$ for $x \le 0$

The molecular diffusion term D_s is given by:

$$D_s = \frac{k_b T_w}{6\pi\mu D} \tag{B-18}$$

in which k_b is the Boltzman constant (= $1.38{\cdot}10^{-23}$ J/K) and T_w is absolute water temperature. The influence of the suspended sediment concentration on the bulk fluid density is given by the equation of state:

$$\rho\left(S, c^{(i)}\right) = \rho_w(S) + \sum\left\{\left[1-\frac{\rho_w(S)}{(i)}\right]c^{(i)}\right\} \tag{B-19}$$

where $\rho_w(S)$ is the density of the water due to salinity only.

B.1.3 The $k-\varepsilon$ turbulence model

The $k-\varepsilon$ turbulence model consists of transport equations for the turbulent kinetic energy k and the turbulent dissipation ε, neglecting horizontal transport components:

$$\frac{\partial k}{\partial t} = \frac{\partial}{\partial z}\left\{\left(\nu + \nu_t\right)\frac{\partial k}{\partial z}\right\} + \nu_t\left(\frac{\partial u}{\partial z}\right)^2 + \frac{g}{\rho}\Gamma_t\frac{\partial \rho}{\partial z} - \varepsilon \qquad \text{(B-20)}$$

$$\frac{\partial \varepsilon}{\partial t} = \frac{\partial}{\partial z}\left\{\left(\nu + \frac{\nu_t}{\sigma_t^{\varepsilon}}\right)\frac{\partial \varepsilon}{\partial z}\right\} + c_{1\varepsilon}\frac{\varepsilon}{k}\nu_t\left(\frac{\partial u}{\partial z}\right)^2 + \left(1 - c_{3\varepsilon}\right)\frac{g}{\rho}\Gamma_t\frac{\varepsilon}{k}\frac{\partial \rho}{\partial z} - c_{2\varepsilon}\frac{\varepsilon^2}{k} \qquad \text{(B-21)}$$

The various coefficients in the standard $k-\varepsilon$ turbulence model are summarised in table B.1:

						stable	unstable
c_μ	$c_{1\varepsilon}$	$c_{2\varepsilon}$	σ_t	σ_ε	κ	$c_{3\varepsilon}$	$c_{3\varepsilon}$
0.09	1.44	1.92	0.7	1.3	0.41	1	0

Table B.1: Coefficients in standard $k-\varepsilon$ turbulence model

The model is subject to the following set of boundary conditions:

$$k\big|_{x_3=Z_b} = \frac{u_*^2}{\sqrt{c_\mu}}\ , \quad \varepsilon\big|_{x_3=Z_b} = \frac{u_*^3}{\kappa z_{wc}}\ , \quad k\big|_{x_3=Z_s} = \frac{u_{*,s}^2}{\sqrt{c_\mu}}\ , \quad \varepsilon\big|_{x_3=Z_s} = \frac{u_{*,s}^3}{\kappa z_{wc}}$$

where z_{wc} is the roughness length for current and waves. When no waves are present $z_{wc} = z_0$, which is the well-known roughness length for flow only. The effect of surface waves can be accounted for by the 1DV POINT MODEL. However the effect of waves is out of the scope of this research and is not taken into account in the simulations of the 1DV model. For details on the effect of surface waves reference is made to *Winterwerp* [2000].

B.1.4 The flocculation model

The flocculation model, as implemented in the 1DV POINT MODEL, contains the following set of equations:

$$\frac{\partial N}{\partial t}+\frac{\partial}{\partial z}\left(\frac{(1-\phi_*)(1-\phi_p)}{(1+2.5\phi)}w_{s,r}N\right)-\frac{\partial}{\partial z}\left(\Gamma_t\frac{\partial N}{\partial z}\right)= \\ -k'_A k_N^3(1-\phi_*)Gc^{\frac{3}{n_f}}N^{\frac{2n_f-3}{n_f}}+k'_B k_N^{2q}G^{q+1}\left(k_N c^{\frac{1}{n_f}}N^{\frac{-1}{n_f}}-D_p\right)^p c^{\frac{2q}{n_f}}N^{\frac{n_f-2q}{n_f}} \tag{B-22}$$

where

a_{eb}	=	break-up efficiency parameter
D_m	=	diameter of mud flocs
D_p	=	diameter of primary particles
e_c	=	efficiency coefficient for coagulation
e_d	=	efficiency coefficient for diffusion
F_y	=	yield strength of flocs
G	=	dissipation parameter: $G=\sqrt{(\varepsilon/\nu)}$
k'_A	=	flocculation parameter: $k'_A=1.5e_c\pi\, e_d$
k'_B	=	floc break-up parameter: $k'_B=a_{eb}D_p^{-p}\left(\mu_s/F_y\right)^q$
k_N	=	$\left(D_p^{n_f-3}/f_s\rho_s\right)^{\frac{1}{n_f}}$
N	=	number concentration of the mud flocs
n_f	=	fractal dimension
p_f	=	empirical coefficient: $p_f=3-n_f$
q_f	=	empirical coefficient: $q_f=0.5$
μ_s	=	dynamic viscosity of sediment suspension

The relation between the number concentration N, the mass concentration c and the floc diameter D_m, and between the volumetric and mass concentration ϕ and c is given by simple algebraic relations:

$$N=\frac{1}{f_s}\frac{c}{\rho_s}D_p^{n_f-3}D^{-n_f} \tag{B-23}$$

$$\phi = \left(\frac{\rho_s - \rho_w}{\rho_f - \rho_w} \right) \frac{c}{\rho_s} = \frac{c}{\rho_s} \left[\frac{D}{D_p} \right]^{3-n_f} \tag{B-24}$$

where f_s is a shape factor and ρ_f is the floc density. Note that the gelling concentration c_{gel} is obtained for unit volumetric concentration, i.e. $\phi = 1$, yielding:

$$c_{gel} = \rho_s \left[\frac{D_p}{D} \right]^{3-n_f} \tag{B-25}$$

The relation between the floc size D and the settling velocity $w_{s,r}$ for a single particle in still water is given by:

$$w_{s,r} = \frac{f_{sed}}{18\beta} \frac{(\rho_s - \rho_w)g}{\mu_s} D_p^{3-n_f} \frac{D^{n_f - 1}}{1 + 0.15 \mathrm{Re}_p^{0.687}} \tag{B-26}$$

where f_{sed} is a shape factor for sediment and Re_p is the particle Reynolds number: $\mathrm{Re}_p = w_{s,r} D / \nu$. The evolution of the settling velocity in the 1DV POINT MODEL is obtained by a simultaneous solution of (B.18) and (2-19), thereafter the floc diameter D and the settling velocity $w_{s,r}$ are obtained from equation (B-19) and (B-22), using equation (B.20) to establish the fractal dimension n_f, together with the following boundary conditions, split again in 2x2 equations:

$$\begin{aligned} &\{w_s N\}\big|_{z=Z_s} = 0 \quad ; \quad \left\{ (D_s + \Gamma_t) \frac{\partial N}{\partial z} \right\}\Big|_{z=z_s} = 0 \text{ and} \\ &\{w_s N\}\big|_{z=Z_b} = E_{b,N} \; ; \; \left\{ (D_s + \Gamma_t) \frac{\partial N}{\partial z} \right\}\Big|_{z=z_b} = 0 \end{aligned} \tag{B-27}$$

and

$$E_{b,N} = -\frac{(1-\phi_*)(1-\phi_p)}{(1+2.5\phi)} w_{s,r} N \mathrm{S}(1-\theta_d) + \frac{M}{f_s D_e^3 \rho_{f,e}} \mathrm{S}(\theta_e - 1) \quad \text{at} \quad z = z_b \tag{B-28}$$

where z_b is the bed level and z_s is the level of the water surface. The equilibrium floc diameter D_e and the equilibrium floc density $\rho_{f,e}$ are given by:

$$D_e = D_p + \frac{k_A c}{k_B \sqrt{G}} \tag{B-29}$$

$$\rho_{f,e} = \rho_w + (\rho_s - \rho_w)\left[\frac{D_p}{D_e}\right]^{3-n_f} \tag{B-30}$$

with:

$$k_A = 0.75 e_c \pi \, e_d / f_s \rho_s D_p$$

$$k_B = k_B' / n_f$$

The model contains the following empirical parameters: a_{eb}, $e_c e_d$, D_p, F_y, f_s, n_{f1}, n_{f2}, p and q which have to be specified by the user through the input to the model.

B.1.5 The consolidation model

The consolidation model, as implemented in the 1DV POINT MODEL, contains the following set of equations:

$$\frac{\partial c}{\partial t} - \frac{\partial}{\partial z}(\Xi_s c) - \frac{\partial}{\partial z}\left((D_s + \Gamma_t + \phi_*^2 \Gamma_c)\frac{\partial c}{\partial z}\right) = 0 \tag{B-31}$$

Where:

$$\Xi_s = f_{hs} + \frac{f_c}{1+\eta f_c}, \quad \text{with :}$$

$$f_{hs} = w_{s,r}\frac{(1-\phi_*)(1-\phi_p)}{1+2.5\phi}, \quad \text{and} \qquad \text{(B-32)}$$

$$f_c = k\frac{\rho_s-\rho_w}{\rho_w}\phi_p$$

$$\Gamma_c \equiv \frac{2K_k K_\sigma}{(3-n_f)g\rho_w}$$

$$k = K_k \phi_p^{\left(\frac{-2}{3-n_f}\right)}$$

$$p^s = K_p \phi_p^{\left(\frac{2}{3-n_f}\right)}$$

At the water surface and the bed, the boundary conditions read:

$$\{\Xi_s c\}\big|_{z=z_s} = 0 \;;\; \left\{\left(D_s + \Gamma_t + \phi_*^2\Gamma_c\right)\frac{\partial c}{\partial z}\right\}\Big|_{z=z_s} = 0 \text{ and}$$

$$\{\Xi_s c\}\big|_{z=z_b} = 0 \;;\; \left\{\left(D_s + \Gamma_t + \phi_*^2\Gamma_c\right)\frac{\partial c}{\partial z}\right\}\Big|_{z=z_b} = 0 \qquad \text{(B-33)}$$

The stress tensor τ_{xz}^s for consolidating fluid mud is given by the following rheological model:

$$\tau_{xz}^s = \mu_{mud}\frac{\partial u}{\partial z} \text{ with } \mu_{mud} = \frac{a_y\tau_y}{1+a_y|\partial u/\partial z|} + \mu^s \qquad \text{(B-34)}$$

where a_y is a coefficient (a_y = 0.02 implies $\tau_{xz}^s = 0.95\tau_y$ for $\partial u/\partial z = 10^{-3}\ s^{-1}$). Furthermore the parameters μ^s and τ_y are defined as:

$$\mu^s = K_\mu \phi_p^{n_c}, \quad \text{and}$$

$$\tau_y = K_y \phi_p^{\frac{3}{3-n_f}}$$

The empirical parameters K_k, K_p, K_y, K_μ, n_c and η have to be specified by the user through the model input: n_c can vary between about 2 and 6 for various muds. Through the formulation of (B-30) for μ_{mud} it is ascertained that is defined for all values of the shear rate. The eddy diffusivity at the water-mud interface is set to zero when the yield strength of the mud exceeds the turbulent stress:

B.2 Numerical implementation of the 1DV equations

In the 1DV POINT MODEL we apply a simplified version of the so-called σ-coordinate transformation:

$$\frac{\partial}{\partial z} = \frac{1}{h}\frac{\partial}{\partial \sigma} \quad \text{with} \quad \sigma \equiv \frac{z - Z_s(t)}{h};\ h = Z_s(t) - Z_b \tag{B-35}$$

This implies that for a conserved constituent, like suspended sediment, the depth-mean sediment concentration remains constant with varying water level. However, the total mass, integrated over the water column, is not conserved. The equations are solved on a staggered grid. The vertical grid size distribution does not have to be uniform. The sketch below shows where the various parameters are defined.

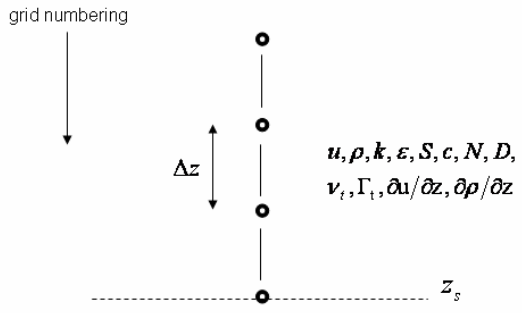

The time discretisation in the numerical solution technique is based on the θ-method; all simulations are carried out with $\theta = 1$, i.e. Euler-implicit time integration. In the vertical direction a first-order upwind scheme is used, together with a central difference scheme for

the diffusion operator. All source terms are modelled explicitly. The sink terms are modelled such that the relevant variables, i.e. k, ε, S, c, N and D never become negative; for details the reader is referred to *Uittenbogaard et al.* [1997]. A sub-time step can be set by the parameter n_{sub} through which the advection-diffusion equation for flocculation can be solved efficiently with a smaller effective time step than that for the overall process. The communication between the various modules is given in the sketch below.

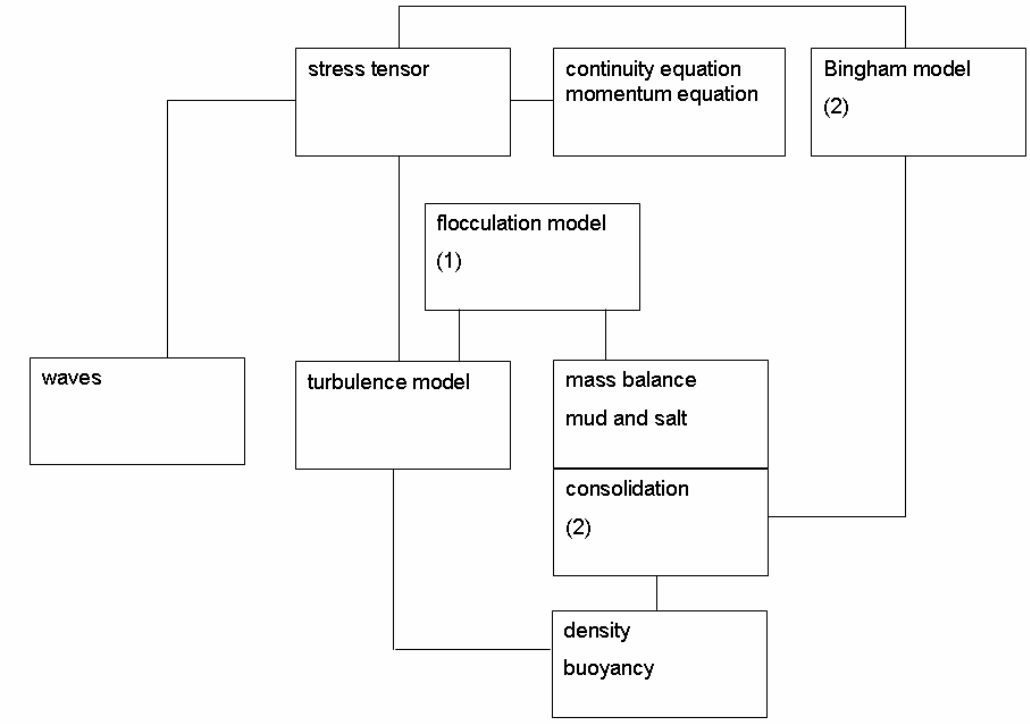

Figure B.1.: Set up of and communication between modules: (1) only if floc evolution is simulated, (2) only if consolidation is simulated. (1) and (2) not together.

B.3 Requirements for numerical accuracy

Due to the implicit solvers and conservative form of the equations, the numerical scheme is stable and mass conserving for all numerical parameters. However, because of accuracy the following requirements have to be followed:

1. The grid-size may be chosen non-equidistant. However, it is recommended that the sizes of two neighbouring grid cells do not differ by more than a factor 1.5.
2. The size of the lowest grid cell should be smaller than the thickness of the fluid mud layer, that is when all sediment in the water column has settled.

3. From numerical experiments it appears that an optimal choice for the relaxation time is $T_{rel} = 2 \cdot \Delta t$

4. The time step Δt should be small enough to accommodate for advective effects properly: $\Delta t < \Delta z / w_s$,

5. The numerical diffusivity D_{num} for the upwind scheme used amounts to $D_{num} = w_s \Delta z / 2$

6. The parameter η in equation (B-28) is set at 10^5 s/m to obtain a smooth transition between consolidation and hindered settling.

C DELFT3D-FLOW

Delft3D is an integrated flow and transport modelling system; it consists of several modules of which the flow module (Delft3D-FLOW) forms the hydrodynamic basis. This is also the module that was used in the present study. The Delft3D-FLOW module is a hydrodynamic flow simulation program that simulates transport phenomena while solving the unsteady shallowwater equations. Phenomena as tide, wind and wavedriven flows, stratified and density flows can be included in simulations while bottom level, water level and velocity field change continuously. To solve the shallowwater equations, these are transformed to the discrete space.

The equations can be solved in different dimensions. When depth averaged velocities are used in an area model, the model is 2Dh (two dimensional horizontal). If vertical layers are distinguished the model is 3D. In 3D the vertical layers can be specified proportional to the local water depth.The different types of models domains are shown in figure C.1.

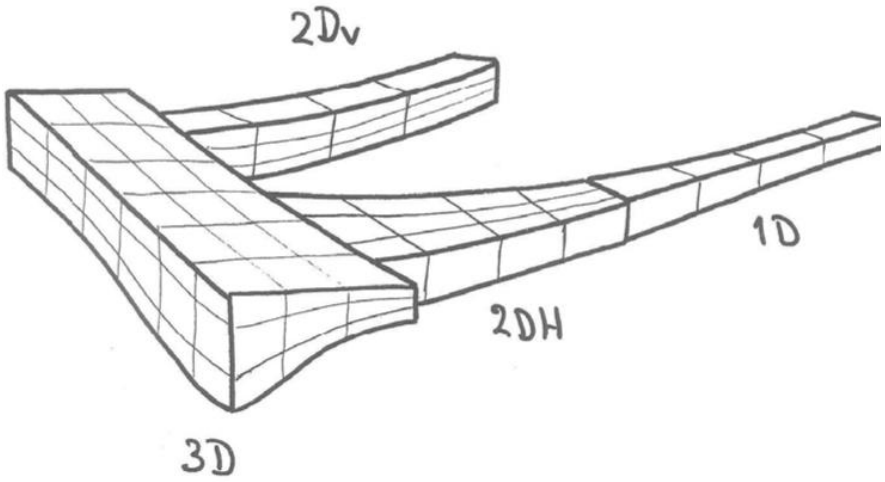

Figure D.1: Example of model domains (Source: WL | Delft Hydraulics, 2005)

For an elaborate overview of the entire numerical modelling system Delft3D, the reader is referred to the various Delft3D User Manuals (WL|Delft Hydraulics, 2005).

D Calibration

D.1 Calibration 3D model

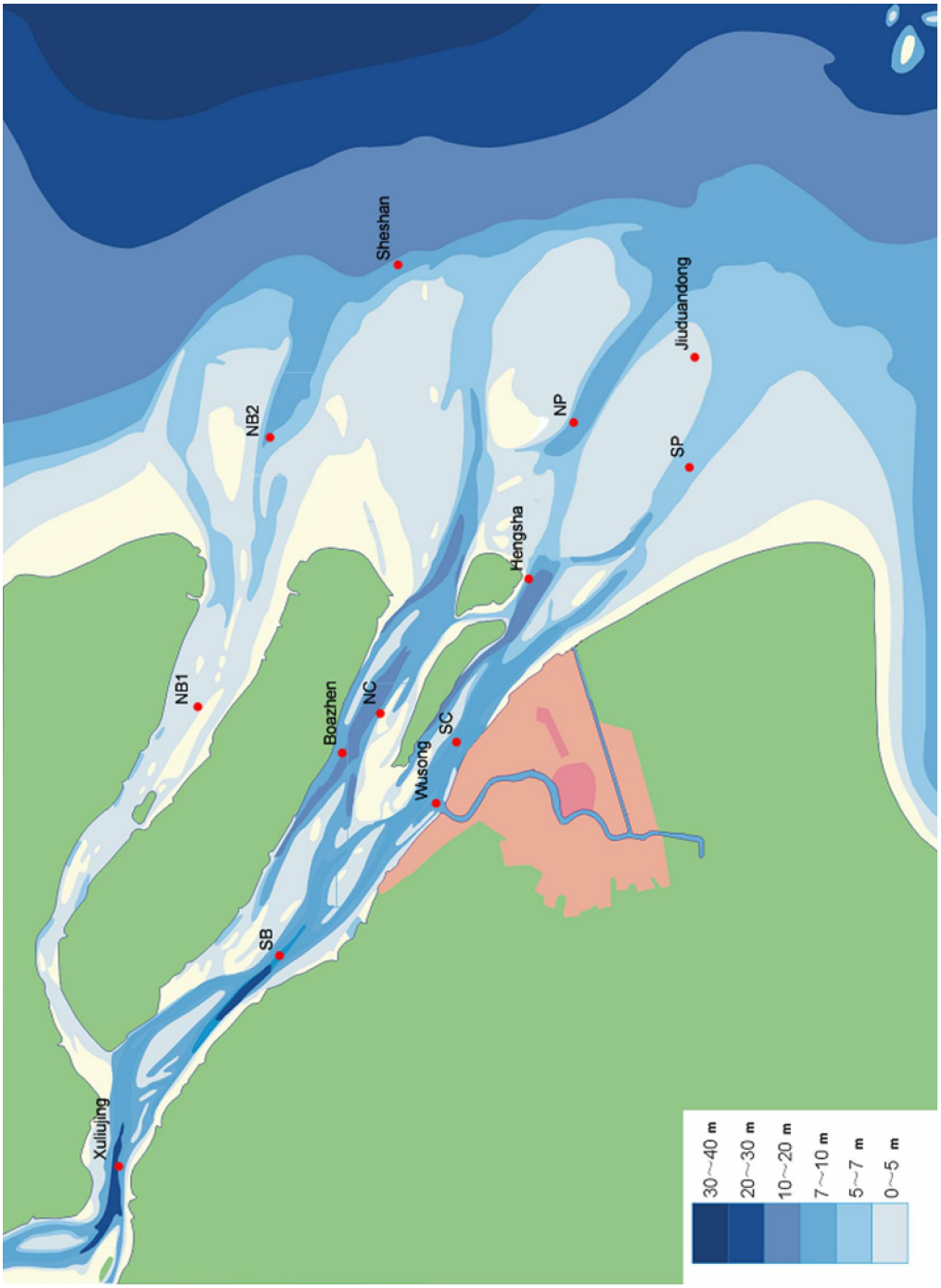

Figure D.1: Monitoring stations

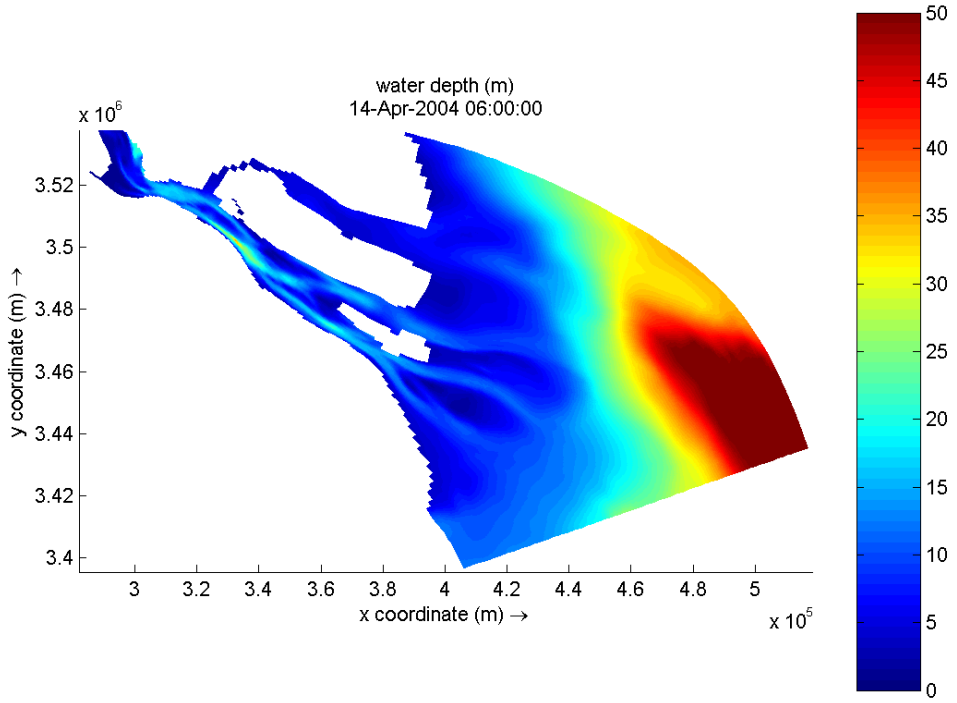

figure D.2: Water depths in the estuary

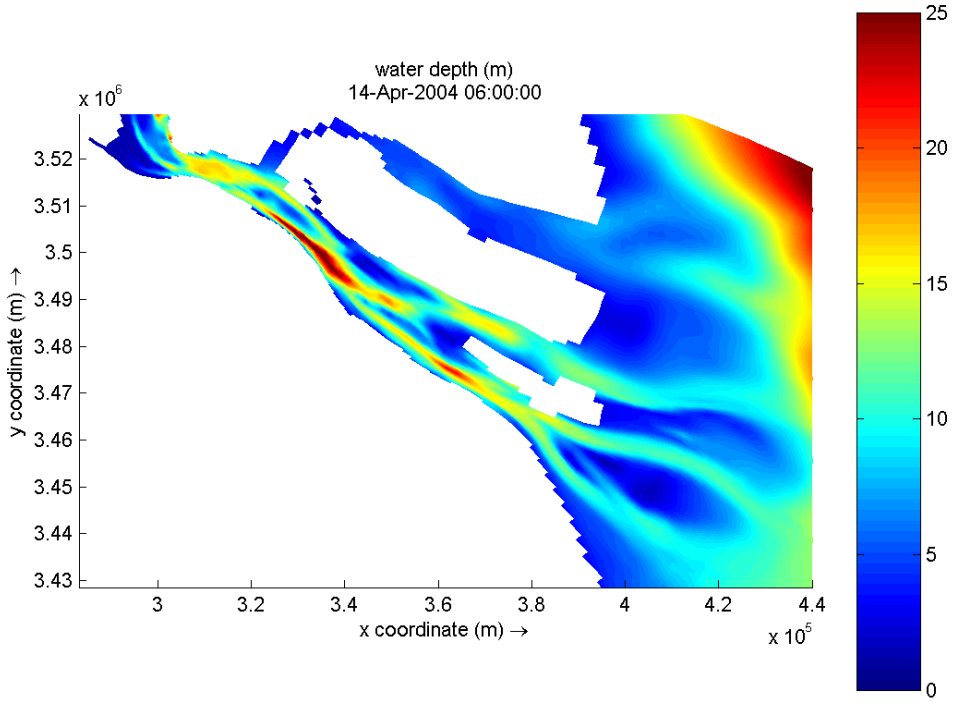

figure D.3: Water depths in the channels of the estuary

D.1.1 Tidal constituents

			K1	O1	P1	M2	S2	N2	K2	M4	MS4	M6
OBS	Baozhen	A	0.221	0.164	0.055	0.981	0.361	0.216	0.180	0.159	0.185	0.036
OBS		G	223.7	164.2	265.7	14.0	67.7	3.7	41.4	324.7	21.4	238.0
COM		A	0.205	0.168	0.041	0.964	0.285	0.121	0.163	0.175	0.188	0.048
COM		G	224.8	166.4	198.0	28.3	63.4	358.7	43.4	313.3	3.2	234.6
COM / OBS		A	0.93	1.02	0.75	0.98	0.79	0.56	0.91	1.10	1.02	1.33
COM - OBS		G	1	2	-68	14	-4	-5	2	-11	-18	-3
OBS	Wusong	A	0.213	0.165	0.055	0.915	0.318	0.201	0.183	0.146	0.169	0.032
OBS		G	228.0	171.7	275.0	14.5	63.8	359.4	49.2	13.3	15.6	4.4
COM		A	0.201	0.165	0.040	0.903	0.265	0.114	0.152	0.162	0.174	0.043
COM		G	228.1	169.4	201.2	33.6	68.6	3.3	48.6	310.5	1.8	237.8
COM / OBS		A	0.94	1.00	0.73	0.99	0.83	0.57	0.83	1.11	1.03	1.34
COM - OBS		G	0	-2	-74	19	5	4	-1	297	-14	233
OBS	Heng-Sha	A	0.233	0.172	0.064	1.075	0.379	0.209	0.223	0.133	0.156	0.044
OBS		G	215.5	166.1	278.8	343.5	35	331.7	15.2	259.8	315.5	112.3
COM		A	0.204	0.166	0.041	0.959	0.304	0.129	0.174	0.162	0.165	0.048
COM		G	213.0	165.3	186.2	350.8	25.7	322.4	5.7	262.9	313.0	88.4
COM / OBS		A	0.88	0.97	0.76	0.89	0.80	0.62	0.78	1.22	1.06	1.09
COM - OBS		G	-2	-1	-93	7	-9	-9	-9	3	-3	-24
OBS	Sheshan	A	0.244	0.132	0.065	1.126	0.529	0.201	0.150	0.080	0.062	0.008
OBS		G	178.5	129.4	171.8	311.6	357.2	299.1	354	192.8	246.4	293.4
COM		A	0.201	0.146	0.040	1.086	0.385	0.165	0.221	0.007	0.008	0.010
COM		G	191.5	132.4	164.7	312.8	346.4	285.0	325.4	19.1	43.4	184.8
COM / OBS		A	0.82	1.11	0.62	0.96	0.73	0.82	1.47	0.09	0.13	1.25
COM - OBS		G	13	3	-7	1	-12	-14	-29	-174	-202	-109

Table D.1: Tidal analyses 3D model, Chézy=110 $m^{1/2}s^{-1}$.

OBS = observation data (Wang [1994]); COM = computed data (Yangtze estuary model)

A=tidal amplitude; G=tidal phase

			K1	O1	P1	M2	S2	N2	K2	M4	MS4	M6
OBS	Boazhen	A	0.221	0.164	0.055	0.981	0.361	0.216	0.180	0.159	0.185	0.036
OBS		G	223.7	164.2	265.7	14.0	67.7	3.7	41.4	324.7	21.4	238.0
COM		A	0.205	0.168	0.041	0.926	0.271	0.115	0.155	0.160	0.173	0.039
COM		G	226.3	166.4	199.5	29.9	65.9	2.8	46.9	314.1	2.6	230.3
COM / OBS		A	0.93	1.02	0.75	0.94	0.75	0.53	0.86	1.01	0.94	1.08
COM - OBS		G	3	2	-66	16	-2	-361	4	-11	-19	-8
OBS	Wusong	A	0.213	0.165	0.055	0.915	0.318	0.201	0.183	0.146	0.169	0.032
OBS		G	228.0	171.7	275.0	14.5	63.8	359.4	49.2	13.3	15.6	4.4
COM		A	0.201	0.165	0.040	0.869	0.253	0.108	0.145	0.147	0.160	0.033
COM		G	229.3	169.3	202.5	35.1	71.1	7.4	51.1	311.5	1.4	232.7
COM / OBS		A	0.94	1.00	0.73	0.95	0.80	0.54	0.79	1.01	0.95	1.03
COM - OBS		G	1	-2	-72	21	7	8	2	298	-14	228
OBS	Heng-Sha	A	0.233	0.172	0.054	1.075	0.379	0.209	0.223	0.133	0.156	0.044
OBS		G	215.5	156.1	278.8	343.5	35	331.7	15.2	259.8	315.5	112.3
COM		A	0.206	0.166	0.041	0.940	0.293	0.125	0.168	0.148	0.152	0.042
COM		G	214.2	155.5	187.4	353.6	29.6	327.6	9.6	265.1	314.2	82.9
COM / OBS		A	0.88	0.97	0.76	0.87	0.77	0.60	0.75	1.11	0.97	0.95
COM - OBS		G	-1	-1	-91	10	-5	-4	-6	5	-1	-29
OBS	Sheshan	A	0.244	0.132	0.065	1.126	0.529	0.201	0.150	0.080	0.062	0.008
OBS		G	178.5	129.4	171.8	311.6	357.2	299.1	354	192.8	245.4	293.4
COM		A	0.202	0.147	0.040	1.085	0.382	0.164	0.219	0.006	0.007	0.008
COM		G	192.3	132.7	165.4	313.5	346.4	286.3	326.4	19.2	36.2	194.0
COM / OBS		A	0.83	1.11	0.62	0.96	0.72	0.82	1.46	0.08	0.11	1.00
COM - OBS		G	14	3	-6	2	-11	-13	-28	-174	-209	-99

Table D.2: Tidal analyses 3D model, Chézy=110 $m^{1/2}s^{-1}$ *, without sediment.*

OBS = observation data (Wang [1994]); COM = computed data (Yangtze estuary model)

A=tidal amplitude; G=tidal phase

			K1	O1	P1	M2	S2	N2	K2	M4	MS4	M6
OBS	Boachen	A	0.221	0.164	0.055	0.981	0.361	0.216	0.180	0.159	0.185	0.036
OBS		G	223.7	164.2	265.7	14.0	67.7	3.7	41.4	324.7	21.4	238.0
COM		A	0.192	0.161	0.038	0.869	0.259	0.110	0.149	0.158	0.174	0.038
COM		G	228.9	172.2	202.1	29.1	64.3	0.2	44.3	326.5	15.8	230.5
COM / OBS		A	0.87	0.98	0.69	0.89	0.72	0.51	0.83	0.99	0.94	1.06
COM - OBS		G	5	8	-64	15	-3	-363	3	2	-6	-8
OBS	Wusong	A	0.213	0.165	0.055	0.915	0.318	0.201	0.183	0.146	0.169	0.032
OBS		G	228.0	171.7	275.0	14.5	63.8	359.4	49.2	13.3	15.6	4.4
COM		A	0.188	0.158	0.037	0.814	0.241	0.103	0.138	0.144	0.161	0.034
COM		G	232.1	175.4	205.3	34.0	69.2	4.5	49.2	324.7	15.3	231.7
COM / OBS		A	0.88	0.96	0.67	0.89	0.76	0.51	0.75	0.99	0.95	1.06
COM - OBS		G	4	4	-70	19	5	5	0	311	0	227
OBS	Heng-Sha	A	0.233	0.172	0.054	1.075	0.379	0.209	0.223	0.133	0.156	0.044
OBS		G	215.5	156.1	278.8	343.5	35	331.7	15.2	259.8	315.5	112.3
COM		A	0.194	0.160	0.039	0.910	0.288	0.121	0.165	0.137	0.147	0.046
COM		G	216.1	159.1	189.2	351.9	27.5	324.4	7.5	275.2	324.4	89.2
COM / OBS		A	0.83	0.93	0.72	0.85	0.76	0.58	0.74	1.03	0.94	1.05
COM - OBS		G	1	3	-90	8	-7	-7	-8	15	9	-23
OBS	Sheshan	A	0.244	0.132	0.065	1.126	0.529	0.201	0.150	0.080	0.062	0.008
OBS		G	178.5	129.4	171.8	311.6	357.2	299.1	354	192.8	245.4	293.4
COM		A	0.201	0.145	0.040	1.089	0.386	0.165	0.221	0.010	0.010	0.007
COM		G	191.6	132.6	164.8	313.0	345.6	285.4	325.6	30.8	54.1	200.3
COM / OBS		A	0.82	1.10	0.62	0.97	0.73	0.82	1.47	0.13	0.16	0.88
COM - OBS		G	13	3	-7	1	-12	-14	-28	-162	-191	-93

Table D.3: Tidal analyses 3D model, Chézy=90 $m^{1/2}s^{-1}$ *, with sediment.*

OBS = observation data (Wang [1994]); COM = computed data (Yangtze estuary model)

A=tidal amplitude; G=tidal phase

D.1.2 Water level

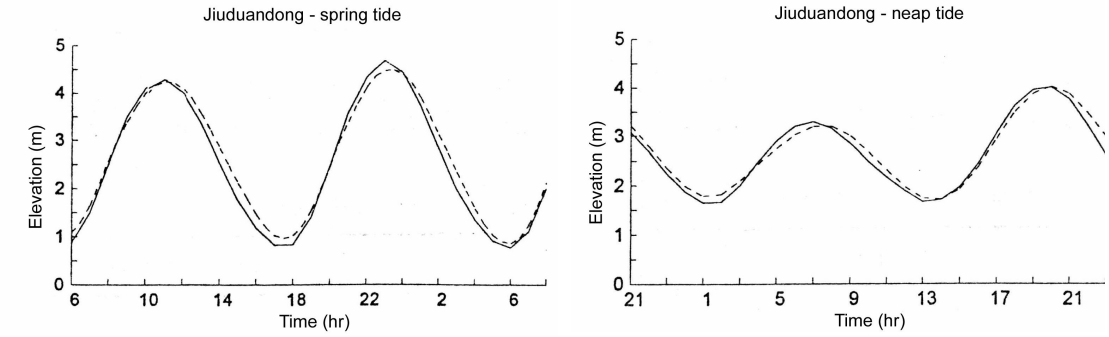

Figure D.4: Observed water levels (dotted line) from Hu et al. [2000] at monitoring station Jiuduandong

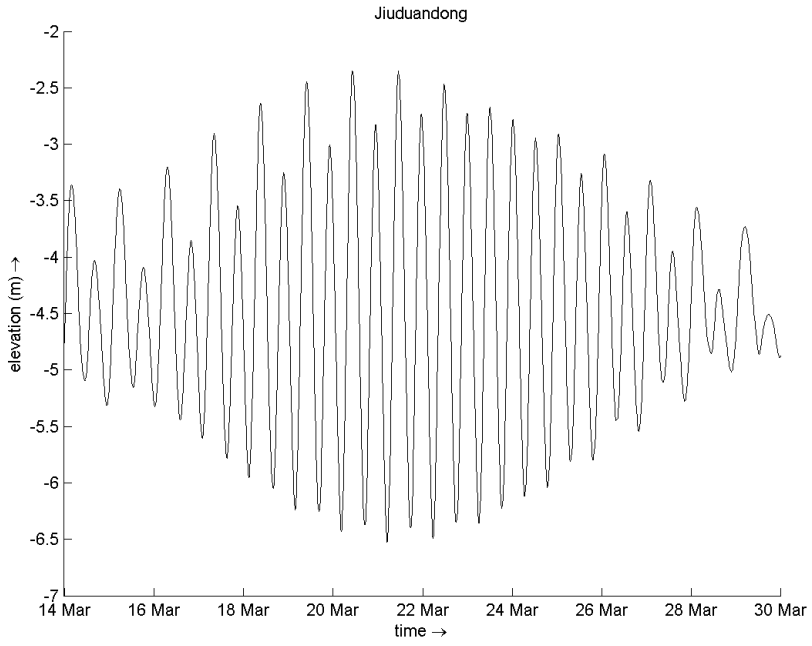

Figure D.5: Computed water levels (3D model) at monitoring station Jiuduandong

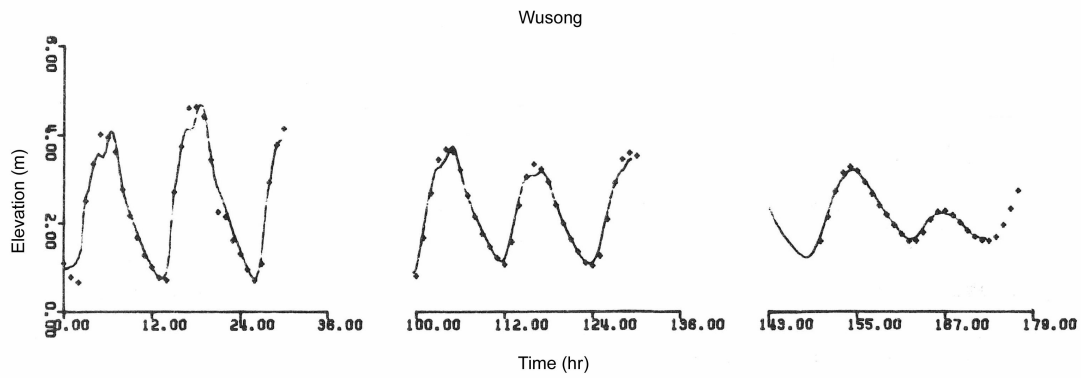

Figure D.6: Observed water levels (dots) from Wang [1989] at monitoring station Wusong

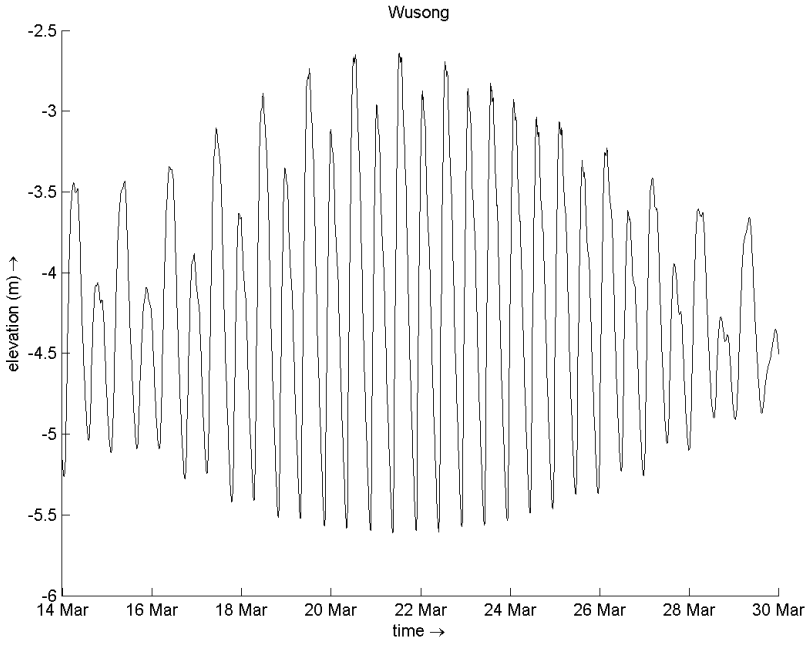

Figure D.7: Computed water levels (3D model) at monitoring station Wusong

D.1.3 Flow velocity

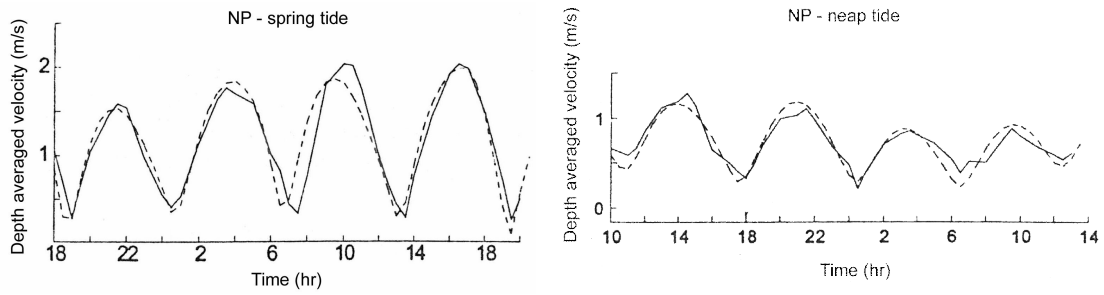

Figure D.8: Observed velocities (dotted line) from Hu et al. [2000] at monitoring station NP

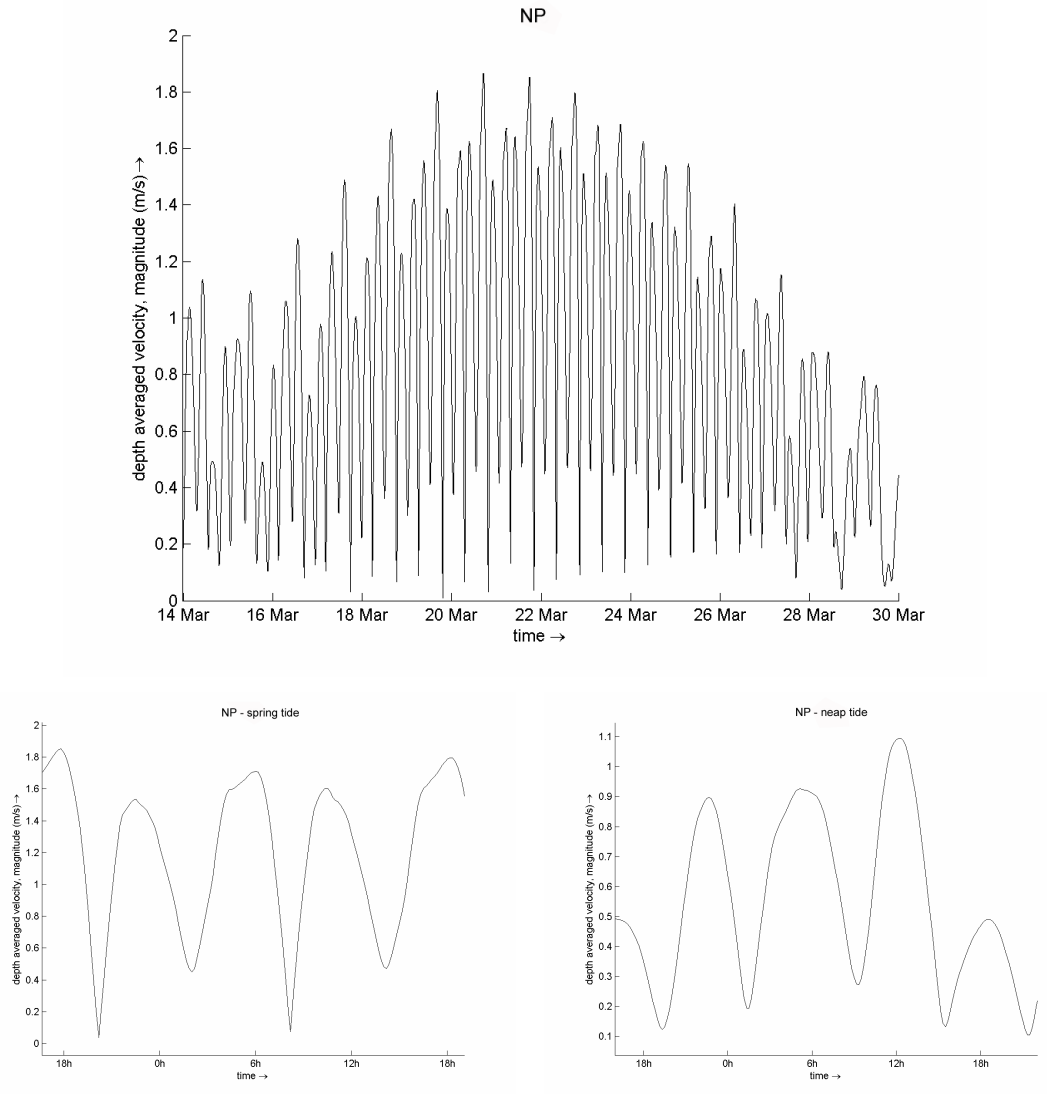

Figure D.9: Computed velocities (3D model) at monitoring station NP

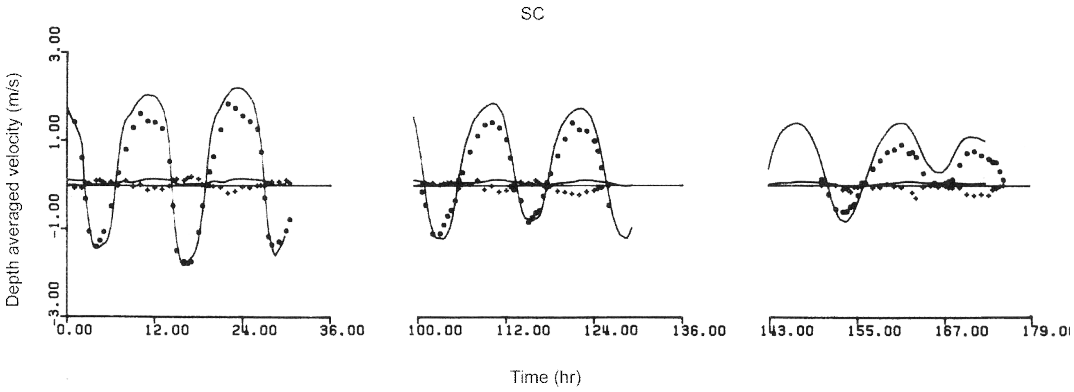

Figure D.10: Observed velocities (dots) from Wang [1989] at monitoring station SC

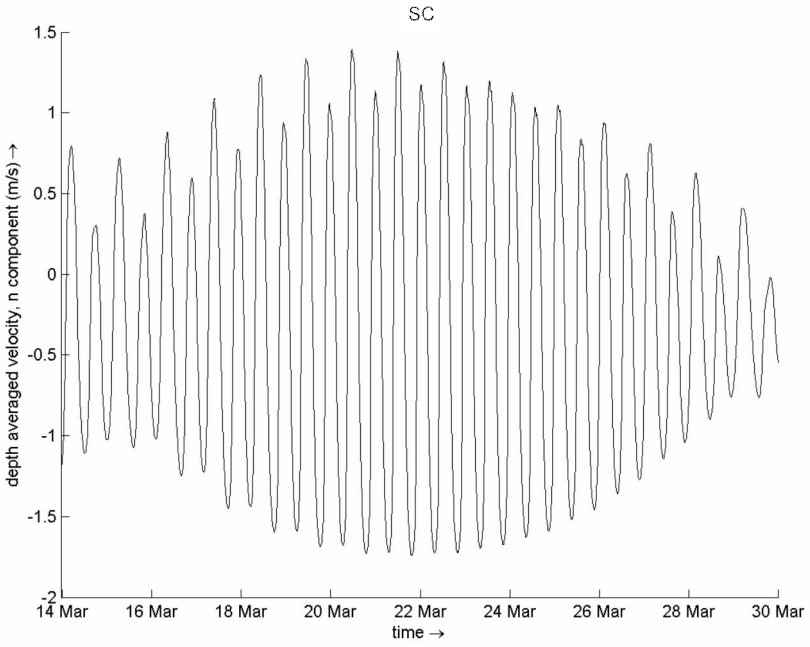

Figure D.11: Computed velocities (3D model) at monitoring station SC

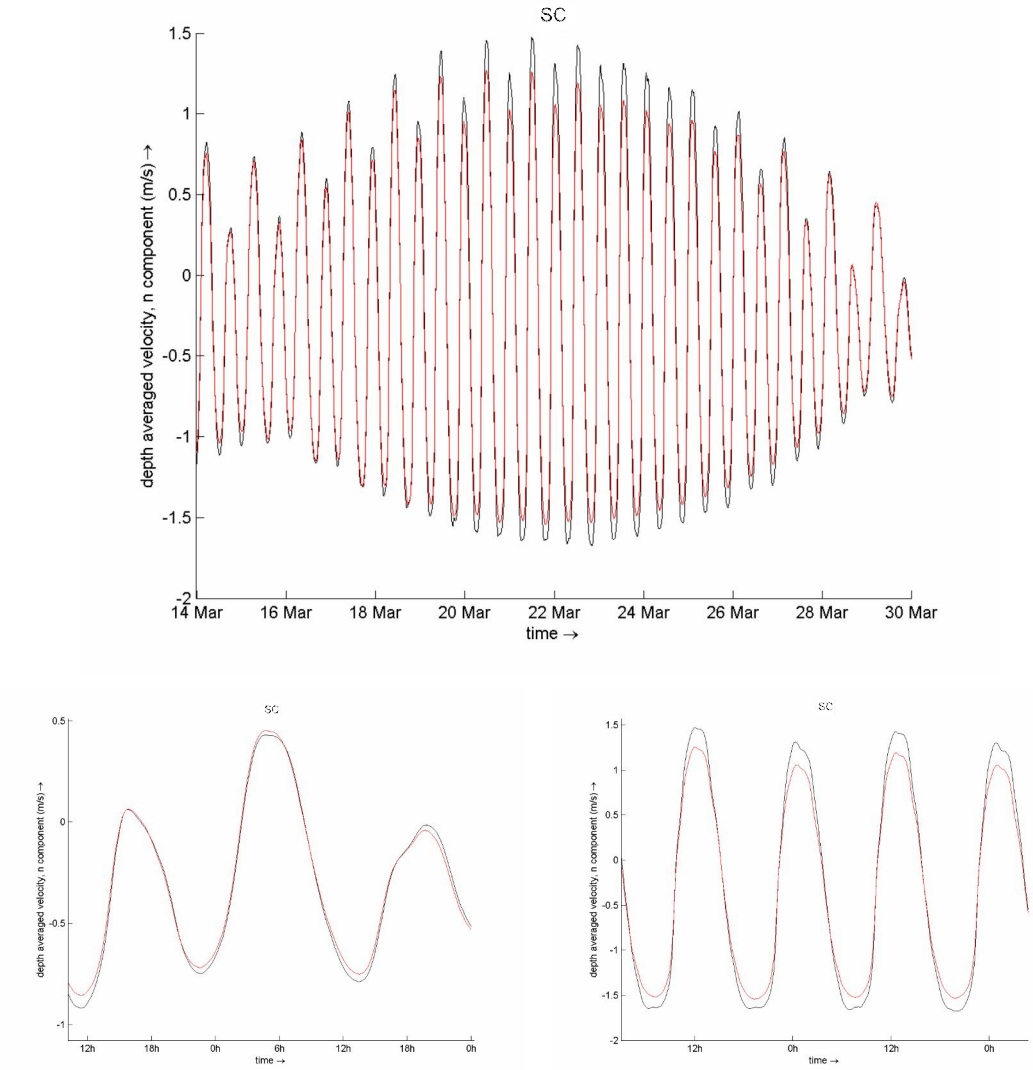

Figure D.12: Difference between velocity with and without sediment effect

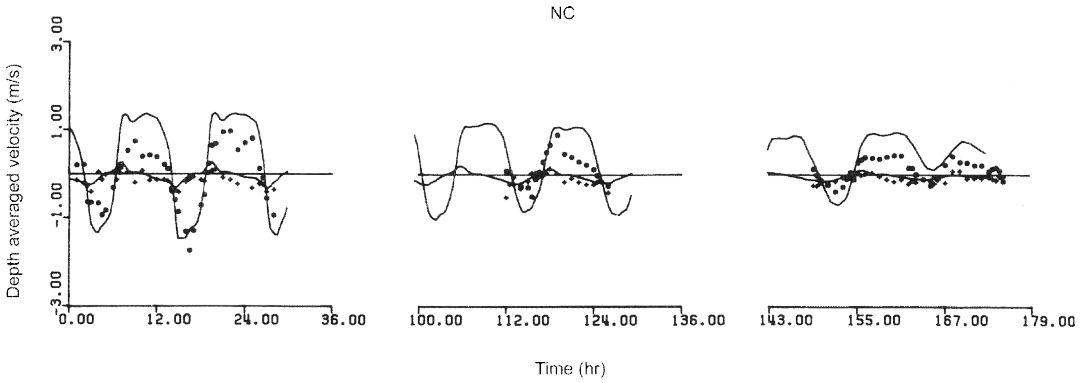

Figure D.13: Observed velocities (dots) from Wang [1989] at monitoring station NC

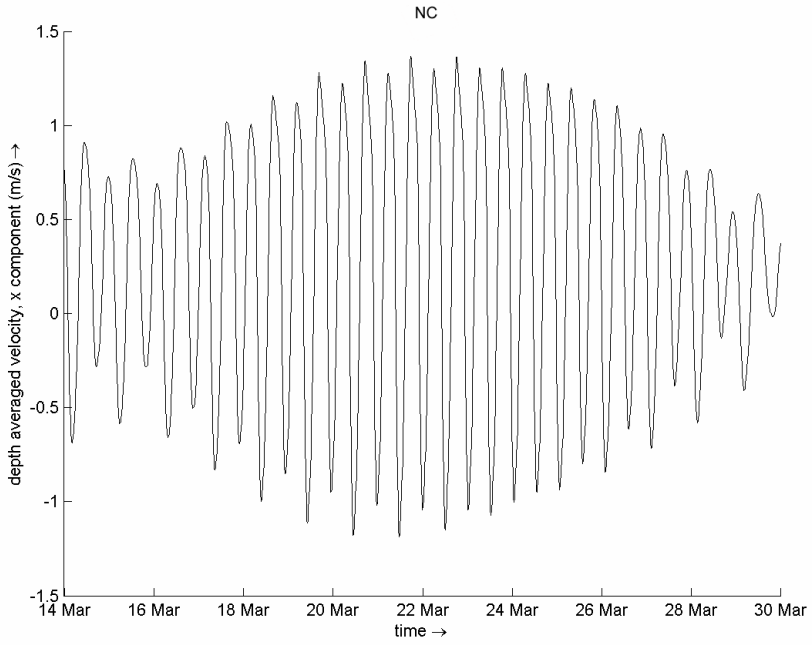

Figure D.14: Computed velocities (3D model) at monitoring station NC

D.1.4 Salinity

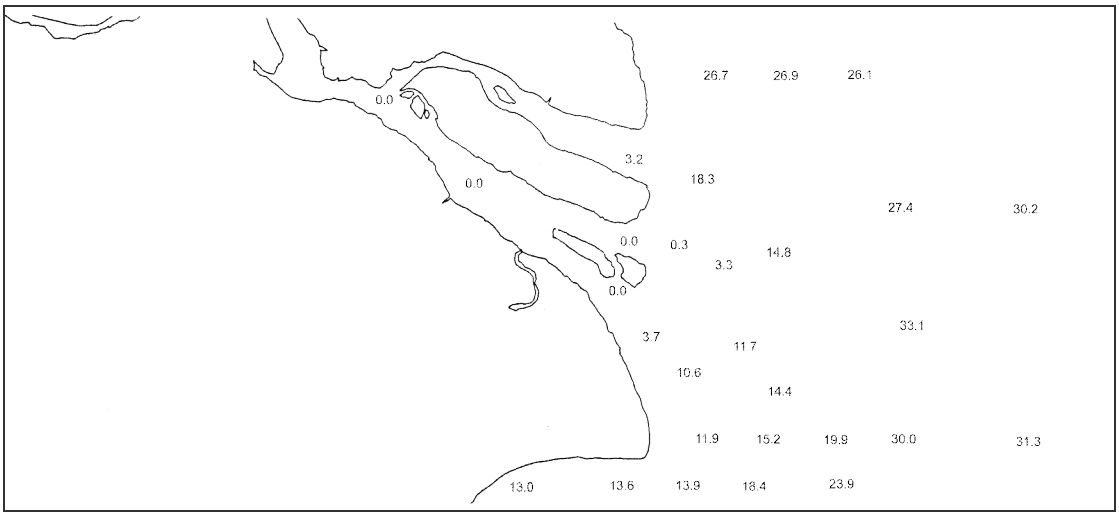

Figure D.15: Survey data for salinity (Wang [1994])

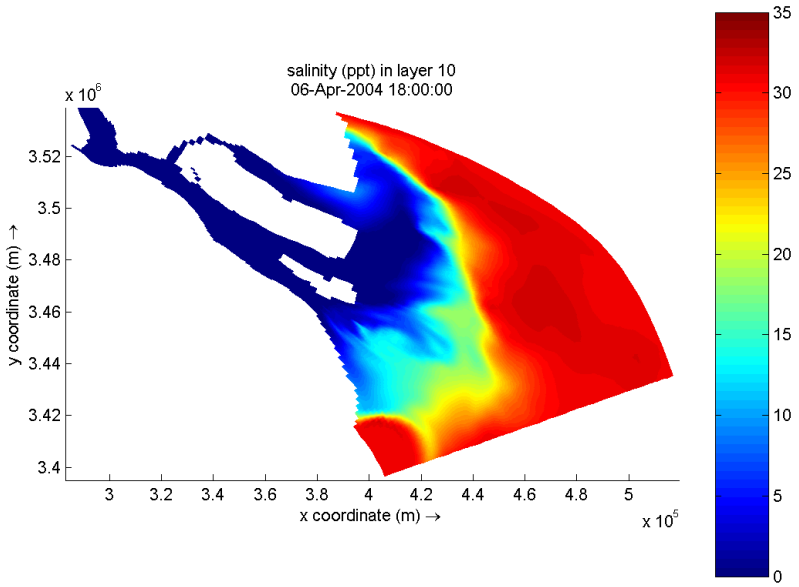

Figure D.16: 3D model results for horizontal salinity distribution, layer 10, Low Water, Spring Tide

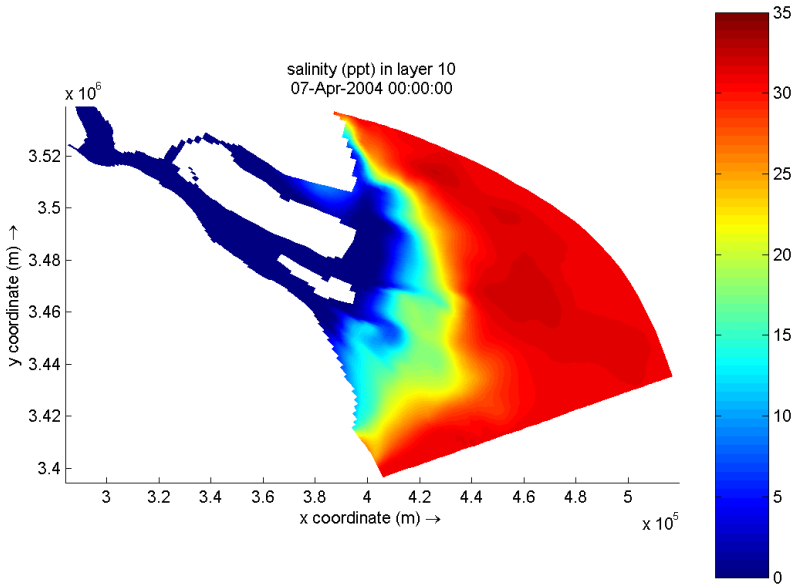

Figure D.17: 3D model results for horizontal salinity distribution, layer 10, High Water, Spring Tide

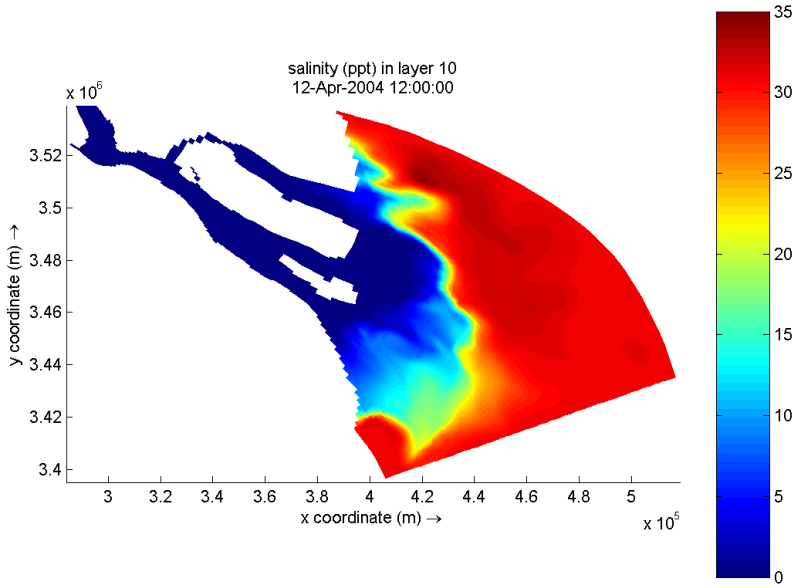

Figure D.18: 3D model results for horizontal salinity distribution, layer 10, Low Water, Neap Tide

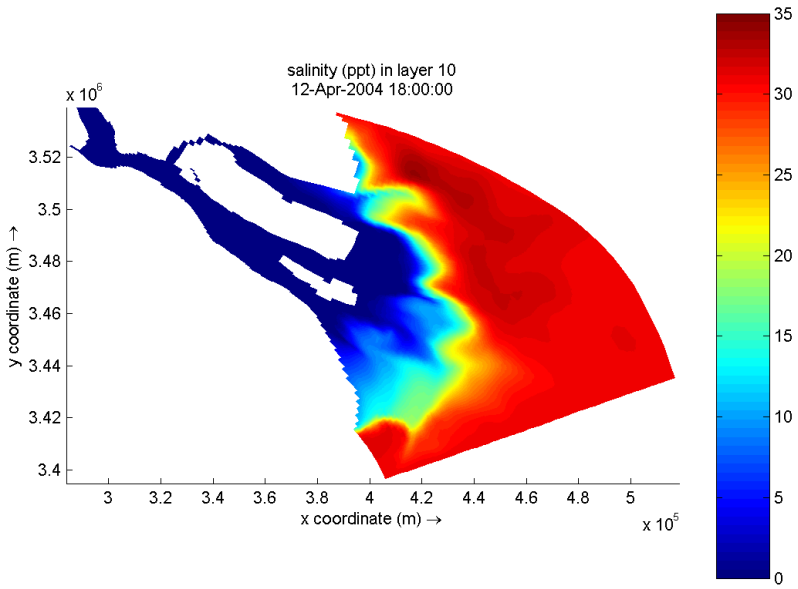

Figure D.19: 3D model results for horizontal salinity distribution, layer 10, High Water, Neap Tide

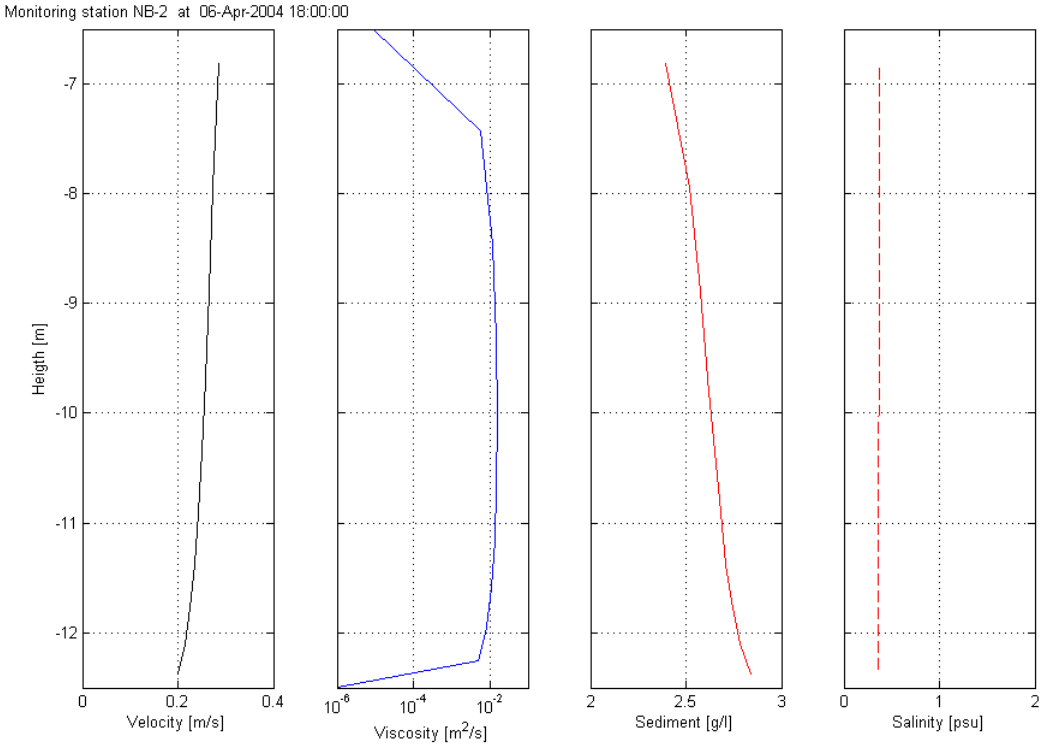

Figure D.20: Model results for vertical profiles for velocity, viscosity, sediment and salinity for monitoring station North Branch-2, Low Water, Spring tide

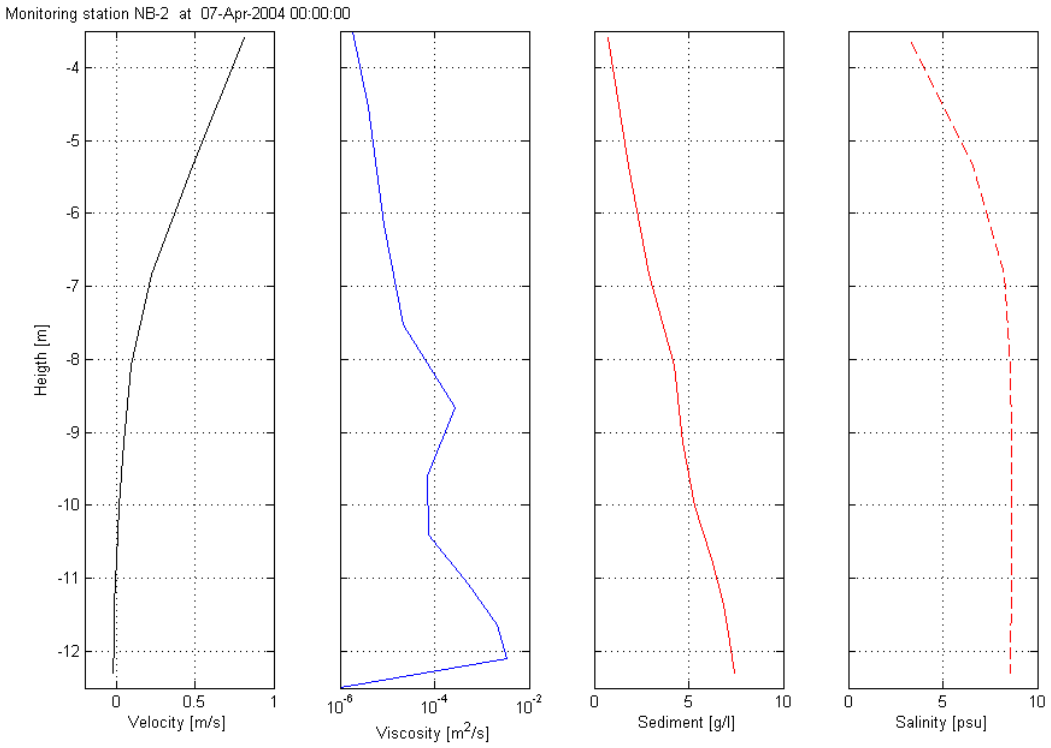

Figure D.21: Model results for vertical profiles for velocity, viscosity, sediment and salinity for monitoring station North Branch-2, High Water, Spring tide

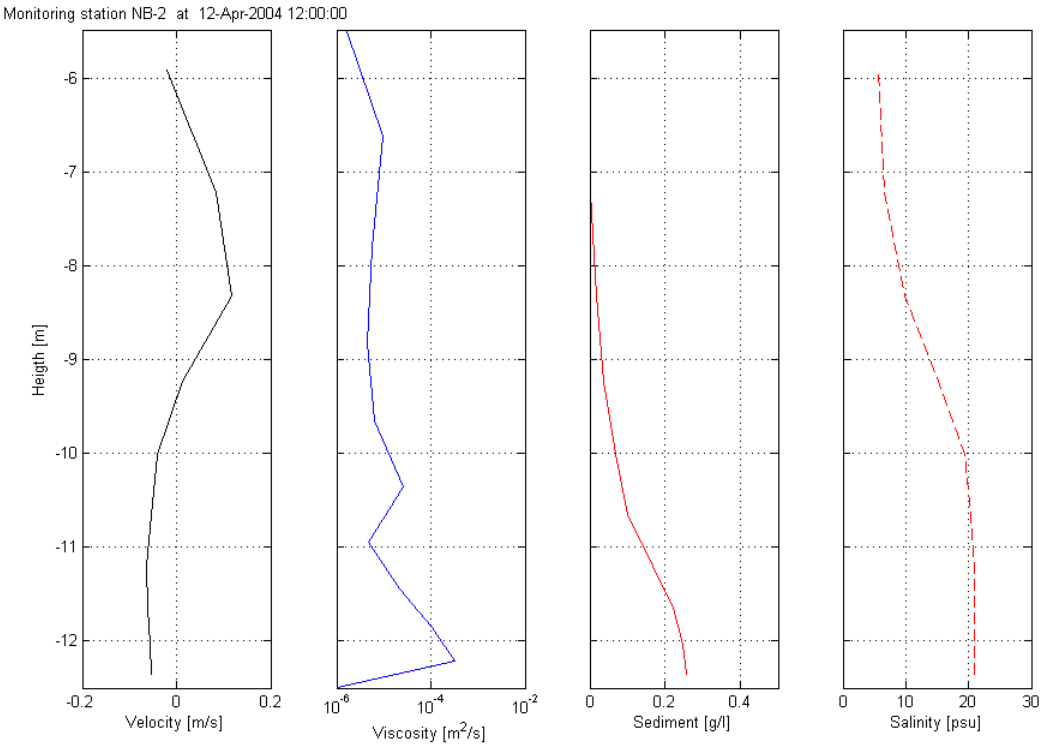

Figure D.22: Model results for vertical profiles for velocity, viscosity, sediment and salinity for monitoring station North Branch-2, Low Water, Neap tide

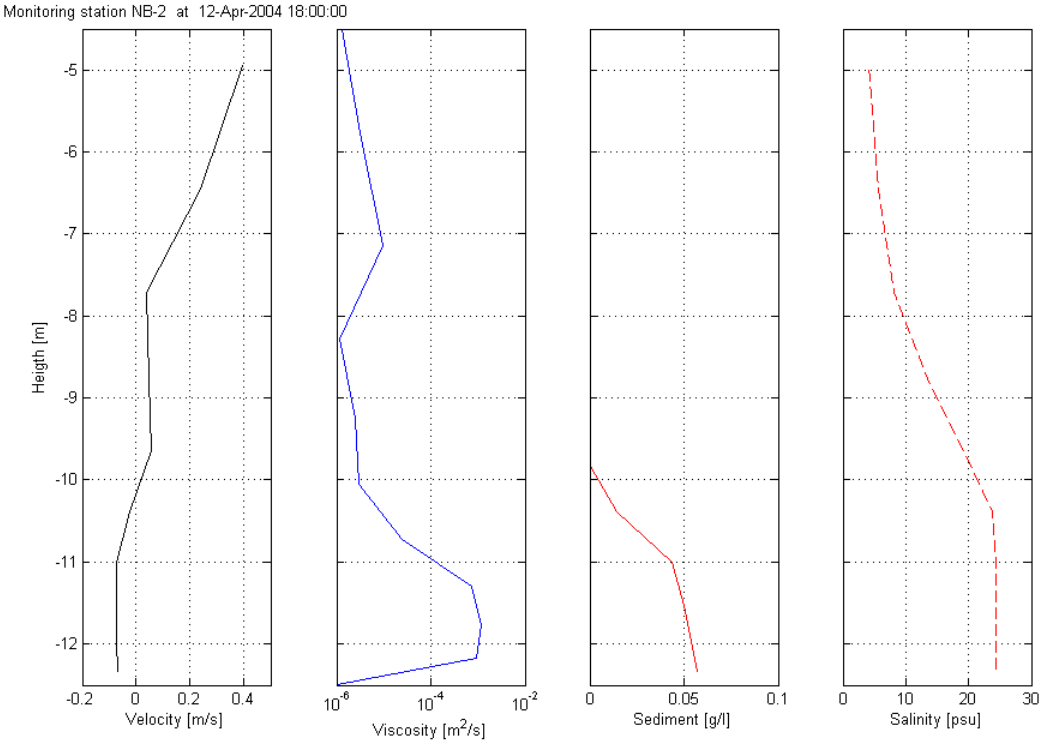

Figure D.23: Model results for vertical profiles for velocity, viscosity, sediment and salinity for monitoring

station North Branch-2, High Water, Neap tide

D.1.5 Sediment

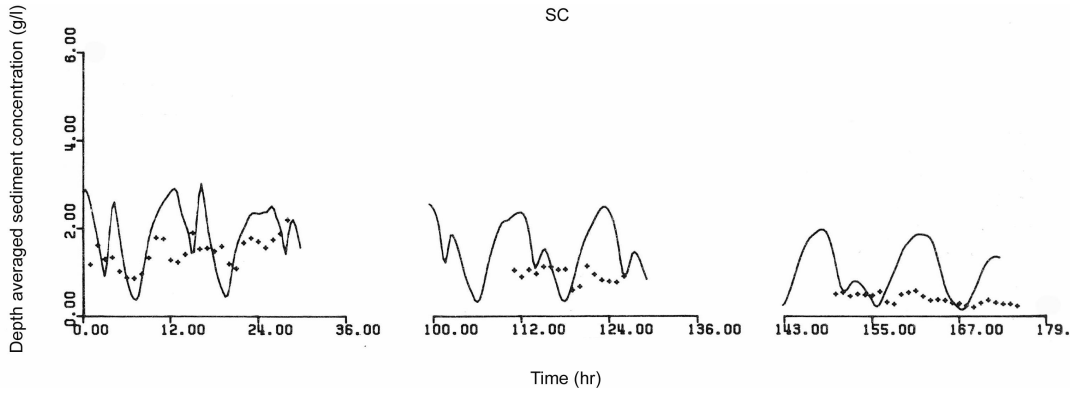

Figure D.24: Observation data for sediment concentration (dots) from Wang [1989] at monitoring station SC

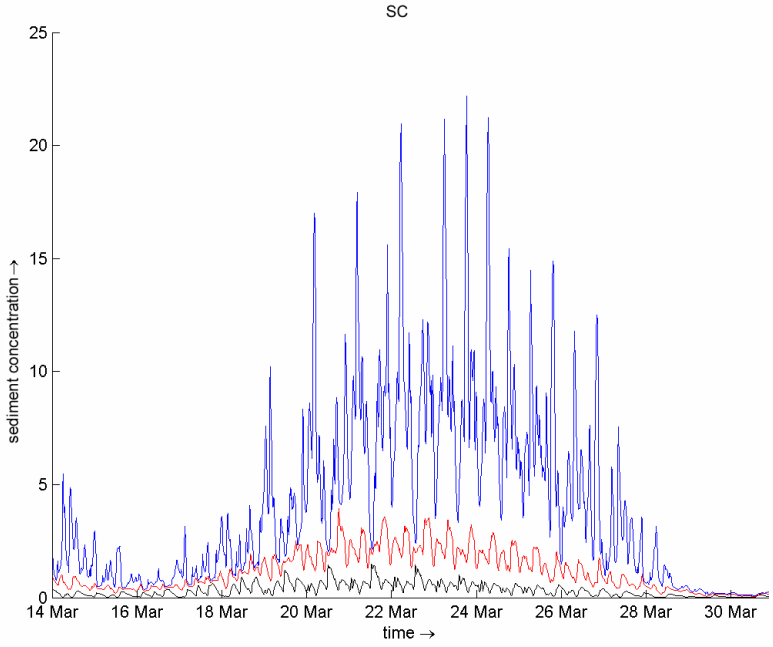

Figure D.25: Model results for sediment concentration for layer 1 (surface; black line), 5 (middle; red line) and 10 (bottom; blue line) for monitoring station SC

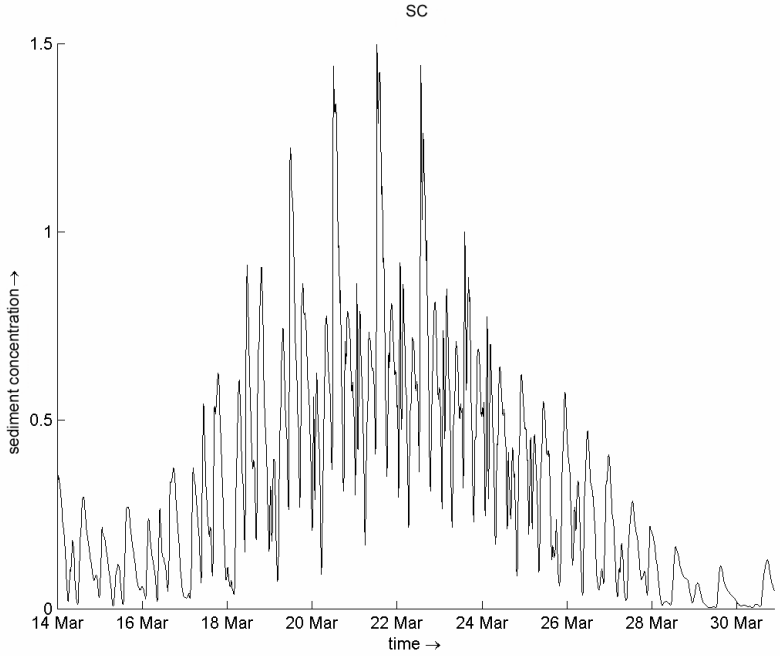

Figure D.26: Model results for sediment concentration for layer 1 (surface layer) for monitoring station SC

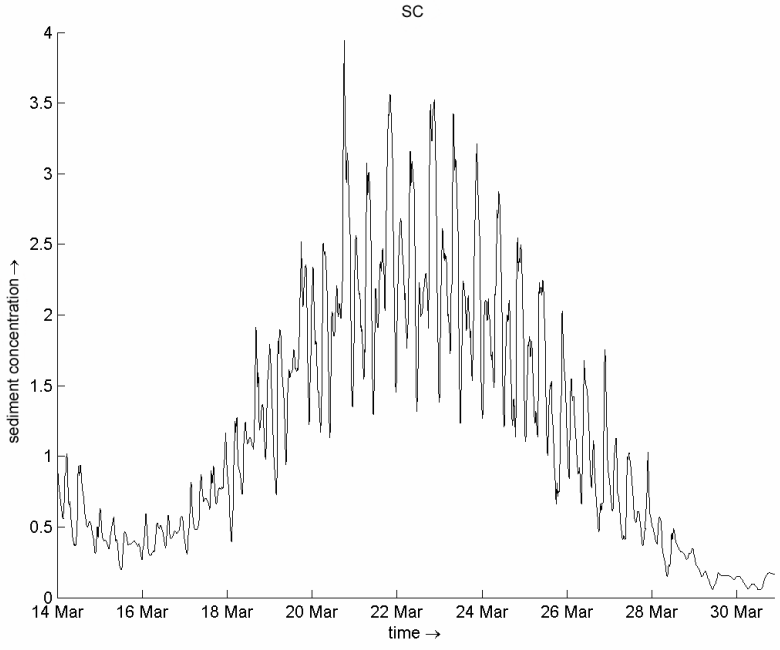

Figure D.27: Model results for sediment concentration for layer 5 (middle layer) for monitoring station SC

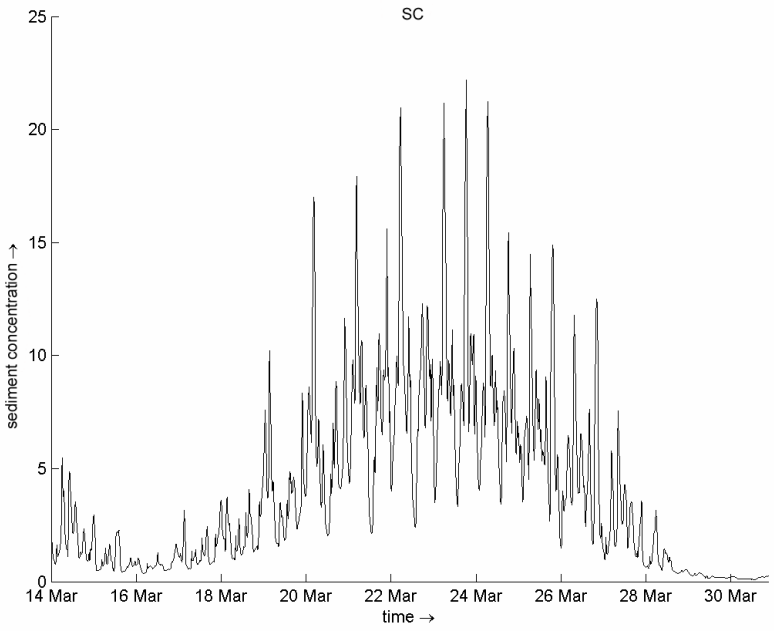

Figure D.28: Model results for sediment concentration for layer 10 (bottom layer) for monitoring station SC

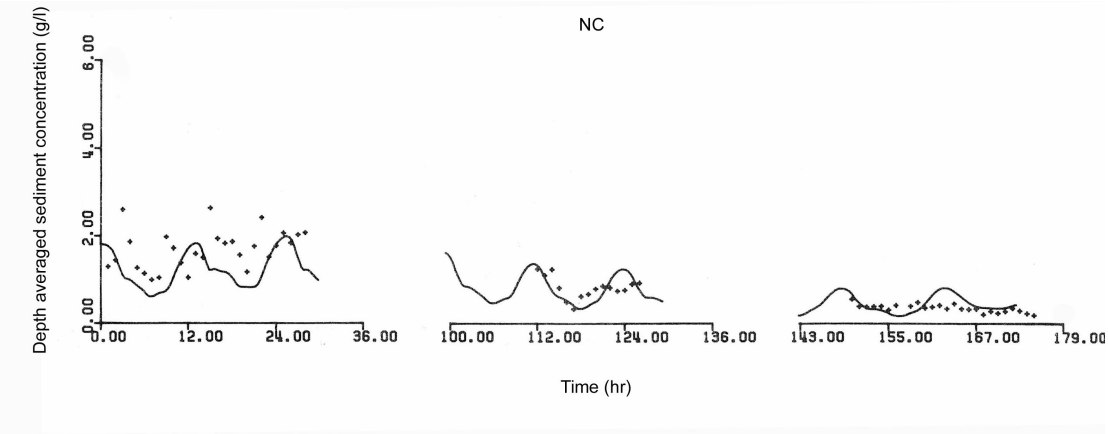

Figure D.29: Observation data for sediment concentration (dots) from Wang [1989] at monitoring station NC

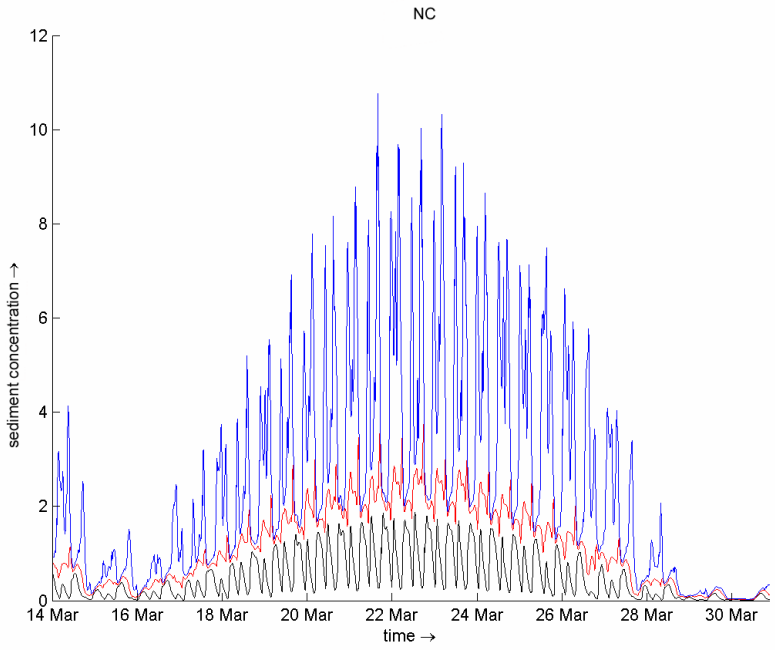

Figure D.30: Model results for sediment concentration for layer 1 (surface; black line), 5 (middle; red line) and 10 (bottom; blue line) for monitoring station NC

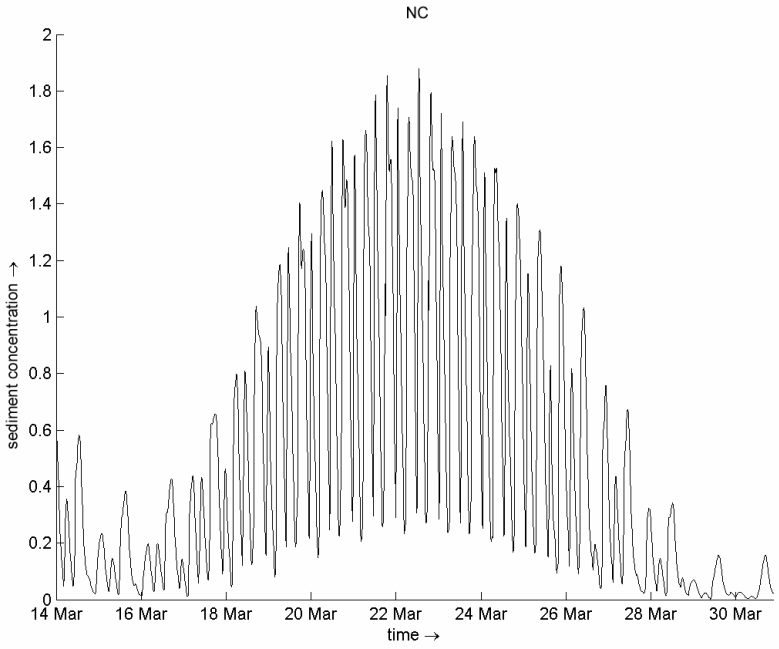

Figure D.31: Model results for sediment concentration for layer 1 (surface layer) for monitoring station NC

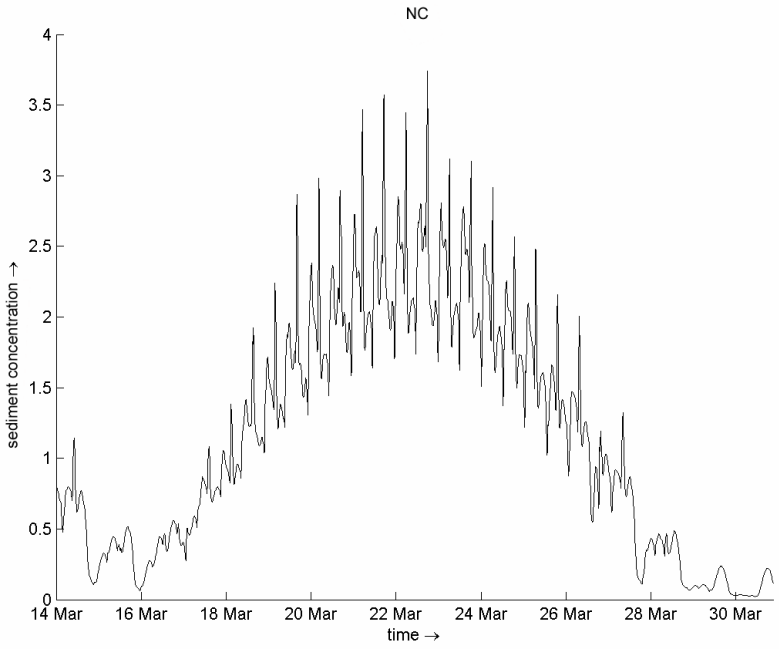

Figure D.32: Model results for sediment concentration for layer 5 (middle layer) for monitoring station NC

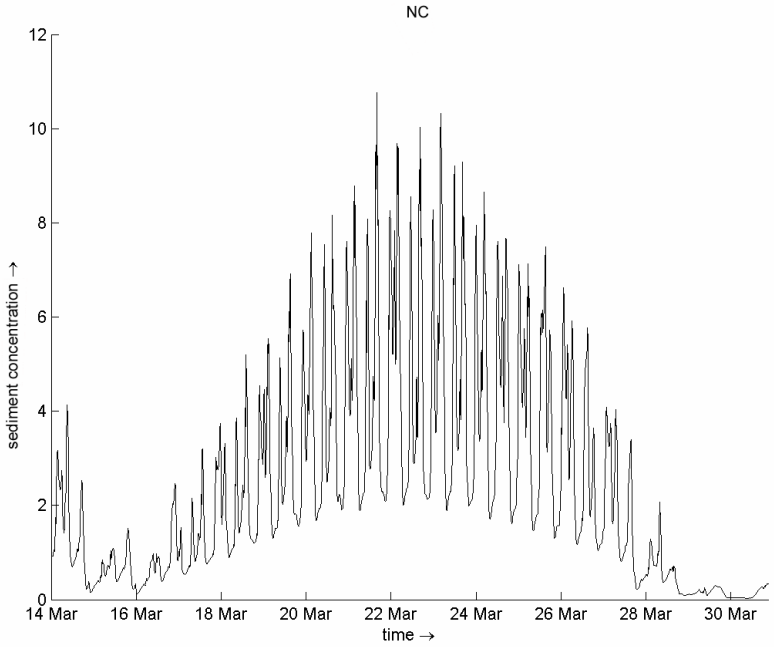

Figure D.33: Model results for sediment concentration for layer 10 (bottom layer) for monitoring station NC

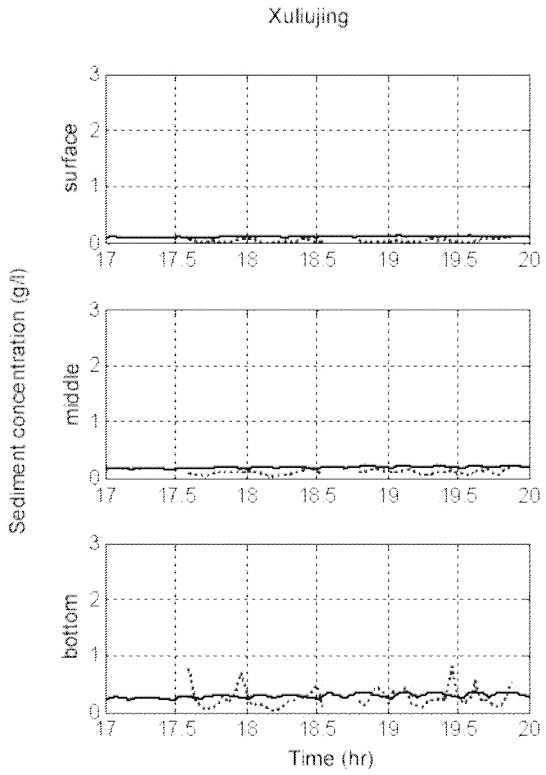

Figure D.34: Observation data for sediment concentration (dotted line) from Hu [2006] at monitoring station Xuliujing

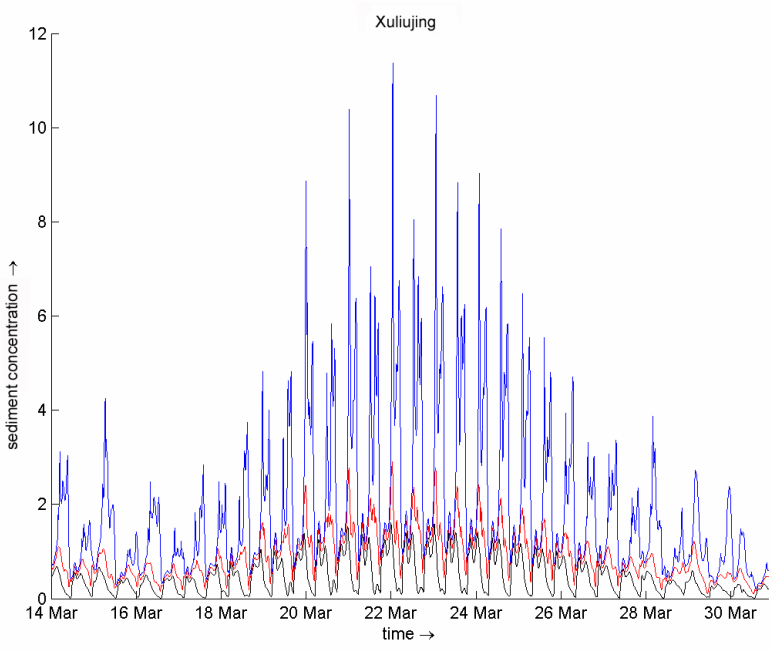

Figure D.35: Model results for sediment concentration for layer 1 (surface; black line), 5 (middle; red line) and

10 (bottom; blue line) for monitoring station Xuliujing

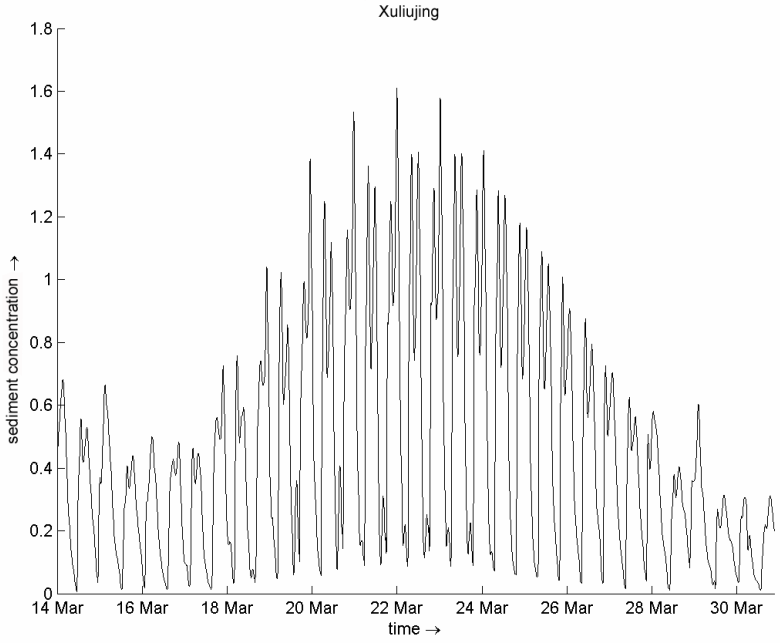

Figure D.36: Model results for sediment concentration for layer 1 (surface layer) for monitoring station Xuliujing

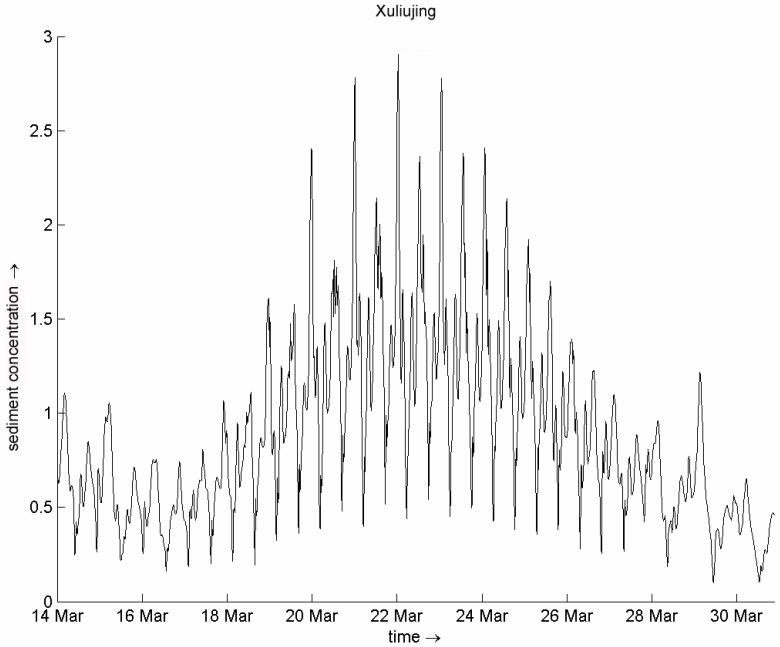

Figure D.37: Model results for sediment concentration for layer 5 (middle layer) for monitoring station Xuliujing

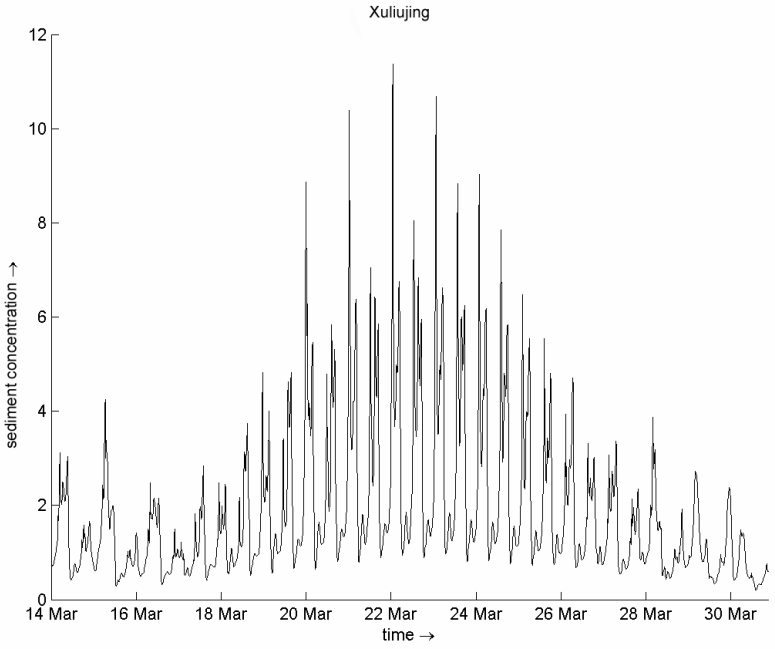

Figure D.38: Model results for sediment concentration for layer 10 (bottom layer) for monitoring station Xuliujing

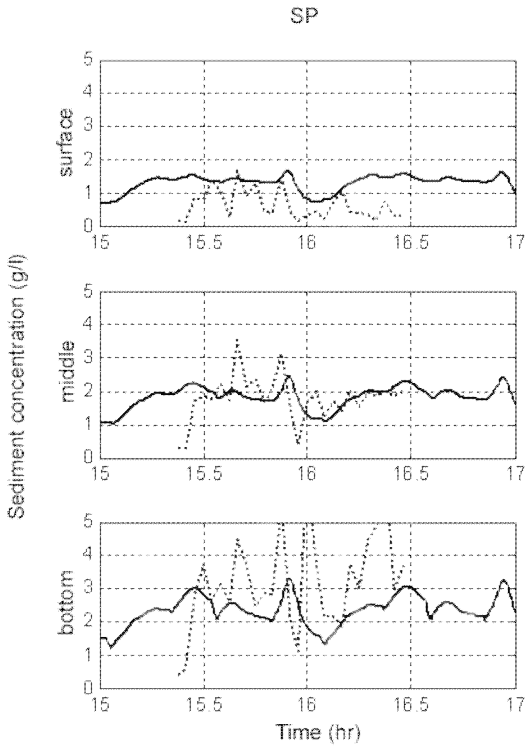

Figure D.39: Observation data for sediment concentration (dotted line) from Hu [2006] at monitoring station SP

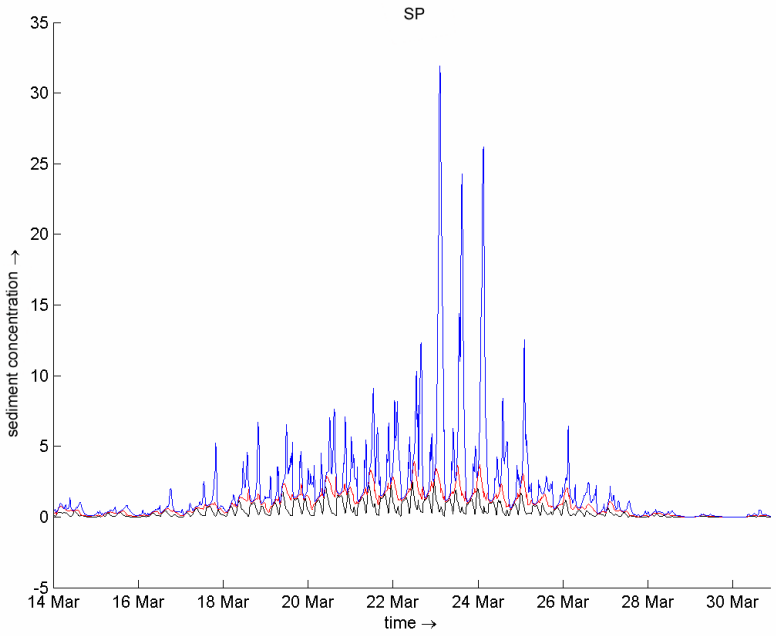

Figure D.40: Model results for sediment concentration for layer 1 (surface layer) for monitoring station SP

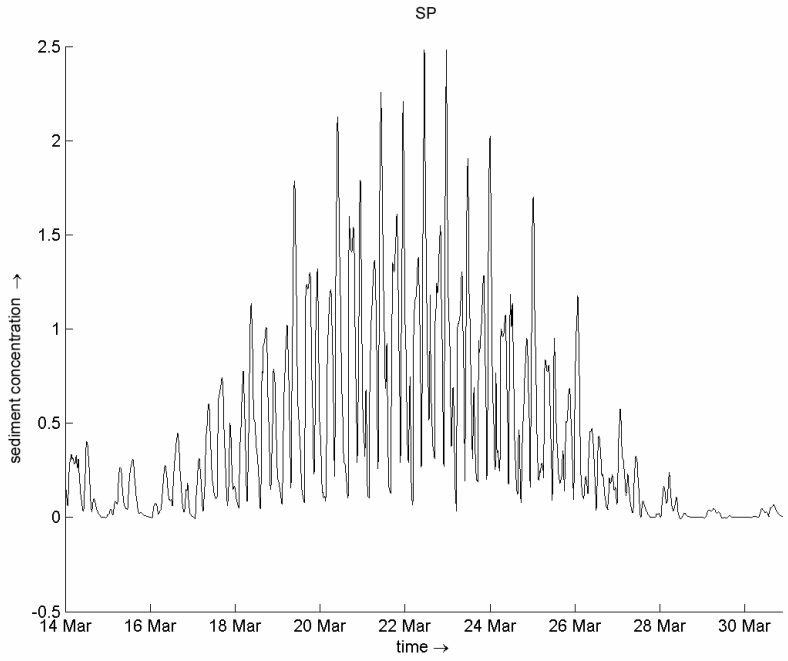

Figure D.41: Model results for sediment concentration for layer 1 (surface layer) for monitoring station SP

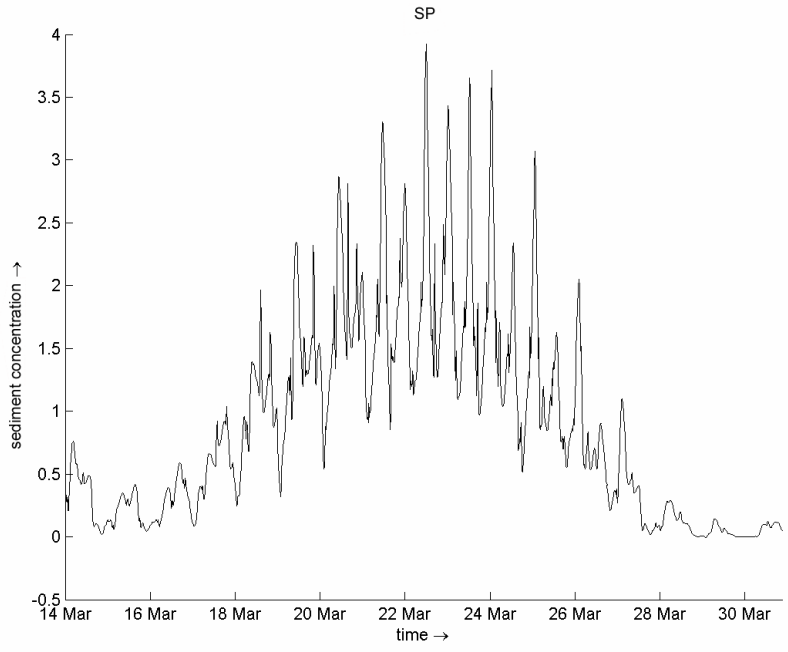

Figure D.42: Model results for sediment concentration for layer 5 (middle layer) for monitoring station SP

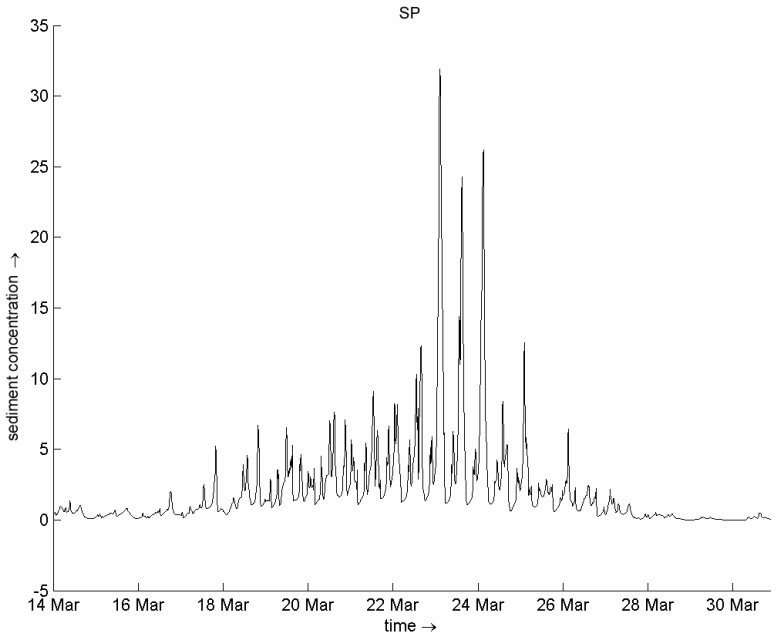

Figure D.43: Model results for sediment concentration for layer 10 (bottom layer) for monitoring station SP

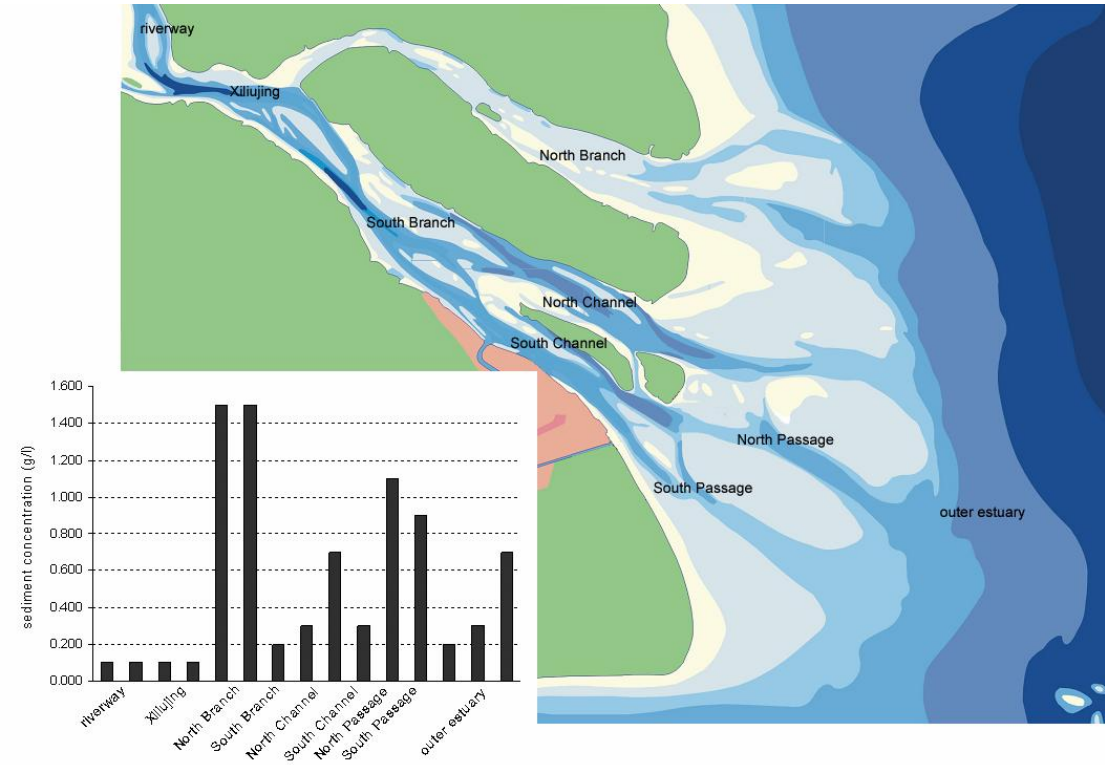

Figure D.44: Observation data for horizontal suspended sediment distribution from He [2006]

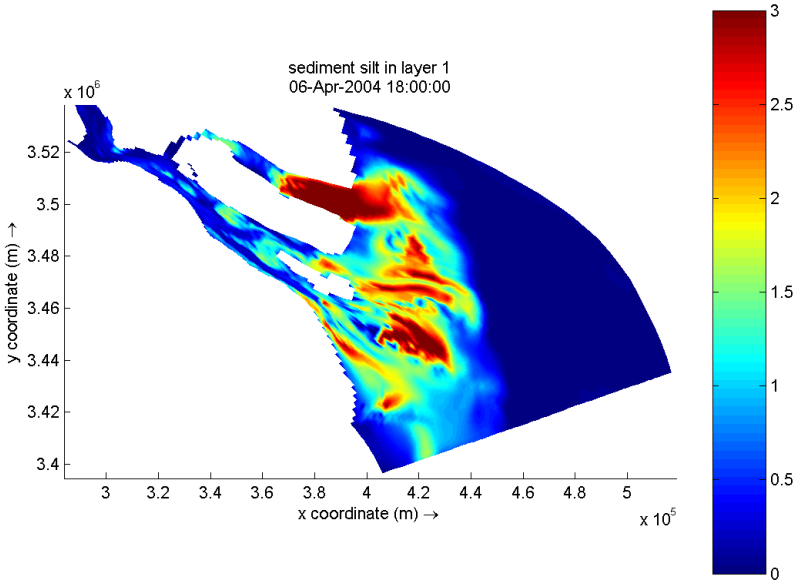

Figure D.47: Model results for horizontal suspended sediment distribution, layer 1, Low Water, Sping tide

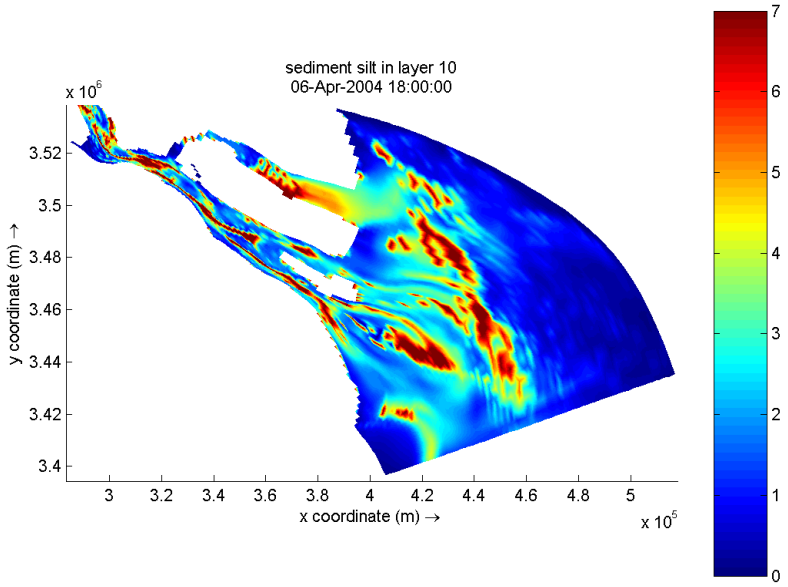

Figure D.48: Model results for horizontal suspended sediment distribution, layer 10, Low Water, Sping tide

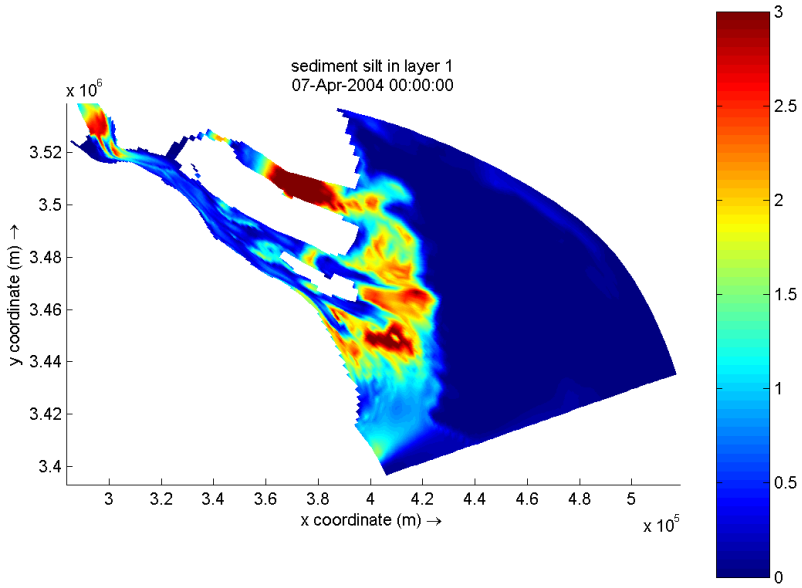

Figure D.45: Model results for horizontal suspended sediment distribution, layer 1, High Water, Sping tide

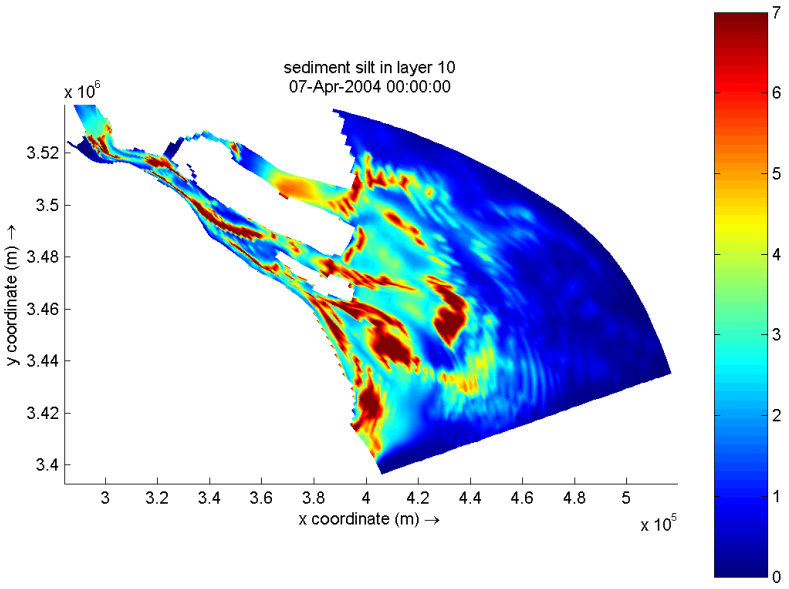

Figure D.46: Model results for horizontal suspended sediment distribution, layer 10, High Water, Sping tide

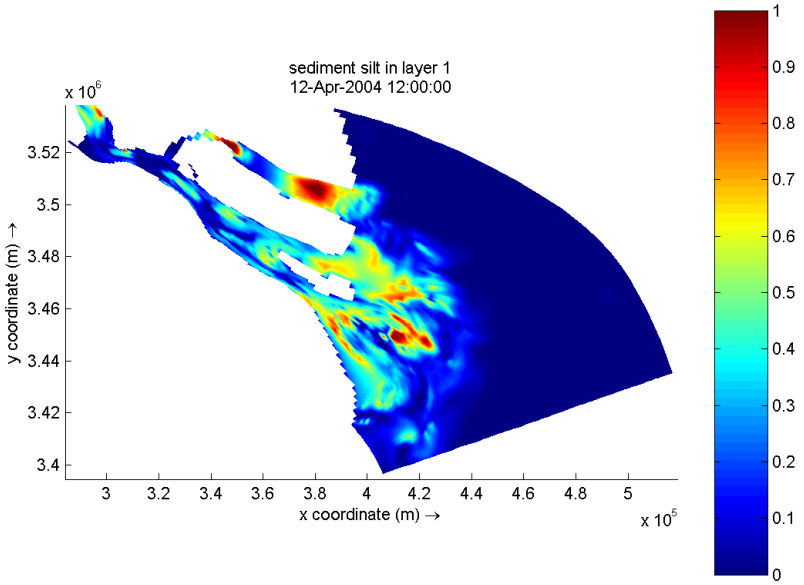

Figure D.51: Model results for horizontal suspended sediment distribution, layer 1, Low Water, Neap tide

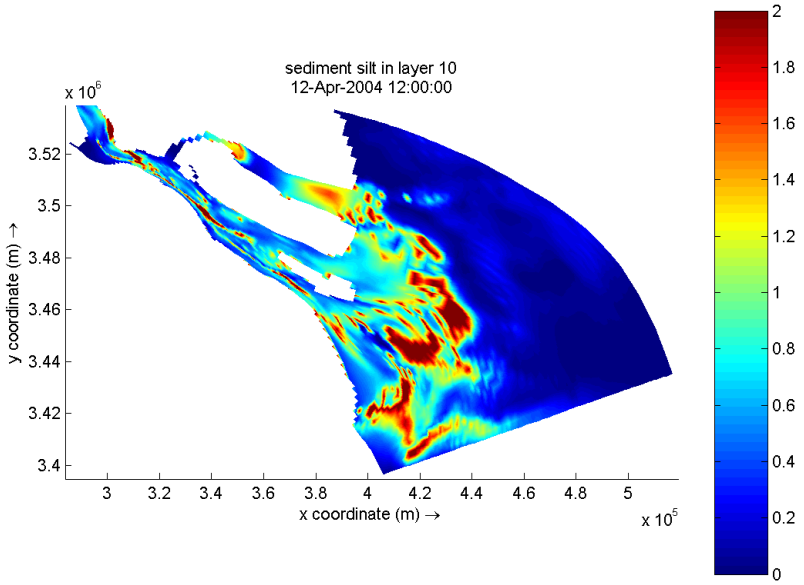

Figure D.52: Model results for horizontal suspended sediment distribution, layer 10, Low Water, Neap tide

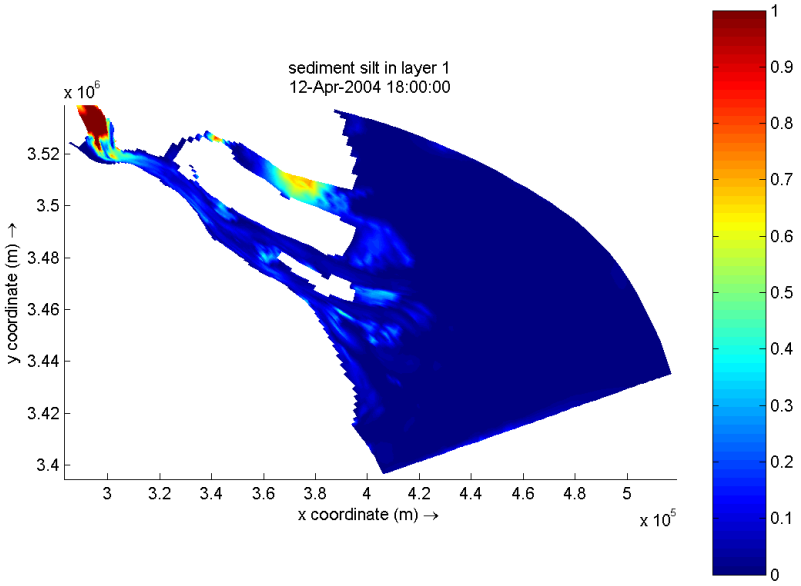

Figure D.49: Model results for horizontal suspended sediment distribution, layer 1, High Water, Neap tide

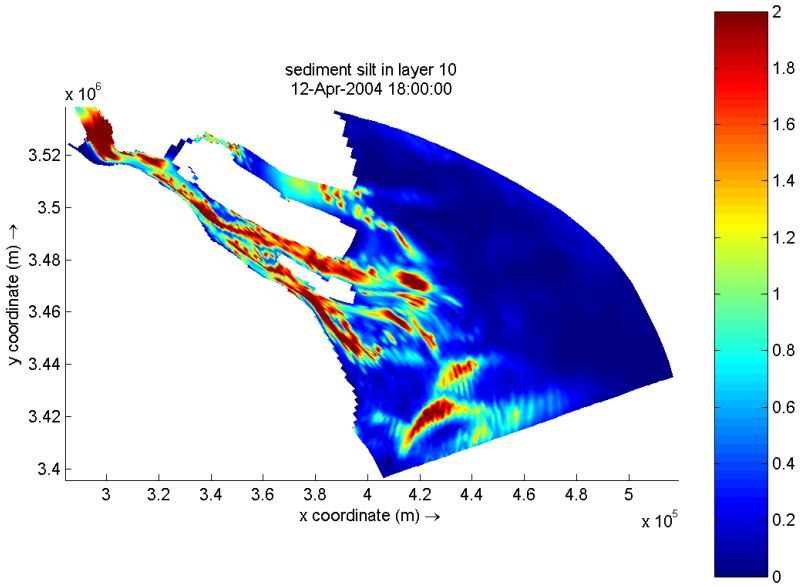

Figure D.50: Model results for horizontal suspended sediment distribution, layer 10, High Water, Neap tide

D.2 Calibration 2Dh model

D.2.1 Tidal constituents

			K1	O1	P1	M2	S2	N2	K2	M4	MS4	M6
OBS	Baozhen	A	0.221	0.164	0.055	0.981	0.361	0.216	0.180	0.159	0.185	0.036
OBS		G	223.7	164.2	265.7	14.0	67.7	3.7	41.4	324.7	21.4	238.0
COM		A	0.205	0.166	0.041	0.910	0.272	0.116	0.156	0.160	0.175	0.041
COM		G	227.1	167.5	200.4	30.5	66.3	3.7	46.3	312.5	0.4	228.8
COM / OBS		A	0.93	1.01	0.75	0.93	0.75	0.54	0.87	1.01	0.95	1.14
COM - OBS		G	3	3	-65	17	-1	0	5	-12	-21	-9
OBS	Wusong	A	0.213	0.165	0.055	0.915	0.318	0.201	0.183	0.146	0.169	0.032
OBS		G	228.0	171.7	275.0	14.5	63.8	359.4	49.2	13.3	15.6	4.4
COM		A	0.201	0.163	0.040	0.853	0.253	0.109	0.145	0.148	0.163	0.035
COM		G	230.3	170.5	203.6	35.9	71.6	8.5	51.6	309.8	358.9	231.9
COM / OBS		A	0.94	0.99	0.73	0.93	0.80	0.54	0.79	1.01	0.96	1.09
COM - OBS		G	2	-1	-71	21	8	9	2	-64	-17	228
OBS	Heng-Sha	A	0.233	0.172	0.054	1.075	0.379	0.209	0.223	0.133	0.156	0.044
OBS		G	215.5	156.1	278.8	343.5	35	331.7	15.2	259.8	315.5	112.3
COM		A	0.204	0.163	0.041	0.909	0.290	0.125	0.166	0.152	0.158	0.044
COM		G	215.8	157.0	189.0	354.2	30.0	328.4	10.0	263.4	311.8	84.3
COM / OBS		A	0.88	0.95	0.76	0.85	0.77	0.60	0.74	1.14	1.01	1.00
COM - OBS		G	0	1	-90	11	-5	-3	-5	4	-4	-28
OBS	Shashan	A	0.244	0.132	0.065	1.126	0.529	0.201	0.150	0.080	0.062	0.008
OBS		G	178.5	129.4	171.8	311.6	357.2	299.1	354	192.8	245.4	293.4
COM		A	0.194	0.141	0.039	1.043	0.367	0.158	0.210	0.005	0.005	0.007
COM		G	192.7	133.6	165.9	312.6	345.3	285.5	325.3	23.7	18.9	216.8
COM / OBS		A	0.80	1.07	0.60	0.93	0.69	0.79	1.40	0.06	0.08	0.88
COM - OBS		G	14	4	-6	1	-12	-14	-29	-169	-227	-77

Table D.4: Tidal analyses 2Dh model, Chézy=110 $m^{1/2}s^{-1}$*. OBS = observation data (Wang [1994]); COM = computed data (Yangtze estuary model)*
A=tidal amplitude; G=tidal phase

			K1	O1	P1	M2	S2	N2	K2	M4	MS4	M6
OBS	Boazhen	A	0.221	0.164	0.055	0.981	0.361	0.216	0.180	0.159	0.185	0.036
OBS		G	223.7	164.2	265.7	14.0	67.7	3.7	41.4	324.7	21.4	238.0
COM		A	0.211	0.170	0.042	0.961	0.287	0.123	0.165	0.172	0.185	0.044
COM		G	226.1	164.7	198.2	29.5	65.2	2.3	45.2	307.5	355.8	230.9
COM / OBS		A	0.95	1.04	0.76	0.98	0.80	0.57	0.92	1.08	1.00	1.22
COM - OBS		G	1	1	-67	16	-2	-1	4	-17	-26	-7
OBS	Wusong	A	0.213	0.165	0.055	0.915	0.318	0.201	0.183	0.146	0.169	0.032
OBS		G	228.0	171.7	275.0	14.5	63.8	359.4	49.2	13.3	15.6	4.4
COM		A	0.207	0.166	0.041	0.900	0.267	0.115	0.153	0.161	0.174	0.038
COM		G	228.2	167.6	201.3	34.7	70.4	6.9	50.4	304.3	353.9	233.6
COM / OBS		A	0.97	1.01	0.75	0.98	0.84	0.57	0.84	1.10	1.03	1.19
COM - OBS		G	0	-4	-74	20	7	7	1	-69	-22	229
OBS	Heng-Sha	A	0.233	0.172	0.054	1.075	0.379	0.209	0.223	0.133	0.156	0.044
OBS		G	215.5	156.1	278.8	343.5	35	331.7	15.2	259.8	315.5	112.3
COM		A	0.208	0.166	0.041	0.937	0.299	0.129	0.171	0.165	0.169	0.048
COM		G	214.1	154.9	187.3	352.9	28.6	326.7	8.6	268.6	307.0	85.5
COM / OBS		A	0.89	0.97	0.76	0.87	0.79	0.62	0.77	1.24	1.08	1.09
COM - OBS		G	-1	-1	-92	9	-6	-5	-7	-1	-8	-27
OBS	Shashan	A	0.244	0.132	0.065	1.126	0.529	0.201	0.150	0.080	0.062	0.008
OBS		G	178.5	129.4	171.8	311.6	357.2	299.1	354	192.8	246.4	293.4
COM		A	0.194	0.141	0.039	1.046	0.368	0.158	0.211	0.005	0.006	0.008
COM		G	192.5	133.3	165.7	312.2	344.8	284.9	324.8	10.7	8.4	201.4
COM / OBS		A	0.80	1.07	0.60	0.93	0.70	0.79	1.41	0.06	0.10	1.00
COM - OBS		G	14	4	-6	1	-12	-14	-29	-182	-237	-92

Table D.5: Tidal analyses 2Dh model, Chézy=120 $m^{1/2}s^{-1}$*. OBS = observation data (Wang [1994]); COM = computed data (Yangtze estuary model)*

A=tidal amplitude; G=tidal phase

			K1	O1	P1	M2	S2	N2	K2	M4	MS4	M6
OBS	Boazhen	A	0.221	0.164	0.055	0.981	0.361	0.216	0.180	0.159	0.185	0.036
OBS		G	223.7	164.2	265.7	140	67.7	3.7	41.4	324.7	21.4	238.0
COM		A	0.215	0.172	0.043	0.994	0.296	0.126	0.170	0.181	0.195	0.051
COM		G	223.3	162.6	196.5	29.1	64.8	1.3	44.8	301.8	350.4	231.8
COM / OBS		A	0.97	1.05	0.78	1.01	0.82	0.58	0.94	1.14	1.05	1.42
COM - OBS		G	0	-2	-69	15	-3	-2	3	-23	-31	-6
OBS	Wusong	A	0.213	0.165	0.055	0.915	0.318	0.201	0.183	0.146	0.169	0.032
OBS		G	228.0	171.7	275.0	145	63.8	359.4	49.2	13.3	15.6	4.4
COM		A	0.211	0.168	0.042	0.932	0.276	0.119	0.158	0.170	0.183	0.044
COM		G	226.5	165.6	199.7	34.7	70.4	6.4	50.4	298.5	348.4	235.7
COM / OBS		A	0.99	1.02	0.76	1.02	0.87	0.59	0.86	1.16	1.08	1.38
COM - OBS		G	-2	-6	-75	20	7	7	1	-75	-27	231
OBS	Heng-Sha	A	0.233	0.172	0.054	1.075	0.379	0.209	0.223	0.133	0.156	0.044
OBS		G	215.5	156.1	278.8	343.5	35	331.7	15.2	259.8	315.5	112.3
COM		A	0.211	0.167	0.042	0.952	0.304	0.131	0.174	0.178	0.181	0.048
COM		G	212.9	153.4	186.0	352.5	27.8	325.6	7.9	254.8	303.6	84.6
COM / OBS		A	0.91	0.97	0.78	0.89	0.80	0.63	0.78	1.34	1.16	1.09
COM - OBS		G	-3	-3	-93	9	-7	-6	-7	-5	-12	-28
OBS	Sheshan	A	0.244	0.132	0.065	1.126	0.529	0.201	0.150	0.080	0.062	0.008
OBS		G	178.5	129.4	171.8	311.6	357.2	299.1	354	192.8	245.4	293.4
COM		A	0.194	0.141	0.039	1.046	0.367	0.157	0.210	0.005	0.008	0.009
COM		G	192.5	133.2	165.7	312.0	344.4	284.5	324.4	353.7	356.8	188.6
COM / OBS		A	0.80	1.07	0.60	0.93	0.69	0.78	1.40	0.06	0.13	1.13
COM - OBS		G	14	4	-6	0	-13	-15	-30	161	111	-105

Table D.6: Tidal analyses 2Dh model, Chézy=130 $m^{1/2}s^{-1}$*. OBS = observation data (Wang [1994]); COM = computed data (Yangtze estuary model)*

A=tidal amplitude; G=tidal phase

D.2.2 Water level

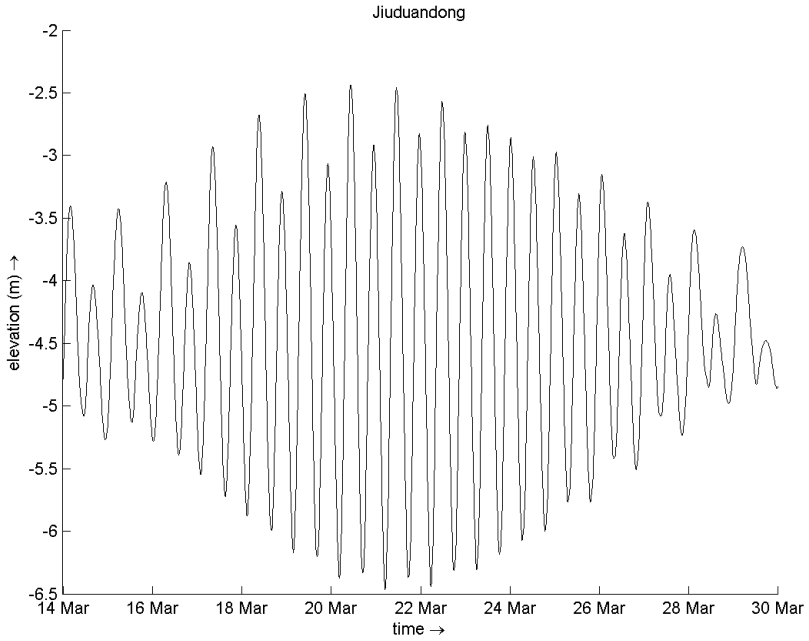

Figure D.53: Computed water levels (2Dh model) at monitoring station Jiuduandong

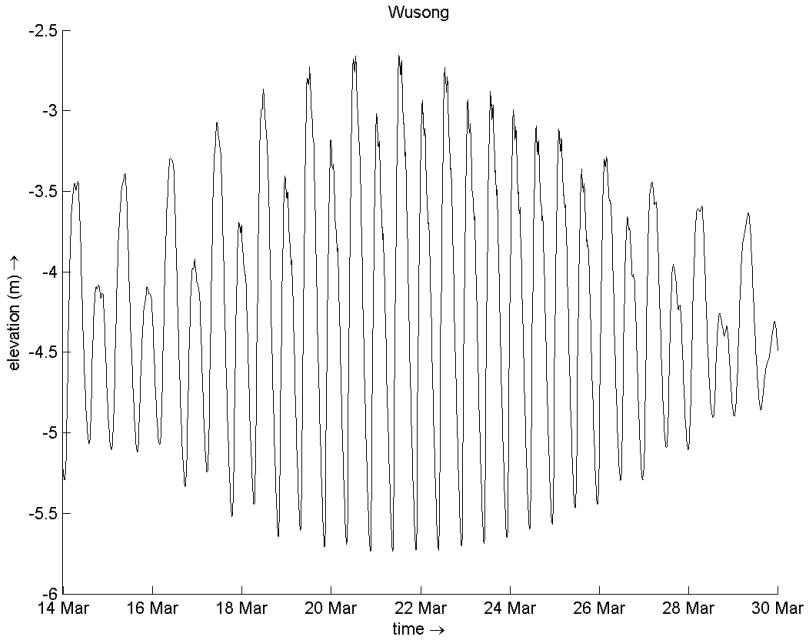

Figure D.54: Computed water levels (2Dh model) at monitoring station Wusong

D.2.3 Flow velocity

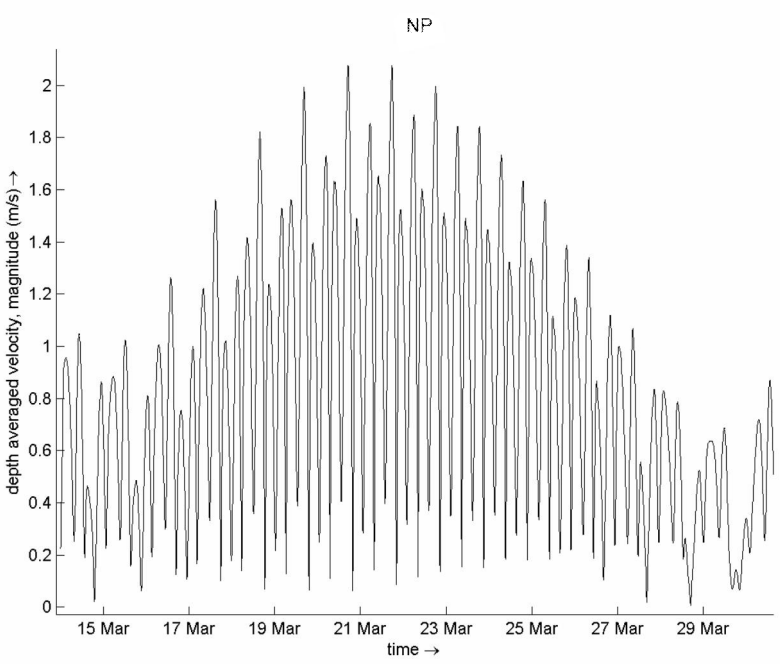

Figure D.55: Computed velocities (2Dh model) at monitoring station NP

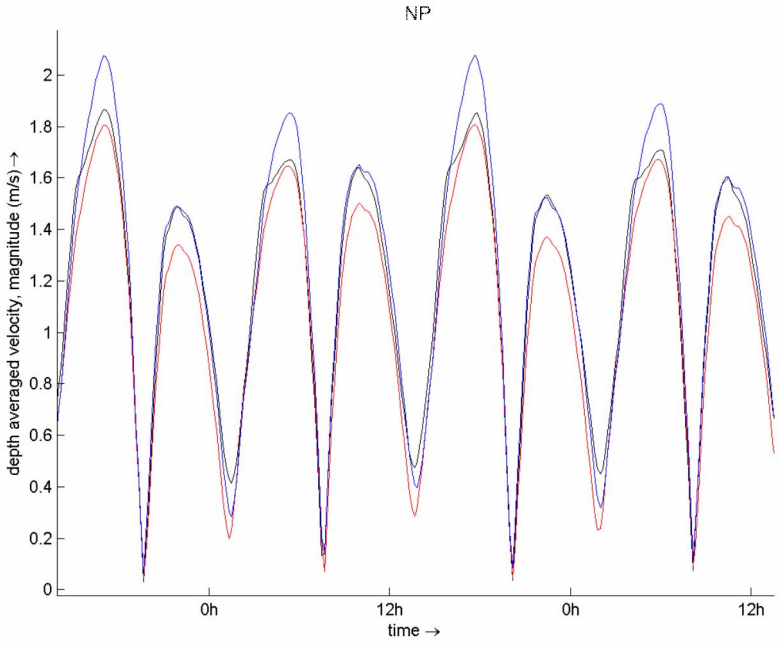

Figure D.56: Computed velocities at monitoring station NP during spring tide
black line: results for 3D model, Chézy coefficient = 110 $m^{1/2}s^{-1}$
red line: results for 2Dh model, Chézy coefficient = 110 $m^{1/2}s^{-1}$
blue line: results for 2Dh model, Chézy coefficient = 130 $m^{1/2}s^{-1}$

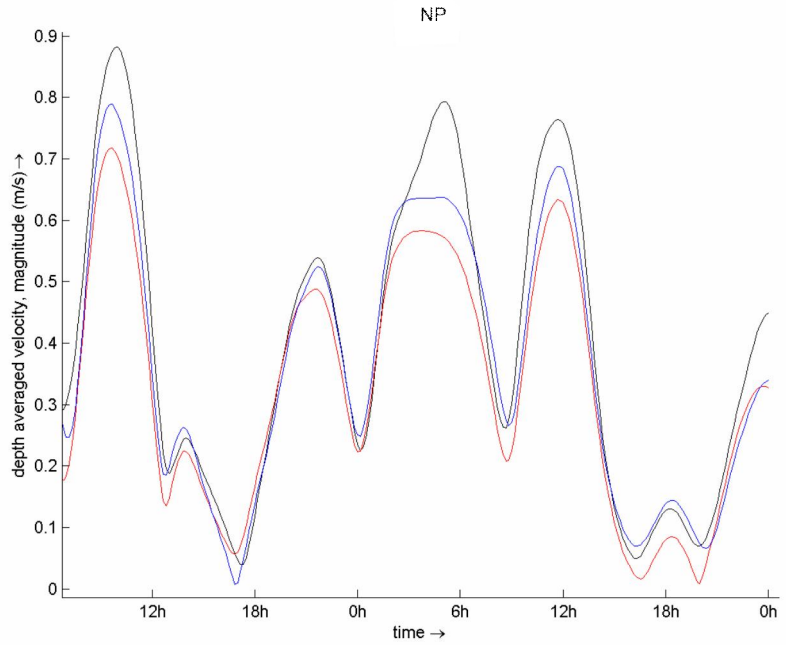

Figure D.57: Computed velocities at monitoring station NP during neap tide
black line: results for 3D model, Chézy coefficient = 110 $m^{1/2}s^{-1}$
red line: results for 2Dh model, Chézy coefficient = 110 $m^{1/2}s^{-1}$
blue line: results for 2Dh model, Chézy coefficient = 130 $m^{1/2}s^{-1}$

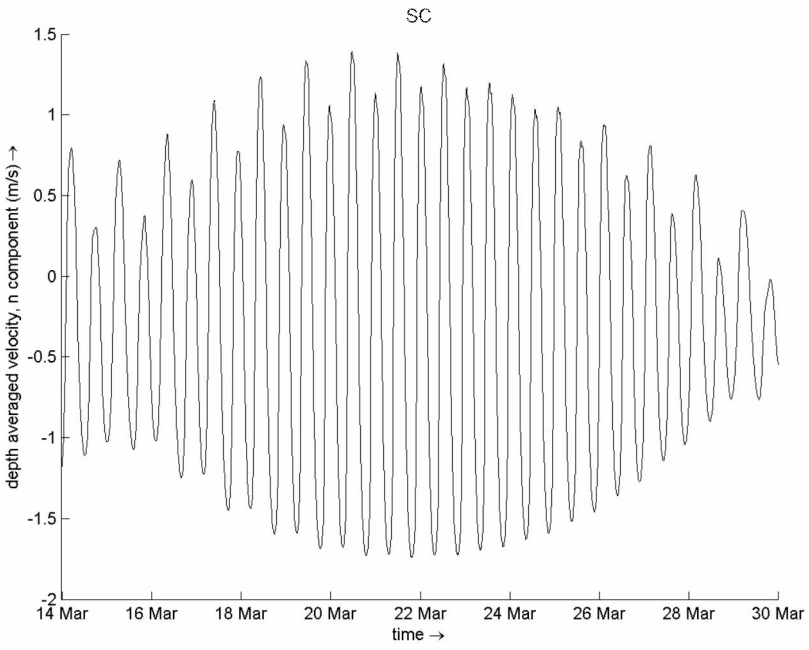

Figure D.58: Computed velocities (2Dh model) at monitoring station SC

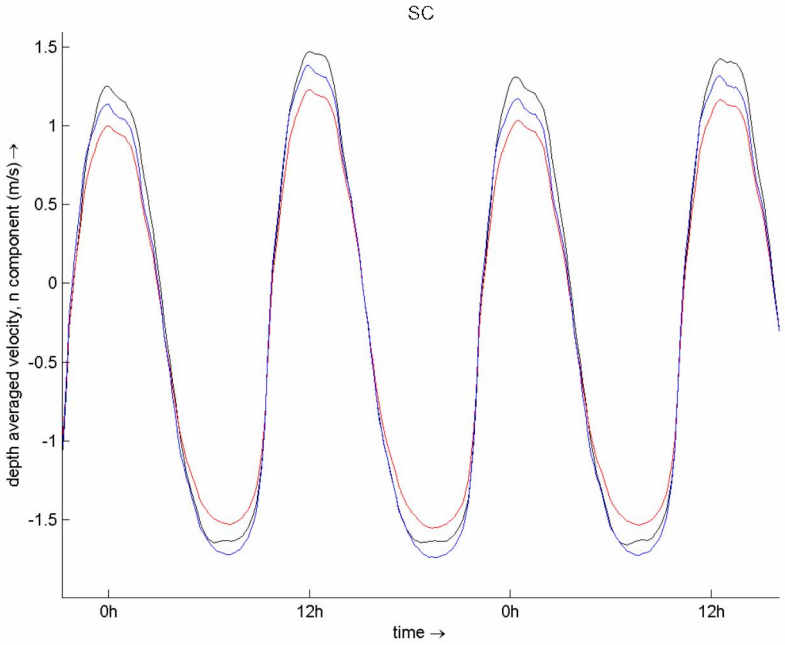

Figure D.59: Computed velocities at monitoring station SC during spring tide
black line: results for 3D model, Chézy coefficient = 110 $m^{1/2}s^{-1}$
red line: results for 2Dh model, Chézy coefficient = 110 $m^{1/2}s^{-1}$
blue line: results for 2Dh model, Chézy coefficient = 130 $m^{1/2}s^{-1}$

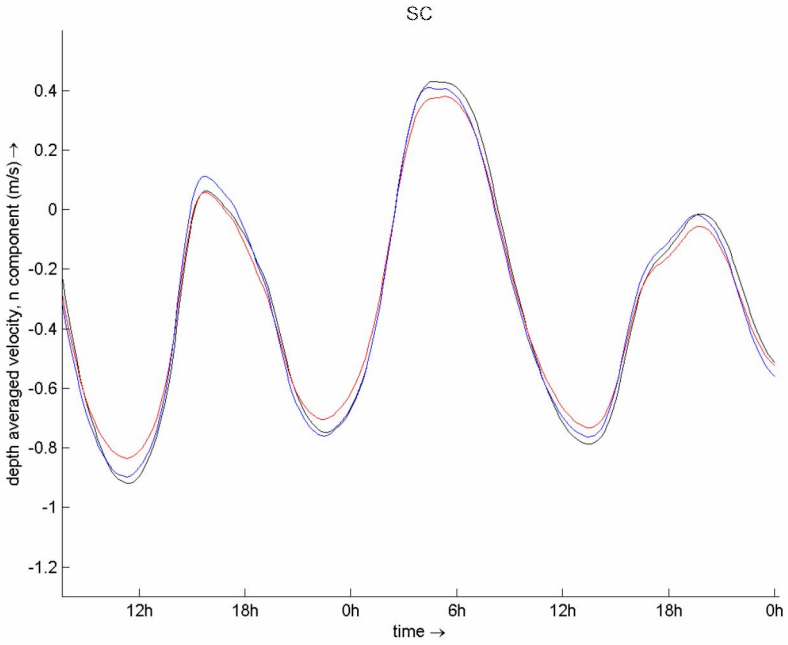

Figure D.60: Computed velocities at monitoring station SC during neap tide
black line: results for 3D model, Chézy coefficient = 110 $m^{1/2}s^{-1}$
red line: results for 2Dh model, Chézy coefficient = 110 $m^{1/2}s^{-1}$
blue line: results for 2Dh model, Chézy coefficient = 130 $m^{1/2}s^{-1}$

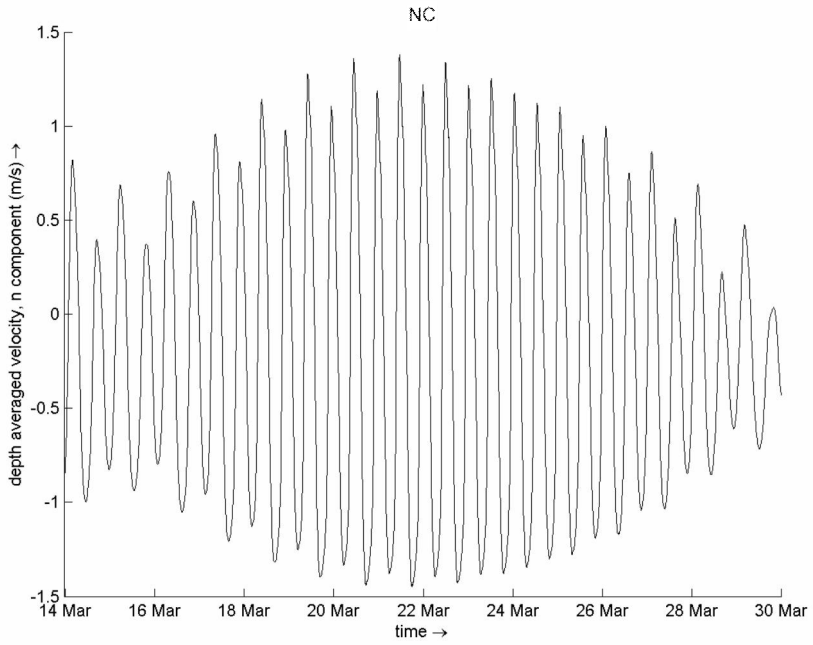

Figure D.61: Computed velocities (2Dh model) at monitoring station NC

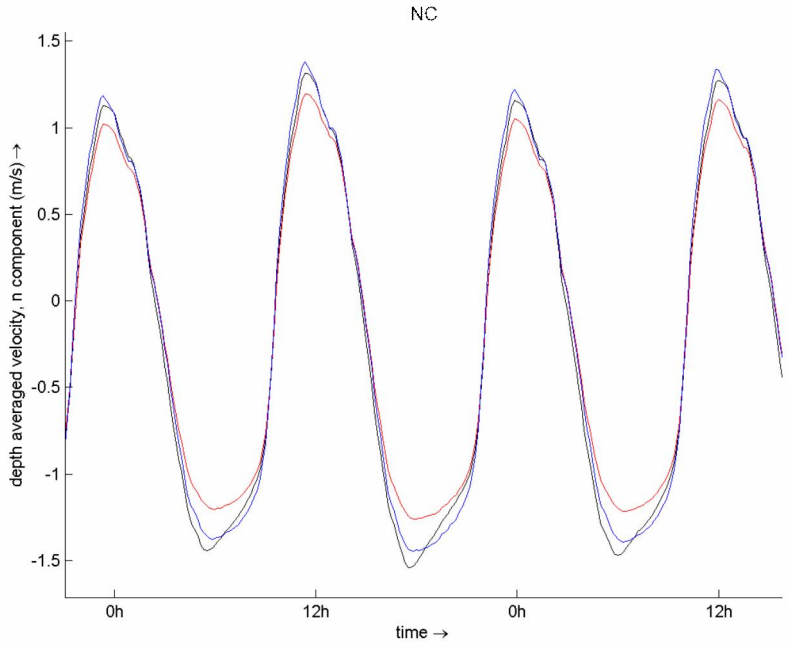

Figure D.62: Computed velocities at monitoring station NC during spring tide
black line: results for 3D model, Chézy coefficient = 110 $m^{1/2}s^{-1}$
red line: results for 2Dh model, Chézy coefficient = 110 $m^{1/2}s^{-1}$
blue line: results for 2Dh model, Chézy coefficient = 130 $m^{1/2}s^{-1}$

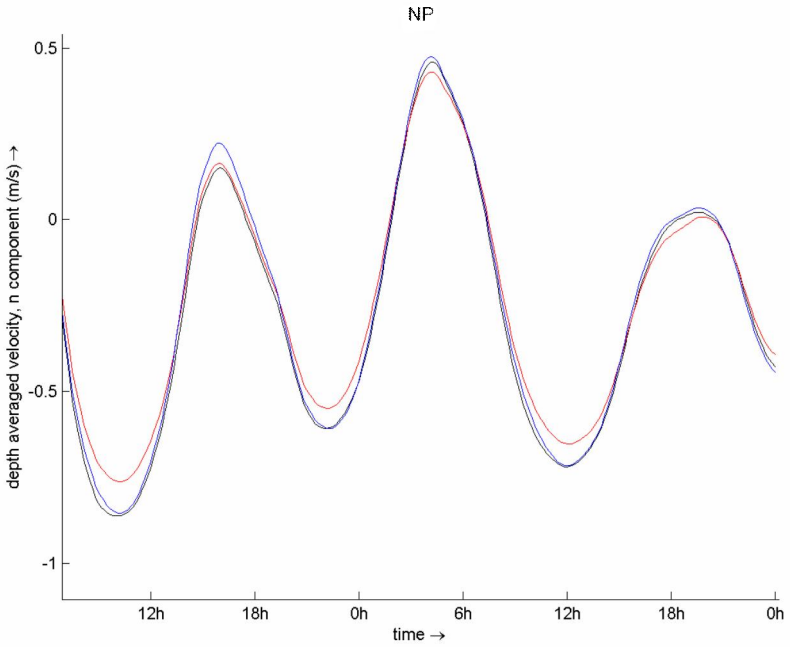

Figure D.63: Computed velocities at monitoring station NC during neap tide
black line: results for 3D model, Chézy coefficient = 110 $m^{1/2}s^{-1}$
red line: results for 2Dh model, Chézy coefficient = 110 $m^{1/2}s^{-1}$
blue line: results for 2Dh model, Chézy coefficient = 130 $m^{1/2}s^{-1}$

D.2.4 Salinity

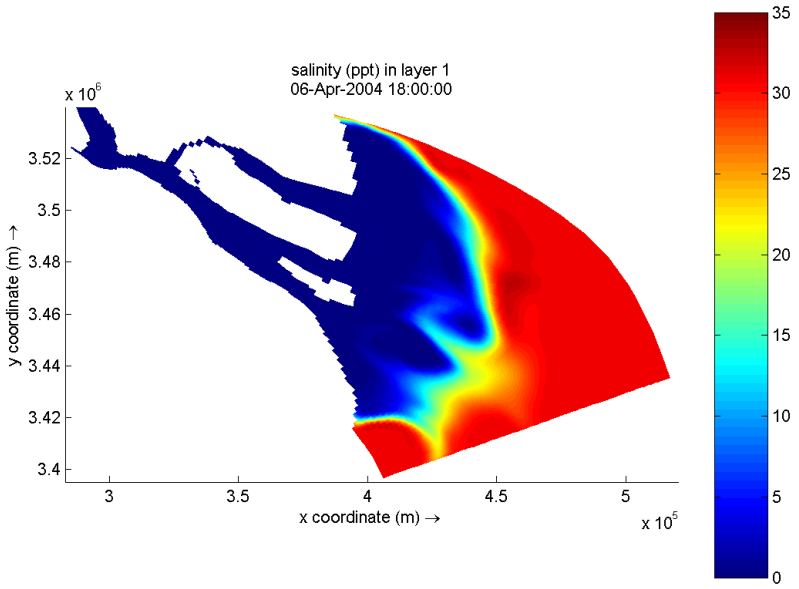

Figure D.64: 2Dh model results for horizontal salinity distribution, layer 10, Low Water, Spring Tide

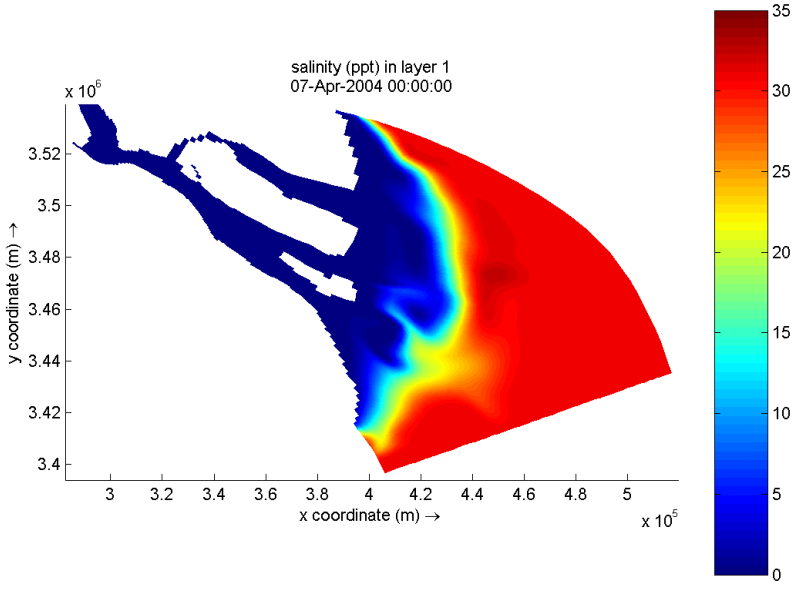

Figure D.65: 2Dh model results for horizontal salinity distribution, layer 10, High Water, Spring Tide

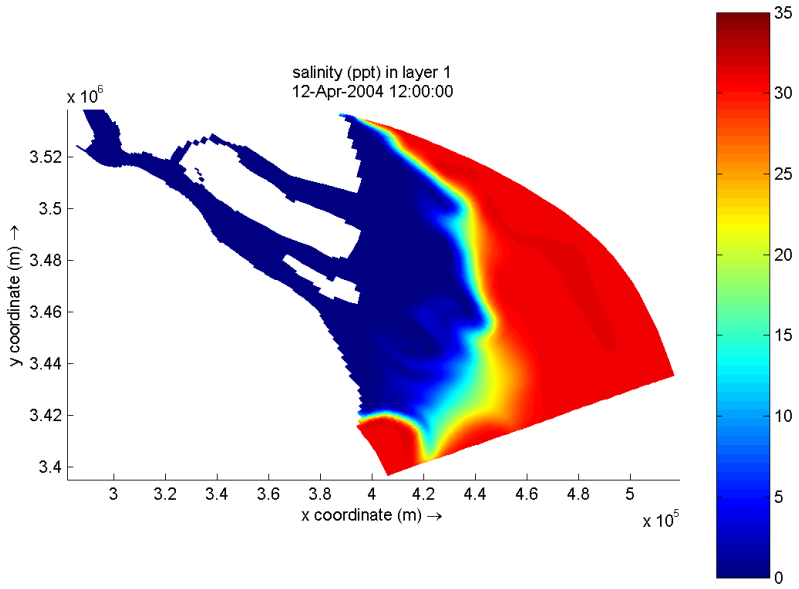

Figure D.66: 2Dh model results for horizontal salinity distribution, layer 10, Low Water, Neap Tide

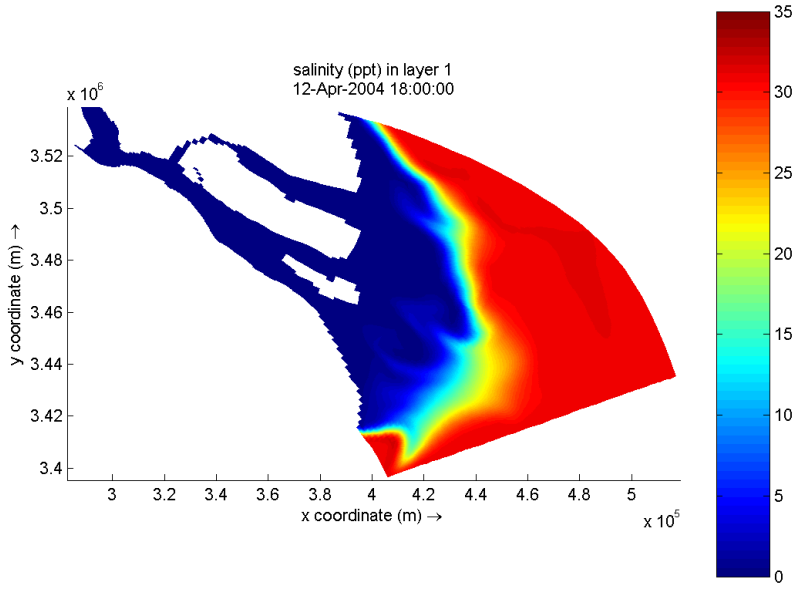

Figure D.67: 2Dh model results for horizontal salinity distribution, layer 10, High Water, Neap Tide

D.2.5 Sediment

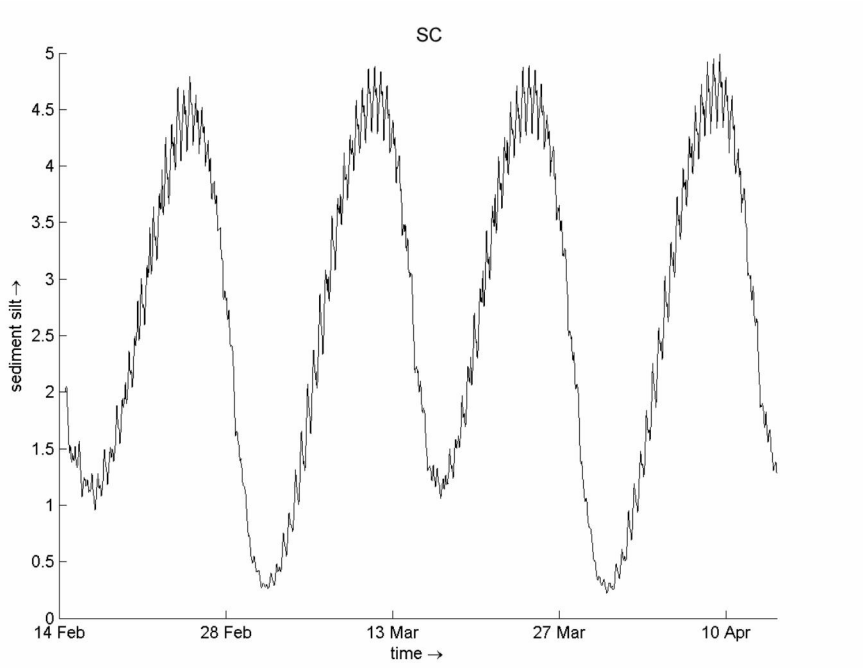

Figure D.68: 2Dh model results for sediment concentration for monitoring station SC, for a period of 2 months

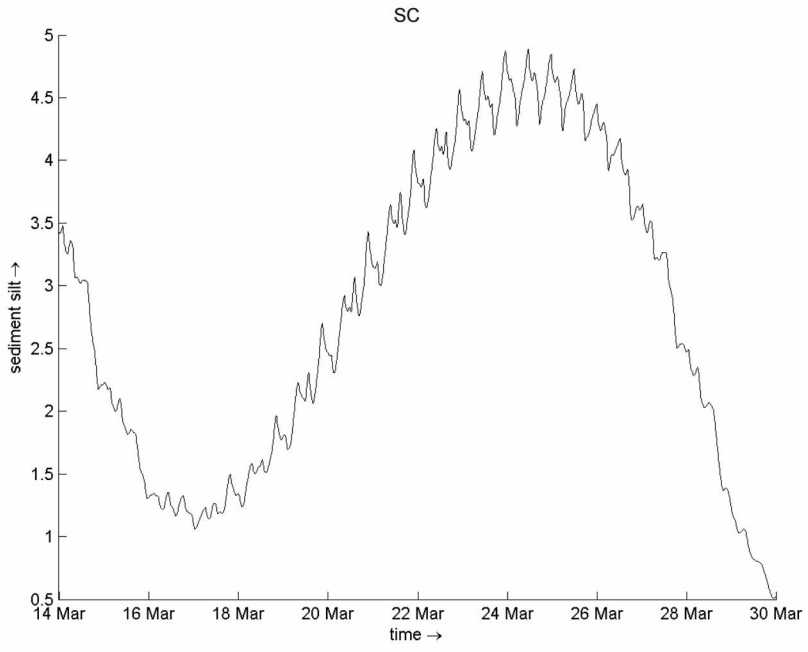

Figure D.69: 2Dh model results for sediment concentration for monitoring station SC, for 1 spring-neap tidal cycle

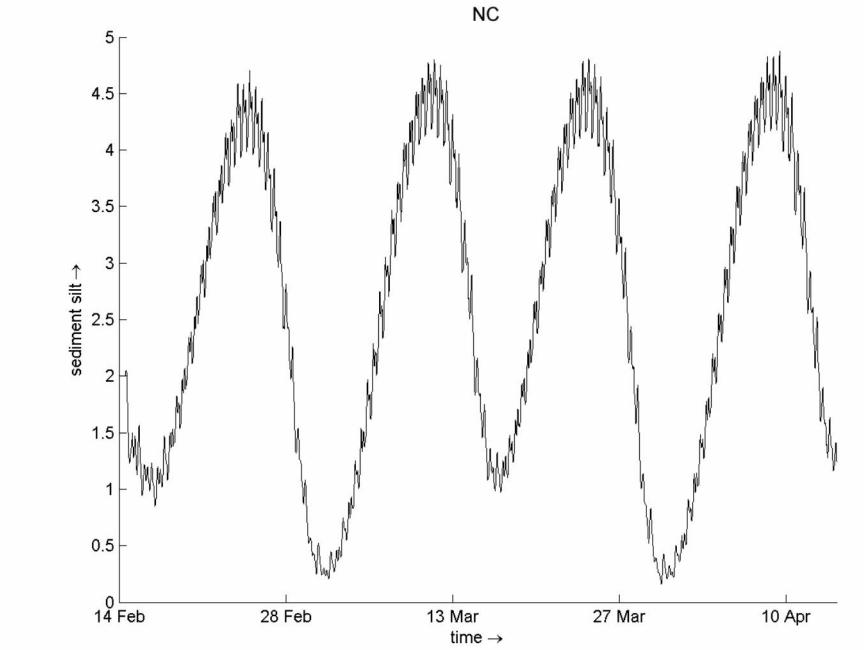

Figure D.70: 2Dh model results for sediment concentration for monitoring station NC, for a period of 2 months

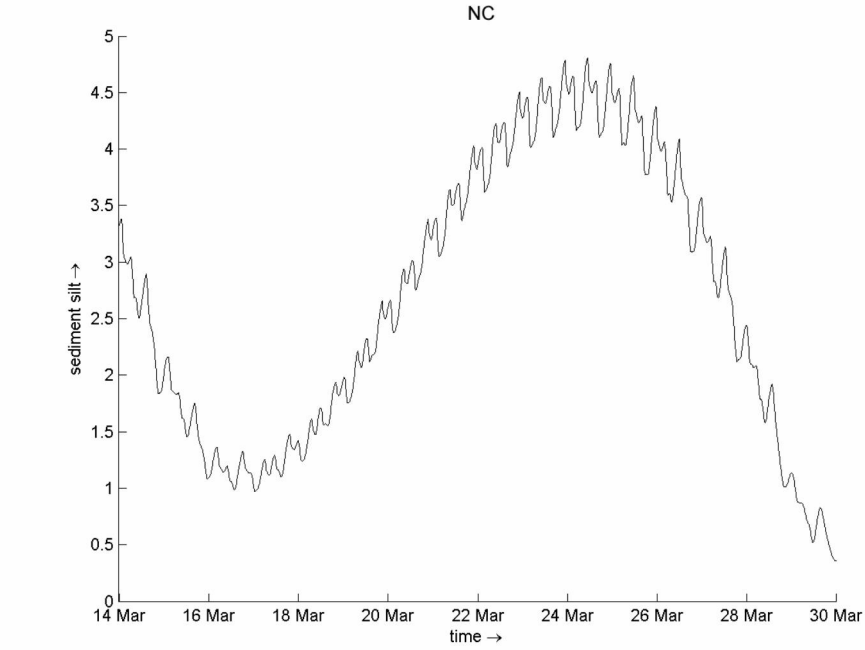

Figure D.71: 2Dh model results for sediment concentration for monitoring station NC, for 1 spring-neap tidal cycle

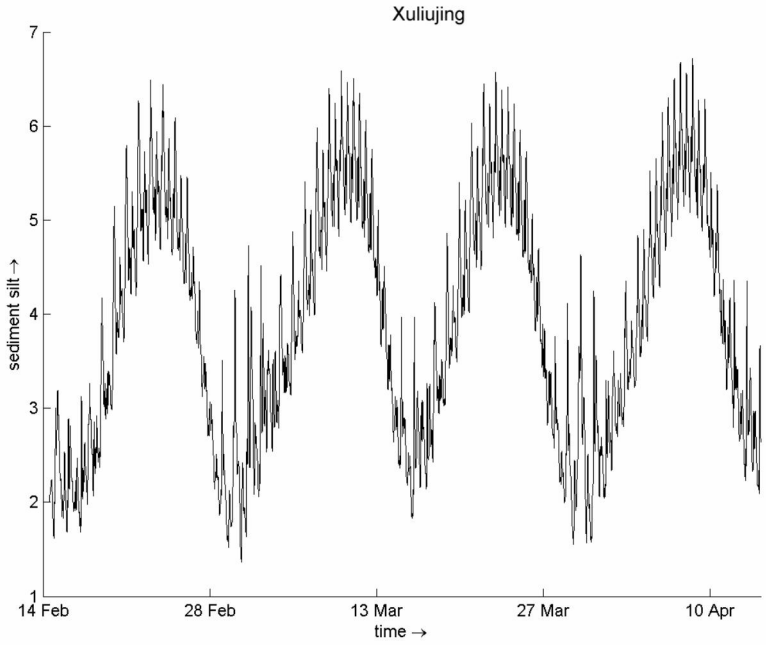

Figure D.72: 2Dh model results for sediment concentration for monitoring station Xuliujing, for a period of 2 months

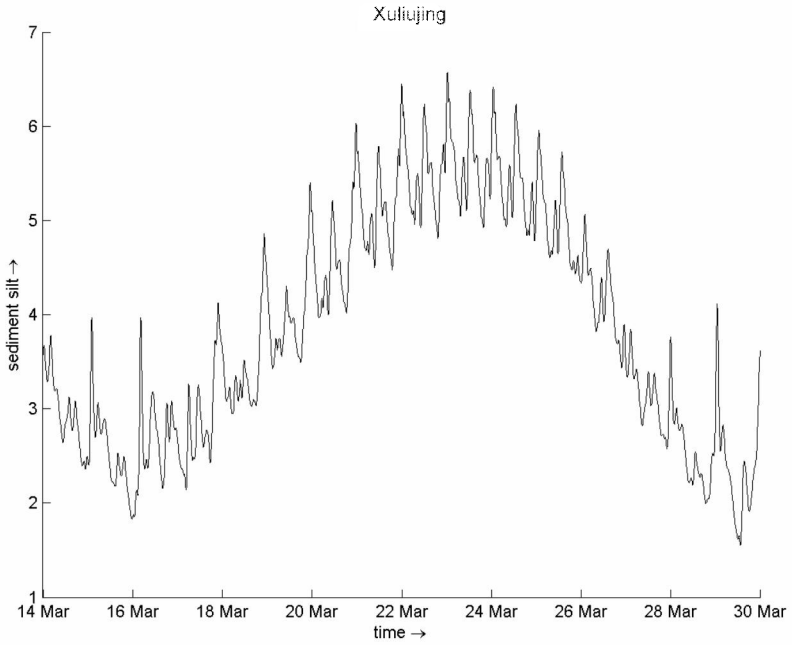

Figure D.73: 2Dh model results for sediment concentration for monitoring station Xuliujing, for 1 spring-neap tidal cycle

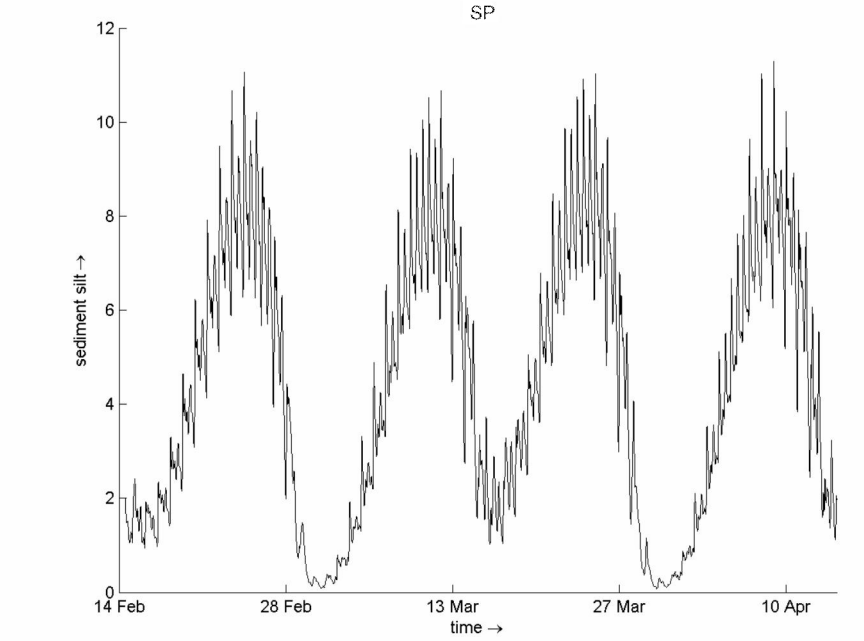

Figure D.74: 2Dh model results for sediment concentration for monitoring station SP, for a period of 2 months

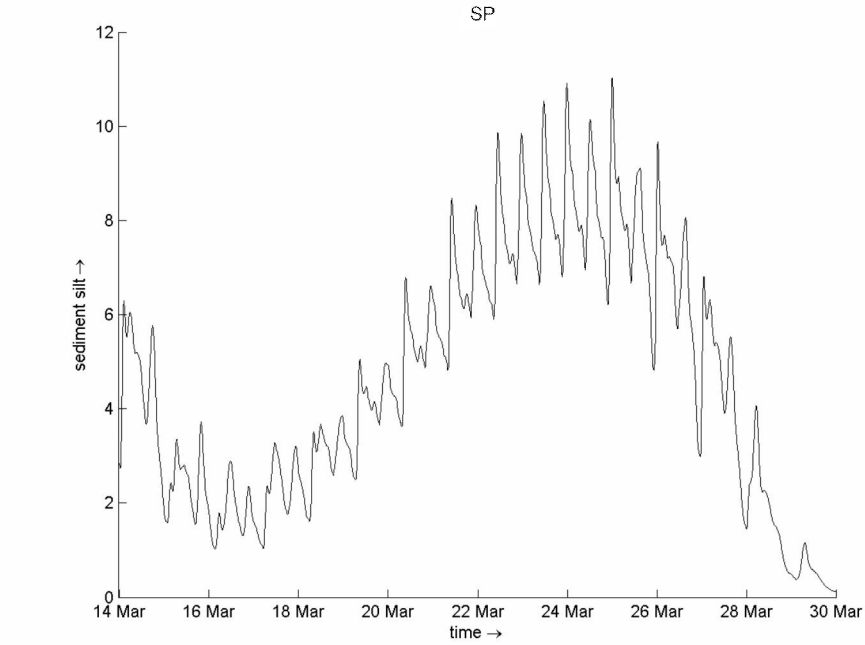

Figure D.75: 2Dh model results for sediment concentration for monitoring station SP, for1 spring-neap tidal cycle

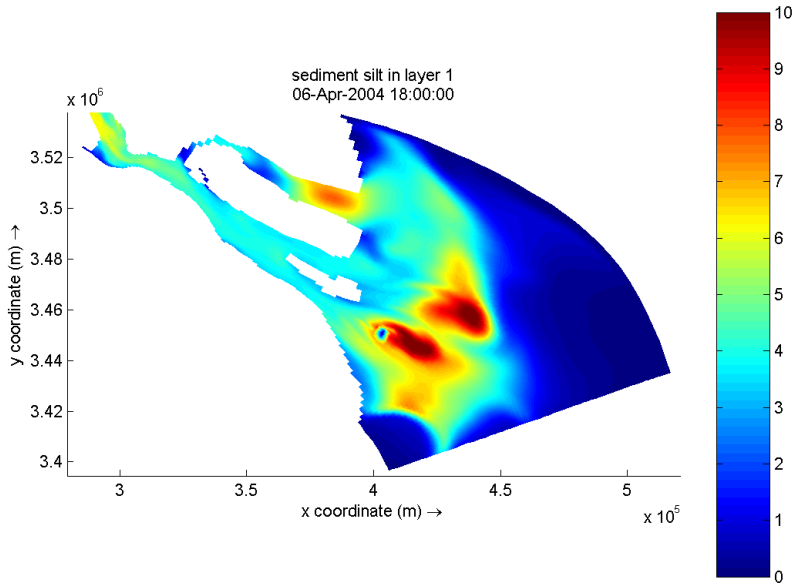

Figure D.76: 2Dh model results for horizontal suspended sediment distribution, Low Water, Spring tide

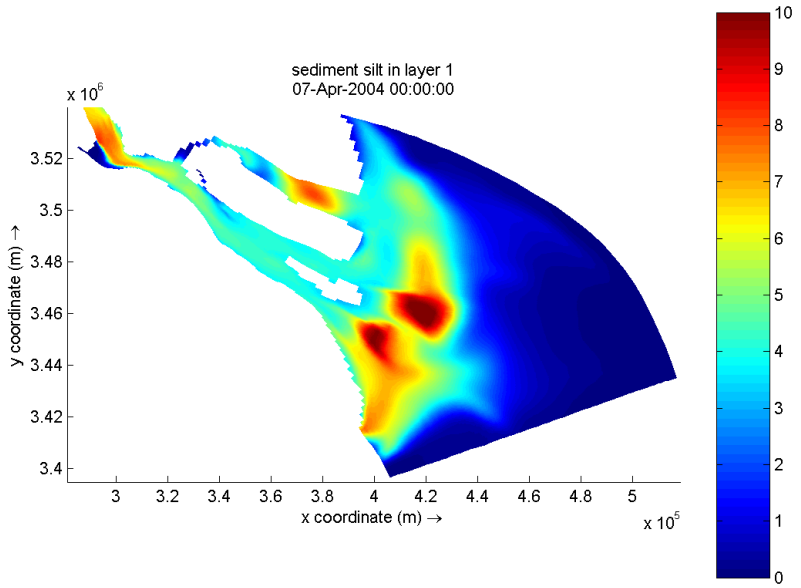

Figure D.77: 2Dh model results for horizontal suspended sediment distribution, High Water, Spring tide

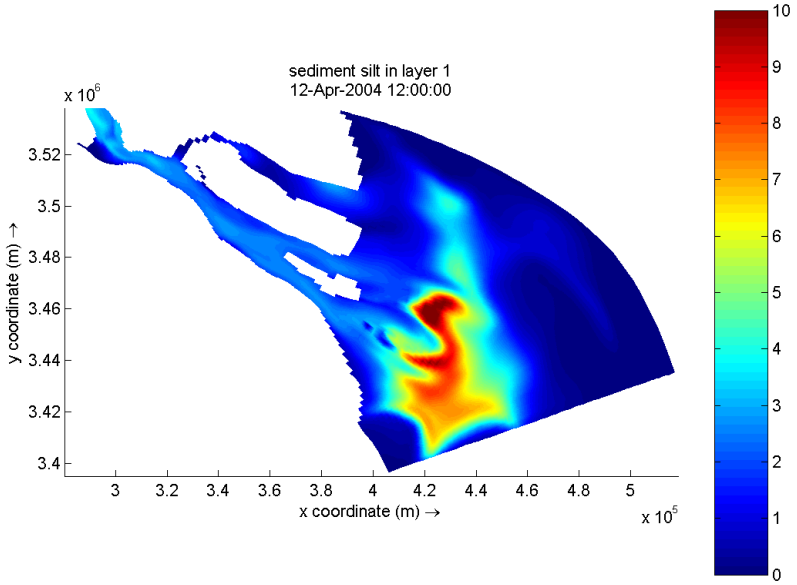

Figure D.78: 2Dh model results for horizontal suspended sediment distribution, Low Water,Neap tide

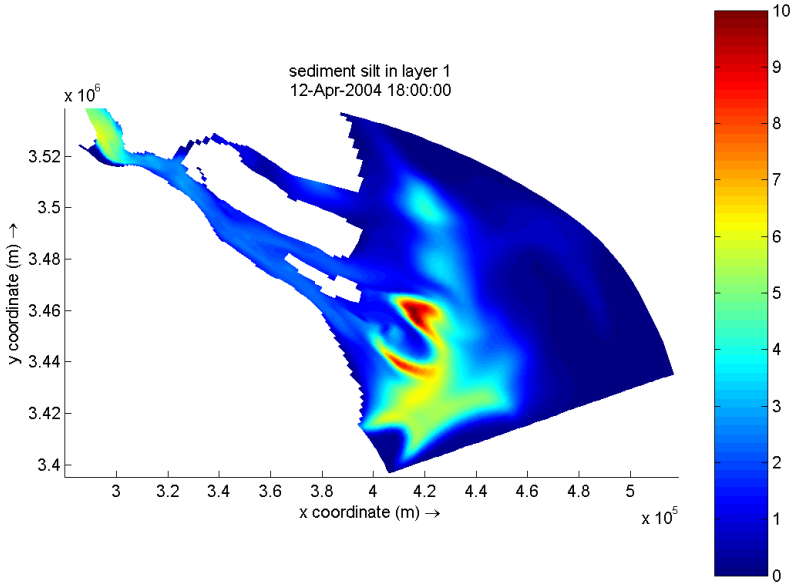

Figure D.79: 2Dh model results for horizontal suspended sediment distribution, High Water, Neap tide